Crystallinity of laser heated thermoplastic composite tapes

An experimental investigation into the development of degree of crystallinity in CF/PPS tapes during the heating phase of LAFP

Master thesis

Charlotte M. Iványi

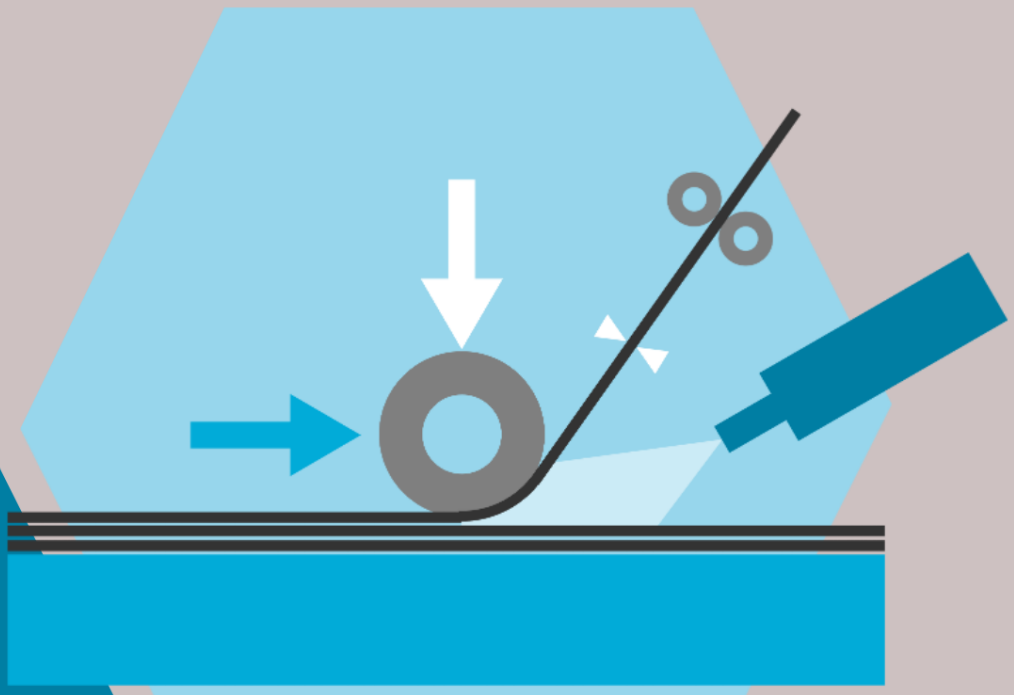

Delft University of Technology

TU Delft

Crystallinity of laser heated thermoplastic composite tapes

An experimental investigation into the development of degree of crystallinity in CF/PPS tapes during the heating phase of LAFP

by

Charlotte M. Iványi

to obtain the degree of Master of Science
at the Delft University of Technology,
to be defended publicly on Friday February 17, 2023 at 09:30 AM.

Student number: 4466942

Project duration: December 6, 2021 – February 17, 2023

Thesis committee:

Dr. Julie Teuwen,	TU Delft, Supervisor and Chair
Dr. Kunal Masania,	TU Delft, Examiner
Dr. Sergio Turteltaub,	TU Delft, Examiner
Alejandro Jimenez del Toro, MSc.,	TU Delft, Examiner

TU Delft

Preface

It is with great pleasure that I present my thesis report, the result of a challenging yet rewarding journey that I undertook over the past 15 months. During this period, I immersed myself in the field of polymer science and gained a deeper understanding of the complex kinetics and mechanisms governing the crystallization of polymers. My interest in the field grew throughout my thesis, and I can now honestly say I really enjoy reading scientific papers about polymer science. The experimental work was a true highlight of my thesis work for me. I devoted countless hours to laser heating of samples and even more time characterizing them, and I gained invaluable knowledge and hands-on experience in material characterization. The data analysis was a task that I initially underestimated, but it taught me a valuable lesson about the importance of thorough preparation and precise analysis that I will carry with me in the future. One of the biggest challenges I faced was academic writing, and I hope my dedication to improve in this area is reflected in the quality of my thesis report.

I could not have completed this journey without the invaluable guidance and support of my two supervisors, Julie Teuwen and Alejandro Jimenez del Toro. I always looked forward to our meetings, as they always left me with new ideas and renewed energy to keep going. I am extremely grateful to Julie for her patience, feedback and critical questions, that challenged me to think deeply and find the answers myself. Thank you for always guiding me towards the right path, even when I lost sight of the purpose of my thesis. I would also like to extend my heartfelt thanks to Alejandro, whose sharp inputs and extensive knowledge of polymer science played a significant role in the success of my thesis. Thank you for your dedication, and for always being available for questions and discussions.

During my thesis I spent a lot of time in the Delft Aerospace Structures and Materials Laboratory, and had the pleasure of getting to know the staff. I would like to especially thank Dave Ruijtenbeek and Alexander Uithol for their help with any problems that I faced, for always thinking along and for checking in regularly. I would like to thank Roy Awater for his support with the equipment in the physics lab and for the patience and time he took to help me. I deeply appreciate everyone from the staff for creating such a positive, friendly and supportive atmosphere.

I would also like to thank the members of my thesis committee for taking the time to review my work and for their interest in my research. Thank you Sergio Turteltaub and Kunal Masania.

A special thanks goes to my study friends Aike and Emma, their companionship and encouragement during the long study nights and stressful moments was invaluable. I would also like to thank the fellow ASM students in room NB1.07, for making the coffee and lunch breaks something to look forward to every day. Thank you Sian, Anup, Linde, Thom and Buse. You have all made this experience so much more memorable and enjoyable.

Last but not least, I would like to thank my boyfriend, parents, sisters and housemates for their unwavering love and support throughout my master's thesis journey. Thank you for being my biggest cheerleaders and for always believing in me.

Charlotte M. Iványi
Delft, February 2023

Summary

A growing interest in the use of thermoplastic composites (TPCs) in high-performance components is seen over the past decades, due to their numerous advantages compared to the widely used thermoset composites. These advantages include excellent damage tolerance, high fracture toughness, resistance to chemicals and solvents, recyclability, and the ability to be manufactured through in-situ consolidation. TPCs are particularly well-suited for fast automated manufacturing techniques, such as fusion bonding, which involves the application of heat and pressure. This makes TPCs a superior choice compared to thermoset composites, which require chemical curing processes to achieve the final mechanical properties and shape. The curing of thermosets is based on the use of an autoclave step, which is both expensive and energy-intensive, and requires a significant amount of manual labor.

Laser-assisted fiber placement (LAFP) is a promising manufacturing technique for thermoplastic composites, allowing for out-of-autoclave production and eliminating the need for post-consolidation steps in an oven, press, or autoclave. In LAFP, thermoplastic carbon fiber tapes are heated above their melting point using a laser heat source and are then placed into the desired layup by a robot, while being compressed by a pressure roller to generate intimate contact between the subsequent layers.

Although LAFP has many advantages, the technology is not yet ready for commercial use. One of the major limitations is the quality of the laminate produced and the degree of consolidation achieved. A key factor affecting the achieved intimate contact is the processing viscosity of the thermoplastic matrix. As the material is heated, the thermoplastic matrix softens and its viscosity decreases, making it easier for the surfaces to create a bond. In addition to temperature and pressure, the degree of crystallinity plays a crucial role in determining the processing viscosity and thereby affects the mechanisms that control the consolidation and laminate quality.

Despite extensive research on the polymer crystallization kinetics of thermoplastic materials, numerous knowledge gaps persist. The crystallization behavior of thermoplastics in fiber-reinforced composites, particularly in the context of rapid processing conditions in LAFP, has received limited attention in previous research. The state of crystallinity in rapidly laser-heated TPCs remains unknown, precluding the accurate determination of the matrix-fiber processing viscosity. This limits the ability to predict the achieved intimate contact and laminate quality in LAFP, making optimization of the process for industrial applications difficult. The focus of this thesis is therefore on investigating the impact of rapid laser heating on the crystallization of TPCs.

The experimental research work is divided into two primary phases. The first phase involves the production of laser-heated samples using an experimental setup equipped with a vertical cavity surface emitting laser (VCSEL) unit. During the heating process, a thermal camera is used to measure the surface temperature of the samples in real-time. Two types of samples are produced based on the heating, to temperatures either completely above or completely below the melting point. The results are used to establish the correlation between the applied laser input and the achieved sample temperature. The investigation revealed differences in heating and cooling times and rates, as well as temperature gradients within the sample.

The second phase involves characterizing the samples using various characterization methods. Differential scanning calorimetry (DSC) and X-ray diffraction (XRD) are used to study the crystallization state of the material and calculate the degree of crystallinity. Both the laser-heated samples and the as-received samples are analyzed to provide a comparative baseline. An increase in crystallinity is observed for all laser heated samples, regardless of whether they are heated above or below their melting temperature (T_m). For the samples heated below T_m and S-shaped correlation of the degree of crystallinity to the surface temperature as well as the heated time are observed. For the samples heated above T_m, lower levels of crystallinity are obtained compared to the samples heated below T_m and no correlation between the temperature evolution and crystallinity is identified.

Contents

Nomenclature

Abbreviations

Abbreviation	Definition
AFP	Automated fiber placement
ATP	Automated tape placement
CFRP	Carbon fiber reinforced polymer
CF/PEEK	Carbon fiber reinforced polyether ether ketone
CF/PPS	Carbon fiber reinforced polyphenylene sulfide
DOC	Degree of crystallinity
DSC	Differential scanning calorimetry
IR	Infra-red
LAFP	Laser-assisted fiber placement
PBT	Polybutylene terephthalate
PPS	Polyphenylene sulfide
TGA	Thermogravimetric analysis
TPC	Thermoplastic composite
VCSEL	Vertical cavity surface emitting laser
XRD	X-ray diffraction

Symbols

Symbol	Definition	Unit
m	Mass	[g]
t	Time	[s]
t_h	Heating time	[s]
t_c	Cooling time	[s]
T	Temperature	[°C]
T_d	Degradation temperature	[°C]
T_g	Glass transition temperature	[°C]
T_m	Melting temperature	[°C]
T_{m_0}	Equilibrium melting temperature	[°C]
$\dot{T}_h$	Heating rate	[°C/s]
$\dot{T}_c$	Heating rate	[°C/s]
V_f	Fiber volume fraction	[-]
W_f	Fiber weight fraction	[-]
X_c	Degree of crystallinity	[%]
ΔH_c	Enthalpy of cold-crystallization	[J/g]
ΔH_m	Enthalpy of melting	[J/g]
$\Delta H_{f,100\%}$	Enthalpy of fusion of 100% crystalline material	[J/g]
ρ	Density	[kg/m^3]
ρ_m	Matrix density	[kg/m^3]
ρ_f	Fiber density	[kg/m^3]
μ	Viscosity	[Pa.s]
$\tau_{1/2}$	Crystallization half-time	[s]
2θ	Bragg angle	[°]

1 Introduction

1.1. Background

The trend seen for technological innovations in the manufacturing industry is to make components lighter and stronger and processes faster and cheaper. These efforts have led to the successful implementation of composite materials such as continuous carbon fiber reinforced polymers (CFRP). Over the past decades, CFRPs have been increasingly used as a replacement for metals in structural and load-carrying components in aerospace, automotive, marine and wind applications. The main advantage of CFRPs is their high specific strength and stiffness, resulting in a reduction of structural weight. Additionally, they offer excellent durability and fatigue resistance, and a high chemical corrosion and wear resistance. Due to their great design flexibility and high anisotropy, complex optimized designs with tailored properties can be created, reducing the number of components in a part. These properties do not only result in weight reduction and strength increase, but also an extended lifetime of produced parts [1][2][3].

Thermoplastic composites

The two types of polymers used as matrix materials in structural composites are thermosets and thermoplastics. The fundamental difference between the two is their chemical microstructure. Thermosets form a rigid structure held together by strong chemical bonds referred to as cross-links, while thermoplastics consist of flexible structure held together by weak intermolecular forces and entanglements [4]. As a result they behave differently when exposed to heat, affecting their processing and the properties of the final product. At the moment, thermoset polymers are the preferred matrix material in high-performance structural applications.

The rigid thermoset is created from a viscous resin through an hardening process, referred to as curing. After curing, a cross-linked network is formed, making the structure of the polymer fixed and the cure process thermally and mechanically irreversible [5]. An advantage of thermosets is their low processing viscosity prior to curing, leading to high fiber volumes achievable in thermoset composites. In combination with their attractive properties, such as high thermal resistance and minimal compressive creep, this makes thermosets the currently preferred matrix material in high-performance structural applications.

On the downside, thermosets cannot be reshaped and offer limited recyclability after the completion of the curing process, due to the formed cross-links. Additionally, long production and curing cycles are required for structural parts, needed to achieve the desired composite microstructure and mechanical properties. Current manufacturing processes for thermoset composites rely on an autoclave step to cure the thermoset polymer, which is an expensive step due to the high amount of energy, time and manual labor involved [4].

A promising material able to overcome the need of a curing step and thereby achieve shorter cycle times are thermoplastic composites. Composite thermoplastic resins consist of long linear flexible chains

held together by entanglements and weak van der Waals forces, making the melting and solidification process reversible. The processing of thermoplastic prepreg composites is achieved through fusion bonding, during which heat and pressure are applied and polymer chains diffuse across the boundaries of the interfaces to form a bond. As a result, both solidification and consolidation are achieved in a single step, referred to as in-situ consolidation [4], and the need for a separate autoclave curing step is eliminated. Additionally, thermoplastics have a high impact resistance and excellent fracture toughness due to their flexible structure.

A number of disadvantages are related to the processing of thermoplastics. Due to the high processing viscosity and temperature of thermoplastics, they cannot be used in liquid composite moulding processes, currently widely used to produce large structural thermoset components [4]. Additionally, the lack of tack and drape of thermoplastic composite prepregs increases the generation of defects. Especially out-of-plane buckling is observed, as the lack of tack decreases the strength of the attachment of the prepreg to the substrate [3][6].

So far, thermoplastic composites have been mainly used for the production of small structural components and substructures, such as the inboard leading edge of the Airbus A380 and the floor panels of various aircraft, including the Airbus Beluga transport aircraft or the Gulfstream G400 and G500 business jets [7]. The size of these parts and the production rates achieved are still very low in comparison with thermosets. This makes the product development of thermoplastic composites expensive and time consuming, and the possibility of further (large-scale) applications of the technology limited. With a deeper understanding of the materials and processes at a fundamental level, thermoplastics do have the potential to be a more cost-effective alternative to thermosets and provide higher production rates with more sustainable resources [8].

Laser-assisted fiber placement (LAFP)

In order to achieve the higher production rates driven by the growing global demand for composite parts, not only the right material is needed, but also a suitable combination with a production process. The production volumes of structural composites are currently limited due to two main reasons. Firstly, a great amount of manual labor is involved in the layup and curing process of composite parts, especially for large structures used in the aerospace, marine or wind energy industry. Secondly, long curing times, usually using an autoclave, are associated to the use of thermoset polymers [1].

These limitations have resulted in the development of automated manufacturing processes, decreasing the amount of manual labor throughout the manufacturing process, and the development of thermoplastic matrix materials, eliminating many disadvantages related to thermosets and providing the option of out-of-autoclave (OOA) in-situ consolidation and welding. Both these developments set out to contribute to the increase of production volume, but currently still lack in maturity to achieve the same level of quality as thermoset autoclave-cured parts.

A promising manufacturing method combining automated lay-up, in-situ consolidation and the use of thermoplastics is Laser-Assisted Fiber Placement (LAFP). The method can be classified as additive manufacturing as it builds a part ply by ply. The thermoplastic composite prepreg tape is heated above its melting temperature and subsequently compressed by a compaction device. This way the melted tape is bonded with the previous layer and in-situ consolidation takes place continuously as the part is built up. With this method the post-consolidation step in an autoclave, oven or press can be omitted and therewith a potential reduction in cycle time, energy consumption and cost. Thanks to the automated robotic deposition head supplying the prepreg tapes, optimized structures can be manufactured by steering fibers and material waste can be reduced by producing near net shape components [9].

For LAFP to be successfully used as a manufacturing technique for large structural components, a sufficient part quality must be achieved with economically beneficial cycle times, both depending on the industry of application. The part quality is used as a general term for the combination of desired end-product properties. Many industries have fixed requirements for the mechanical and structural properties of the components used, making the part quality an important factor in the development of thermoplastic composites and LAFP. The part quality depends on various parameters, such as the void content and the degree of crystallinity. A lower void content is achieved for well consolidated parts with a high degree of intimate contact between the layers and plays an important role in the final mechanical properties [10]. A higher degree of crystallinity also affects the mechanical properties, such as the

stiffness and tensile strength [11].

The achieved quality of a part produced with LAFP is linked to a large number of phenomena occurring during the process. Due to the high speed of the process these phenomena are interconnected and result from the three phases of LAFP: the heating, consolidation and cooling phases. The crystallization mechanisms observed throughout the process are linked to all three phases, making the understanding of LAFP very complex and currently still limited [9].

1.2. Motivation

So far, full in-situ consolidation, defined as a composite part with less than 1% void content and perfect bonding between plies, has not yet been achieved using LAFP. A commonly assumed reason for this is the insufficient reduction in the thermoplastic viscosity at the rapid heating rates, causing a low mobility of polymer chains needed to create a bond [12]. As the viscosity of semi-crystalline polymers is highly influenced by the crystallinity [13], the crystallinity has both a directly affect on the part quality and properties, as well as indirectly affects the consolidation quality. This makes it highly interesting to study and better understand the process of crystallization during LAFP, at rapid heating and cooling rates.

At the moment, the knowledge about the processes taking place within the material before compaction is limited, making the prediction of degree of intimate contact and consolidation inaccurate. A deeper understanding of the crystallization taking place during LAFP is a first step in better understanding the material reaction to the rapid laser heating and improve the accuracy of used models.

1.3. Outline

The aim of this thesis is to contribute to the understanding of the crystallization mechanisms that play a role during LAFP, by investigating the effect the temperature evolution as a result of the laser heating phase on development of crystallinity.

Chapter 2 provides a concise version of literature review conducted, which is split up into two main parts. The first part gives a general overview of the LAFP process and the significance of crystallinity. The second part delves into the current state of knowledge on polymer crystallinity in more detail. Based on the literature assessment, the gaps are identified and the research questions and hypotheses are formulated in Chapter 3. Chapter 4 presents the methodology used for the research, and describes the experimental set-up, used material and characterization methods employed. The temperature measurement results are presented in Chapter 5, and the effect of laser heating on the temperature evolution in the tape is discussed. In Chapter 6, the crystallinity characterization results are shown and a thorough discussion on the effect of temperature evolution on the degree of crystallinity provided. Finally, in Chapter 7 the research is concluded and recommendations for the direction of further research presented.

2

Literature review

In order to identify the state-of-the-art and gaps in knowledge about the LAFP process and specifically the crystallinity of samples produced using LAFP, a background literature study is performed. In this chapter a concise version of the literature review is presented, containing the general background information about LAFP and further focusing on the main phenomena of polymer crystallization.

First, the working principle of LAFP is presented in Section 2.1. The following topics are discussed in this section: the process phases, the process variables and the parameters affecting the final laminate quality. The second section of the literature review focuses on the crystallization process of polymers and reviews the available literature about polymer crystallinity studied during LAFP or similar processes.

2.1. Laser-assisted fiber placement

Laser-assisted fiber placement (LAFP) is a manufacturing technique based on automated fiber placement (AFP) technology. This process allows for in-situ out-of-autoclave consolidation, occurring dynamically as the tape or laminate are in motion with respect to the heating and consolidation device.

The LAFP process was first demonstrated in the late 1980s by Beyeler et al. [14] and has gained renewed interest in recent years due to its high energy efficiency and precise control of the laser heating device, as compared to other AFP processes. This allows for efficient and accurate heating of only specific regions of the material, reducing cycle times and energy consumption, and ultimately reducing the cost of manufacturing [1].

However, to be competitive in industry, LAFP with in-situ consolidation must be able to achieve part performance comparable to autoclave-produced parts at feasible process speeds [15]. The feasible process speed is dependent on the industry of application and cannot be easily quantified. In previous research a wide range of placement speeds between 10 and 400 mm/s has been studied [16]. So far, acceptable quality has only been reported for placement speeds up to 100 mm/s, while the feasible placement speeds for industry are often higher, in the range of 200 to 800 mm/s [17][18].

2.1.1. Process phases of LAFP

LAFP consists of three main phases, namely heating, consolidation, and release or cooling, as shown in Figure 2.1. The process starts with the fiber tow being fed through a deposition head to the surface of the tool or previous substrate layer. Clamps and rollers are used to guide the tape to the right place on the tool, achieving a highly precise fiber alignment. A laser heat source is used to heat both the incoming tow and the substrate, after which the two melted surfaces are brought together at the so-called nip point and pressure is applied by a compaction device, resulting in intimate contact and a bond between subsequent layers of the lay-up [1].

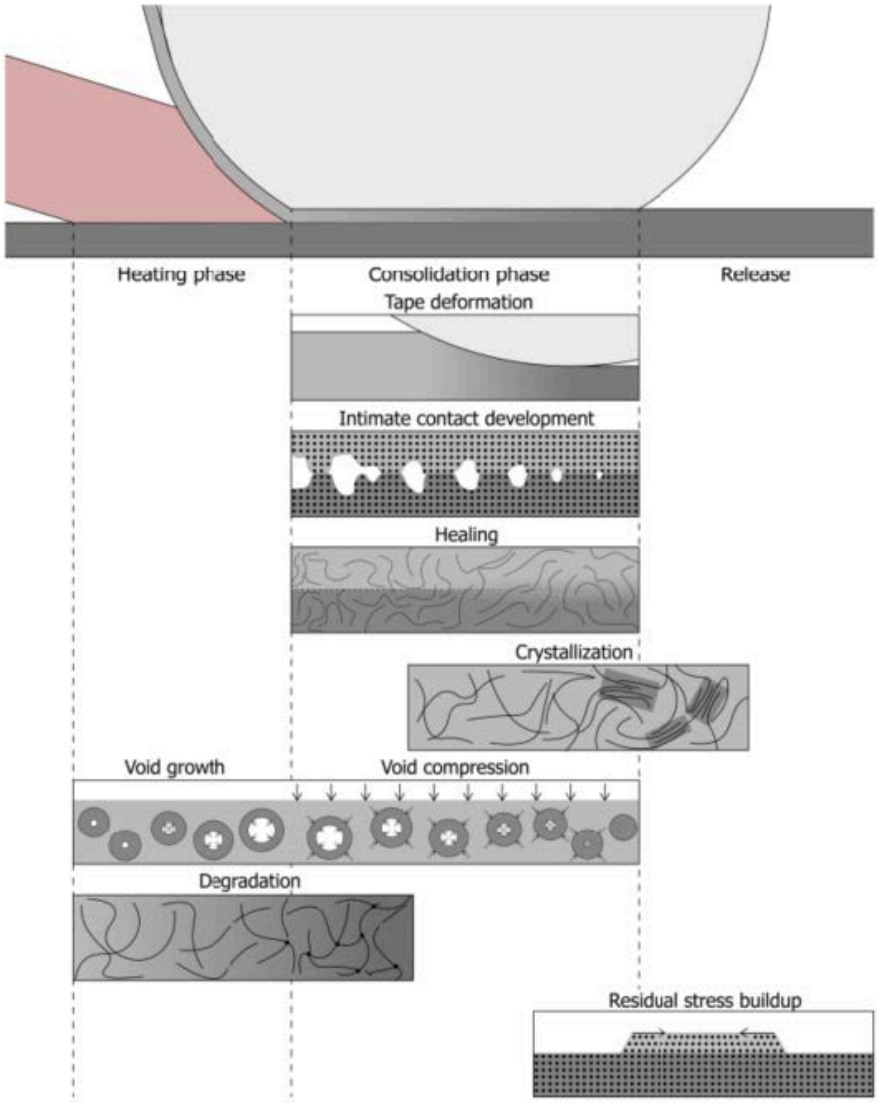

Figure 2.1: Overview of the phases of the LAFP process and related governing mechanisms [19]

Heating

During the heating phase the incoming tape and substrate are continuously heated by the laser at a rapid rate controlled by the placement speed. The resulting tape and substrate temperature is dependent on the thermal properties of the material, including heat capacity and thermal conductivity, as well as surface roughness and fiber distribution. The main process variables affecting the temperature are the laser intensity, incidence angle and distance, the heated spot size, the shadow region, the placement rate and the boundary conditions, such as the tool temperature and material and the ambient temperature. These variables do not only affect the surface temperature but also the laser energy penetration depth and thereby the heat soak and through-thickness temperature distribution [15].

As no pressure is applied during the heating phase, certain phenomena can be observed. As the temperature increases in the tape, voids and volatiles in the material are allowed to expand, due to the release of elastic energy stored in the fibers and the thermal pressure building up in the voids. When the tape reaches the glass transition temperature (T_g) thermal deconsolidation of the tape takes place, caused by the melting of the amorphous phase and a decrease in elastic modulus of the thermoplastic. Thermal deconsolidation is characterized by an increase in tape thickness due to fiber decompaction, increase in surface roughness and tape waviness and increase in void content [20]. When heated further the melting temperature T_m is reached, marking the transition of a solid phase into a liquid phase. If no pressure is applied, the material stays in a severely deconsolidated state above T_m, but out-of-

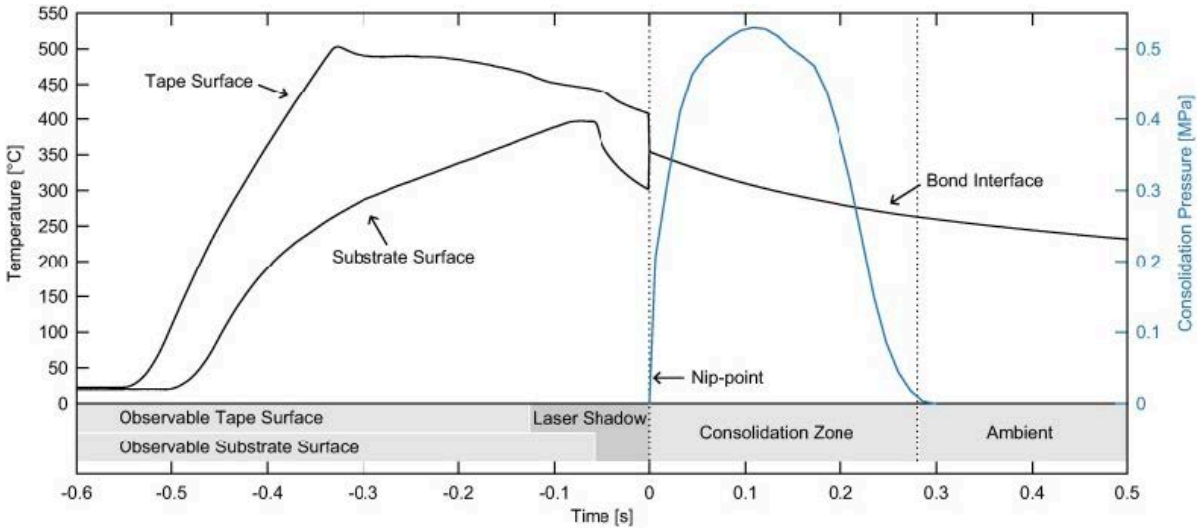

Figure 2.2: A typical temperature distribution during the phases of the LAFP process [16]

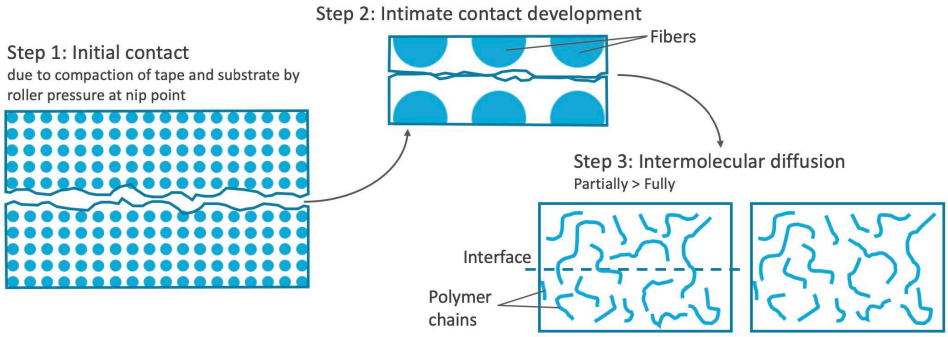

Figure 2.3: Mechanism of bond development in LAFP (adapted from [23])

plane deformations are limited as they cannot be structurally supported by the melted polymer. In the case that the tape is exposed to extremely high temperatures above the degradation temperature (T_d) thermal degradation will occur, resulting in changes in the chemical structure of the material, like chain-scission, branching and cross-linking, having a negative effect on the performance of the final laminate [21].

The nip-point is the location where the incoming tape and substrate meet at the end of the heating phase. As it lies in the shadow region in which the laser beam is blocked by the geometry of the roller and no longer heats up the tape and substrate, the maximum temperature is reached before the “actual” nip-point at the “visible” nip-point. How much the tape cools between these points depends on a number of factors, such as the geometry of the roller and tool, the process speed, the composite material properties and laser wave length [22]. Additionally, the temperature of the tooling and surrounding material affect the nip-point temperature through heat transfer.

In the plot in Figure 2.2 a typical temperature distribution is shown. The temperature of the tape and substrate at the nip-point, but also the related viscosity and crystallinity of the material, are the input variables for the next phase, the consolidation. Therefore, the heating phase parameters are determining for the final laminate quality and properties achieved.

Consolidation

The consolidation phase starts at the nip-point, where the incoming heated tape and substrate meet. At this point pressure is applied by the compaction roller, deforming the tape and substrate to align with each other and develop intimate contact. This allows the polymer chains to diffuse across the interface between the layers, referred to as autohesion or healing, and create a bond. Provided the polymer

chains have enough mobility and sufficient pressure is applied for a sufficient time, the interface between the substrate and tape completely disappears and a full bond can be obtained. The steps of the autohesion mechanism of two interfaces is shown in Figure 2.3. Additionally, tape deformations on the top surface of the tape are flattened by the compaction roller, such as the roughness created by the deconsolidation process, and the expanded voids are compressed again.

Apart from compression, cooling and solidification take place due to heat dissipation from the tape to the roller, gradually increasing the viscosity and elastic modulus of the thermoplastic matrix. As a result, residual stresses are built up in the compressed tape, as it is only locally heated and compressed. If the temperature drops too fast, the high viscosity can prevent the surfaces from creating intimate contact and the voids from compacting. On the other hand, if the temperature is too high and still above T_m when the compaction pressure is removed, voids can expand again due to the low viscosity.

The consolidation phase parameters have a direct effect on the degree of intimate contact developed, but also affects the cooling of the material and thereby final laminate properties such as the degree of crystallinity (DOC) and void content. It can again be stated that the consolidation phase is determining for the final laminate quality and properties achieved.

Release

Finally, the pressure is removed as the roller loses contact with the tape. After this the temperature further decreases and the process of crystallization and thermal and residual stress build-up in the material continues. The rate at which the material cools is determined by the previous phases and surrounding temperature of the atmosphere, tool and laminate. The cooling rate strongly affects the final laminate properties such as the DOC.

2.1.2. Process variables

LAFP is considered a complex process in terms of the wide range of parameters and mechanisms occurring. To achieve consistent and high-quality results, the process requires precise control of several variables, including laser intensity, incidence angle and distance, heated spot size, shadow region, placement rate, and boundary conditions. Additionally, the process must be optimized for the specific material and application being used, as the properties of the material and desired end-use requirements will affect the process parameters and outcome [1].

A summary of the variables affecting the outcomes of the LAFP process can be found in Table 2.1. They are divided into three main groups, related to the set-up, the material, and the processing, and will be further discussed in more detail in the following sections.

Table 2.1: Main LAFP variables affecting the outcomes of the process [1][24][20]

Set-up			Material	Process
	Hardware	Settings		
Laser	• Laser type • Incidence angle • Distance from laser to substrate / tape	• Heating intensity • Intensity variation • Heating spot size	• Fiber material • Resin material • Tape geometry	• Placement speed • Preheating operations
Compaction roller	• Compaction roller material • Compaction roller shape • Number of rollers	• Compaction force • Compaction roller temperature	• Fiber volume fraction • Fiber distribution • Thermal history dependent properties	
Tool	• Tool material	• Tool temperature		

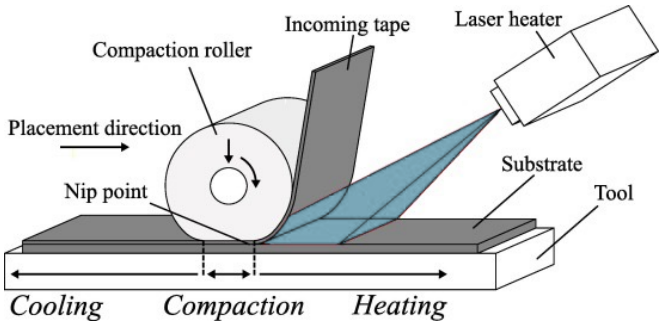

Figure 2.4: Three main LAFP tools: laser heater, compaction roller and tool

Material

Both the choice of material, as well as its specific as-received properties have a big effect on the LAFP process. Parameters such as DOC, fiber volume content, melting and glass transition temperatures, thermal conductivity, heat capacity and optical properties can vary for different tapes of the same material, as they depend on the way of manufacturing and the thermal history of the composite [25]. Based on the selected composite material, some of these properties can fixed or limited in range. Additionally, the geometry of the used tape influences the process, depending on the tape thickness and width, but also less obvious properties such as the surface roughness.
As laser heating is used, the choice of reinforcement fiber material is limited. The reason for this is that thermoplastics are optically transparent for the wavelength of laser radiation, and therefore do not heat up directly from the laser radiation. Carbon fibers are on the other hand highly absorbing, and therefore generate heat upon laser radiation, which can further heat up the thermoplastic matrix through heat conduction [26]. Glass fiber reinforced thermoplastics cannot be used in combination with a laser heat source, as glass is also transparent to laser irradiation, and are therefore unsuitable for LAFP.

The thermoplastic matrix material used during this thesis is **polyphenylene sulfide (PPS)**, a semicrystalline thermoplastic polymer with symmetric rigid backbone consisting of aromatic rings linked by sulfides, as shown in Figure 2.4. It exhibits several appealing physical and chemical properties, such as high thermal stability, excellent flame and chemical resistance and dimensional stability, high modulus and tensile strength and good friction properties. Compared to other thermoplastics, PPS has a relatively low melting viscosity (200 Pa.s), which makes the material a good choice for products with high fiber content. Low viscosity also positively affects the degree of intimate contact developed, easing the material flow at the layer interfaces [21]. The T_g of PPS lies at around 90°C and melting occurs at a T_m of around 285°C [27] [28] [29] [30]. In combination with reinforcement fiber, carbon fiber reinforced polyphenylene sulfide (CF/PPS) is a perfect material for thermoplastic structural components. To date, PPS composites (both carbon and glass fiber reinforced) have been used mainly in aircraft structural applications, such as in wing structures of the Airbus A340-500/600 [31] [32].

Hardware

In Figure 2.4 the tools used in a LAFP configuration are shown. Three main tools are needed: a heating device, specifically a laser, a compaction device, often in the form of a roller, and a tool or mould defining the shape of the final part. All three components will be discussed in this section in more detail.

Using a laser heating device as **heat source** has multiple advantages. Compared to alternatives, such as a hot gas torch or IR (infra-red) devices, lasers provide the highest heating efficiency with shortest response time. These have an effect on the placement velocity, allowing not only extremely fast tape placement, but also large variations in placement speed useful in complex geometries. Additionally, lasers provide a high energy density that can be localized to a precise region, providing focused controlled heating. As a result, the induced stresses and material damage can be minimized. On the downside, lasers are expensive and require strict safety precautions and equipment. Laser heating systems are typically large, limiting the complexity of the parts produced [33] [14].

The thermal state achieved by laser irradiation heating is determined by the optical properties of the composite material, governed by the absorption and scattering characteristics of its individual components and its structural arrangement. Since thermoplastics are optically transparent to the wavelength

of laser radiation, the heat absorption is entirely controlled by the reinforcement fibers. The laser light is either directly absorbed by the carbon fibers on the surface of a heated sample, or scattered and absorbed by the neighboring fibers. Due to the structure of composites, almost complete absorption can be achieved in the first few fiber layers, leading to a high amount of energy concentrated at the surface. This results in steep temperature gradients observed in laser-heated composites [34].

Based on different studies, three main laser parameters influencing the quality of the LAFP produced laminate have been indicated. These are the laser power, laser angle, and laser spot size (controlled by both the laser settings as well as distance between laser and substrate). With different combinations of these parameters, an endless variety of heating profiles in terms of size and shape can be obtained [35].

The primary function of the **compaction roller** is to control the placement of the fibers or tapes and apply a force pressing the melted layers together, resulting in development of intimate contact and suppressing of voids. A secondary function of the roller is the cooling of the substrate after melting. The temperature and material of the roller affect the heat dissipation from the tape. The final layup quality is affected by the stiffness and architecture of the rollers, determining among others the applied pressure, time of consolidation, cooling rate and casted shadow prior to the nip point [1].

As thermoplastics are processed at high melting temperatures the compaction roller must be able to sustain these temperatures as well. For this reason, steel is the most commonly used material for rollers, however silicone rollers have been used as well on more complex shapes [1]. Different types of roller geometries are available, ranging from the simplest single roller set-up to more complex multiple roller systems and area compactors. Systems with a single roller can potentially suffer from higher void contents, mostly seen in the last layers of the laminate. This can be avoided by using a set-up with multiple rollers or adding a repetitive pass [33].

The term **tool** is used in LAFP for the surface or mold the lay-up is placed on. Tool material and temperature are the main two factors affecting the process outcome, as they influence the heat transfer in the tape. Depending on the tool material and temperature, a certain amount of heat can dissipate from the substrate to the tool. To control the temperature of the tool, heated tools are used. The maximum temperature of the tool is usually below the T_g of the laid down tape. This ensures the amorphous part of the compacted tape stays in the glassy state and prevents unwanted changes in the microstructure [26]. The effect of the tool material and temperature is more visible for thin laminates. For thicker laminates only the lower layers are affected by the tool.

Process speed

In addition to the above discussed hardware selection, the speed of the process is a key factor affecting the final laminate properties. To achieve full bond development between the layers, sufficient dwell times above the bond development temperature in combination with ample consolidation pressure are required. This means the laser does not only have to provide enough heat to the surface but also enough heat soak, defining how well the material can retain the high temperature. The process speed directly affects the the time available for heating, and thereby the heat soak. For higher process speeds, a reduction in heat soak is observed, resulting in faster cooling during the consolidation and release phase. The increase in cooling rate negatively affects the development of intimate contact and limit the crystallization process [16].

Effect of variables on heating and cooling rates

Some of the most important parameters affected by the process variables are the heating and cooling rate. The achieved rates depend on all three categories, as they are the result of the selected material and its properties, the laser heater settings, the compaction roller, tool and ambient temperatures, and the placement speed.

The typical heating and cooling rates for LAFP are determined based on the experimental work performed by Comer et al. [17] and Stokes-Griffin and Compston [16], both done using carbon fiber reinforced polyether ether ketone (CF/PEEK). Comer et al. analyzed the temperature distribution during processing with a placement speed of 133 mm/s and a laser power that resulted in a top surface temperature of 420°C. Under these conditions, they observed heating rates of approximately 440°C/s and cooling rates of 430°C/s during the consolidation phase and 124°C/s during the release phase.

Stokes-Griffin and Compston a laser power of 745W at a speed of 100 mm/s, resulting in a heating rate of 2150°C/s for the placed tape and 900°C/s for the substrate, and a cooling rate of 250°C/s. The temperature profile they obtained is illustrated in Figure 2.2.

In conclusion, a wide range of heating and cooling rates are relevant for LAFP. Still, the heating and cooling rates extensively studied in literature are significantly lower compared to the rates reported by Comer et al. [17] and Stokes-Griffin and Compston [16]. This could have a significant impact on the observed phenomena and process outcomes. As a result, the findings from studies conducted at lower rates cannot be directly applied to LAFP.

2.1.3. Laminate quality

The term ”laminate quality” refers to the overall mechanical performance of a laminate, which is determined by various physical parameters, including the void content and the DOC. High DOC and low void contents are considered favorable as they result in enhanced mechanical properties, such as increased stiffness, shear strength, and tensile strength. Numerous studies have documented the effect of LAFP processing on these parameters and their impact on the laminate's mechanical behavior [31][11][36].

Thermal deconsolidation

Thermal deconsolidation is a crucial process that occurs in fiber-reinforced thermoplastic composites, when heated above their glass transition temperature without the application of pressure. As such, it has a significant impact on the achieved laminate quality during LAFP, specifically during the heating phase. During thermal deconsolidation, the matrix becomes soft, allowing the fiber reinforcement to decompact and realign, and the resin to migrate. This can lead to meso-structural disintegration and a reduction in mechanical properties of initially well-consolidated composites. The changes observed in the meso-structure include void formation, delamination, buckling and surface roughening [37].

The driving forces behind the deconsolidation originate during the manufacturing of the sample. To produce a composite prepreg sheet, external load is applied to compact and compress the fibers, squeeze air and resin out, suppress voids, and increase the fiber volume fraction. During this process elastic energy is stored in the fibers in the form of residual stress. This energy is released as the thermoplastic resin softens when above T_g, resulting in the decompaction of the fiber bed. As stated by Ye et al., the release of elastic energy is considered as the dominant force driving the void growth during deconsolidation [38].

Brezeski and Mitschang summarize the main causes affecting deconsolidation based on literature in four points. These are the decompaction of the fiber reinforcement network due to the release of residual stresses, the thermal expansion of the matrix due to viscoelastic behavior, the expansion of voids due to thermal expansion and internal void pressure and the shrinkage and coalescence of smaller voids into larger voids due to surface tension [39].

Deconsolidation for rapid heating rates, as observed during LAFP, has been studied by Çelik et al. Significant changes in the micro- and meso-structure of the tape for heating times of as little as 0.2 and 0.8 seconds are observed, confirming that rapid laser heating also results in deconsolidation. The changes observed include increases in surface roughness, out-of-plane deformation, width, void content and thickness [15].

Bussink studied three different levels of deconsolidation: as-received samples, slight deconsolidated samples heated to temperatures between T_g and T_m, and highly deconsolidated samples heated above T_m. A small increase in surface roughness was found between the as-received and slightly deconsolidated sample. For the highly deconsolidated sample a severe increase in roughness was observed, while a more gradual increase was observed for the void content and waviness of the sample [40].

Void content

Currently one of the biggest challenges regarding the quality of in-situ consolidated LAFP laminates is their high void content. The voids can either develop and grow as a reaction to the heating of the tape or already be present in the initial tape. Based on the location of the voids in a laminate, they can be split into interlaminar voids between the plies or intralaminar voids within a ply. The intralaminar voids are related to the void content in the initial tape. As the quality of the raw thermoplastic materials has increased over the past years, this type of void content has been almost completely eliminated [19]. The interlaminar voids are on the contrary still strongly present in LAFP laminates and caused

by insufficient bond quality between the tape and substrate [17][1]. So far, a minimum void content of 1.4% achieved for placement speeds of 133mm/s has been reported by Comer et al. [17], and an increase in reported void content is observed as the studied placement speeds increase. To put this value into perspective, the void content acceptance criterion set for aerospace applications is 1% for primary load-carrying structures [41].

Degree of intimate contact

The interlaminar physical properties of the laminate are related directly to the quality of the bond between subsequent layers. Among the first to describe the bond mechanism of thermoplastic composites were Dara and Loos, who divided the process into two steps: the creation of intimate contact followed by adhesion, as shown earlier in Figure 2.3. The prerequisites for autohesion to take place are a random entangled chain network and macromolecules able to move within the bulk material. The strength of the bond is a function of three processing parameters: applied pressure, temperature and time of contact [42].

During the first step of the bonding process intimate contact is established, which is necessary for the subsequent autohesion to take place. During this step, at temperatures above T_g localized deformations occur making the bonding surfaces fit on macroscopic level. The strength of the bond is then developed during the next autohesion step. As a result of the increased molecular free volume at temperatures above T_g, the polymer chains can move freely and diffuse across the interface. At long contact times, in combination with the right pressure and temperature applied, the increase in penetration depth of diffusing chains results in complete interfacial diffusion and the interface no longer detectable in the bulk material [42].

Mantel and Springer present a simplified expression for the degree of bonding shown in Eq. 2.1, where D_{ic} is the degree of intimate contact and D_{ah} the degree of autohesion [43]. As a simplification, instantaneous autohesion is often assumed, as its completion is two orders of magnitude faster as compared to the development of intimate contact [23]. In other words, the degree of intimate contact can be considered to be the main parameter used to quantify the bond quality.

$$D_b = D_{ic} D_{ah} \approx D_{ic} \tag{2.1}$$

Several models have been proposed for the intimate contact development, most of which are based on the transverse squeeze flow of surface asperities. In these models it is assumed that the flattening of the surface asperities is the governing mechanism behind the intimate contact development. As the surface asperities are squeezed they increase in width and the distance between them decreases until the point where they touch and full intimate contact can be obtained. These models suggest that other mechanisms, such as percolation flow and fiber bed compaction can be neglected [19]. In squeeze flow models, the surface asperities are modeled as rectangles. In Figure 2.5 the most simple surface geometry representation is shown, with uniform asperity dimensions. With this model the intimate contact can be rewritten as shown in Eq. 2.2 [19], where a_0, b_0 and w_0 are the initial height, width and gap between in the asperities respectively and $a(t)$ and $b(t)$ are the height and width of the asperities varying over time. The two forms of the equation are related through the fact that the volume of the asperities remains constant and $a_0 b_0 = a(t)b(t)$.

$$D_{ic} = \frac{b(t)}{b_0 + w_0} = \frac{a_0/a(t)}{1 + w_0/b_0} \tag{2.2}$$

Apart from a representation of the surface geometry, the inputs needed to determine $b(t)$ and calculate the intimate contact are the applied pressure (indicated in Fig. 2.5 with the letter P) and the material viscosity of the fiber-matrix. The equation used by Mantel and Springer used for this can be found in Equation 2.3 [43]. The newly introduced variables in this equation are the applied pressure P_{app}, fiber matrix viscosity μfm and the contact time t_c during which pressure is applied. This equation shows the dependence of the achieved degree of intimate contact on the time-dependent viscosity.

$$\begin{aligned} D_{ic} &= \frac{1}{1 + \frac{w_0}{b_0}} \left[1 + 5 \left(1 + \frac{w_0}{b_0} \right) \left(\frac{a_0}{b_0} \right)^2 \int_0^{t_c} \frac{P_{app}}{\mu_{mf}} dt \right]^{1/5} \\ &\approx \frac{1}{1 + \frac{w_0}{b_0}} \left[5 \left(1 + \frac{w_0}{b_0} \right) \left(\frac{a_0}{b_0} \right)^2 \int_0^{t_c} \frac{P_{app}}{\mu_{mf}} dt \right]^{1/5} \end{aligned} \tag{2.3}$$

In recent studies it was shown that only relying on the squeeze flow mechanism for the determination on intimate contact is not sufficient, and through-thickness percolation flow plays an important role as well [19][44]. During LAFP the surface of the tapes is rapidly heated prior to the pressure application, making deconsolidation of the material unavoidable. As a result of deconsolidation, a local increase in intralaminar void content and a rough and fiber rich surface are obtained. The intimate contact development in fiber rich areas cannot be explained by the squeeze flow, as resin infiltration is needed. Through percolation flow, the resin can permeate towards the surface and wet the dry fibers, in order to enable intimate contact development. According to the results of an experimental analysis presented by Kok [19], his intimate contact model based on percolation flow is better capable of predicting the results for various LAFP process settings than the previously available models based on squeeze flow.

The relation used by Kok is shown in Equation 2.4, where z_{imp} is the depth of the dry fiber bed that can be impregnated. To determine the value of z_{imp} Kok derived a governing partial differential equation, with the following input variables: the fiber volume content, the matrix viscosity, and the permeability of the fiber bed and fiber bed compaction stress, which are both a function of fiber volume content. As the fiber-matrix volume is a function of both the matrix viscosity and fiber volume content, it can be stated that the fiber-matrix viscosity is again the key parameter affecting the degree of intimate contact obtained. As the viscosity and fiber volume content decrease, the value of z_{imp} increases and higher degrees of intimate contact can be achieved.

$$D_{ic} = 42.8ln\frac{z_{imp}}{2} \tag{2.4}$$

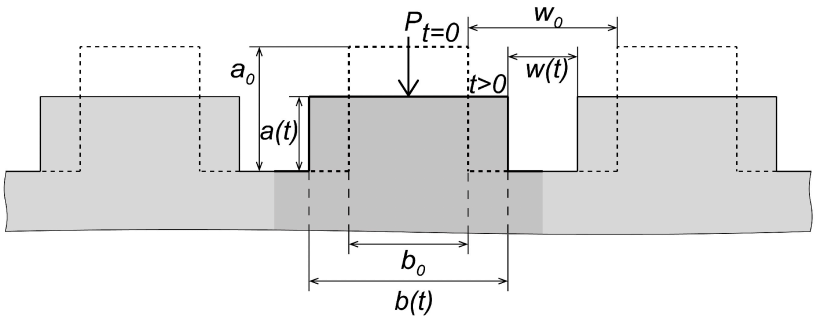

Figure 2.5: Rectangular asperity elements considered for the squeeze flow modeling of surface roughness flattening and intimate contact development [23]

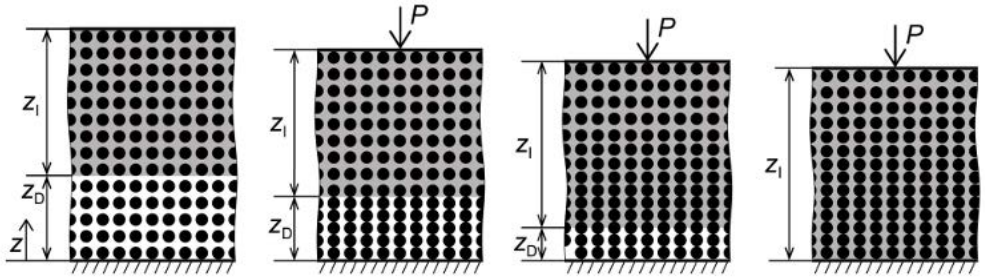

Figure 2.6: Percolation flow of a molten resin through a fiber bed [19]

Viscosity

For both intimate contact models discussed, viscosity is the key input variables. The viscosity used is either the pure matrix viscosity, reasoned by the fact that the asperity size is smaller than the diameter of fibers [40], or fiber-matrix viscosity. To determine the fiber-matrix viscosity a range of different methods can be used, resulting in a range of viscosity values presented in literature. For example for CF/PEEK composites, the values reported are found to differ by up to 2 orders of magnitude [40]. In Figure 2.7 the variation between different models used in literature is plotted [19].

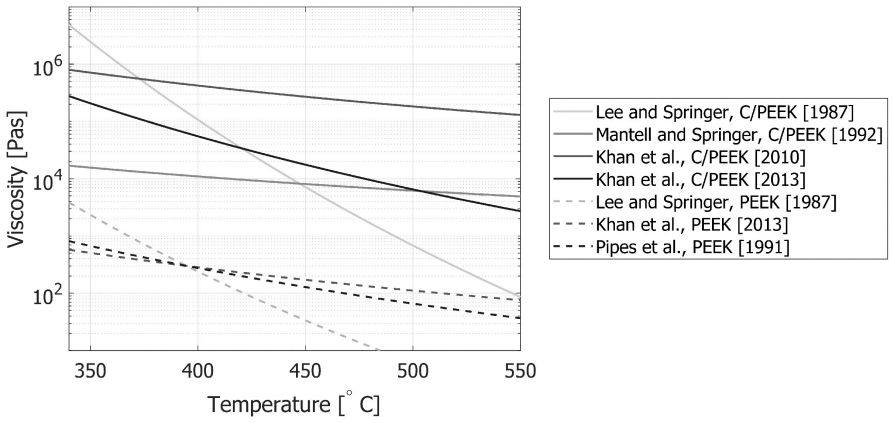

Figure 2.7: Fiber-matrix viscosity of CF/PEEK and PEEK as a function of temperature, reported by different researchers [19]

Experimentally, the viscosity can be determined using different methods, such as off-centered rheology, picture-frame experiments, fiber pull-out set-up or squeeze flow method [40]. However, the listed methods are not suitable to experimentally measure the viscosity during LAFP.

Alternatively, the viscosity can be determined numerically, using an Arrhenius type equation as shown in Eq. 2.5, expressing the viscosity as a function of temperature. In this equation c_μ and c_b are parameters used to fit the model to experimental results and T is the absolute temperature [19]. The difficulty in using this model is the determination of the experimental parameters, as well as the measurement of the temperate during the LAFP process.

$$\mu_0(T) = c_\mu . exp^{(c_b/T)} \tag{2.5}$$

Eq. 2.5 describes the increase of viscosity as a function of decreasing temperature. However, in addition to temperature, the applied pressure and the crystallinity of the material also affect their viscosity. During the consolidation phase of LAFP, shear thinning occurs as pressure is applied. Shear thinning is a rheological property of thermoplastic polymers, defined by an viscosity decreases with applied pressure. This is beneficial for processing TPCs and enhances consolidation. During the heating and release phases of LAFP, no pressure is applied and shear thinning is not relevant [1]. Conversely, higher viscosity is observed in more crystalline materials, which negatively impacts the processing of TPCs. For semi-crystalline polymers heated above T_g, the mobility of chains in the amorphous phase is hindered by the crystalline regions, resulting in higher viscosity [45]. Additionally, studies have shown a memory effect is present some semi-crystalline thermoplastics. Due to this effect, residual metastable nuclei remain and a significant degree of order is detected at temperatures of far above the T_m. For PPS the memory effect was observed at temperatures of 370°C [46]. The previous crystallinity thus still has an effect on the viscosity, even above the melting point.

As a result, different viscosity of the thermoplastic matrix in composites can be achieved for the same temperatures and pressure conditions, depending on the degree of crystallinity and crystalline morphology [13][47]. Due to the importance of viscosity for the LAFP process, a better prediction of its values is needed than the one obtained with Eq. 2.5, for which the effect of crystallinity must be taken into account. In addition to its impact on the processing of thermoplastic composites, crystallinity can thus also be used to better understand the rheological behavior and viscosity evolution during rapid temperature-varying processes such as LAFP.

Crystallinity

Achieving high levels crystallinity is currently one of the two main challenges of in-situ consolidation techniques, alongside perfect consolidation [48][36]. The crystallinity of a polymer matrix is a key property that significantly affects the mechanical and physical properties of composite components, including stiffness, shear strength, tensile strength, fracture toughness, damage tolerance, thermal stability, and chemical resistance [49][50][51]. The DOC and the size and orientation of crystallites play a crucial role in determining these properties, making the understanding and control of crystallinity in the polymer matrix crucial for LAFP.

During LAFP, non-isothermal crystallization is observed due to the continuous variation in temperature. There are several non-isothermal crystallization kinetics that occur during heating and cooling of thermoplastics, including cold-crystallization, melt-crystallization, and recrystallization. Cold-crystallization occurs when the polymer is heated above T_g and crystals form from the polymer chains in a glassy state. Conversely, melt-crystallization takes place when the material is cooled below T_m from a molten state. Recrystallization occurs as a result of changes in the molecular arrangements, during which metastable crystals are transformed into more thermodynamically stable crystal structures [52]. Additionally, isothermal crystallization may be seen in special cases when keeping the material at a constant temperature above T_g, which can be achieved by for example heating the tool and compaction roller [36].

A number of studies have reported the cooling rate to be the primary processing parameter that affects the DOC, crystal size, and shape [53][1]. The crystallinity is found to decrease for higher cooling rates. As a result, the DOC in laminates produced by LAFP is lower compared to those manufactured using autoclave or hot-press processes. Ray et al. compared the crystallinity of CF/PEEK composites manufactured by autoclave and LAFP and reported values of over 40% and 17.2% respectively [54]. To control the cooling rate during LAFP, the temperature of the tooling can be adjusted. Comer et al. and Chen et al. showed that by increasing the tool temperature and thus decreasing the cooling rate, a significant increases the DOC can be achieved [55]. Comer et al. showed an increase in DOC from 17.6% to 29% for CF/PEEK (which has a T_g of 145°C) when heating the tool from room temperature to 120°C [17].

Even though numerous studies on the crystallinity of composites manufactured using AFP are available, the focus has been mainly on the impact of processing conditions, particularly tool temperature, with limited attention paid to the underlying crystallization kinetics. As a result, the principal cause of the low crystallinity reported in literature for LAFP manufactured composites remains unknown. Several hypotheses have been put forth, including fast cooling or insufficient heating, but further research is necessary to gain a full understanding of the crystallization mechanism and arrive at a definitive conclusion [54].

Therefore, the aim of this thesis is to expand the understanding of the crystallization mechanism and influencing factors during rapid laser heating and subsequent cooling. To provide a strong foundation for the study, the following section will provide a review of the current knowledge on polymer crystallinity.

2.2. Polymer crystallinity

In this section, the mechanisms and kinetics governing the crystallization process in polymers are introduced. First, a short general introduction about polymer semi-crystallinity is provided. Next, the phase transitions related to the crystallization are discussed and the relevant knowledge about melting kinetics provided. Finally, an overview of the current knowledge about crystallization kinetics is provided, and the specific kinetics of non-isothermal melt-, cold- and recrystallization explained.

2.2.1. Semi-crystallinity

The PPS matrix of the CF/PPS samples studied during this thesis is a semi-crystalline polymer. This means its structure consists of both crystalline and amorphous regions. As the amorphous and crystalline phases have different physical and mechanical properties, the proportion of these two phases in the material has a key influence on its properties. To quantify the proportion of the two phases in the material, the degree of crystallinity X_c is defined as shown in Eq. 2.6, where ρ_s is the density of the whole sample and ρ_a and ρ_c are the densities of a fully amorphous and crystalline polymer respectively.

$$X_c = \frac{\rho_c(\rho_s - \rho_a)}{\rho_s(\rho_c - \rho_a)}.100 \tag{2.6}$$

Properties influenced by the DOC include hardness, strength, chemical resistance, stiffness, optical clarity, and melting point. The crystalline phase has a positive effect on the stiffness and tensile strength, whereas the amorphous phase increases the fracture toughness and the ability to absorb impact energy [56]. For higher DOC in a polymer, both its melting temperature and enthalpy of fusion increase due to

stronger, more thermally stable intermolecular bonds within the crystalline regions as compared to the amorphous regions. These bonds require more thermal energy to be overcome [57].

2.2.2. Phase transitions

The crystallization process takes place between two phase transitions, namely the glass transition and melting. At temperatures below the glass-transition temperature T_g, the high viscosity results in insufficient mobility of the polymer chains to move and arrange into crystals. At temperatures above T_m, the crystals become unstable and melt. Understanding the effect of the phase transitions and especially the crystal melting above T_m is essential in order to later properly analyze the crystallinity of laser heated samples.

The glass transition is a reversible process of gradual change from a hard and brittle state into a viscous and rubbery state upon heating and vice versa. Below the T_g the chains of the amorphous materials are frozen in place and behave like solid glass. Above the T_g the chains gain more flexibility and the semi-crystalline material softens. Fully fluid behavior is not achieved, as the crystalline raction remain stable below T_m, preventing the material from flowing [56].

The glass transition temperature is not a fixed material property and depends on the packing of the polymer molecules and chains. The transition is a result of free volume available around the polymer chains. In the crystalline phase the space is minimized due to the optimization of all the intermolecular forces, while in an amorphous solid there is more free volume available [35]. It can therefore be concluded that the T_g increases with an increasing DOC. Other factors increasing the T_g are higher molecular weight, stiffer molecular backbone, chain symmetry and the presence of polar groups. During processing, a fast rate of cooling, resulting in a lower DOC, and the addition of additives, such as plasticizers, both decrease the T_g [58][59].

Above the melting temperature T_m the crystalline regions gain sufficient energy to move around freely in the form of a viscous fluid also known as melt. The thermoplastic melt can be processed and formed into desired shapes and structures [56] [60]. The ideal melting can be considered as the reverse process to crystallization, describing the transition between the fully entangled equilibrium melt and ideal fully extended chain crystals. In reality, metastable states exist in between the ideal melt and crystal. In the metastable crystalline phase small crystals (nucleus or embryo) or chain-folded crystals can be seen, in the form of a randomly coiled or a locally ordered melt. The ideal melt is only achieved after the equilibrium melting temperature T_{m_0} is reached. T_{m_0} is the melting point of a completely crystalline polymers with all crystals in the extended chain conformation. In practice this means that above T_{m_0} no crystals remain, as both the folded and extended chain crystals melt, and an ideal melt is obtained. Below T_{m_0} local order in the amorphous phase of the polymer remains and the polymer is in a metastable form [61]. Whether a sample has been cooled above T_{m_0} has a direct influence on the melt-crystallization during subsequent cooling [46].

Vice-versa, the melting process is also highly dependent on the thermal history of the crystallization process. During crystallization upon cooling from a melt, randomly coiled entangled molecules form either an amorphous or crystalline phase, determining the DOC and affecting the melting temperature. The molecules in the crystalline phase can adopt an extended chain macro-conformation in equilibrium state or form a folded chain crystal in non-equilibrium. The proportion of the different crystal conformations also affects the melting temperature [62]. Generally, polymers crystallize in a chain folded fashion upon cooling, because the energy required to unfold the polymer chain is greater than the energy gained by folding the chain back into a compact form. When heated, the chain-folded crystallites can reorganize into more-stable extended states [63].

The complex melting behaviour of chain folded crystals has been studied by Toda et al., who identified three characteristic phenomena:

- Firstly, a broad melting temperature range is seen, caused by the varying T_m of the different crystal conformations in the polymer.
- Secondly, melting occurs in parallel with recrystallization and reorganization. Recrystallization is defined as the crystallization of molten crystals into a more stable state. The chain-folded crystals are metastable and melt at a lower temperature compared to the more-stable extended-chain

crystals. This allows them to melt and subsequently recrystallize before reaching the equilibrium melting temperature of the extended-chain crystals. This melting, recrystallization and remelting behavior is another reason for the broad melting temperature range.

- The third phenomenon is the superheating-dependent melting kinetics. Superheating is the term used to describe the shift of the melting temperature to higher values for fast heating rates. At these rates the polymer crystals are subjected to temperatures exceeding their melting point, yet remain in a solid state due to the rapid rate of heating, which exceeds the rate of heat transfer within the material leading to deformation rather than complete melting of the polymer crystals [48][64]. As a result, a superheated liquid state in which the polymer chains are partially melted and partially ordered is obtained [65]. This behavior is explained by a so-called kinetic barrier, created by the melting and recrystallization acting in opposite direction and thereby competing against each other [66][63].

In summary, melting occurs over a wide range of temperatures and the on- and offset of this range depend on the heating rate applied. The dependency of the melting temperature range on the heating rate is demonstrated in Figure 2.8.

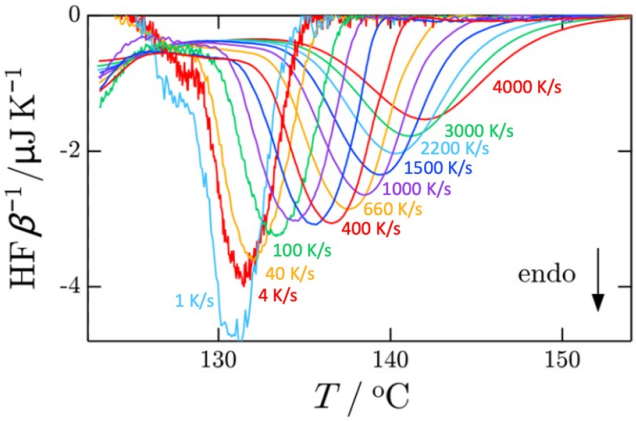

Figure 2.8: Normalized endothermic melting peaks for heating rates from 1 to 4000 K/s [63]

Melt relaxation and memory effect

An interesting phenomenon seen during melting and greatly affecting the crystallization kinetics is the so-called “memory effect”. This effect refers to the metastable crystalline phase that remains in the melt prior to reaching an ideal fully molten state. These metastable phases are ordered domains in the melt, serving as a memory of the previous solid-state structure and morphology, and act as nuclei for the following crystallization, speeding up this process. The size and amount of these ordered regions in the melt depends on multiple parameters, specifically the thermal history, initial DOC and stresses imposed on the liquid polymer [67]. The full dissolution of these ordered regions is referred to as melt relaxation.

Specifically for PPS, its rigid backbone with phenyl groups restricts the mobility of the chains and slows down their relaxation, resulting in stronger effects of thermal history compared to flexible polymers. It is therefore an ideal material to study the memory effect experimentally on and has been used extensively to characterize the relationship between thermal history and crystallization.

D’Ilario et al. studied the isothermal crystallization as a function of the temperature and time of dwell in the melt state. They found that with increasing the temperature and dwell time, the rate of crystallization decreased, but did not reach a plateau even above Tm0 when all predetermined nuclei were destroyed completely. This suggests that for rigid polymers like PPS, the memory effect cannot be erased completely [67].

Finally, Yan et al. have come up with new insights into the memory effect of PPS. They studied the melting and subsequent crystallization behavior of powder PPS, which consist of folded- and extended-chain crystals. Due to the different crystal morphologies, two melting peaks are observed. Therefore, the folded-chain crystals are eliminated completely at their Tm of 350°C, while extended-chain crystals

remain in the material until 370°C. The fact that the memory effect is still active after long dwell times at 370°C is explained by the slow melting relaxation of rigid polymers. During melting, the crystals first undergo a fast conformational change from lamellar structure to an amorphous cluster. This is followed by a slower topological change from large clusters to random coils with saturated entanglement concentration. The longer the melting dwell time, the more time the material has to disentangle and form into an equilibrium topological state with low entanglement density. The time needed for this melting relaxation including the development of ordered regions to occur is very large for rigid polymers due to their low chain mobility, which is the reason why the decrease in crystallization rate does not level off [46].

The long times needed for the memory effect to be erased in PPS suggest that during LAFP thermal history will have a big impact on crystallization and material performance. However, as the memory effect has never been studied under rapid processing conditions, the extent of the melting relaxation at extremely short dwell times is unknown.

2.2.3. Crystallization kinetics

The crystallization process can be split up into two phenomena occurring: an initial nucleation step followed by a growth process. Nucleation is the initial process of the formation of a crystal, possible in polymer melts below the thermodynamic melting temperature. During crystal growth the pre-existing nuclei increasing in size, forming crystal structures. The growth continues until full impingement is reached, as long as the sample stays within the crystallization temperature range, characteristic of each material [68]. Polymers are able to crystallize at a temperature range extending from about 30°C above T_g to about 10°C below T_m. The crystallization window for PPS is one of the most extensive ones reported for any polymer thus far. Lovinger et al. reported a crystallization temperature range of 100-280°C [69], while Zhao et al. determined the range to be 87–270°C [36].

The overall crystallization rate is governed by the system's enthalpy and entropy balance. The energy required to form new crystalline regions is represented by an increase in enthalpy. The reduction of disorder, on the other hand, increases entropy, resulting in the release of energy in the form of an enthalpy. Crystal growth can occur if the decrease in enthalpy achieved by increasing order is greater than the increase in enthalpy required for crystal formation [70].

Nucleation can be either homogenous or heterogenous. During homogenous crystallization small regions of the crystalline phase in the pure supercooled melt are formed by the polymer chains themselves. Heterogenous nucleation is the formation of crystalline regions on or near surfaces of heterogeneities in the polymer, such as fillers, reinforcing materials or nucleating agents, but also the processing tools or laboratory equipment. During processes like LAFP we therefore speak of heterogenous nucleation [62][71].

Crystal growth occurs after nucleation and involves the expansion and refinement of the nuclei into larger crystallites. This stage is characterized by the gradual ordering and alignment of the polymer chains into a crystalline structure, increasing both the size and mass of the crystalline regions. The crystal growth kinetics consist of two processes: primary and secondary crystallization. Primary crystallization occurs directly after nucleation, as the nuclei begin to grow into spherulites that expand radially. Secondary crystallization occurs as the existing crystallites continue to thicken and refine. The rate of these two processes differs, as the primary crystallization is faster and follows the Avrami equation, and secondary crystallization occurs at a slower rate and shows a square root time dependency [72]. The basic form of the Avrami equation is given in Eq. 2.7, where $(X(t)$ is the degree of crystallinity, t the crystallization time, k a crystallization rate constant, and n the Avrami exponent [1].

$$X(t) = 1 - exp\left[-kt^n\right] \tag{2.7}$$

Crystallization can occur under either isothermal or non-isothermal conditions. Studies on crystallization kinetics often start by considering experiments performed under isothermal conditions. This provides idealized constant crystallization conditions, where cooling rates and thermal gradients can be neglected. Additionally, when studying isothermal crystallization experimentally problems due to instrumental lag and thermal gradients within the sample are also limited. However, industrial processes, including LAFP, often take place under continuously changing external conditions, making the non-isothermal crystallization process more complex, which is why the focus of this thesis will be on non-istothermal crystallization behavior [73].

Crystal nucleation often occurs around well-defined foreign bodies. These vary from processing and laboratory tools, such as moulds or DSC pans, to internal objects, such as fillers or reinforcing materials. In some cases, specific substances are added with the purpose to promote intense homogenous nucleation, referred to as nucleating agents. As a result, an increase in crystallization rate and crystallization temperature as well as a decrease in crystal size is generally observed [74]. Whether these geometries induce crystallization is determined by the competition between heterogenous nucleation in the bulk polymer and on the geometry surface [69]. In the case of a high density of active nuclei on the surface of a fiber, full extension of the spherulites is hindered and crystal growth is forced in perpendicular direction. Such growth results in a layer of column-shaped crystals, known as transcrystallinity [27]. Transcrystallinity is found to positively affect the mechanical properties of composites. An increase in interfacial bond strength between fiber and matrix is observed. This effect is most profound for low fiber volume contents, as there is more space between the fibers for large transcrystalline regions to form [27][75].

Due to the reduced and often relatively small percentage of matrix polymer in composites it can be assumed that the crystallization behavior of PPS within a composite shows differences from that of the neat polymer. Additionally, fillers are often added to the matrix by the composite manufacturer to improve processing speed, dimensional stability, and physical properties, further changing the crystallization behavior compared to the neat polymer.

2.2.4. Non-isothermal crystallization

The three main types of non-isothermal crystallization are shown in Figure 2.9 [52]. Melt-crystallization is observed when a polymer is cooled from a molten state, whereas cold- and recystallization are obtained from the glassy state.

Melt-crystallization

The process of melt-crystallization involves the transformation of polymer chains from a disordered state in the melted form to an ordered and periodic structure. The long polymer chains must untangle and fold upon themselves during this process, leading to the formation of the crystal phase. The result of this process is a decrease in conformational entropy due to the decreased flexibility and reduced movement of the polymer molecules. The slow crystallization process in polymers compared to materials with lower molecular weights, such as metals, can be attributed to the higher entropy losses due to the complex polymer chains [70].

The cooling rate is considered to be one of the main factors affecting melt-crystallization. During the melt-crystallization process, the release of energy results in an exothermic heat flow peak. As the cooling rate increases, this peak shifts towards lower temperatures, and the enthalpy of crystallization, equal to the area under the peak, decreases, leading to lower degrees of crystallinity.

The crystallization behavior is highly dependent on the type of polymer. For slow crystallizing polymers with rigid chains and bulky side groups, rapid cooling can result in a supercooled liquid state, where the polymer remains in a disordered and amorphous form instead of crystallizing. This state can only be crystallized by subsequent heating above its T_g [62]. On the other hand, for polymers with highly flexible molecular chains, avoiding crystallization is not possible.

PPS belongs to the slow crystallizing polymers due to its symmetric rigid backbone. In different studies a critical cooling rate of 20-30°C/s has been found, above which no crystallinity develops [30] [76]. However, as additives are often added to the PPS matrix in composites and the ability to crystallize is also affected by the heterogeneities in the material, this value could vary per sample studied. For instance, a DOC of 20% was reached for CF/PPS composites using an experimental LAFP set-up at a placement speed of 100mm/s in study conducted by Zhao et al. [36], despite the fact that typical cooling rates exceed 100°C/s for such placement speeds [17].

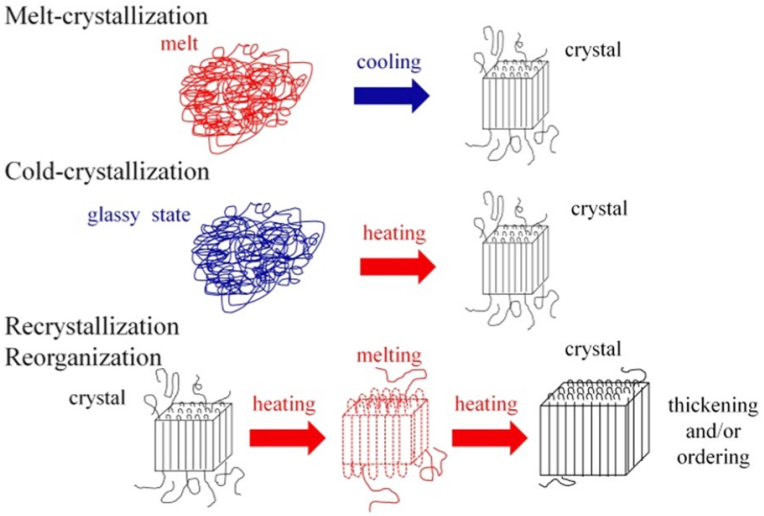

Figure 2.9: Schematic representation of the three types of non-isothermal crystallization of polymers [52]

Cold-crystallization

Cold-crystallization occurs above T_g, as the molecules in the glassy state gain more freedom to move and organize into more stable crystalline structures during heating. For low heating rates, the metastable crystals can undergo further structural changes into stable structures during heating, called recrystallization.

The enthalpy of cold-crystallization can be used to quantify the amount of nuclei present in the material before heating. Whether cold-crystallization occurs depends on the number of nuclei and the time for growth. The first is affected by the thermal history and previous cooling rates applied to the material. The second is affected by the heating rate, and whether the sample spends sufficient time within a temperature range between T_g and T_m so that the crystallinity can develop [77].

Furushima et al. have studied the effect of previous cooling rate and heating rate on the cold-crystallization enthalpy ΔH_c for polybutylene terephthalate (PBT), showing a general trend observed amongst others for PPS. The relationship between enthalpy of cold-crystallization and previous cooling rate for different heating rates is shown in Figure 2.10. Above a certain heating rate, the cold-crystallization can be suppressed due to insufficient time for crystals to grow from the limited number of heterogenous or homogenous nuclei. On the other hand, for a sufficiently low heating rate the cold-crystallization is constant independently of the previous cooling rate, as enough time is available for both nucleation and subsequent crystal growth. The gradual decrease of cold-crystallization enthalpy with the increase of previous cooling rate is caused by the decrease in the number of nuclei formed during cooling, that can grow during the following heating process. Above a certain cooling rate, no nuclei form and thus no cold-crystallization enthalpy is observed during heating for the higher heating rates [52].

Another observation made by Furushima et al. in their study is the fact that cold-crystallization upon heating is faster than crystallization upon cooling. This was observed in measurements done with PBT and talc-PBT, crystallized from a supercooled liquid without preexisting nuclei. They explain this by the fact that the range for homogenous nucleation lies closer to T_g than to T_m , meaning that during cold-crystallization more homogenous nuclei develop at an earlier stage in the crystallization process and more time is available for these nuclei to grow [52].

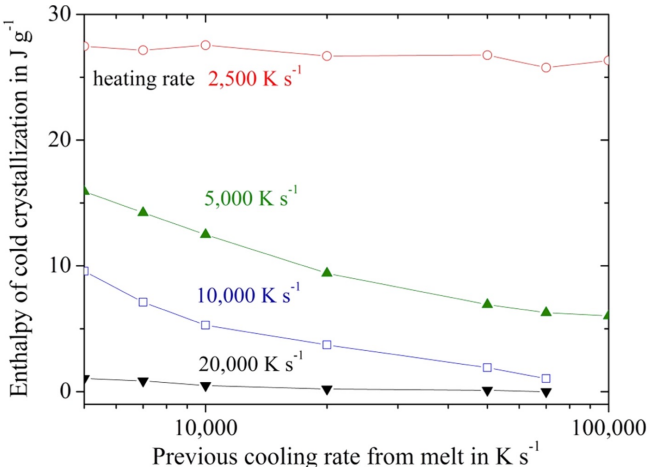

Figure 2.10: Enthalpy of cold-crystallization as function of previous cooling rate from the melt for PBT samples [76]

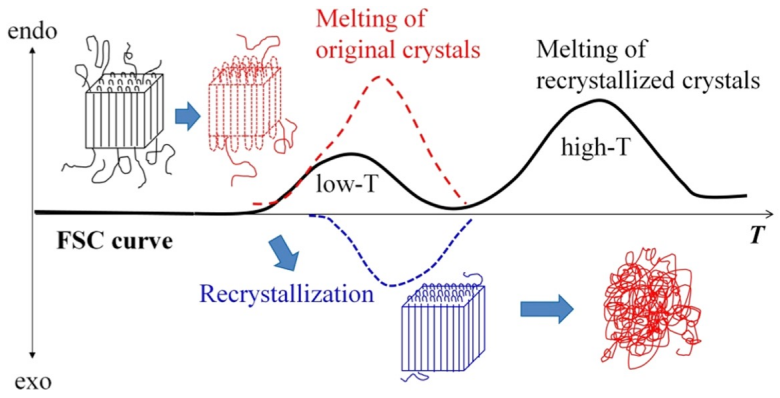

Figure 2.11: Schematic description of the progress of melting and recrystallization during heating [52]

Recrystallization

Recrystallization is the process of the reorganization of crystals with a low thermal stability into more stable crystalline structures. With an increase in temperature, energy is provided due to which the unstable crystals can melt, resulting in an endothermic heat flow peak. Simultaneously, the melted crystal recrystallize into a more stable crystal structure, resulting in an exothermic heat flow peak. The combination of melting and recystallization results in an endothermic peak, as can be seen in 2.11 [76].

Similarly to cold-crystallization, the process of recrystallization is affected by the heating rates applied and the melting temperature of the crystal structures present in the material, a result of the previous cooling rates applied. The heating rate determines how much time there is for the molten crystals to recrystallize before they reach the temperature of the second melting peak. If the melting temperatures of the original unstable and newly formed stable crystals lies close to each other, double melting peaks can be observed. The double melting peak can also be observed for fast heating rates [76].

At high heating rates above 10 000°C/s, recrystallization is the fastest process, compared to cold- and to melt-crystallization. At these rates the crystals that melt at the lower T_m peak do not have time to fully disorder and therefore act as nuclei for recrystallization. At slower rates cold-crystallization becomes the faster process, due to the high number of homogenous nuclei developed at an early stage in the process [52]. For typical LAFP heating rates, cold-crystallization is thus the predominant crystallization type.

2.2.5. Crystallization parameters

Important parameters used to describe the crystallization process are the conversion rate and degree of conversion. The conversion degree is the ratio of the transformed volume or mass to the entire

volume or mass of the crystallizing polymer. The conversion rate is the increment of the conversion degree in an infinitely small time interval. The conversion rate is a function of both the rate of formation of nuclei (above the critical size) and the rate of growth of these nuclei to the final crystalline aggregates, as shown in Figure 2.12 on the left [62]. Due to the location of the nucleation and growth rate peaks, the total crystallization is faster during heating compared to cooling. This can be explained by the fact that the range for homogenous nucleation lies closer to T_g than to T_m , meaning that during cold-crystallization more homogenous nuclei develop at an earlier stage in the crystallization process and more time is available for these nuclei to grow [52][78].
The bell-shape of the curves is given by the increase in viscosity close to T_g and decrease in thermodynamic drive close to T_m, both slowing down the growth rate of crystals [73].

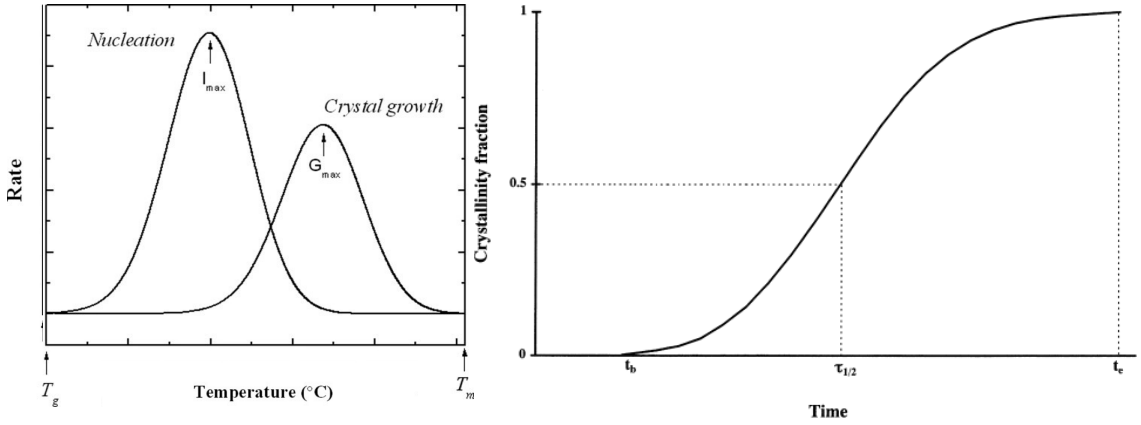

Figure 2.12: Crystallization rate and degree of crystallinity evolution over time [73][73]

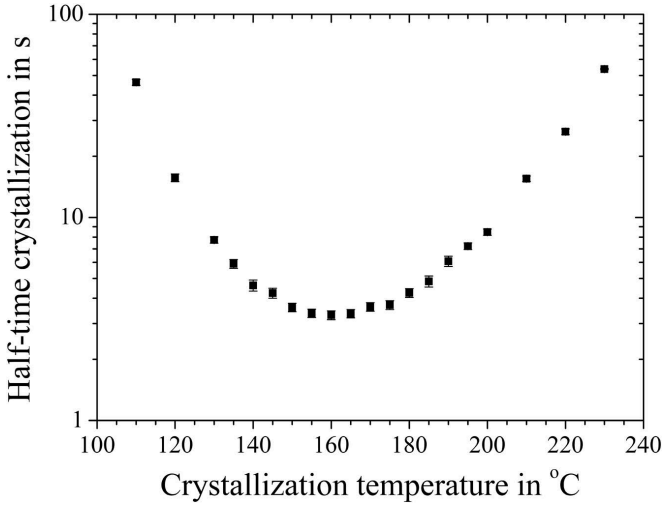

Figure 2.13: Half-time crystallization of PPS at different isothermal crystallization temperatures [76]

During experimental analysis of the process, additional parameters can be identified. These include the crystallization half-time $\tau_{1/2}$ equal to the time needed to reach half of the final crystallinity, the nucleation density D equal to the number of nuclei per unit volume, the onset time of crystallization t_b, the time required for the sample to crystallize completely t_e and the broadness of the transition Δt equal to the difference $t_e - t_b$. These parameters are shown in Figure 2.12 for a non-isothermal crystallization process as a function of time [73].

The half-time crystallization of isothermally melt-crystallized PPS is determined by Furushima et al. and shown in Figure 2.13 for temperatures ranging from 110 to 230°C. The minimum value of this curve, equal to the temperature at which the crystallization rate is fastest, is at 160°C, for which a half-time of 3 seconds is measured [76].

2.3. Conclusion

The LAFP process was introduced and the purpose of the distinct heating, consolidation and release phases explained. LAFP is found to be a complex process, with a large number of variable determining the outcome parameters and quality, but also affecting each other. To gain a better overview of the process, all influencing variables are identified and sorted into different categories, including the fixed material, hardware choices and variable process settings. The process choices made with regard to the heating phase greatly affect the consolidation phase and thereby the quality of the final laminates produces with LAFP, making the motivation to focus on the impact of laser heat input on the crystallization kinetics in PPS/CF tapes clear.

The following phenomena related to the heating phase were analyzed in more detail:

- **Phase transitions:** The influence of the DOC and thermal history on the glass transition and melting temperature is discussed. During the heating phase of LAFP, both the crystallinity and thermal history of the sample change, having an effect on the values of T_g and T_m and the peaks observed in DSC analysis.
- **Deconsolidation:** The micro- and macro-scale changes observed in thermoplastics upon heating without pressure application are explained. In recent studies the presence of deconsolidation effects at rapid heating rates, characteristic for LAFP, have been verified.
- **Crystallization:** The complex crystallization process is introduced and the effect of the material properties and thermal, geometrical and mechanical parameters discussed. For LAFP the thermal parameters are most relevant, such as the heating and cooling rate, but also the effect of thermal gradient. Parameters to quantify crystallization are the DOC and crystallization rate. Additionally, the crystal morphology can provide useful insights into the crystallization process. The critical rate at which melt-crystallization is observed is 20°C/min, at higher rates crystallization from melt is supressed.
  Recrystallization and Cold-crystallization: The two types of non-isothermal crystallization upon heating are introduced and their effect on melting and melt-crystallization researched. Re- crystallization was found to be more severe during high heating rates and thus more relevant for LAFP. For rates above 10000°C, recrystallization is the fastest process, below this rate cold-crystallization occurs at the fastest rate. For any rate, these two types of crystallization are faster than the melt-crystallization during cooling.
- **Melt relaxation:** This phenomenon is observed in the material melt, where for longer dwell times the amorphous phase has time to disentangle and ordered amorphous regions with long entanglement density are formed, decreasing the crystallization rate. For rigid polymers such as PPS the melting relaxation is found to be very slow and thus not expected to have a large effect during the rapid LAFP process.

3

Research framework

3.1. Gaps in literature

The high process speeds required by industry currently limit the laminate quality achievable with the state-of-the-art LAFP process. The main reason for the poor quality is the low degree of intimate contact between subsequent layers. Recent studies show the degree of intimate contact is affected not only by squeeze flow on the surface, but also the percolation flow in thickness direction. This makes the viscosity an important variable in the ply consolidation process. In order to improve the LAFP process and optimize the in-situ consolidation, more insight into the evolution of viscosity of the composite during heating is needed.

Generally, viscosity is a function of temperature and time. As the temperature and heating time increase, so does the viscosity. For thermoplastics, there is a maximum in the form of thermal degradation temperature. Additionally, the viscosity is affected by matrix properties, such as crystallinity, and composite properties, such as fiber volume fraction or dry fiber bed depth.

The fiber volume fraction is a fixed parameter for the selected composite material and cannot be altered during LAFP. The crystallinity, on the other hand, is not only determined by the material choice, but affected by the LAFP process as well. This makes the degree of crystallinity one of the key factors influencing the viscosity during LAFP. How the crystallinity develops as a result of the rapid heating and cooling rates characteristic for LAFP is so far unknown.

3.2. Research objective and questions

A research objective is defined and used to aid the formulation of the main research questions. This objective follows from the identified gaps in literature presented in the previous section and is stated as follows:

> *The research objective is to gain more insight into the effects of rapid laser heating on the development of crystallinity in CF/PPS composite, by studying the effect of temperature parameters on the degree of crystallinity of heated samples.*

Based on this objective, the main general research question aimed to answer in this master thesis is:

> **What is the effect of rapid laser heating, as seen during LAFP, on the thermal history and the development of crystallinity in carbon fiber reinforced PPS?**

The main research question can be subdivided and made more specific, resulting in the following set of sub-questions:

RQ1 How does the **laser heating input** affect the **temperature** of the heated sample?

1.1 What is the effect of laser power and heating time on the temperature history of the heated sample?
1.2 What is the effect of heated area on the temperature history of the heated sample?
1.3 How does the temperature distribution through the tape thickness change for different laser energy inputs?
1.4 How does the temperature distribution over time change for different laser energy inputs?

RQ2 How does the **temperature** of the heated sample affect the **crystallization**?

2.1 What temperature distribution parameters have an effect on the final degree of crystallinity?
2.2 How does the crystallinity change for samples heated below and above T_m?
2.3 What is the effect of temperature of the surrounding material (changed by varying the heated area) on the crystallinity?
2.4 What is the contribution of cold-crystallization to the final degree of crystallinity?
2.5 To what extend do crystals melt at temperatures above T_m?
2.6 Does melt-crystallization occur during the cooling phase of LAFP?

3.3. Hypothesis

Based on the state of the art and crystallinity theory discussed in chapter 2, a number of hypotheses are formed. The labels H1 and H2 correspond to research questions 1 and 2 respectively.

H1.1 An increase in laser power and heating time result in higher temperatures obtained in the sample. The same top surface temperature can be achieved with different combinations of laser power and heating time. For these combinations, the temperature distribution through the sample and over time will vary.

H1.2 Combinations with a **longer heating time** and **lower laser power** will experience lower heating and cooling rates and a smaller difference between top and bottom surface temperature, as the sample is heated more gradually and the heat has more time to transfer through the tape (through the thickness, as well as in length and width direction). As a result, the heat sink imposed by the surrounding material on the sample is lower, allowing the sample to maintain the elevated temperature for longer.

H1.3 Combinations with a **shorter heating time** and **higher laser power** will experience higher heating and cooling rates and a will see a bigger temperature gradient through the sample, as the heating is more rapid.

H1.4 When increasing the **heated area**, more material surrounding the sample is heated. This will again result in a lower heat sink and a slower cooling rate.

H2.1 Heating of samples to temperatures between the glass-transition and the melting temperature will result in an increase in DOC. The increase in DOC is the result of cold- and re-crystallization, which can occur during both the heating and cooling phases of the process.

H2.2 Heating samples to temperatures above the melting temperature will result in a decrease in DOC compared to the as-received tape. For these samples, a part of the crystalline regions will melt when exceeding the melting temperature. However, some degree of order might remain in the material due to superheating. The suppression of melt-crystallization at rates above 30°C/min, expected to be seen in laser heated samples, will prevent the sample to re-gain its original crystallinity.

H2.3 Heating samples to temperatures above the equilibrium melting temperature will result in a near-zero in DOC. The reason for the near-zero DOC is the full melting of crystals above the equilibrium melting temperature and the suppression of melt-crystallization at rates above 30°C/min, expected to be seen in laser heated samples.

H2.4 For samples heated to temperatures between the melting end equilibrium melting temperature, crystal nuclei will remaining in the polymer melt due to the memory effect and enhance the subsequent melt-crystallization. As a result, a higher DOC will be obtained compared to samples heated above the equilibrium melting temperature, but lower compared to samples heated below the melting temperature.

H2.5 An increase in DOC is expected as the heating and cooling time increase and the heating and cooling rate decrease.

H2.6 The sample temperature is is expected to have a positive effect on the crystallinity for temperatures below T_m, due to the increase in chain mobility. The biggest effect is expected to be seen in the range between 140 and 180°C, where the isothermal crystallization rate is highest.

4

Experimental methodology

The experimental methodology used is the result of multiple iterations and adjustments, and was adjusted throughout the process based on intermediate results. In this chapter the final methodology used is presented, of which an overview is given in Section 4.1.

For the preparation of laser heated samples, a suitable experimental set-up was built, providing a simplified yet representative version of the heating phase of the LAFP process. With this set-up, a variation of laser heat inputs can be applied to heat the samples while measuring the temperature in-situ. The set-up is discussed in Section 4.2, followed by a description of the used sample material in Section 4.3. Further characterization methods are chosen to analyze the heated samples and determine their degree of crystallinity. Their working principles and the procedures used are presented in Section 4.5. Finally, special attention was paid to the process of selecting the right laser heating settings, in order to obtain wide set of samples with a variation in temperature parameters, as well as crystallinity. As a result, a list of samples to be produced is obtained. Both the process of laser input selection as well as the final set of samples are explained in Section 4.4.

4.1. Methodology flow-chart

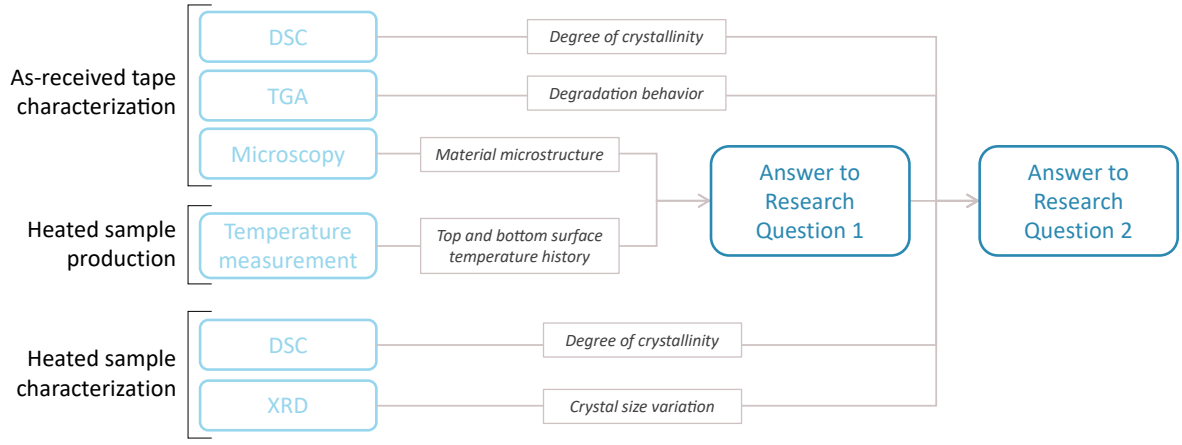

Figure 4.1: Methodology flow-chart of experimental activities performed during thesis

In Figure 4.1 a flow-chart explaining the used methodology, based on the research questions and hypotheses, is shown. The approach consists of three main tasks, namely the characterization of the as-received material, the sample preparation of the laser heated samples using the experimental set-up, and the characterization of these laser-heated samples. The results obtained from the measurements of all three phases are related to the research questions as indicated by the arrows in Figure 4.1. The results of the microscopy analysis of the as-received sample and the temperature evolution measured during laser heating are presented and discussed in Chapter 5. The DSC and TGA characterization of

the as-received sample and the DSC and XRD charaxterization of the heated sample are presented in Chapter 6, and discussed together with the outcomes of Chapter 5.

An important part of the experimental tasks is the characterization of the as-received sample, to which no laser heating was applied. For this three kinds of characterization methods are used. Firstly, DSC is used to determine the degree of crystallinity and study the enthalpies and heat capacity changes related to the glass-transition, cold-crystallization and melting. Secondly, TGA is used to determine the degradation behavior, namely the degradation onset temperature and the effect of different heating rates. Lastly, the as-received material is studied using microscopy, to determine the variation in base-line properties, such as surface roughness and fiber distribution, as these could have an effect on the heat transfer through the tape and the melting and crystallization kinetics.

The preparation of the samples was done using a stationary laser heating set-up, further discussed in Section 4.2. The main goal of the laser heating is to create samples with a wide range of LAFP representative heating inputs, and study whether and how their crystallinity changes. The temperature of the tape surfaces is measured during the laser heating, which allows to relate the final degrees of crystallinity to the temperature of the tape rather than the input laser settings, making the conclusions more generally applicable to LAFP, independently of the laser and set-up used.

Two types of samples are produced based on the temperature they are heated to. The first type of samples is heated to temperatures below T_m but above T_g. These samples are used to isolate and study the cold-crystallization and re-crystallization behavior. The second type of samples is heated to temperatures above T_m, for which the effect of time and temperature above T_m can be studied. In Section 4.4 the test plan used to determine the exact laser input settings is explained and the sets of samples produced are listed.

Finally, the laser heated samples are characterized and compared with the as-received state of the material. DSC is used again to determine the final crystallinity of the samples. Additionally, XRD is used to gain more insight into the crystal size. All characterization methods used are discussed in more detail in Section 4.5.

4.2. Experimental set-up

During LAFP, the final crystallinity is affected by many different process parameters. As the goal of this thesis is to study the crystallinity development as a result of different heating scenarios, it is beneficial to isolate the heating phase from the other phases and focus on the sample laser heating only. For this purpose a simplified stationary set-up is used, consisting of a vertical cavity surface emitting laser (VCSEL) heater, tooling to adjust the sample to and thermal infrared (IR) camera to monitor the surface temperatures.

The laser heater is installed directly above the sample, with the heating modules parallel to the surface of the tape. The distance between the sample was set to 40 mm. The distance could be easily varied, as the laser is attached to vertical aluminum extrusion profiles, but is kept constant for the experiments done during this thesis. The sample itself is attached to the specimen holder using kapton tapes at the outer edges. Markings are used to place all samples at the same location. The thermal camera is installed under an angle of 22° at a distance of 240 mm (top surface measurements) and 280 mm (bottom surface measurements). In Figure 4.4 an actual image of the set-up is shown.

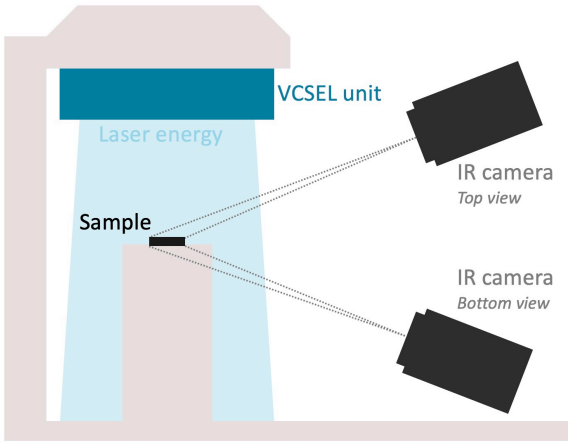

Figure 4.2: 2D sketch of set-up

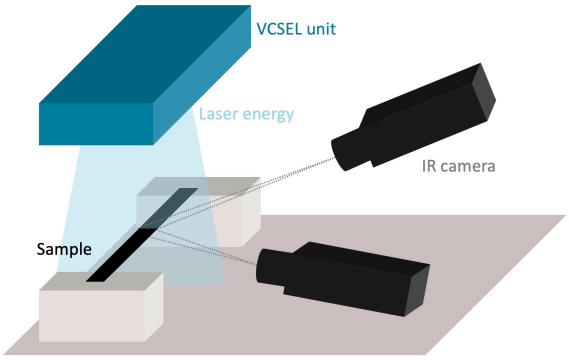

Figure 4.3: 3D sketch of set-up

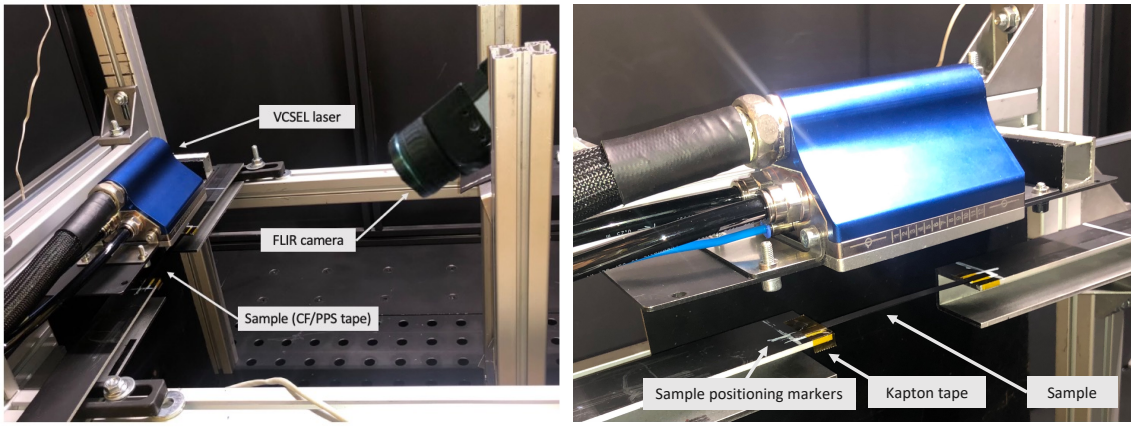

Figure 4.4: Experimental set-up

4.2.1. Boundary conditions

In order to be able to measure both the top and bottom surface temperature, the sample is placed in air, with no tooling on the bottom surface and only clamped to the set-up structure at the ends. On the top surface, the laser energy input is provided, after which the laser heat propagates through the tape. At the bottom surface, heat can leave the sample through convection to air. This convection is also possible at the top surface after the laser is turned off and the sample starts to cool.

The boundary conditions imposed by the surrounding material vary depending on the number of laser emitters used during heating. When heated with 2 emitters, only the tested samples is irradiated directly by the laser, and heat is transferred to the rest of the tape through conduction. When the power is provided to the tape using all 12 emitters, the surrounding tape itself is also heated and less heat is lost from the tested sample through the conduction to the surrounding material. The difference in boundary conditions is visually represented in Figure 4.5. The amount of heat conducted to the surrounding tape depends on the material properties such as the thermal conductivity and emissivity and the temperature of the tape, but is also affected by the other boundary conditions, such as the ambient temperature.

During LAFP the bottom surface boundary condition is the heat transfer to the tool or to previously placed layers. This results in a discrepancy between the used set-up and the actual LAFP process in terms of heat transfer observed in the tape and the final temperatures achieved. Nevertheless, this is not considered a concern, as the focus of this thesis is on the analysis of the relation between DOC and measured temperatures directly.

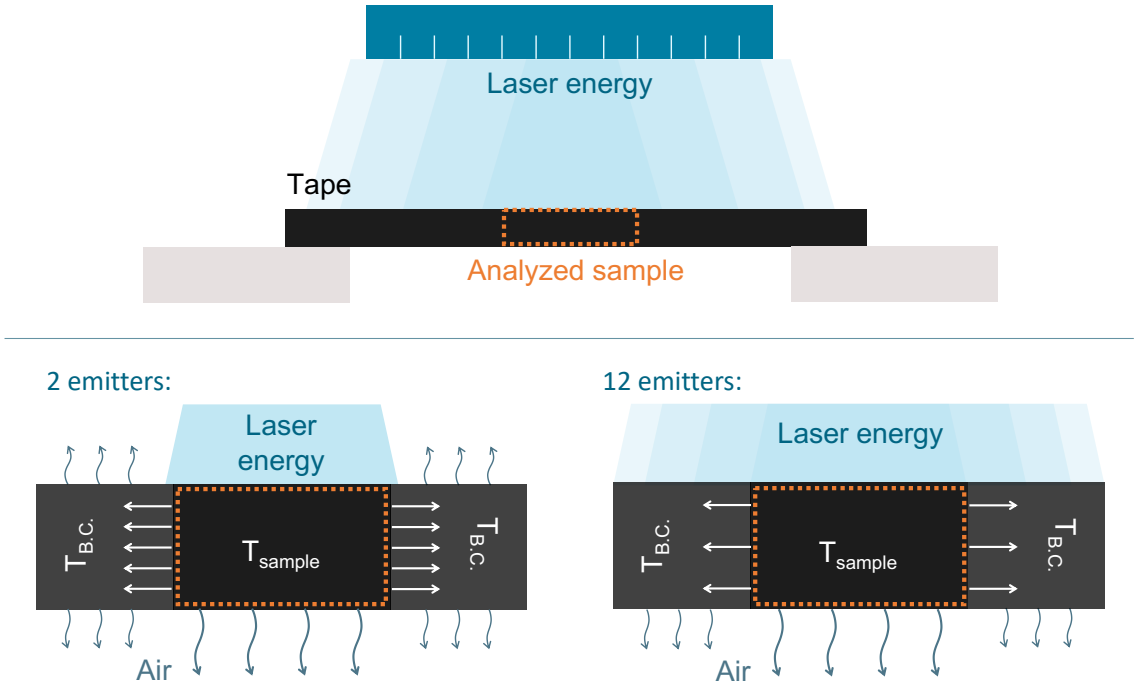

Figure 4.5: Boundary conditions of the studied sample: side view of whole set-up (top) and close-up of the side view of the heated tape for different heated areas (bottom)

4.2.2. Equipment

Laser heater

The heating device used in the experimental set-up is a VCSEL, a type of semiconductor laser diode with a laser beam emitted perpendicular to the top surface. This makes it differ from the more conventional semiconductor lasers, which are edge-emitting. The main advantage of the VCSEL, apart from reduced fabrication costs, is the possibility to be build in two-dimensional arrays. The heating modules are assembled from emitters, each consisting of VCSEL chips and integrated micro-channel water cooling, with thousands of micro lasers per chip. This architecture of the VCSEL heating device allows flexible and dynamic adjustment of the heating intensity profile using discrete electrically-controllable emitter lines [24]. During LAFP this is particularly beneficial, as it allows to control the intensity distribution between the substrate and incoming tape in systems. The former, in combination with the very compact source head and highpower density delivered makes VCSEL heaters the perfect heat source to be used in LAFP [79].

The specific VCSEL used is the TRUMPF PPM412-12-980-24-c module by Philips, shown in Figure 4.6. This laser module emits IR light at a wavelength of 980 nm and can provide a maximum power of 2.4 kWh, divided over 12 heating zones. Each heating zone consists of two lines of emitters and can be individually controlled by the software that connects with the laser driver. By independently activating and adjusting the power of the zones tailored heating profiles can be obtained, offering different heated lengths and heating times [15]. In Figure 4.7 the results of the laser intensity variation in the heating profiles is shown.

Another way the heating profile can be controlled is through the position of the laser. Both the distance to the tape and the angle with respect to the tape have an influence on the laser power provided to the material. For the experiments a constant distance is chosen to eliminate the effect of laser distance on the heat sink when comparing the results obtained. The distance of the laser to the tape is 40 mm in all experiments.

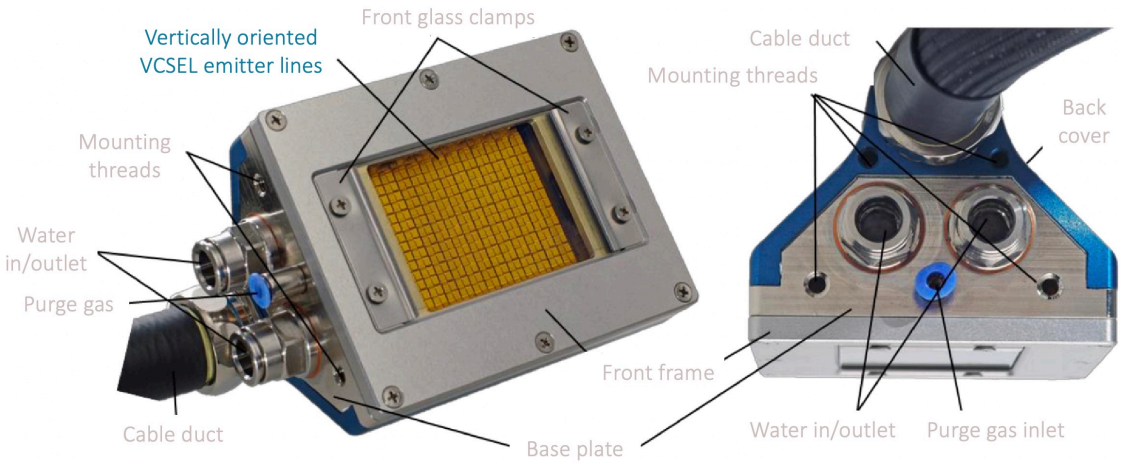

Figure 4.6: Parts of the VCSEL heater (modified from [80])

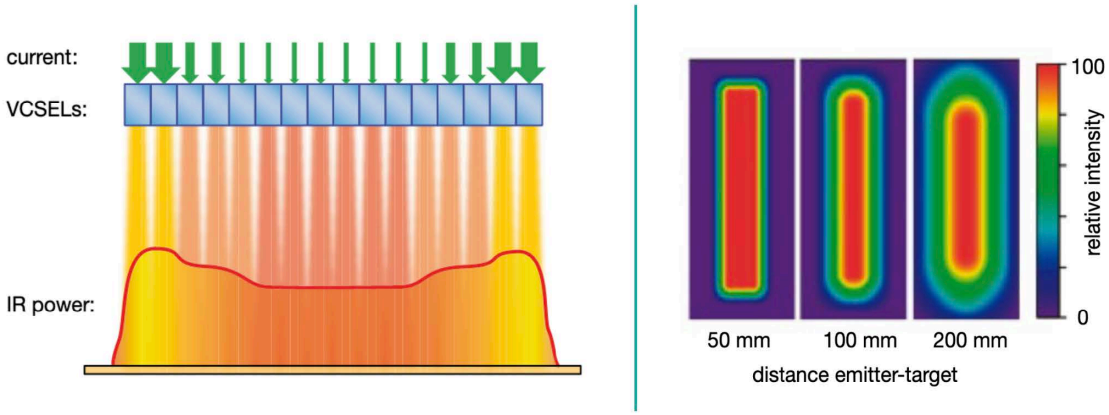

Figure 4.7: Effect of laser power variation and distance to sample on heating profiles [24][79]

Thermal camera

To monitor the temperature development of the sample surface during laser heating, a FLIR A655sc high-resolution IR camera with a FOL25 lens was used. The IR camera was used to capture thermal images of the specimen at a sampling rate of 200 frames per second, meaning the temperature is recorded every 5 milliseconds. For this frame rate the image size is set to 640x120 pixels.
The data obtained from the temperature measurements are analyzed using the FLIR-tools analysis software. From the recorded data, the average, maximum and minimum temperature over time can be plotted for a single point or region. For every sample, the maximum temperature and the average temperature of a ellipse, placed approximately at the same location as the part of the sample cut out for DSC characterization. In Figure 4.8, this is shown for an example.

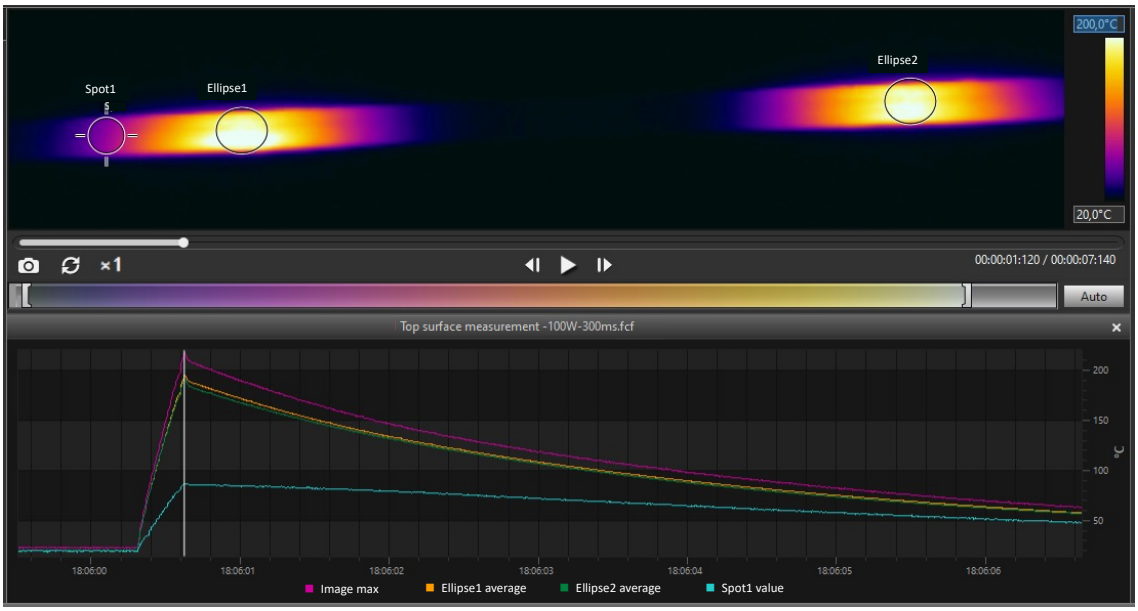

Figure 4.8: Thermal recording of the laser heated tape (for two samples created simultaneously) used to determine the maximum and average surface temperature evolution

4.2.3. Limitations

A few limitations are identified for the used set-up. These are:

- Due to the stationary set-up, it was not possible to use staged heating. Staged heating can only be achieved with a VCSEL laser heating different emitters to a different power, and moving the sample at a certain speed through the created laser power zones.
- Only one thermal camera is available, meaning the top and bottom surface temperature cannot be measures simultaneously. Two samples are therefore created per sample setting, where for one the top temperature is measured and for the other the bottom temperature. These samples are always created on the same day, to minimize the differences in environment, which could affect the obtained temperature.

4.3. Sample material

The samples used for the experiments are carbon-fiber reinforced polyphenylene sulfide (CF/PPS). The composite material was provided by Suprem, in the form of a uni-directional prepreg tapes with a nominal width of 6.35 mm and nominal thickness of 0.14 mm. Other material parameters given by the manufacturer can be found in Table 4.1.

$$W_f = \frac{\rho_f V_f}{\rho_f V f + \rho_m (1 - V_f)} \tag{4.1}$$

To determine the fiber weight fraction, equation 4.1 was used, where V_f is the fiber volume fraction, W_f is the fiber weight fraction and ρ_f the fiber density and ρ_m the matrix density. The calculated weight fraction can also be found in Table 4.1.

The values found in literature for the crystallization enthalpy of 100% crystalline PPS vary from 50 to 150 J/g. The variability is caused by the impossibility of obtaining and measuring a 100% crystalline sample, meaning the value has to be determined indirectly, such as the extrapolation of measured values or the measurement of melting point depression [81]. The most common value used in literature is 80 J/g, based on the early works of Brady [82]. As the calculated degrees of crystallinity are used mainly for a comparative analysis between each other, the exact value used is not critical for the validity of the conclusions drawn.

Table 4.1: Given and derived properties of the CF/PPS prepreg composite tape (the value of $\Delta H_{f,100\%}$ is obtained from [82])

Suprem™ T 51% C10365 / PS1046 0.14 x 6.35			
Property	Description	Value	Unit
T_g	Glass transition temperature	85 - 90	°C
T_m	Melting temperature	280 - 285	°C
ρ_m	PPS / Matrix density	1.35	g/cm³
ρ_f	CF / Fiber density	1.81	g/cm³
V_f	Fiber volume fraction	51	%
W_f	Fiber weight fraction	58.3	%
$\Delta H_{f,100\%}$	Crystallization enthalpy of 100% crystalline PPS	80	J/g

Polyphenylene sulfide

Polyphenylene sulfide (PPS), a semi-crystalline thermoplastic polymer with a symmetric rigid backbone consisting of aromatic rings linked by sulfides, as shown in Figure 4.9. It exhibits several appealing physical and chemical properties, such as high thermal stability, excellent flame and chemical resistance and dimensional stability, high modulus and tensile strength and good friction properties. Compared to other thermoplastics, PPS has a relatively low melting viscosity. Values of around 200 Pa.s have been reported [83], but the exact value of the melt viscosity depends on many factors, such as the molecular weight, temperature, branching and used additives. This makes the material a good choice for products with high fiber content and positively affects the degree of intimate contact development, easing the material flow at the layer interfaces [15].

The glass transition temperature T_g of the PPS matrix lies between 85 and 90°C and the melting temperature T_m between 280 and 285°C. [11][28][84][30] The ideal processing temperature is slightly higher and lies between 305 and 320°C, due to the lower viscosity in this range. Yan et al. investigated the equilibrium melting temperature of a PPS powder containing both folded-chain and extended-chain crystals. They found that the equilibrium melting point at which the crystals were fully eliminated to be at 350°C for the folded-chain crystals and 370°C for the extended-chain crystals. The authors also observed a double melting peak at 281°C and 295°C, which they attributed to the melting of folded-chain and extended-chain crystals, respectively [46].

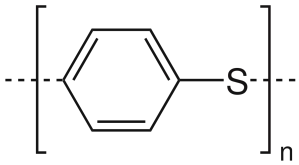

Figure 4.9: Structure of polyphenylene sulfide

The above-described properties in combination with reinforcement fiber make CF/PPS a perfect material for thermoplastic structural components. An important factor affecting the performance of CF/PPS is the degree of crystallinity, which depends on the manufacturing process and thermal history of the material. PPS is known to be able to achieve high levels of crystallinity, reaching values of up to 60% in commercial applications [9]. These values have however not yet been achieved using AFP manufacturing methods, for which the maximum reported value lies at 29%, according to Chen et al. [55].

The exact composition of the CF/PPS composite is unknown and could not be provided by Suprem. However, it can be assumed that additives are added to the PPS matrix, enhancing the composite properties and behavior for desired applications. Additives such as nucleating agents, antioxidants, heat stabilizers, UV stabilizers, plasticizers, pigments, adhesives, nucleating agents, and flame retardant compositions are known to be commonly used in PPS [85]. The effect of the additives could among others result in different crystallization kinetics and transition temperatures, compared to pure PPS.

4.4. Laser heating settings

Using the described set-up, the CF/PPS tapes are heated to different temperatures distributions over time and space. In this section the steps taken to determine the final test plan, and an overview of

all laser input settings used are presented. Two steps are described, namely the exploration and production. During the exploration step the effect of different laser input settings is studied and related to desired sample temperatures. During the production step, the samples are produced using laser inputs based on the findings of the exploration step.

Based on the temperature achieved in the heated samples, two groups of samples are distinguished:

- Samples heated above T_m
- Samples heated below T_m (in these samples temperatures above T_g are reached)

The reason T_m is chosen as a criterion for the division of the samples is its relation to the crystallinity. At temperatures above T_m the crystallinity is known to decrease, due to the melting of the crystalline region. At temperatures between T_g and T_m only the amorphous phase melts, and no decrease in crystallinity is expected. The crystallinity of samples in this temperature range can either increase or stay constant, depending on the cold- and re-crystallization kinetics.

It is also possible to create samples in which the top surface is heated above T_m while the bottom temperature is kept below T_m. It was decided to not use these samples in the analysis, for the following reason: the main goal is to better understand the effect of laser heating and achieved tape temperatures on the crystallinity. As all sample characterization is done for the whole thickness of the tape as a bulk, no distinction can be made between the crystallinity of the parts heated above and below T_m. By heating the complete tape to temperatures either above or below T_m, more uniform crystallization and melting kinetics throughout the tape are expected, and the bulk tape can be used to study the relation between temperature and crystallinity.

Exploration

The settings varied to obtain samples with different temperature histories are the laser power, heating time, and heated area. As a result, the maximum top and bottom surface temperatures, heating rates and heated times are affected. The relation between these three parameters is shown in Figure 4.10. As it is not possible to only vary one of these parameters, while keeping the other parameters constant, a different approach had to be selected. It was chosen to focus on keeping the maximum temperature as constant as possible, while varying the heated time, resulting in different heating rates.

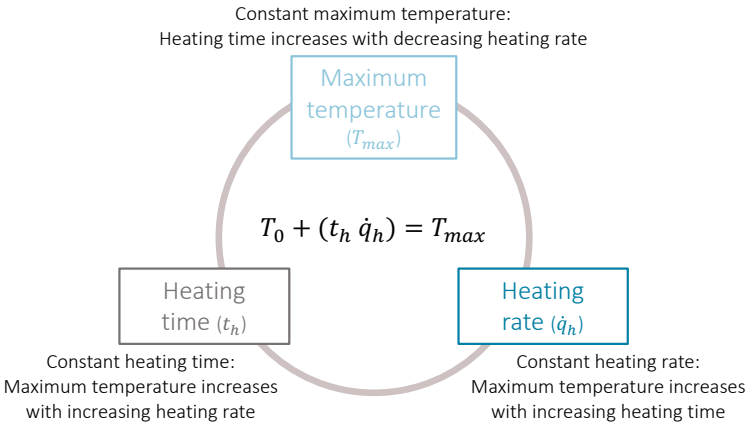

Figure 4.10: The relation between temperature, heating rate and heating time

During the exploration phase, the heated area is kept constant. The distance between the laser and sample was fixed at 40 mm, and a constant number of 2 emitters was used to heat the sample. As the width the irradiation area achieved with two emitters at 40 mm distance is in the same order as the diameter of the tested samples during DSC, only the tested area is heated by the laser directly. Outside of this area, the temperature only increases due to transverse heat flow from the directly heated area, and the surrounding tape acts as a heat sink (as shown in Figure 4.5).

The two laser settings varied during the exploration phase are the laser power and heating time.

The following procedure is used to study the dependence of the temperature evolution on the laser settings:

1. A constant power is applied for a long heating time, until a temperature between **450** and **500°C** is reached. This step is repeated for a laser power of: **50W**, **100W**, **150W**, **200W**, **250W**, **300W** and **400W**.
2. To determine the heating time to be used for "Samples heated between T_g and T_m" for each laser power, the top surface temperature is analyzed (as this is the maximum temperature of the sample and has to be below T_m). The time at which the maximum top surface temperature reaches 220°C is derived from the FLIR camera data.
3. To determine the heating time to be used for "Samples heated above T_m" for each laser power, the bottom surface temperature is analyzed (as this is the minimum temperature of the sample and has to be above T_m). The time at which the maximum bottom surface temperature reaches 350°C is derived from the FLIR camera data.

The times needed to reach these temperatures are calculated directly from the measured temperature data, as shown schematically for a power of 50W in Figure 4.11.The results of the above mentioned steps can be found in Table 4.2, rounded to the nearest multiple of 50 ms as this is the variable time step using the VCSEL unit control software. The calculated times needed to reach 220°C and 350°C are used as a starting point for the production phase.

Table 4.2: Derived times needed to reach the desired temperatures for the two sample sets for laser powers varying from 50 to 400W

Laser power	Time to reach a top temperature of 220°C *	Time to reach a bottom temperature of 350°C *
[W]	[ms]	[ms]
50	**600**	**1700**
100	**300**	**800**
150	**200**	**500**
200	150	**400**
250	150	**300**
300	100	**300**
400	100	**200**

* Rounded to the nearest multiple of 50ms

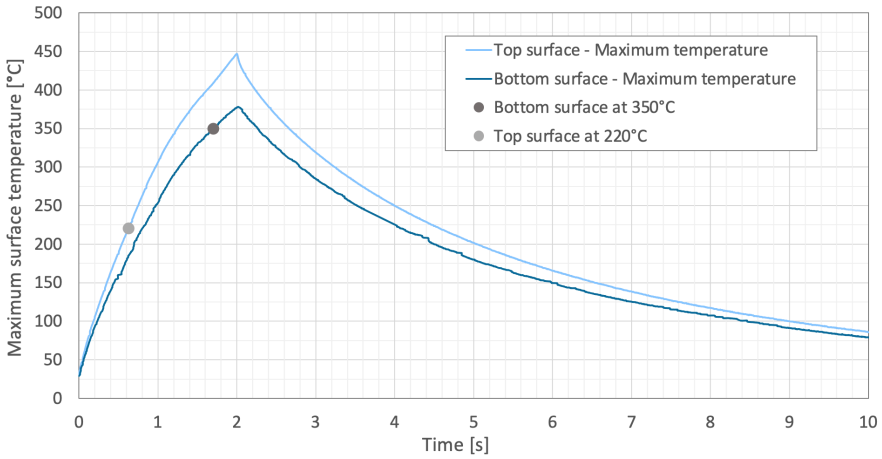

Figure 4.11: Maximum temperature profile of top and bottom surface of a sample heated with a laser power of 50W, with indicated times to reach 220°C at the top surface and 350°C at the bottom surface

Production

For the samples heated between T_g and T_m additional laser power settings are added, due to the short heating times corresponding to the higher powers tested during the exploration phase. The powers

used for the samples in this set are: 20, 30, 40, 50, 75 and 100W. It was found that the heating times presented in Table 4.2 match the actual time needed to reach a maximum top surface temperature of 220°C relatively well, but in some cases small adjustments to heating times were needed. An overview of all settings used to produce samples heated between T_g and T_m can be found in Table 4.3.

For the samples heated above T_m the heating times presented in Table 4.2 did not match the actual time needed to reach a maximum bottom surface temperature of 350°C well. The reason for this could be the difference in heat transfer through the tape, resulting in less consistent bottom surface temperature measurements for constant laser input settings. After slight adjustments, the settings presented in Table 4.3 are used to produce the samples heated above T_m.

An additional set of samples heated above T_m is added, with an increase in heated area. For these samples all emitters are turned on in a pyramid distribution, as shown in Figure 4.12. This choice of a pyramid laser power distribution was made, as using full laser power on all 12 emitters at powers higher than 100W caused the sample to reach the degradation temperature in less than 50ms, which was selected as the smallest time interval that the laser control software and thermal camera can confidently measure. For consistency reasons, the pyramid distribution is also kept for laser powers below 100W. When compared to samples heated with 2 emitters, a higher temperature of the tape surrounding the tested sample is generated. This has the expected effect of a weaker heat sink of the surrounding tape on the tested sample, resulting in lower cooling rates and longer cooling times. An overview of the settings used to produce these samples is also given in Table 4.3.

Table 4.3: Overview of laser settings used to produce heated samples

Heated between T_g and T_m (2 emitters)	
Laser power [W]	Heating times [ms]
20	1000, 1250, 1500, 1600, 1750, 1800
30	850, 950, 1100
40	700, 800
50	500, 600
75	550
100	300, 450

Heated above Tm (2 emitters)	
Laser power [W]	Heating times [ms]
25	2500
50	1300, 1750, 2000
100	600, 850, 900
150	500, 600, 650
200	300, 450
250	350
300	300
400	200, 250

Heated above Tm (12 emitters)	
Laser power [W]	Heating time [ms]
4-6-4	4200
9-12-9	2000
18-24-18	1000
38-50-38	400
75-100-75	200
150-200-150	100

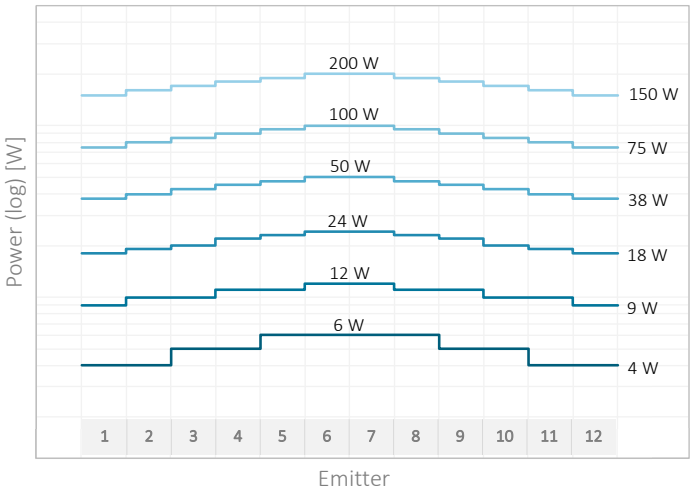

Figure 4.12: Overview of pyramid laser power distributions used for the samples heated using all 12 emitters

4.5. Characterization methods

Characterization methods are used to analytically determine the chemical, microstructure and physical properties of materials. For the purpose of this thesis 4 characterization methods are used, namely differential scanning calorimetry (DSC), X-ray diffraction (XRD), thermogravimetric analysis (TGA) and optical microscopy.

DSC and XRD are both used to study the crystallinity in polymers, but both focus on a different aspect of the broadly used term 'crystallinity'. DSC is used to determine the degree of crystallinity (DOC), defined as the volume ratio of crystal regions to amorphous regions, expressed as a percentage, while XRD is used to study the size of crystallite structures [48] [86].

TGA is a characterization technique used to asses the weight reduction of a sample as a function of temperature, and thereby provide more information about the degradation behavior. It is suggested to do TGA of a sample before using it for DSC, in order to set the temperature range for which the weight reduction of the tested sample is kept below 2%.

4.5.1. Differential Scanning Calorimetry

DSC is a thermal analysis characterization method, used extensively within polymer science to study processes involving a change of heat capacity (second order transformations) or change of enthalpy (first order transformations). The method is commonly used to study the kinetics of melting, crystallization, polymerization and glass transition [70]. During this thesis the focus is on the use of DSC to indirectly calculate the degree of crystallinity.

The general working principle of DSC is based on the measurement of the amount of heat radiated or absorbed by a sample as a function of temperature and time. During DSC the sample is placed in an aluminum pan and the heat flow into or from the sample is measured during an isothermal or dynamic temperature scan. By comparing the results to a reference measurement with an empty pan, the heat transfer of the sample can be separated from the heat transfer of the pan it is placed in [70].

There are two main types of DSC based on the property they measure:

- **Power-differential or power-compensation DSC** measures the rate of heating power absorption, by placing the sample and reference in two thermally insulated furnaces heated separately to the same temperature. A different heating power is needed to heat the two furnaces, which is the value measured. The sign convention in the output diagrams is endothermic heat flow up.
- **Heat-flux DSC** measures the heat emission of sample and reference subjected to the same thermal program by a single heater. The sign convention in the output diagrams is exothermic heat flow up.

A schematic diagram showing the key features of the set-ups used and the typical output diagrams are shown in Figures 4.13 and 4.14. Despite the difference in data measured, both methods are based on the same physical principles and the results that are obtained should theoretically be identical, and only slight differences in accuracy are reported [87]. For the majority of applications, the quality of data obtained with either of the types of DSC is sufficient.

For the measurements performed during this thesis, both types of DSC are used. The reason for this is break down of the primarily used DSC instrumentation throughout the course of the experimental research. For the first part of the measurements the heat-flux TA Instruments DSC 250 machine is used. For the second part of the measurements a switch is made to the power-compensation Perkin Elmer DSC 8000 machine.

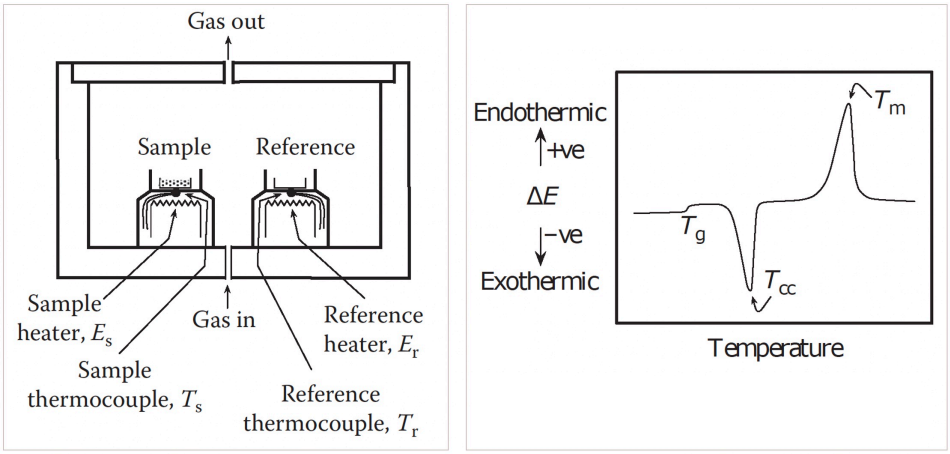

Power-compensation DSC

Figure 4.13: Key features of the cell design and the typical output curve of power-compensation DSC [70]

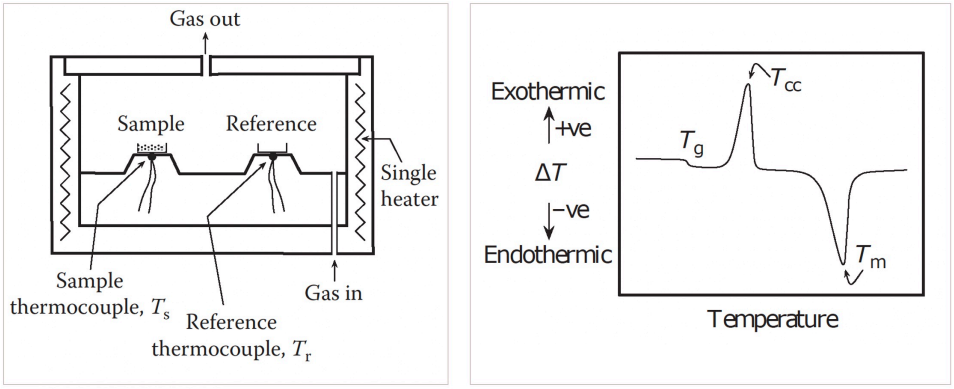

Heat-flux DSC

Figure 4.14: Key features of the cell design and the typical output curve of heat-flux DSC [70]

DSC procedure

For the procedure used to carry out the DSC sample preparation, calibration, set-up, measurement and analysis, the ISO 11357-1 to -3 and ASTM D 3418-03 standards are used as guideline [88][89].

Both types of DSC use the same kind of containers for the samples, specifically small cylindrical aluminum pans with lids. The mass and size of the sample is limited by the dimensions of the container, but generally a smaller sample (between 5-10 mg) is recommended as it gives a better resolution due to more uniform heating. Additionally, good physical and thermal contact between the sample and pan is required, to eliminate barriers in the heat transfer. Bad thermal contact can result in heat flow discrepancies and a temperature lag between the pan and sample [48].

To extract samples for DSC from the prepreg CF/PPS tapes, holes with a diameter of 6 mm are punched out using a hollow punch tool. For the laser heated samples, the location with the highest laser energy input is marked and punched out the sample as closely as possible. The weight of all samples is measured prior to the DSC procedure and used to obtain the weight normalized heat flow. For the prepreg tape used, the weight of the described punched out samples lies between 6-7 mg.

DSC measurements are typically performed at heating rates of 10 to 20 K/min. At higher heating rates, the time necessary for the sample to catch up with the programmed temperature increases, negatively affecting the accuracy of the measurement. During the whole measurement the furnace is filled with nitrogen serving as a purge gas and preventing oxidation of the tested sample. During cooling liquid nitrogen (LN2) is used to provide controlled and efficient cooling.

The temperature cycle used for the experiments is shown in Figure 4.15. The heating from 30°C (room temperature) to 350°C is done at heating rate of 10°C/min, followed by an 5 minute isothermal

hold and cooling back to 50°C at a cooling rate of 20°C/min. The isothermal sections are added to allow the signal to stabilize.

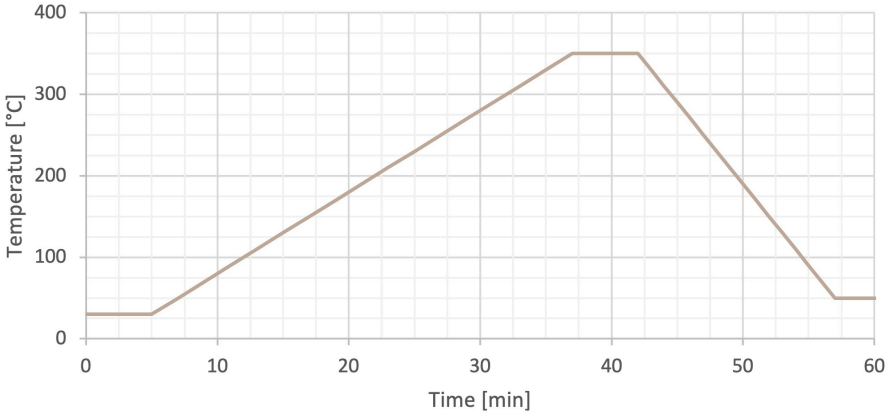

Figure 4.15: DSC temperature cycle

DSC data analysis

Both the TA instruments and Perkin Elmer DSC machines come with a build in software to analyze the measured heat flow. For non-isothermal DSC analysis, the recorded and normalized heat flow is plotted against the temperature experienced by the sample. Using the software the curves (and specifically the peaks in the curves) can be integrated to calculate the change in enthalpy. Additional information, such as transition or peak onset and offset temperatures and peak heights can also be determined.

The peak integration is done with respect to a baseline. In an ideal case, the baseline of the measured curve would be linear between the offset of the glass transition and degradation. This is however often not the case. One reason is the changing heat capacity as a function of temperature. However, other factors such as inconsistent gas flow, unavoidable differences between the sample and reference sensors and their surroundings, and differences in contact between pan and heating surface of the sample and reference pans, can also affect the baseline shape [87].

As suggested in ISO 11357-3:2018 [88], sigmoidal baselines can be used for the peak integration in cases of significant differences in the specific heat capacities around a peak, to improve the results. In Figure 4.16, a schematic diagram is used to shows how quantitative data can be obtained from DSC curves [70]. As not all DSC measurement baselines presented in Chapter 5 are linear, it was decided to keep the analysis consistent and perform all peak integrations with respect to a sigmoidal baseline.

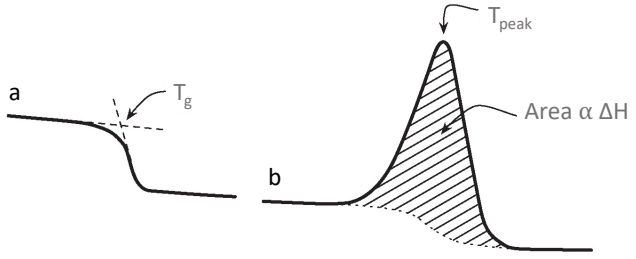

Figure 4.16: Schematic analysis of a heat-flux DSC curve, showing: a) the determination of T_g defined as the onset temperature of the transition step, and b) the peak temperature and area determination for an exotherm peak (the same principles apply to an endotherm peak) [70]

When analyzing the peaks, it is important to keep in mind that both (cold-)crystallization and melting are not instantaneous, and occur over a range of temperatures. This is caused by the characteristic morphology of polymers, and specifically the crystalline portion consisting of a large number of different crystal sizes, all melting and crystallizing at a slightly different temperature [70].
Theoretically, the crystals start to liquefy at the melting peak onset temperature, and are fully melted at the offset temperature [70]. Due to the broad melting peaks observed in the DSC curves of polymers,

the onset temperature cannot be precisely determined and therefore loses its physical meaning. As a result, the peak melting temperature T_m is commonly used in the case of polymers, giving a measure of the average melting temperature of the crystallites in the sample [90].

The results obtained from DSC analysis are directly dependent on the measurement conditions, such as heating rate, sample mass and heat transfer (affected by the contact between sample and pan, as well as the crucible material). The results can therefore not be used to determine the global material properties, and different samples should only be compared for identically performed measurements [90].

DOC calculation

The measurement of DOC using DSC is an indirect method, using the measured heat of fusion to calculate the DOC using Eq. 4.2. In this equation X_c is the the DOC. ΔH_m and ΔH_c are the specific enthalpies of melting and cold crystallization respectively, obtained from the DSC measurements in J/g. W_f is the calculated fiber weight fraction, using the densities of the PPS matrix and CF fiber provided by the manufacturer and Eq. 4.1. Lastly, $\Delta H_{f,100\%}$ is the specific melting enthalpy of an ideal crystal, based on values found in literature ($\Delta H_{f,100\%}$=80 J/g) [82]. It should be noted that the selected value for $\Delta H_{f,100\%}$ does not guarantee an accurately calculated DOC, and the outcomes should therefore only be used to compare the results with each other.

$$X_c = \frac{\Delta H_m - \Delta H_c}{\Delta H_{f,100\%}(1 - W_f)}.100\% \tag{4.2}$$

The principle used in Equation 4.2 to determine the DOC is that it divides the enthalpy needed to melt the crystals present in the sample by the enthalpy that would theoretically be needed if the material was 100% crystalline. Due to the cold-crystallization occurring during the DSC temperature scan, the crystallinity of the sample increases and a higher melting enthalpy is obtained. To compensate for this, the enthalpy of cold-crystallization is subtracted from the melting enthalpy. This way, the DOC prior to the cold-crystallization can be determined.

4.5.2. Microscopy

Cross-sectional microscopy provides insights about sample micro-structure and surface profile. Çelik et al. observed a relation between original surface profile and deconsolidation [91]. As the surface profile of the incoming tape is not completely uniform and includes waviness and roughness, the temperature profile obtained is non-uniform as well due to the various angle of incidence of the laser. This non-uniform heating also affects the crystallization kinetics, and the variation in surface roughness and fiber distribution within the as-received tape thus of relevance for this research.

Specimen preparation

Resin-casting of the tape is used for the preparation of microscopy specimens. The sample tapes are cut with an offset of 3 mm to the area of interest, to account for material removal during grinding and polishing. The cut samples are placed into thin-sample holders by Struers MultiClips to keep them in the desired position, and placed into a cylindrical mould. Next, Struers EpoFix resin is poured into the moulds and left to cure, after which the specimens are ground and polished, using the Struers Tegramin-201 machine. The grinding and polishing routine used is based on the work of Bussink and designed the remove 3 mm of the material [40]. This routine is shown in Table 4.4.

Table 4.4: Grinding and polishing routine used for the microscopy specimen preparation

Plate	Solution	Force [N]	Time [mm:ss]
SiC Foil #180	Water	15	00:15
SiC Foil #320	Water	25	00:25
SiC Foil #1000	Water	25	00:30
SiC Foil #2000	Water	25	00:40
SiC Foil #4000	Water	25	00:40
MD Chem	OP-S NonDry	15	03:00
MD Chem	Water	15	01:00

Sample analysis

The microscopy specimens are studied under the Keyence VK-X1000 Laser Scanning Confocal Microscope (LSCM) using a magnification of 20x to 50x. In order to asses the cross-section properties globally over the whole width, multiple images can be captured and stitched together using the 'Focus Variation' and 'Laser confocal' method of the Keyance software. This method uses the image with the best focused focal depth for the stitching. The obtained cross-section images are analyzed qualitatively, focusing on differences in fiber distribution and void content, both between multiple samples as well as within a single sample.

4.5.3. X-Ray Diffraction

X-ray diffraction (XRD) is a technique used to study the crystal structure of solid materials at atomic scales. The working principle of XRD is based on the fact that the wavelengths of X-rays are in the same order of magnitude as the distance between lattice planes in crystalline materials. These X-rays are directed at the sample, scattered by the electron clouds around the atoms, and the diffracted rays are collected. In the case of a periodical lattice, constructive interference of diffracted rays results in peaks when plotted against the Bragg angle 2θ. From these plotted peaks the lattice distance and an estimation of the crystal size can be calculated [92]. The physical principle in schematically shown in Figure 4.17.

A typical X-ray diffractometer consist of three basic elements: an X-ray tube, a sample holder, and an X-ray detector, as shown in Figure 4.17. For this thesis the D8 ADVANCE diffractometer from Bruker is used to perform wide-angle X-ray diffraction (WAXD) measurements, using a Cobalt radiation source. As an alternative, small-angle X-ray scattering (SAXS) could be used as it can effectively measure the average crystalline lamellae thickness more accurately [86]. This was however not possible with the available equipment.

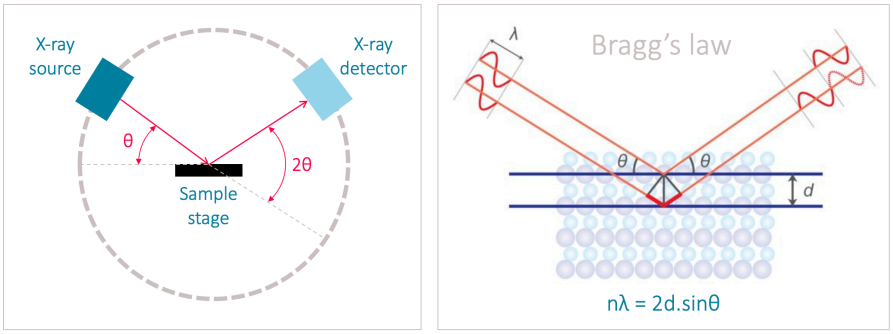

Figure 4.17: X-ray diffractometer components (left) and application of Bragg's law to XRD (right)

The samples used for XRD can either be in powder or tape form. The advantage of using powdered samples is that the bulk property of the material is distributed more uniformly. The area of interest in the samples studied is however only a few mm wide and the thickness of the tapes is 0.3 μm. The X-rays can penetrate through the whole depth of the tape and a width of 3 mm is used in the measurement settings. Therefore, a tape could be used and creating a powder was not necessary.

Additionally, XRD was done on a sample of pure carbon fibers, to be able to distinguish the CF spectrum from the PPS spectrum. In order to separate the fibers from the CF/PPS tape, the tape was heated in an oven under nitrogen purge gas at 600°C for 10 hours. Under these conditions, the PPS matrix can fully dissolve, while the CF remain. As can be seen in Figure 4.18, slight damage to the carbon fibers is observed, most likely due to leakage of oxygen into the oven causing oxidation. The parts of the fibers that were not damaged are used for the XRD analysis.

Figure 4.18: Pure carbon fibers after degradation of the PPS matrix

The average crystallite size d can be calculated using the Scherrer equation 4.3. In this equation, K is the shape factor (usually around 0.9 [86]), λ is the X-ray wavelength (1.789Å for Cobalt), β is the full-width at the half maximum intensity of the diffraction peak and θ is the Bragg angle. In this thesis, XRD is used to compare the morphologies of the heated samples, providing complementary information to the degree of crystallinity obtained from DSC measurements.

$$d = \frac{K\lambda}{\beta.cos\theta} \tag{4.3}$$

4.5.4. Thermogravimetric Analysis

Thermogravimetric analysis (TGA) is an analytical characterization method used to determine a material's thermal stability, in which the mass is monitored as a function of temperature or time while subjected to a controlled temperature program in a controlled atmosphere. This way information about physical and chemical phenomena can be obtained, such as phase transitions and thermal decomposition.

For the experiments in this thesis the Perkin Elmer TGA 4000 is used. A typical thermogravimetric analyzer consists of a sample pan supported by a precision balance, all placed into a furnace with a programmable control temperature. The mass of the sample is continuously monitored during the experiment. The environment within the surface is controlled using a purge gas, which for the experiments performed van nitrogen. The samples used for TGA are similar to the punched out circles used for DSC, but with a smaller diameter of 4 mm in oder to fit in the sample holders.

The main purpose of the TGA measurements is to determine the thermal degradation behavior of the used CF/PPS sample tapes. The onset degradation temperature (T_d) is of importance for both the laser sample heating as well as the DSC analysis. For the laser heating of the samples, the degradation onset temperature should not be exceeded, as this would have an unknown effect on the crystallinity, making the analysis of the results more complicated. For DSC the temperature at which a weight loss of 2% is observed should not be exceeded, as this could damage the equipment.

The TGA experiments are done at two different heating rates, heating from room temperature to 750°C. Different rates are used to determine the effect of heating rate on degradation. The maximum available heating rate of 30°C/min and a very low heating rate of 5°C/min are used.

5

Temperature evolution in laser heated samples

In this chapter the measured temperature evolution, as a result of a variation of laser heating inputs, is analyzed. First, the microstructure of the as-received tape is analyzed in Section 5.1, and the impact on the heat transfer in the material is discussed. In Section 5.2 the measured temperatures are presented and analyzed. The aim of this chapter is to answer **RQ1**: “How does the laser heating input affect the temperature of the heated sample?”, which will be reflected on in Section 5.4.

5.1. Microscopy results

In Figure 5.1, the baseline microscopy images of three samples are shown, captured at a magnification of 50x. The samples used to analyze the microstructure of the as-received tapes are taken from different parts of the roll of tape, at locations approximately 1 meter apart. The images are analyzed visually, and attention is paid to fiber distribution and fiber or resin rich tape surfaces.

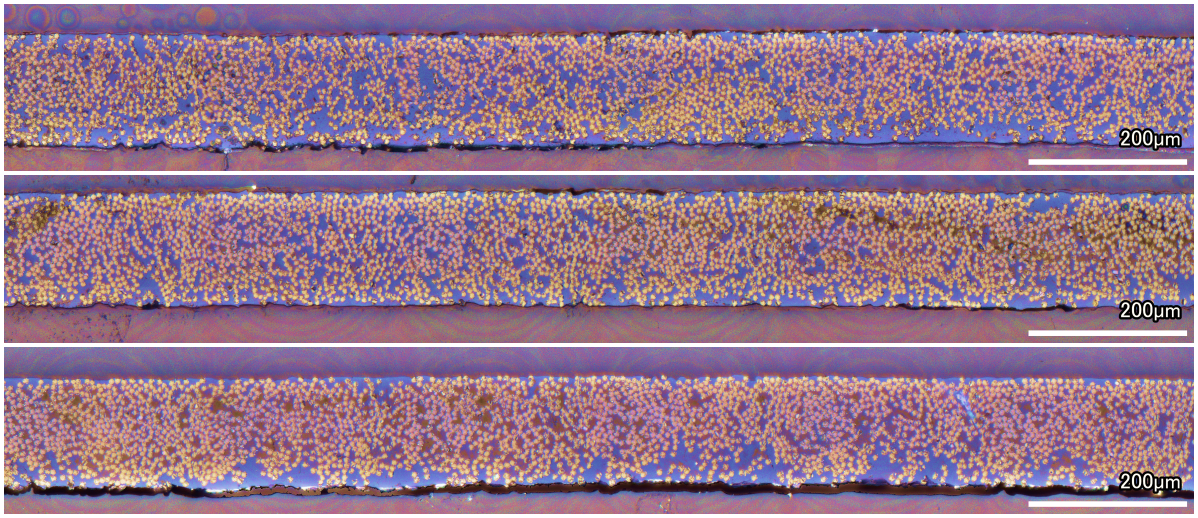

Figure 5.1: Microscopy images of as-received tape

Based on the visual analysis of the images, two main conclusions can be drawn that might have an influence on the heat transfer in laser heated samples. Firstly, the resin rich surfaces are mostly found on the bottom surface of the tape and the top surface is generally more fiber rich. This difference is consistent for all three samples. As a result, the tape orientation could have an effect on the heat transfer within the tape. Therefore, the top surface from the spool is always kept on top during laser

heating, to minimize the effect of variation in surface fiber distribution on the obtained temperatures.

Secondly, a non-uniform fiber distribution throughout the whole thickness of the tape can be observed. In Figure 5.2, these are indicated for one of the baseline images (the top image in Figure 5.1). The effect of this is that for different samples heated using the same laser settings a difference in measured temperatures could be observed, especially at the bottom surface which is more strongly affected by the heat transfer through the tape.

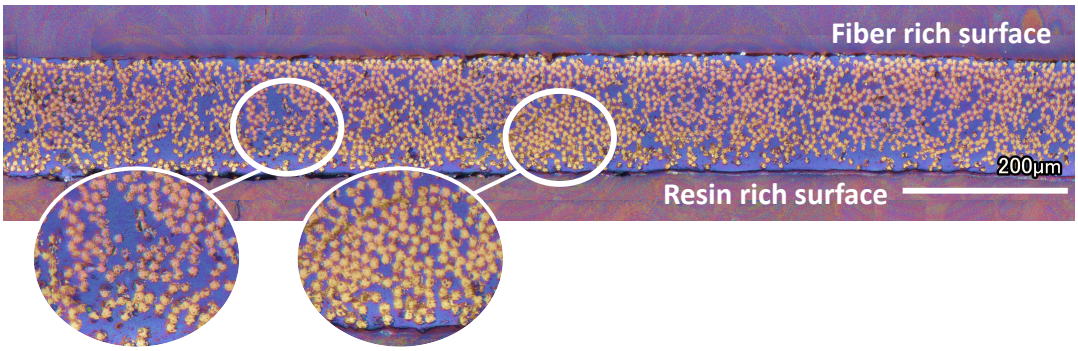

Figure 5.2: Microscopy image of as-received tape with indicated phenomena affecting the laser heated sample production

5.2. Thermal data measurement

In Figures 5.4 to 5.6 the evolution of the surface temperature over time for all samples is presented. The temperature value used in these plots is the maximum temperature. The average temperature is not plotted, but follows a similar trend as the maximum temperature, which is shown for one example in Figure 5.3.

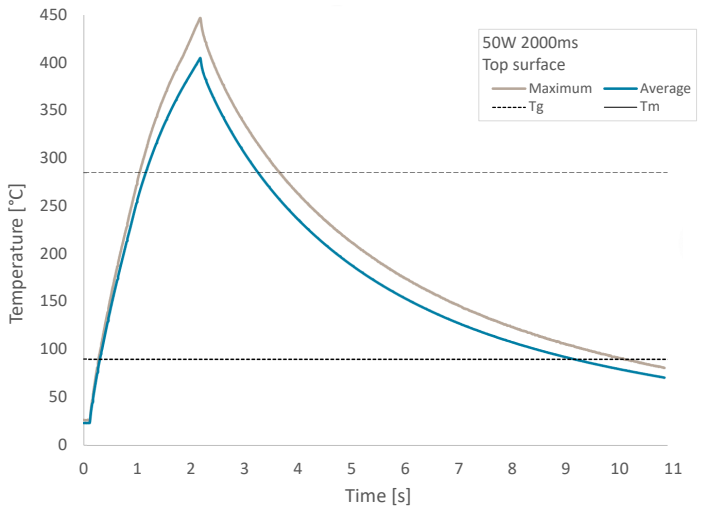

Figure 5.3: Maximum and sample average surface temperature plotted for one example sample, showing the similar shape of both plots

In some of temperature plots, bumps can be seen caused by an error in the temperature data collection by the FLIR camera (for example the “50W 600ms” bottom temperature curve in Figure 5.4 or the “50W 1750ms” bottom temperature curve in Figure 5.5). Depending on the severity and location of the errors in the measurement, some measurements were removed from further analysis.

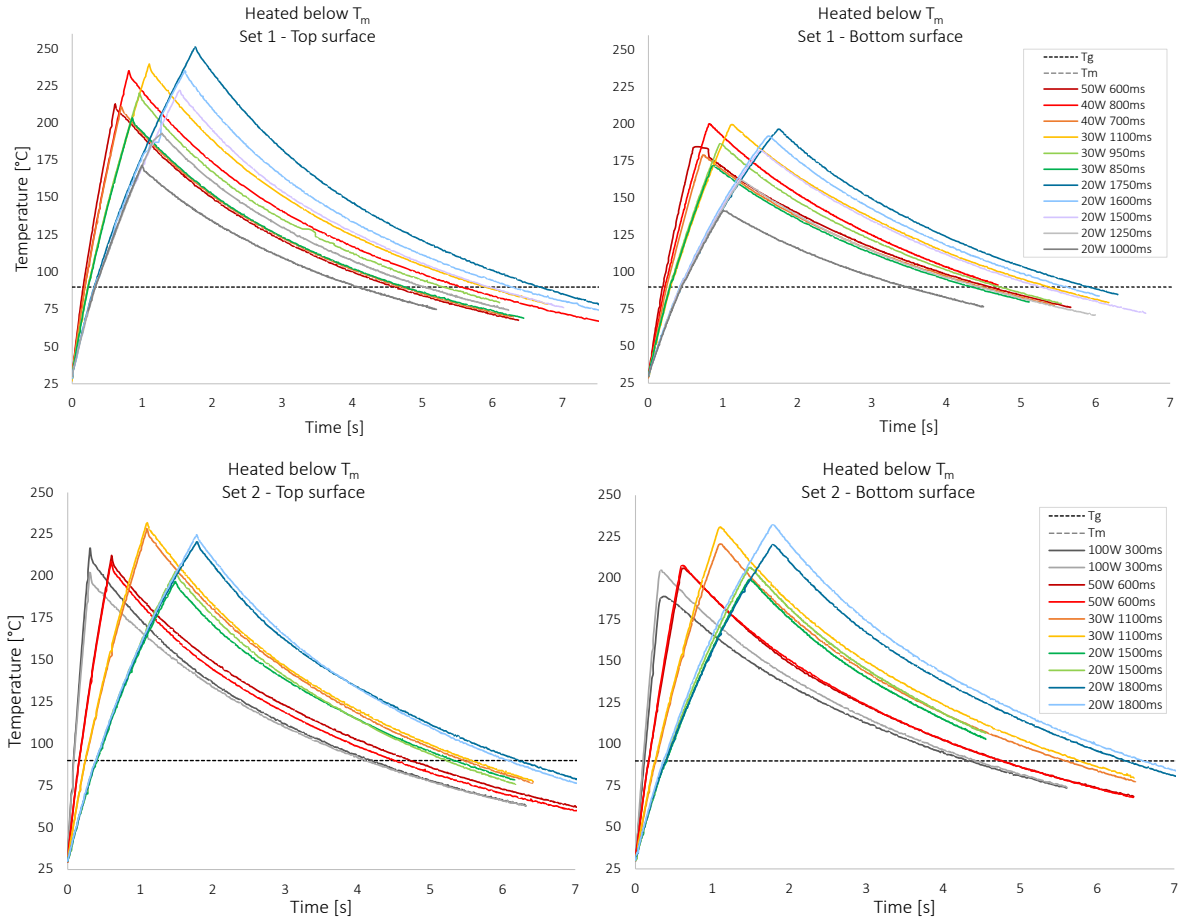

Figure 5.4: Temperature evolution for samples heated to temperatures between T_g and T_m

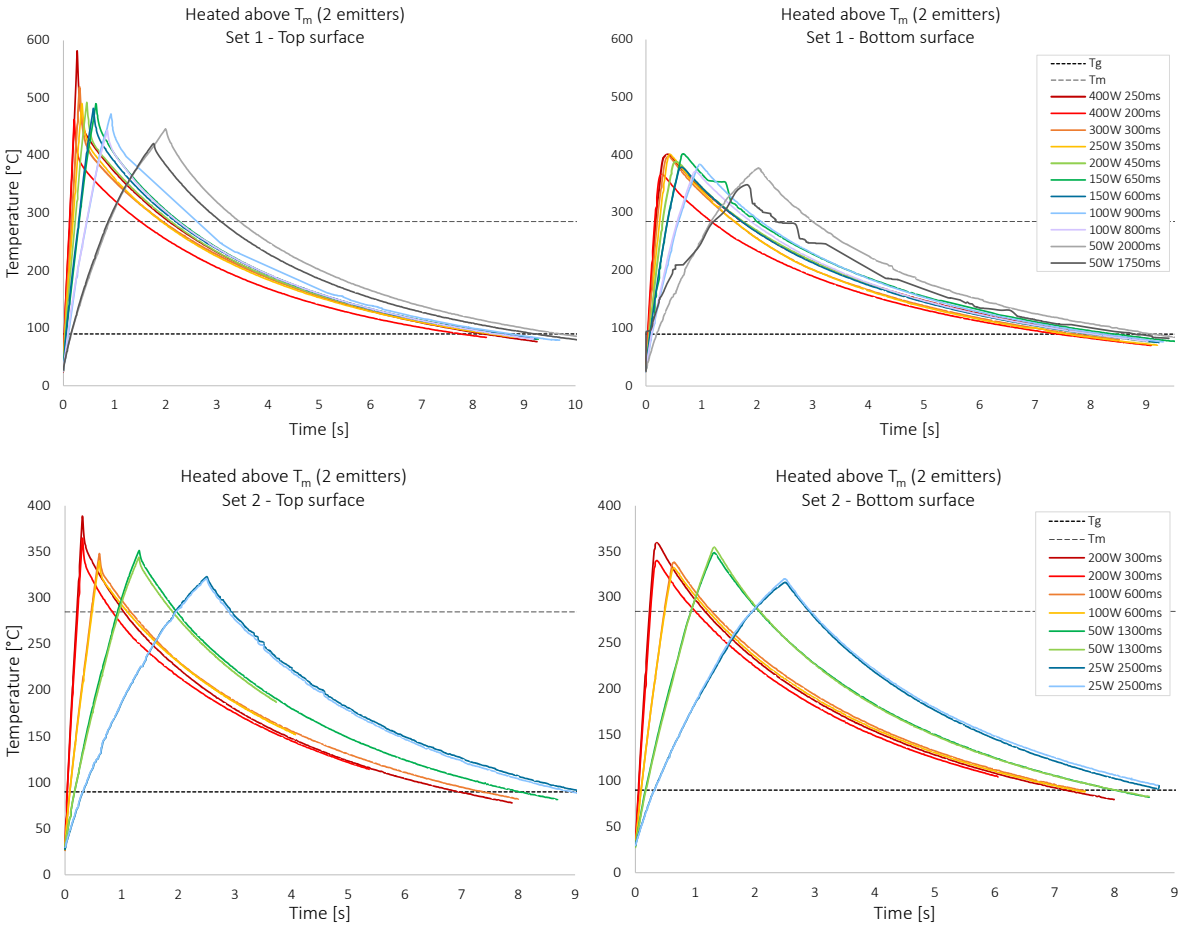

Figure 5.5: Temperature evolution for samples heated to temperatures above T_m using 2 emitters

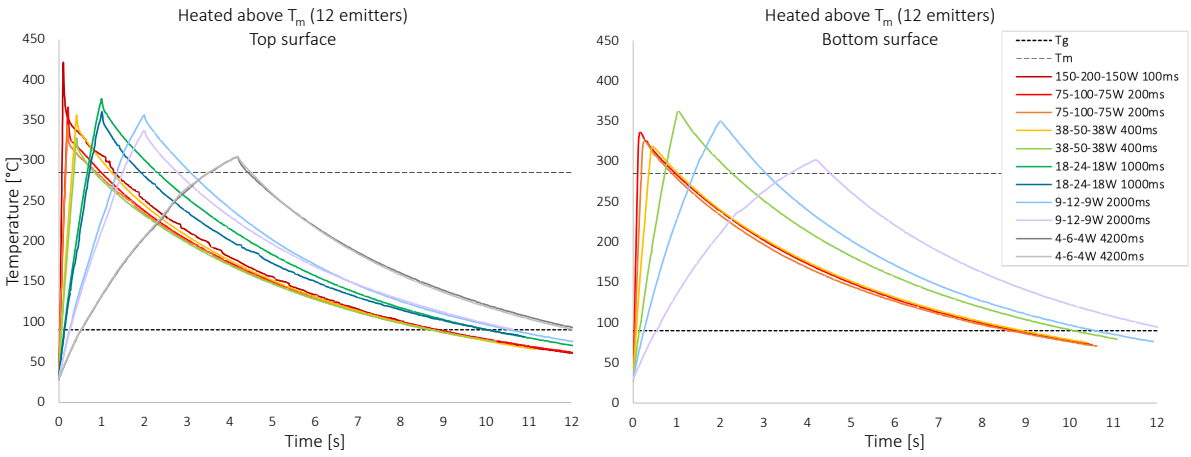

Figure 5.6: Temperature evolution for samples heated to temperatures above T_m using 2 emitters

The peak top and bottom temperatures obtained from the measured temperature evolution are shown in Tables 5.1 and 5.2 for the samples heated with 2 and 12 emitters respectively. In the tables a color scale is added per column, indicating the highest temperature in red and the lowest temperature in green.

Two unexpected trends are seen in the data, when comparing samples heated with identical laser set-

tings, and when studying the effect of increasing heating time for constant laser powers. The samples with identical laser settings are indicated in Tables 5.1 and 5.2 with light gray shading. Temperature differences of up to 25°C are observed between these "identical" samples. For the samples heated with a laser power of 20W for different heating times, a decrease in both top and bottom surface temperature is observed as the heating time increases, for some of the samples heated for 1500-1800ms.

It remains unknown whether the inconsistent temperature measurements are caused by an actual variation in heat transfer between the samples, or the result of inaccurate temperature measurements. The differences in sample microstructure observed in Section 5.1 might affect the heat transfer from the laser through the tape. As not all samples were produced on the same date, external conditions such as ambient temperature could also have an effect on the heat transfer and measured temperatures. On the other hand, the FLIR camera calibration and discrepancies in the positioning of the camera and sample might also result in differences in temperature measurements when carried out on different days.

The comparison of the top and bottom surface temperatures shows varying temperature gradient behavior. For the samples heated below T_m a maximum temperature gradient of 54°C is reached (for the sample heated with 20W for 1750ms), but no evident relation between temperature gradient and used settings is observed. For the samples heated above T_m using 2 emitters, bigger gradients are observed of up to 181°C (for the sample heated with 400W for 250ms). Higher gradients seem to be related to samples heated at higher laser powers, but again no consistent relation is observed. On the contrary, for the samples heated with 12 emitters an increase in temperature gradient is determined for samples heated at higher laser powers for shorter heating times. As can be seen in Figure 5.6, these settings are associated to more rapid heating profiles.

Table 5.1: Peak top and bottom surface temperature obtained for the samples heated with 2 emitters (both the maximum value reached by a single point in the sample and the average value taken over a circular specimen are listed)

Heated below T_m (2 emitters)		Top surface temperature measurement		Bottom surface temperature measurement	
Laser power [W]	Heating time [ms]	Maximum [°C]	Average [°C]	Maximum [°C]	Average [°C]
20	1000	172	153	142	127
20	1250	193	166	162	144
20	1500	222	199	183	159
20	1500	197	187	199	175
20	1500	203	190	206	182
20	1600	235	206	192	169
20	1750	251	217	197	169
20	1800	221	208	220	198
20	1800	225	208	232	212
30	850	204	178	172	153
30	950	221	193	187	163
30	1100	240	211	200	175
30	1100	229	213	221	199
30	1100	232	222	231	204
40	700	211	186	179	158
40	800	236	207	200	173
50	500	192	173	169	157
50	600	213	183	185	163
50	600	212	201	206	188
50	600	209	197	208	187
75	550	260	236	229	211
100	300	217	195	189	168
100	300	203	191	205	189
100	450	279	241	251	226

Heated above T_m (2 emitters)		Top surface temperature measurement		Bottom surface temperature measurement	
Laser power [W]	Heating time [ms]	Maximum [°C]	Average [°C]	Maximum [°C]	Average [°C]
25	2500	324	305	317	281
25	2500	321	301	320	279
50	1300	352	328	349	327
50	1300	344	326	355	318
50	1750	421	389	349	319
50	2000	447	405	378	332
100	600	348	324	339	298
100	600	340	321	333	305
100	850	444	415	372	326
100	900	472	433	384	337
150	500	419	375	355	316
150	600	482	444	379	334
150	650	491	454	402	355
200	300	389	352	360	334
200	300	366	341	340	313
200	450	492	459	389	342
200	450	494	454	397	359
250	350	491	448	402	350
300	300	519	462	398	342
300	300	504	459	410	351
400	200	462	420	366	311
400	250	582	507	401	351

Table 5.2: Peak top and bottom surface temperature and the temperature gradient for the samples heated with 12 emitters (both the maximum value reached by a single point in the sample and the average value taken over a circular specimen are listed)

Heated above T_m (12 emitters)		Top surface temperature measurement		Bottom surface temperature measurement		Temperature gradient (per laser input)	
Laser power [W]	Heating time [ms]	Maximum [°C]	Average [°C]	Maximum [°C]	Average [°C]	Maximum [°C]	Average [°C]
4-6-4	4200	305	273	302	253	1.5	10
4-6-4	4200	305	246	305	246		
9-12-9	2000	357	293	350	291	2.5	3
9-12-9	2000	338	283				
18-24-18	1000	377	312	362	311	7	4
18-24-18	1000	361	318				
38-50-38	400	357	304	318	281	25	13.5
38-50-38	400	329	285				
75-100-75	200	366	319	325	284	30	35
75-100-75	200	344	319				
150-200-150	100	421	390	337	304	84	86

5.3. Temperature data analysis

Apart from the peak surface temperatures, the following parameters can be derived from the temperature evolution data, which will be used as input for the DOC analysis in Chapter 6:

- Heating and cooling time (t_h and t_c)
- Average heating and cooling rate ($\dot{T}_h$ and $\dot{T}_c$)
- Time spent above T_g ($t_{T>T_g}$)
- Time spent above T_m ($t_{T>T_m}$)
- Temperature integral over time spent above T_g
- Temperature integral over time spent above T_m

For the average heating and cooling rate the Equations 5.1 and 5.2 are used. For the time spent above T_g, the time between surpassing T_g during heating and during cooling is taken, meaning it includes the time above T_m as well. The time above T_m is simply the time between surpassing T_m during heating and cooling. Similarly, for the temperature integral above T_g, the whole area under the curve between the passing of T_g during heating and cooling is taken. The whole temperature integral above T_m is thus included in the temperature integral above T_g.

$$\dot{T}_h = \frac{T_{max} - T_g}{t_h} \tag{5.1}$$

$$\dot{T}_c = \frac{T_{max} - T_g}{t_c} \tag{5.2}$$

The temperature integral is related to the heat absorption by the material, as shown in Eq. 5.3, where ΔQ is the heat absorption, c_p is the heat capacity of the material and m is the mass of the system. As the heat capacity is a function of temperature, the temperature integral can be used as a measure of ΔQ for comparison of the samples, as shown in Eq. 5.4.

$$\Delta Q = m \int_{T_2}^{T_1} c_p(T) dT \tag{5.3}$$

$$\begin{aligned} \int T(t) &= \int_{t_{2,(T=T_g)}}^{t_{1,(T=T_g)}} T(t) dt \\ &= \int_{t_{2,(T=T_m),2}}^{t_{1,(T=T_m)}} T(t) dt \end{aligned} \tag{5.4}$$

In Figure 5.7 the derivation of the data listed above is shown schematically. All values can be determined for both the top and bottom temperature, as well as using the maximum temperature or the average sample temperature.

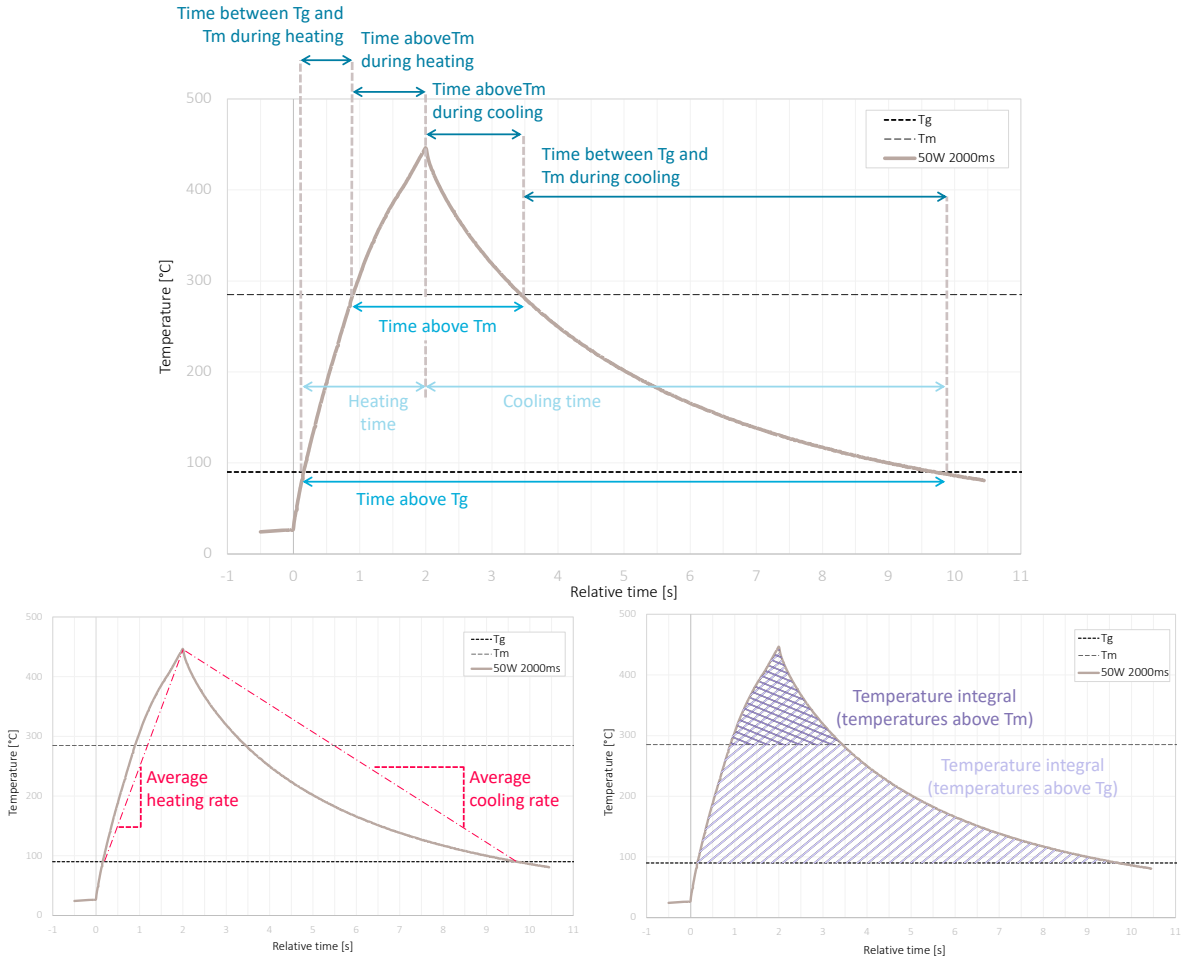

Figure 5.7: Temperature data derived from measured temperature history

The tables containing the calculated parameters for all samples can be found in Appendix A. In Table 5.3 the range obtained per temperature parameter for each set of samples is shown. The bigest temperature range does not necessarily result in the largest variation of other temperature parameters. For the samples heated below T_m a variation of 1.22 and 2.37 seconds are obtained for the heating and cooling time respectively. For the samples heated above T_m with 2 emitters, the range of heating times is similar, and longer cooling times are observed. However, despite the bigger range of temperatures measured, the variation in cooling times is smaller compared to samples heated below T_m. For samples heated with 12 emitters above T_m, the variation in heating time increases. The cooling times increase as well, but again a narrow range of values varying by 1.02 seconds is obtained for all samples in this set.

The main conclusion based on Table 5.3 is that for samples heated above T_m, the heated area is the main factor affecting the cooling time. For a constant number of emitters used to heat the sample, a narrow range of cooling times is obtained.

Table 5.3: Range of values and difference between maximum and minimum value obtained for each temperature parameter, listed per set of samples

	Maximum temperature	Heating time	Cooling time	Total time above T_g	Total time above T_m	Time from T_g to T_m (heating)	Time from T_g to T_m (cooling)	Heating rate	Cooling rate	Temperature integral >T_g	Temperature integral >T_m
	[°C]	[s]	[s]	[s]	[s]	[s]	[s]	[°C / s]	[°C / s]	[°C . S]	[°C . S]
Heated below T_m (2 emitters)											
Range	172 - 279	0.2 - 1.6	3.1 - 5.5	3.8 - 6.4	-	0.2 - 1.6	3.1 - 5.5	95 - 524	27 - 34	470 - 1 193	-
Difference	*107*	*1.22*	*2.37*	*2.61*	*-*	*1.22*	*2.37*	*428*	*8*	*724*	*-*
Heated above T_m (2 emitters)											
Range	321 - 582	0.2 - 2.2	6.6 - 8.2	6.9 - 9.6	0.7 - 2.6	0.1 - 1.6	6.0 - 6.6	106 - 1984	36 - 62	1226 - 2045	207 - 950
Difference	*261*	*2.00*	*1.61*	*2.65*	*1.89*	*1.53*	*0.59*	*1878*	*26*	*819*	*743*
Heated above T_m (12 emitters)											
Range	305 - 421	0.1 - 3.7	8.0 - 9.0	8.7 - 11.7	0.7 - 1.5	0.04 - 3.0	7.7 - 7.9	59 - 4813	27 - 38	1521 - 2138	219 - 479
Difference	*117*	*3.60*	*1.02*	*2.99*	*0.81*	*2.96*	*0.21*	*4754*	*11*	*617*	*260*

As the cooling rate varies significantly over time (see plots in Figures 5.4 to 5.6), which cannot be expressed using the average heating and cooling rates. Therefore, the instantaneous heating and cooling rate are also plotted, providing a better perception of the temperature rate variation over time. In Figure 5.8 this plot can be found for one of the samples, and all the plots can be found in Appendix C. Based on these plots, it can be determined how long the material has been cooled at certain cooling rates. It is interesting to analyze the time during which the sample is cooled at rates below the critical cooling rate of PPS, because at these rates melt-crystallization might take place. For most samples a time of around 2-3 seconds was determined during which the sample is at temperatures above T_g while being cooled at a rate slower than 25°C. This implies that the occurrence of melt-crystallization is theoretically possible and could affect the DOC of the tested samples. Consequently, it is predicted to have a significant effect on hypotheses **H2.2** and **H2.3** which assumed the cooling rates would lie above the critical cooling rate of PPS, and will be further discussed in Chapter 6.

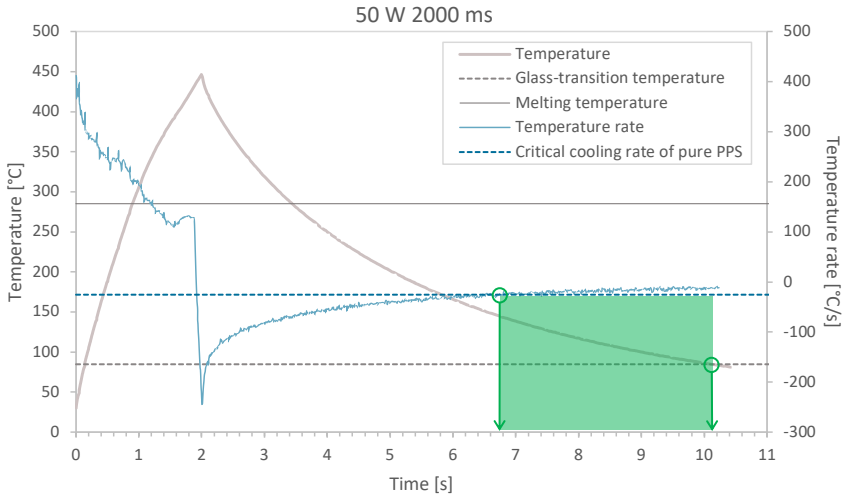

Figure 5.8: Plot showing both temperature and temperature rate evolution over time. The green box indicated the time frame during which the temperature is between T_g and T_m and the heating rate is between the critical cooling rate as reported for pure PPS

5.4. Conclusion

In this chapter the results of the microscopy characterization of the as-receives tape and the temperature measurements done during the sample laser heating are presented and discussed.

The microscopy images of the cross-section of the as-received tape showed a variation in fiber distribution, which is later used to explain the different temperatures measured for samples heated with

identical laser inputs. The difference in temperature is at most 25°C, and could also be caused by inconsistent thermal camera calibration and sample positioning with respect to the laser unit. The observed variation in sample microstructure thus result in a maximum temperature variation of 25°C, for the range of laser inputs tested.

The temperature measurements are used to study the effect of the laser power, heating time and heated area on the thermal evolution of both the top and bottom surfaces of the heated samples. Additionally, the temperature measurements are used to derive a number of temperature parameters.

The temperature measurements reveal the following thermal behavior:

- Rapid laser heating leads to greater temperature gradients within the tape, which is particularly pronounced in the sample heated with 12 emitters.
- An increase in laser power results in faster heating rates and initial cooling rates.
- The cooling rates at temperatures between T_g and T_m remain more or less constant for the samples within the sets.
- The variation of time spent between T_g and T_m during cooling per sample set is less than a second for samples heated to temperatures above T_m. This means that the variation of laser power and heating time mainly affects the heating phase and initial cooling at temperatures above T_m.
- The main outcome of the increase in heated area is the increase in cooling time, presumably caused by the decrease of heat sink in the surrounding tape.
- For all samples, a decrease of cooling rate below 25°C/s is observed at temperatures above T_g over a time of 2-3 seconds.

6

Crystallinity of laser heated samples

This chapter focuses on studying the dependency of degree of crystallinity on the temperature data presented in the previous chapter, and answering **RQ2**: “How does the temperature of the heated sample affect the crystallization?”

Before this can be done, the results of the needed sample characterization (DSC, TGA and XRD) are presented in the first three sections. The TGA results are presented in Section 6.1, providing valuable information about the degradation behavior during heating. In Section 6.2 the XRD results are discussed, adding findings about the crystal structure to the DSC crystallinity analysis. Section 6.3 discusses the DSC analysis of both as-received and laser heated samples and the DOC calculation.

The relationship between thermal history and DOC is discussed in Section 6.4, using the temperature data from the previous chapter, and the determined DOC presented in Section 6.3. The main conclusions of this discussion can be found in Section 6.5.

6.1. TGA results

In Figures 6.1 and 6.2 the changes in sample weight as a function of increasing temperature are plotted for two heating rates, specifically 30°C/min and 5°C/min. For the analysis done at 5°C/min, the first part of the heating up to 250°C is done at a faster rate of 25°C/min to save time, as it is known that no significant change in weight occurs below this temperature. The heating rate of 30°C/min is the maximum heating rate of the Perkin Elmer TGA equipment.

Based on previous experience, the degradation onset temperature is defined as the temperature at which a 2% weight loss is observed. When heating at a rate of 30°C/min, the degradation starts at 525°C. For the slower heating rate of 5°C/min, the degradation onset temperature decreases to 475°C. The computation of T_d is indicated in the plots with arrows. Based on the two measurements, it can be concluded that the degradation temperature depends on the applied heating rate. The same behavior has been reported in literature by Day et al. [93] and Chang et al. [94].

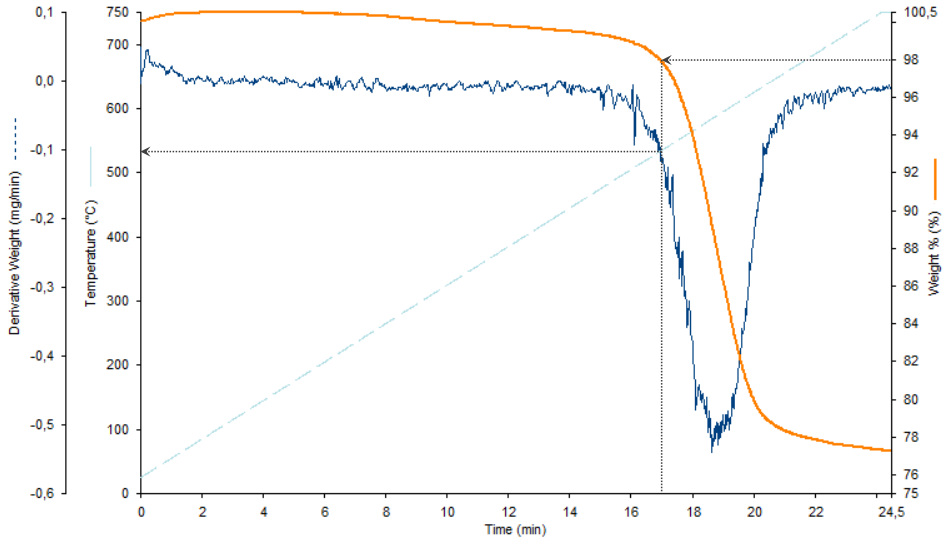

Figure 6.1: TGA results of analysis done at a heating rate of 30°C/min, showing the sample weight (as the percentage of the original weight) and weight derivative as a function of temperature and time

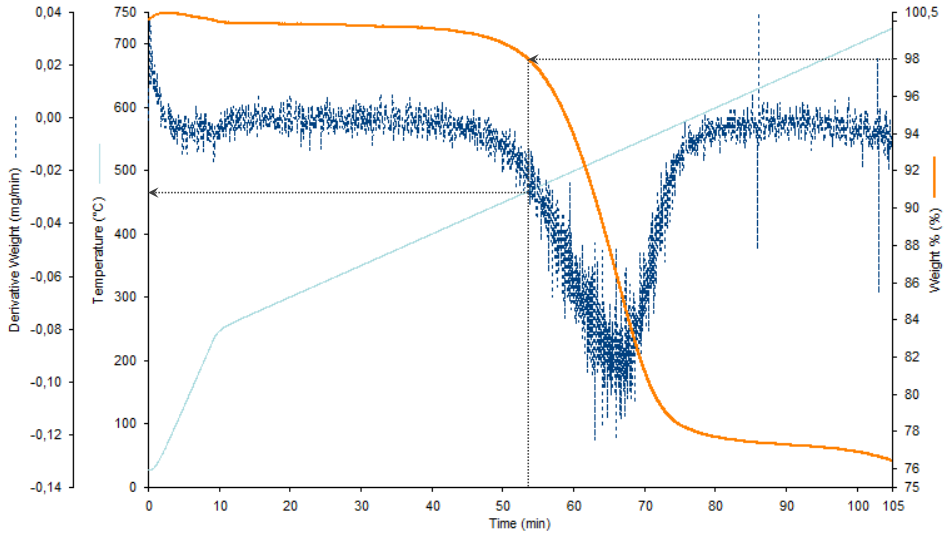

Figure 6.2: TGA results of analysis done at a heating rate of 5°C/min, showing the sample weight (as the percentage of the original weight) and weight derivative as a function of temperature and time

Due to the heating rate limitation of the TGA instrumentation, the onset degradation temperature for rapid heating rates representative for laser heating could not be determined. Additionally, TGA only measures weight loss, and does not provide detailed information about the chemical and structural changes that occur within the material as it degrades. Decomposition of polymer chains is related to the decrease in material weight, while other phenomena such as chain-scission and the formation of by-products only affect the chemical structure and molecular weight, and can thus not be detected using TGA. These changes in the chemical structure are relevant for the analysis of the laser heated samples, as they can result in an alteration of the degree of crystallinity. The effect of thermal degradation on the crystallinity can be either temporary or permanent, depending on the specific conditions and mechanisms involved. The measured values are therefore taken purely as an indication and the fact that degradation might occur at temperatures below 475°C is kept in mind during further analysis.

6.2. XRD results

XRD was used to investigate the effect of different heating conditions on crystal size and shape. In the plot shown in Figure 6.3 the diffraction spectrum obtained for a set of samples with varying laser heating settings and DOC are presented. As XRD is a non-destructive characterization method, the samples could be further used for DSC analysis, which is how the DOC of the samples was determined. The results show a perfect overlap in peak locations, and a difference in peak height a 2θ angle of $20°$.

A sample of pure carbon fiber was also examined, for which a similar intensity is measured. The only difference is seen around the peak at $26°$, where the pure carbon shows a single peak, while the carbon PPS samples show a double peak. This means that the peak at $20°$ is characteristic for the PPS matrix of the composite sample, and all other peaks observed are caused by the diffraction of carbon fibers.

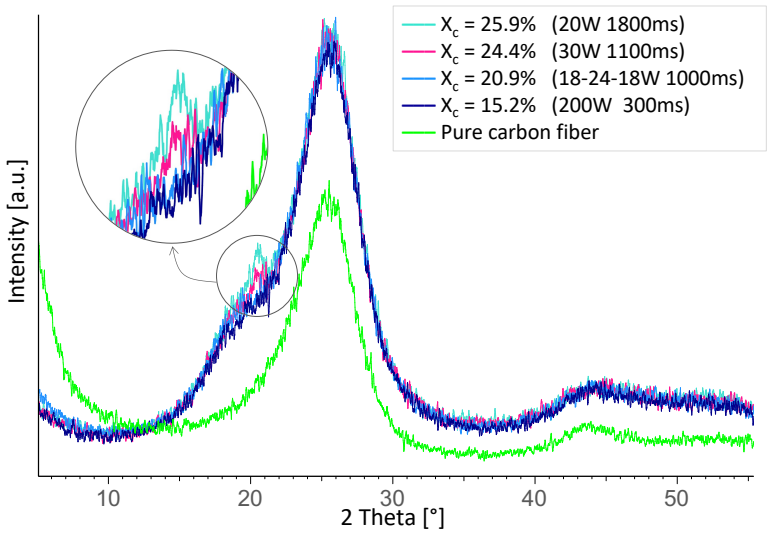

Figure 6.3: XRD spectrum of pure CF and CF/PPS samples with different degrees of crystallinity

The tested samples consist of two samples heated below T_m (20W for 1800ms and 30W for 1100ms) and two samples heated above T_m (18-24-18W for 1000ms and 200W for 300ms). The increase in peak height is observed for the two samples heated above T_m and seems to be stronger as the DOC increases. As the number of crystal planes available to diffract the X-rays increases for higher DOC, an increase in the intensity of the diffraction peaks relative to the background intensity is expected. However, other factors, such as the crystal size, orientation, and crystal shape, can also influence the peak height in XRD. An increase in crystal size results in higher diffraction peaks, and commonly appears along with higher DOCs [95]. However, as the location of the diffraction peaks is not affected by the different temperature histories of the tested samples, this indicates that the same type of crystal is formed for all samples.

Theoretically, different crystallization mechanisms could result in a variation in crystal size and shape. Generally, larger highly-oriented crystals are formed during cold-crystallization and melt-crystallization results in smaller, more random crystals [96]. However, this depends on the exact crystallization conditions, and cannot be confirmed based on the generated experimental data.

6.3. DSC results

The DSC analysis was carried out for both as-received samples and laser heated samples. The calculated DOC for the as-received samples serve as a baseline for the crystallinity, that the laser heated samples can be compared to. The DOC of the laser heated samples is used to further study the effect of temperature parameters on the DOC.

The DSC analysis was done using two different types of equipment, namely the TA Instruments DSC and Perkin Elmer DSC. The switch to the Perkin Elmer DSC had to be made due to failure of the TA Instrument DSC. The results are presented separately, after which a comparison of the results is

done.

6.3.1. As-received samples

The DOC of the as-received sample is determined for both the TA Instruments and Perkin Elmer DSC. All DSC measurements were performed at a heating rate of 10°C/min, except for sample *TA1*, which was tested at 5°C/min. The cold-crystallization (ΔH_c) and melting (ΔH_m) enthalpies used for the DOC calculation and the final DOC values are presented in Table 6.1. The measured DSC curves can be found in Figures 6.4 and 6.5. The peak integration performed on these curves to determine the enthalpies of cold-crystallization and melting can be found in Appendix B.

Table 6.1: Measured cold-crystallization and melting enthalpies and calculated DOC of as-received samples using **a)** TA Instruments (TA) and **b)** Perkin Elmer (PE) DSC

	Heat of fusion (cold-cryst.) ΔH_c	Heat of fusion (melting) ΔH_m	**Degree of crystalinity**
Sample	[J/g]	[J/g]	**[%]**
TA 1*	11.20	16.66	**16.6**
TA 2	8.02	12.81	**14.6**
TA 3	9.89	15.21	**16.2**
TA 4	8.60	13.56	**15.1**
TA 5	9.37	13.13	**11.4**
Average	**9.4**	**14.3**	**14.8**

* *Analysis done at a slower rate of 5°C/min*

	Heat of fusion (cold-cryst.) ΔH_c	Heat of fusion (melting) ΔH_m	**Degree of crystalinity**
Sample	[J/g]	[J/g]	**[%]**
PE 1	7.22	10.36	**9.4**
PE 2	8.78	11.84	**9.2**
PE 3	8.33	11.70	**10.1**
PE 4	8.36	12.12	**11.3**
PE 5	8.51	11.88	**10.1**
PE 6	9.27	13.13	**11.6**
PE 7	8.63	12.16	**10.6**
PE 8	8.84	11.92	**9.2**
Average	**8.5**	**11.9**	**10.2**

The results show a significant difference between the DOC for the two types of DSC. Using the TA Instruments DSC an average DOC of 14.8% is obtained, whereas the average DOC obtained using the Perkin Elmer DSC is 10.2%. The main reason for this is the difference in the melting enthalpy, which lies between 12.8 and 15.2 J/g for the TA Instruments DSC (for the samples analyzed at a heating rate of 10°C/min) and between 10.4 and 13.1 J/g for the Perkin Elmer DSC. For the cold-crystallization enthalpy, similar values in the range of 7.2 to 9.9 J/g are obtained for both types of DSC.

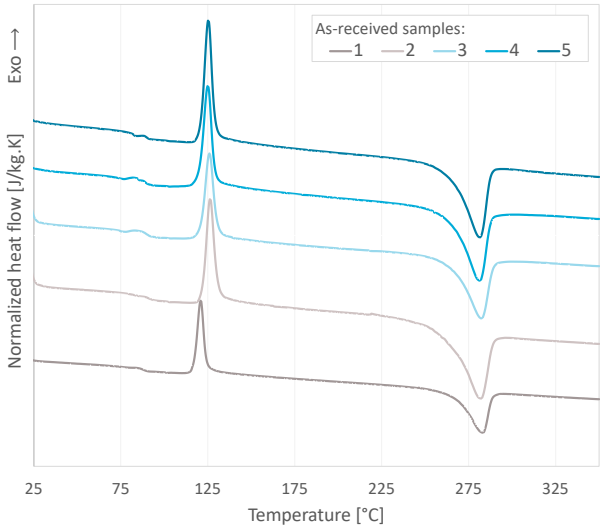

Figure 6.4: DSC curves of the as-received samples tested using the TA Instruments DSC

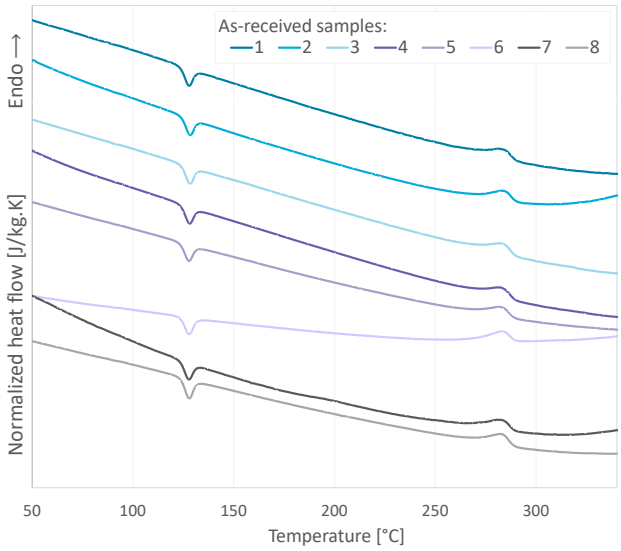

Figure 6.5: DSC curves of the as-received samples tested using the Perkin Elmer DSC

For the DSC curves obtained using the TA Instruments DSC, the cold-crystallization and melting peaks and the overall baseline curve remain constant for all measured samples. A small difference can be seen for sample *TA 1*, which was tested at a slower heating rate resulting in a lower cold-crystallization peak temperature and higher melting onset temperature [97]. For the Perkin Elmer DSC curves, the location of both the cold-crystallization and melting peak is constant, but a variation in the baseline curve of the measurements is observed. The region in which this is most eminent is at high temperatures around T_m, where the baseline is no longer linear and an upward curve is observed for some of the samples. Additionally, the slope of sample *PE 6* varies significantly from all other samples. Even though the baseline is not related to the cold-crystallization and melting enthalpies directly, it does affect the peak integration.

To conclude, a difference is seen in baseline of DSC curves between the TA Instruments and Perkin Elmer measurements. Additionally, a curvature seen in the baseline of the Perkin Elmer measurements around T_m. As a result, a lower melting enthalpy is obtained for the Perkin Elmer analysis, resulting in a different range of DOC values obtained for the two types of DSC.

6.3.2. Laser heated samples

In Tables 6.2, 6.3 and 6.4, the cold-crystallization and melting enthalpies and final DOC values are presented for the samples heated below T_m and above T_m respectively. The maximum top surface temperature is included in the tables along with the used settings, to provide more insight into the applied laser heating.

Table 6.2: Overview of degrees of crystallinity obtained for samples **heated between T_g and T_m**, measured using both types of DSC

	Laser power	Laser heating time	Maximum top surface temperature	Heat of fusion (cold-cryst.) ΔH_c	Heat of fusion (melting) ΔH_m	**Degree of crystalinity X_c**
	[W]	[ms]	[°C]	[J/g]	[J/g]	**[%]**
TA Instruments	20	1000	172	8.97	14.71	**17.2**
	20	1250	193	8.25	14.51	**18.8**
	20	1500	222	5.72	12.78	**21.2**
	20	1600	235	5.32	15.29	**29.9**
	20	1750	251	5.12	15.79	**32.0**
	30	950	221	5.64	12.44	**20.4**
	30	1100	240	6.40	14.57	**24.5**
	40	700	211	8.05	15.88	**23.5**
	40	800	236	6.52	14.42	**23.7**
	50	500	192	9.36	15.60	**18.7**
	50	600	213	8.04	15.78	**23.2**
	75	550	260	7.75	16.34	**25.8**
	100	450	279	8.80	14.88	**18.2**
Perkin Elmer	20	1500	200	6.08	13.86	**23.3**
	20	1500	200	5.68	13.65	**23.9**
	20	1800	223	4.98	13.51	**25.6**
	30	1100	230	6.43	14.45	**24.0**
	30	1100	230	6.20	13.52	**22.0**
	50	600	211	6.98	14.01	**21.1**
	50	600	211	6.69	14.44	**23.2**
	100	300	210	7.42	13.46	**18.1**

Table 6.3: Overview of degrees of crystallinity obtained for samples **heated above T_m with 2 emitters**, measured using both types of DSC

	Laser power	Laser heating time	Maximum top surface temperature	Heat of fusion (cold-cryst.) ΔH_c	Heat of fusion (melting) ΔH_m	**Degree of crystalinity X_c**
	[W]	[ms]	[°C]	[J/g]	[J/g]	**[%]**
TA Instruments	50	1750	421	8.24	12.90	**14.0**
	50	2000	447	9.83	15.95	**18.3**
	100	850	444	10.91	18.19	**21.8**
	100	900	472	9.03	14.58	**16.6**
	150	500	419	9.85	15.59	**17.2**
	150	600	482	9.19	14.76	**16.7**
	150	650	491	8.70	14.24	**16.6**
	200	450	493	9.56	14.40	**14.5**
	200	450	493	9.03	13.95	**14.7**
	300	300	511	8.19	13.90	**17.1**
	300	300	511	9.64	16.01	**19.1**
	400	200	462	9.41	15.59	**18.5**
	400	250	582	8.72	14.99	**18.8**
Perkin Elmer	25	2500	322	7.78	13.95	**18.5**
	25	2500	322	8.71	15.51	**20.4**
	50	1300	348	9.00	15.14	**18.4**
	50	1300	348	8.61	15.06	**19.4**
	100	600	344	9.10	15.33	**18.7**
	200	300	377	8.20	13.70	**16.5**

Table 6.4: Overview of degrees of crystallinity obtained for samples **heated above T_m with 12 emitters**, measured using Perkin Elmer DSC

	Laser power	Laser heating time	Maximum top surface temperature	Heat of fusion (cold-cryst.) ΔH_c	Heat of fusion (melting) ΔH_m	**Degree of crystalinity X_c**
	[W]	[ms]	[°C]	[J/g]	[J/g]	**[%]**
Perkin Elmer	4-6-4	4200	305	8.38	13.39	**15.0**
	9-12-9	2000	347	8.20	13.99	**17.4**
	18-24-18	1000	369	8.35	16.32	**23.9**
	38-50-38	400	343	8.53	13.67	**15.4**
	75-100-75	200	355	8.73	15.49	**20.3**
	75-100-75	200	355	7.91	14.92	**21.0**
	150-200-150	100	421	8.97	15.61	**19.9**

In Figures 6.6 and 6.7, examples of the cold-crystallization and melting peak integration are shown for the TA instruments and Perkin Elmer data respectively. In Appendix B, the computation of the enthalpies for all other samples are presented.

Figure 6.6: Example of enthalpy computation from DSC plots, for the sample heated at 400W for 250ms

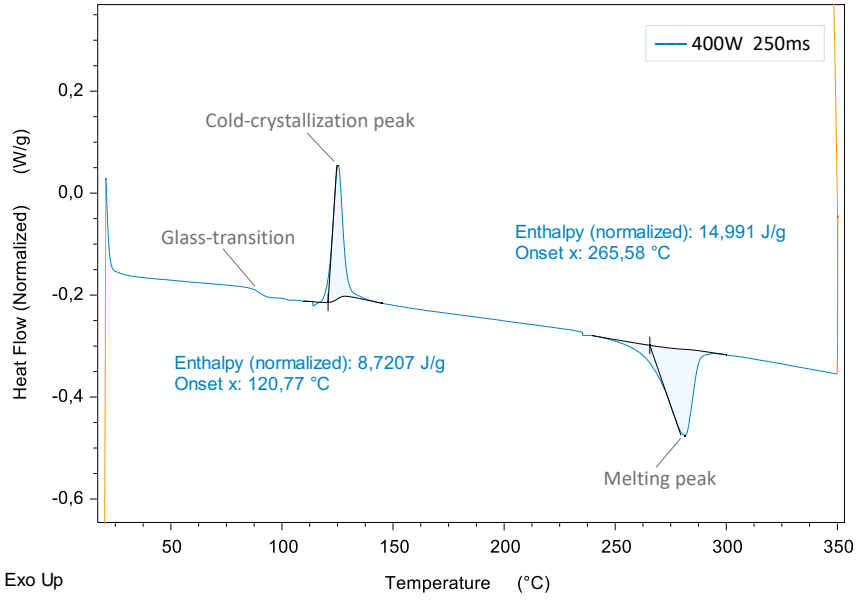

Figure 6.7: Example of enthalpy computation from DSC plots, for the sample heated at 50W for 1300ms

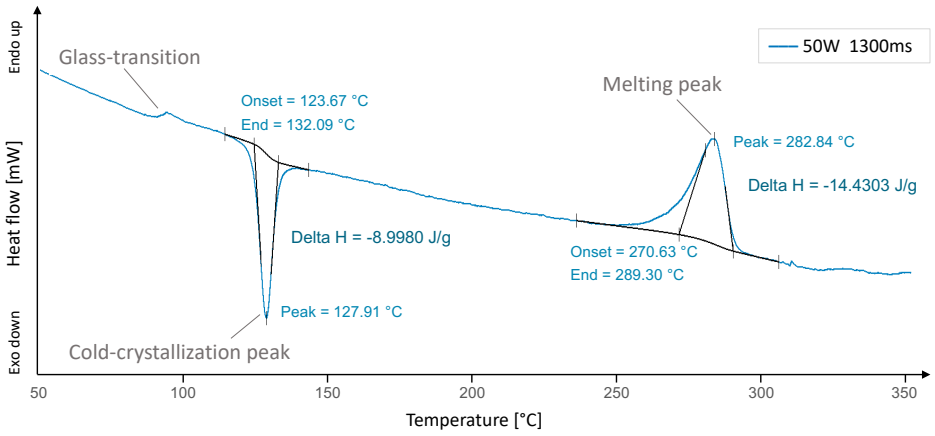

6.3.3. Comparison of TA Instruments and Perkin Elmer DSC

Next to the as-received samples, a number of samples with identical laser heating settings have also been characterized using both types of DSC. These samples can be used to compare the results of the TA Instruments and Perkin Elmer DSC. In Table 6.5 the measured top surface temperature and cold-crystallization and melting enthalpies, and the calculated DOC are listed. A difference of less than 2% DOC is obtained between the two types of DSC for all laser heated samples, based on which it was decided to not distinguish between the DSC equipment used to determine the DOC for the further analysis of the relation between crystallinity and temperature parameters in Section 6.4.

The purpose of the as-received sample characterization is to provide a baseline DOC value of the material prior to laser heating. Due to the difference in DOC for the two types of DSC, a range of 10.2 to 14.8% is used for the baseline DOC. An increase in DOC is defined for values above 14.8%, and decrease for DOC values below 10.2%.

Based on this definition, a small decrease is only obtained for 3 samples, all heated to temperatures above T_m. These are the sample heated with 50W for 1750ms, for which a DOC of 14% is measured, the two samples heated with 200W for 450ms, for which DOC values of 14.5% and 14.7% are measured. For all other samples an evident increase in DOC is observed.

Table 6.5: Comparison of TA Instruments and Perkin Elmer DSC results for measurements using samples with identical laser heating settings

		TA Instrument DSC				Perkin Elmer DSC				Comparison	
Power	Time	T_{max} (top surface)	ΔH_c	ΔH_m	**DOC**	T_{max} (top surface)	ΔH_c	ΔH_m	**DOC**	ΔT_{max}	Δ DOC
[W]	[ms]	[°C]	[J/g]	[J/g]	[%]	[°C]	[J/g]	[J/g]	[%]	[°C]	[%]
As-received		-	9.4	14.3	14.8	-	8.5	11.9	10.2	-	4.57
20	**1500**	222	7.0	14.5	**22.5**	200	6.1	13.9	**23.3**	**22**	**1.28**
							5.7	13.6	**24.2**		
30	**1100**	240	7.8	16.0	**21.2**	230	6.4	14.5	**24.0**	**10**	**1.96**
							6.2	13.5	**22.3**		
50	**600**	213	9.2	16.6	**21.2**	211	7.0	14.0	**21.4**	**2**	**1.29**
							6.7	14.4	**23.6**		
200	**300**	354	9.1	14.7	**16.8**	377	8.2	13.2	**15.2**	**23**	**1.63**

6.4. Relationship between temperature evolution and DOC

In this section, the parameters derived from the measured temperature data as explained in Section 5.2 are combined with the DOC determined using the DSC characterization. First, a number of general observations is discussed. In the following sections, the effect of each temperature parameter on the DOC is discussed separately. For most parameters, a distinction is made between the samples heated below and above T_m, as different phenomena are believed to affect the final DOC in these samples.

6.4.1. General observation

In Table 6.6 the range of the DOC obtained for each set of samples is listed. The variance of the DOC provides a measures of the spread of the data around the mean, where a higher variance means a bigger spread of data. A significantly higher variance is obtained for samples heated below T_m than for samples above T_m. In Figure 6.8 the spreading of the DOC measurements is shown visually. The following two general observations are made:

- Higher DOC's and a bigger range of DOC values is obtained for samples heated to temperatures below T_m, in line with hypothesis **H2.1**.
- Lower DOC's and a smaller range of DOC values is obtained for samples heated to temperatures above T_m.

These obtained range of DOC values is also affected by the variation of laser heating settings and the resulting temperature histories. Therefore, it is not conclusive that the extent of DOC variation is directly related to heating to temperatures below or above T_m.

Table 6.6: Maximum and minimum DOC and variance in measured values, listed for sample sets with different temperature ranges

	Maximum DOC	Minimum DOC	DOC variance
Heated below T_m	32%	17%	13.90
Heated above T_m (2 emitters)	22%	14%	3.97
Heated above T_m (12 emitters)	21%	15%	4.68

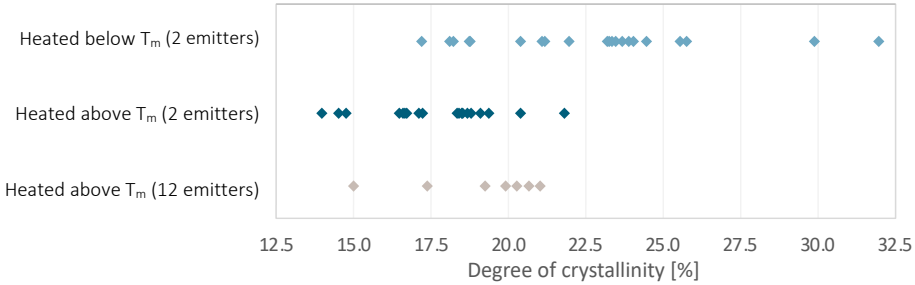

Figure 6.8: Distribution of measured DOC values of all tested samples, presented for sample sets with different temperature ranges

The results in Table 6.6 challenge hypotheses **H2.2** and **H2.3**, as the DOC values indicate that samples that were rapidly cooled from temperatures both above T_m and T_{m_0} have a DOC that is equal to or higher than the original as-received tape. These hypotheses were premised on the belief that the cooling rate would not surpass 25°C/s, and that such a rate would prevent melt-crystallization.

Despite the average cooling rate for samples heated above T_m being between 36-62°C/s, Section 5.3 highlights that the cooling rate decreases below 25°C/s during cooling at temperatures above T_g. This provides the necessary conditions for melt-crystallization to occur. Moreover, it is also possible that melt-crystallization may happen even when the cooling rate exceeds 25°C/s. The following theories might explain a possible increase in critical cooling rate and melt-crystallization at elevated cooling rates:

- The unique **memory effect** seen in PPS leads to a faster crystal growth during the subsequent melt-crystallization, caused by the ordered structure that can survive in a polymer melt even after all nuclei are eliminated at temperatures above $T_{m,0}$ [46]. The increase in crystallization rate results in higher critical cooling rates. However, the memory effect was studied by Yan et al. for long heating dwell times in the range of minutes [46], and has not yet been studied for rapid heating cycles as the ones applied to the tested samples.
- Well-defined **foreign bodies** such as nucleating agents, fillers and reinforcing fibers can serve as nucleation sites for crystal growth, resulting in an increase in crystallization rate and crystallization temperature [74][70]. The critical cooling rate of 20°C/min was determined experimentally for pure PPS samples [30] [69] and is expected to be higher for PPS formulations with additives and PPS reinforced composites. Higher critical cooling rates of up to 5°C/s have so far been reported for studies using commercial CF/PPS composite prepregs.

6.4.2. Maximum temperature

In Figure 6.9, the top and bottom surface temperatures are plotted against the DOC. The vertical lines indicate the T_m of 285°C and a range for T_{m_0} between 350°C, reported by Yan et al. to be the equilibrium melting temperature at which folded-chain crystals are completely eliminated. This value is used, as the melting peaks observed for the heat flow curves obtained by DSC lies between 280°C and 285°C, which is assigned to the melting of folded-chain crystals in the same study [46].

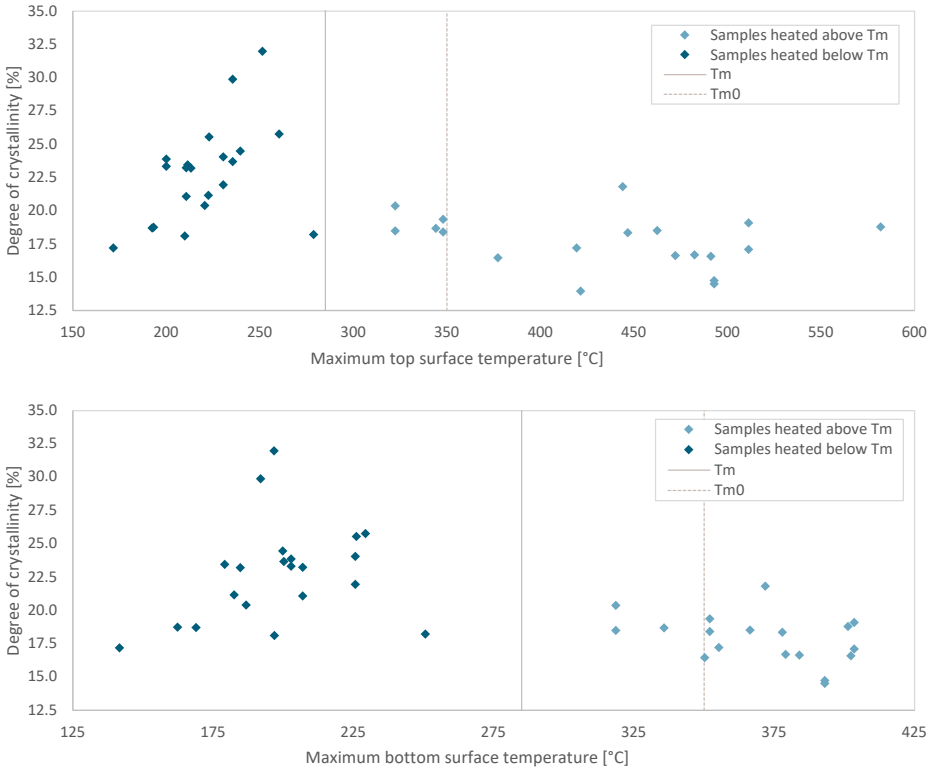

Figure 6.9: The relationship between measured surface temperatures (top and bottom) and the determined DOC

For the top surface temperature, an increase in DOC is observed for temperatures between 172°C and 251°C. At 251°C a maximum DOC of 32% is measured, after which a significant decrease in DOC is observed for all samples with higher top surface temperatures. A dependence on temperature is thus observed for top surface temperatures of up to around 260°C, after which the DOC stays within the range of 14% to 18% independently of the temperature.

As can be seen from the DSC heat flow measurements presented in Appendix B, the onset of the melting peaks starts around temperatures of 250°C. The partial melting occurring in the parts of the sample heated above 250°C could be the reason for the observed decrease in DOC at temperatures below the T_m of 280-285°C.

An S-shaped trend is observed for the samples heated to temperatures between 172°C and 251°C, consisting of an initial gradual increase in DOC, followed by a steeper increase at temperatures between 200 and 235°C, after which it flattens off. For the bottom surface temperature, the shift from initial gradual DOC increase to a steeper increase occurs at a lower temperature of around 175°. An explanation for the variation in DOC increase rate could be the different crystallization rates and their dependence on temperature. The highest crystallization rates are observed at 160°C for isothermal crystallization. This temperature seems to be higher for the rapid non-isothermal crystallization during laser heating.

For samples heated above T_m, the independence of the DOC on the maximum temperature is not surprising. As the melt-crystallization, presumed to be a likely cause for the measured crystallinity in these samples, occurs at temperatures between T_m and T_g, the peak temperature above T_m does not affect the crystallization directly. However, what is expected to be affected by the maximum temperature above T_m are the melting kinetics, namely the superheating and memory effect, influencing the presence of unmelted crystals, ordered conformations and entanglements in the melt. The dependence of the melting kinetics on the maximum temperature, and its effect on the final crystallinity, could not be proved based on the results obtained.

For samples heated above T_m, the lack of dependence of DOC on the maximum temperature attained is not unexpected. As the phenomenon of melt-crystallization, which is believed to be a likely contributor to the observed crystallinity in these samples, occurs in the temperature range between T_m

and T_g, the maximum temperature attained above T_m does not have a direct impact on the crystallization itself. However, it is expected that the maximum temperature above T_m would influence the melting kinetics, including superheating and memory effects, which can affect the presence of unmelted crystals, ordered conformations, and entanglements in the melt. The dependence of the melting kinetics on the maximum temperature, and its effect on the final crystallinity, could not be conclusively shown based on the results obtained.

For the bottom surface temperature, the above described behavior is less prominent in the range between T_g and T_m, as the variation in DOC obtained for samples with similar bottom temperatures is bigger. The most extreme example of this is a DOC of 32% and 18.1%, obtained for a samples with the same bottom surface temperature of 197°C. In Figure 6.10 the temperature range between top and bottom surface is shown for samples heated below T_m. The big variation in temperature gradient between the samples explains the difference observed between the top and bottom surface temperature plots.

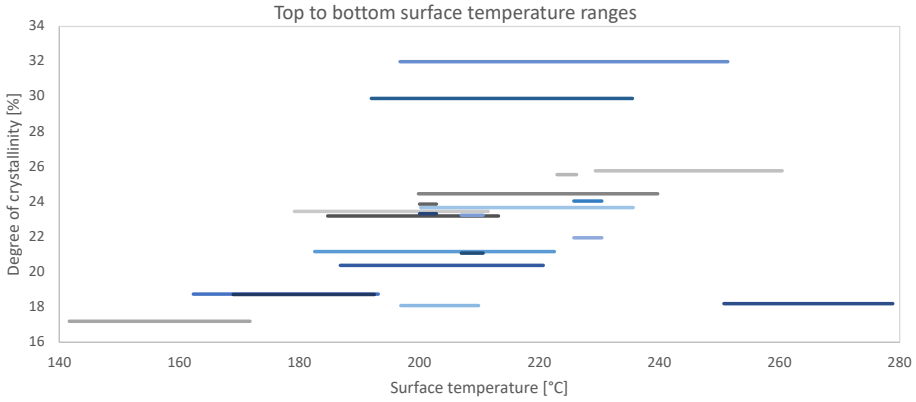

Figure 6.10: Relation between DOC and temperature gradient (range between the surface top and bottom maximum value)

For the samples heated above T_m no difference in DOC is observed when the temperature of the sample exceeds the equilibrium melting temperature, above which all residual nuclei are completely eliminated [46]. This could be caused by a number of reasons. As the T_{m_0} of 350°C was determined for pure PPS, the actual T_{m_0} for the PPS formulation used in the samples might be higher. This could result in residual nuclei remaining in the microstructure even if the temperature is increased above 350°, having the same effect of the crystallization and DOC odf all samples. On the other hand, it is also possible that these residual nuclei are removed immediately after the melting temperature, resulting in no impact on the crystallization in any of the tested samples. No conclusive evidence of the effect of residual nuclei on the DOC can be determined based on the obtained data. The results suggest that in the temperature range between the T_m and 410°C, the maximum bottom surface temperature, no effect of the residual nuclei on the DOC was observed.

6.4.3. Total heating and cooling time

The plots showing the relation between the DOC and the total heating and cooling time can be found in Figure 6.11. A comparable range of heating times is obtained for samples heated both below and above T_m. For the cooling times on the other hand, significantly higher values are obtained for samples heated above T_m, compared to those heated below T_m.

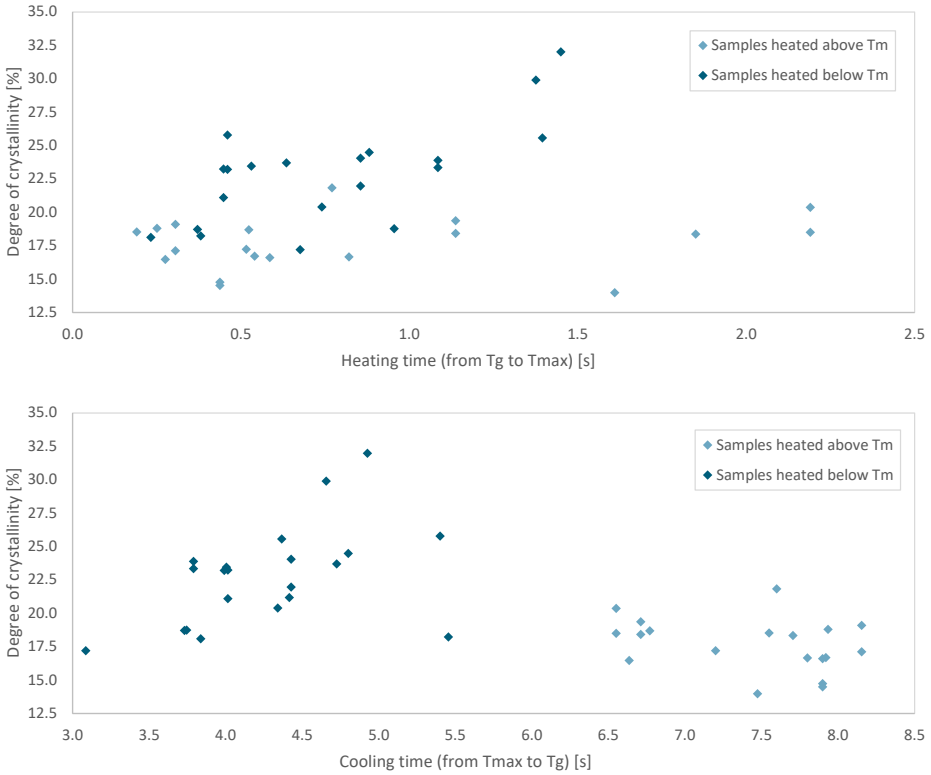

Figure 6.11: The relationship between DOC and the heating time (top plot) and cooling time (bottom plot)

Figure 6.12 displays the relationship between DOC and heating and cooling time, for samples heated below T_m only. The data shows an increase in DOC for both increasing heating time and cooling time, which supports hypothesis **H2.5**. This can be explained by the fact that cold-crystallization can occur continuously throughout the heating and cooling cycle, and thus, a longer duration of heating and cooling provides more time for crystals to grow, leading to higher DOC values.

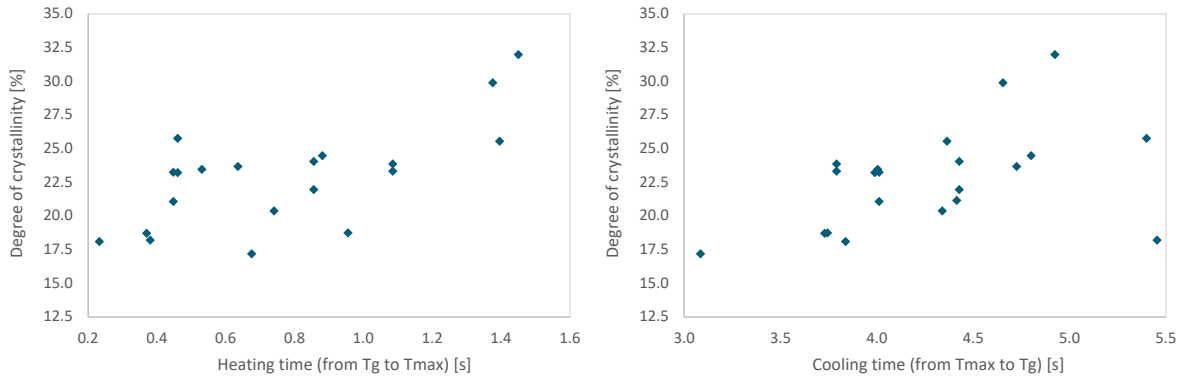

Figure 6.12: The relation between DOC and heating (left) and cooling time (right) for the samples heated to temperatures below T_m

The rate of cold-crystallization during the process is dependent on temperature and the heating and cooling rates, and it generally occurs at a faster rate during heating than cooling [52]. This would suggest that the heating time is the main influencing factor for the final DOC. On the other hand, substantially more time is spent in cooling compared to heating, allowing more crystals to form during this stage and making the cooling time the more important factor. To isolate the effects of heating and cooling time, Figure 6.13 presents the DOC values of groups of samples with consistent heating and cooling times. This allows for the separate examination of the effects of heating and cooling times on

the DOC.

In the left plot, the influence of cooling time on DOC is analyzed for groups of samples with similar heating times. For the sample groups with lower heating times (0.37-0.38s and 0.46s) the DOC remains relatively constant and no effect of cooling time on the DOC is observed. For the groups with higher heating times (0.64-0.74s and 0.86-0.96s), a slight increase in DOC is seen with increasing cooling time. Between the groups, no increase in DOC is observed as the heating time increases.

In the right plot, an increase in DOC with increasing heating time is seen for the groups with longer cooling times (4.34-4.43s and 4.66-4.93s). This is not the case for the group with a cooling time of 3.73-4.01s where the relation between DOC and heating time is less clear. A vague trend towards an increase in DOC with increasing cooling time was also observed between the groups.

The results in both plots show an inconsistent dependency of DOC on the heating and cooling time. Based on these observations, it can be concluded that the DOC is the result of a complex interplay between heating and cooling time, as well as other factors, leading to the unsteady relations observed in Figure 6.13. Therefore, it is not possible to solely use heating or cooling time to analyze the DOC and both must be taken into account.

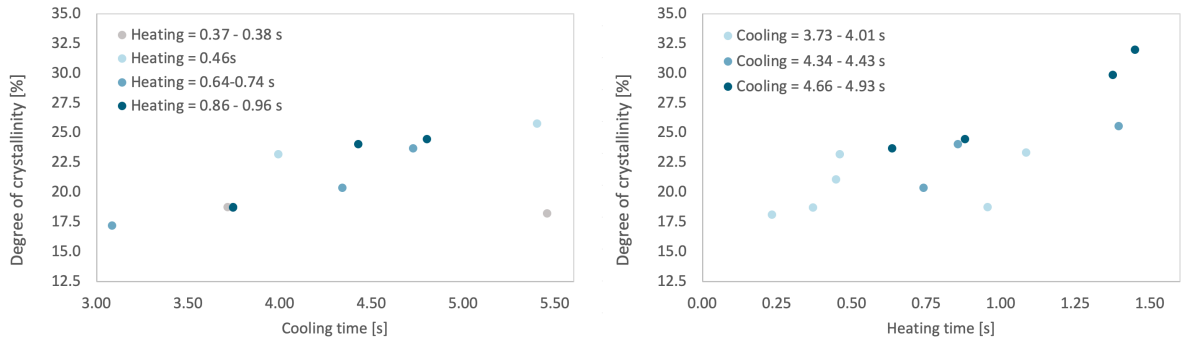

Figure 6.13: Plots showing the relation between the DOC and:
a) the cooling time for groups of samples with similar heating times, and **b)** the heating time for groups of samples with similar cooling times

6.4.4. Time between the glass-transition and melting temperature

In Figure 6.11 the plots showing the relation between the DOC and time spent between temperatures of T_g and T_m both during heating and cooling are presented. For the samples heated below T_m, this parameter is equal to the total heating and cooling time discussed above, which is why only the samples heated above T_m will be discussed in this section.

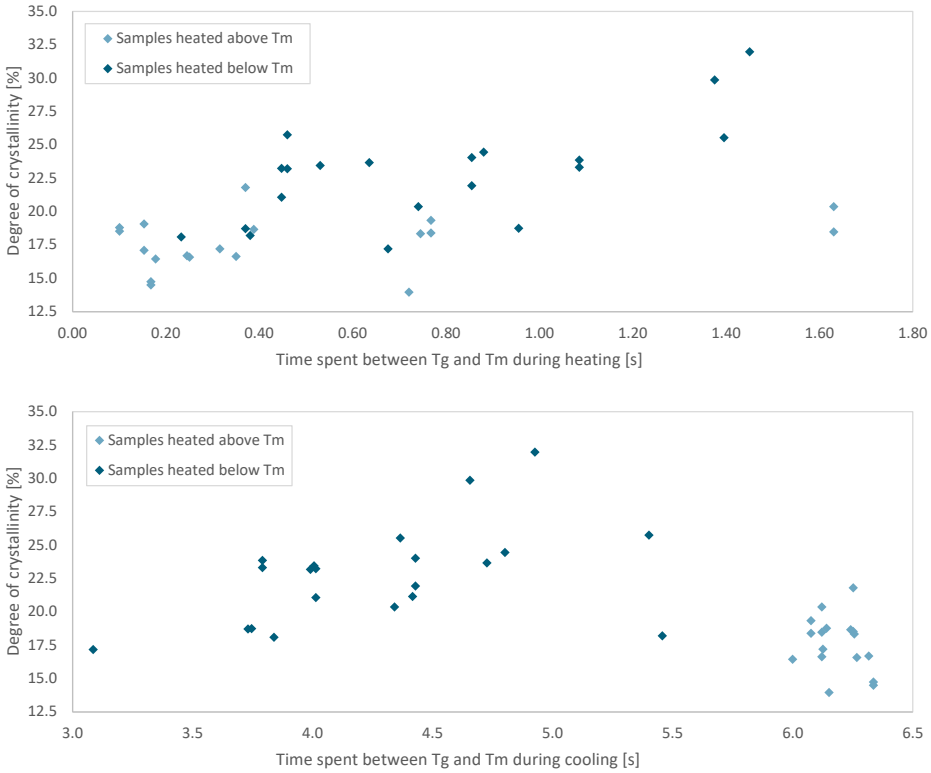

Figure 6.14: The relationship between DOC and heating and cooling time spent between T_g and T_m

In Figure 6.15 the two parameters are plotted for the samples heated above T_m only. No dependence of the DOC on the time spent between T_g and T_m is seen, for neither heating nor cooling. The heating time between T_g and T_m is only expected to have an impact on the DOC if the cold-crystallization that occurs during this period survives the melting phase. The absence of an effect on heating time between T_g and T_m on the DOC may indicate that no cold-crystallization occurs during heating, or that there is no occurrence of superheating during melting, or that the influence of melt-crystallization on the DOC is significantly stronger.

For the cooling time between T_g and T_m, a direct effect on the melt-crystallization and thus the final DOC are expected, with longer times resulting in a higher DOC. However, the data does not show any correlation. A possible explanation for this may be the small range of relatively constant cooling times obtained for the tested samples, all lying between 6 seconds to 6.42 seconds. This variation is much smaller compared to samples heated below T_m (as seen in Figure 6.14). As a result, almost the same amount of time is available for the melt-crystallization for all samples in this set. To better analyze the effect of cooling time between T_g and T_m on DOC, a sample set heated above T_m with a wider range of cooling times is needed.

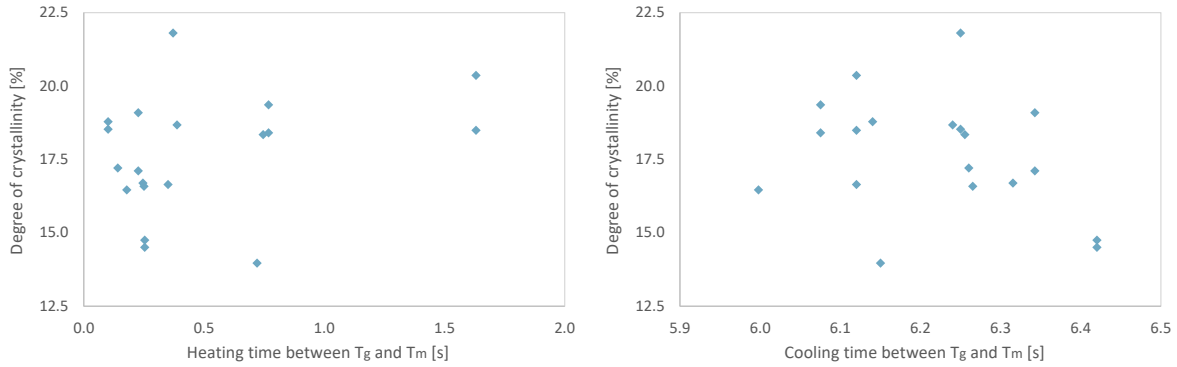

Figure 6.15: The relation between DOC and time spent between T_g and T_m during heating (left) and cooling (right) for the samples heated to temperatures above T_m

6.4.5. Time above the glass-transition temperature

In Figure 6.16 the plots showing the relation between DOC and the time spent above T_g and the integral taken over this time range are presented. The total time spent above T_g is the sum of the heating and cooling time. Previous findings indicate that for samples heated above T_m, no correlation exists between heating time and DOC and that the range of cooling time was insufficient to study its effect on DOC. Therefore, additional analysis of the effect of the total time spent above T_g on DOC for samples heated above T_m is not deemed necessary.

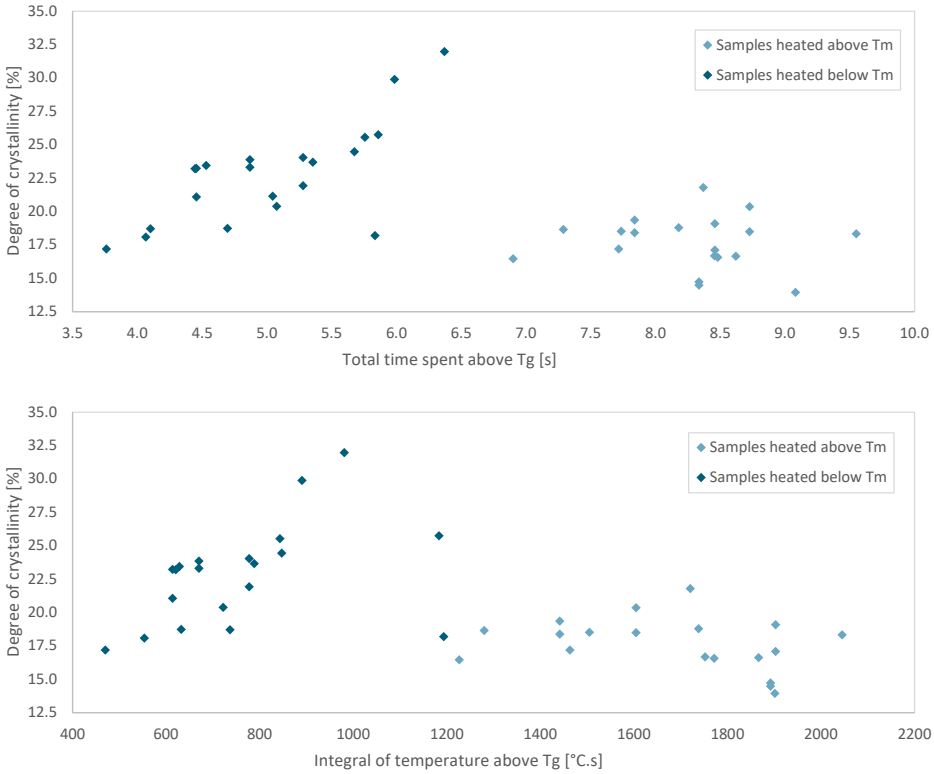

Figure 6.16: The relationship between the DOC and the total time spent above T_g (top plot) and the temperature integral for temperatures above T_g (bottom plot)

For the samples heated below T_g an increase in DOC is observed as the time above T_g increases. This is consistent with the results obtained from the heating and cooling time and can be related to the longer time available for cold-crystallization to take place. A stronger and more confined correla-

tion between DOC and the time spent above T_g is observed compared to the relations seen for the separately analyzed heating time and cooling time (shown in Figure 6.12). The correlation between the parameters can be best described by an S-shaped trend. The initial increase in the DOC is slow, followed by a more substantial growth between 4.75 and 6 seconds, beyond which the trend levels off. A similar trend has been described in literature for the relation between crystallization time and DOC for isothermal crystallization, caused by the different rates of primary and secondary crystallization. In Figure 6.17 the relation between isothermal crystallization time and DOC is shown for PPS [76], showing the effect of the fast primary and slow secondary crystallization. For comparison, the relation between DOC and time above T_g is shown in Figure 6.18 for all samples heated with a laser power of 20W, for which the similar S-shaped trend is very clear. Even though the crystallization studied is not isothermal, the crystallization rates dependence on crystallization time could be used to explain the S-shaped behavior.

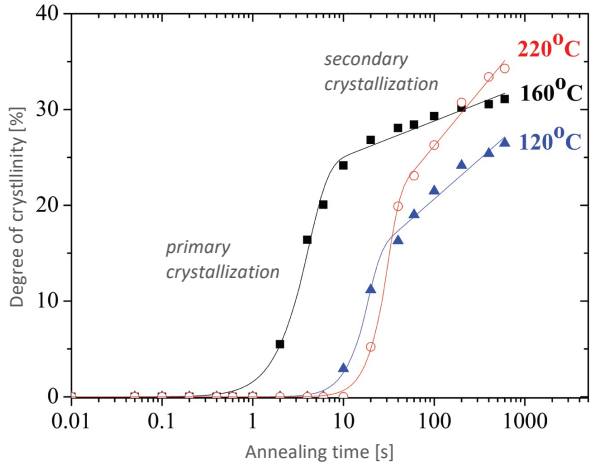

Figure 6.17: Crystallinity as a function of annealing time for PPS annealed at different temperatures (120 to 220 °C) obtained by Furushima et al. [76]

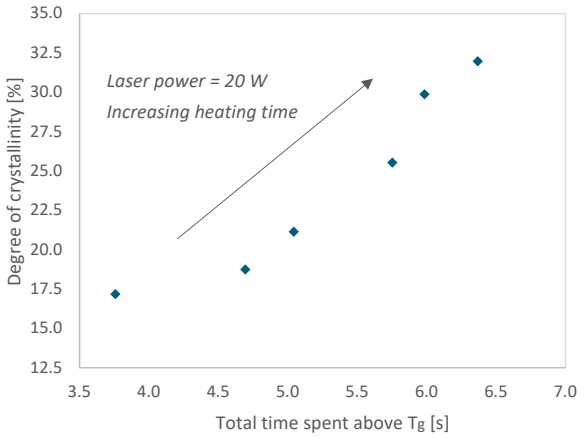

Figure 6.18: The relation between the DOC and time spent at temperatures above T_g for samples heated using a laser power of 20W and varying heating times between 1000ms and 1800ms

A parameter related to the total time above T_g is the integral over temperatures above T_g. Using this parameter the influence of temperature evolution over time can be quantified, combining both the effect of temperature and time on the DOC. The downside of this parameter is that it cannot distinguish between samples slowly heated to lower temperatures and samples heated rapidly to higher temperatures. Despite this, an increasing DOC can be observed for higher integral values for samples heated below T_g. Again, the parameter seems to follow an S-shaped trend.

6.4.6. Time above the melting temperature

The relation between the DOC and the time above T_m and integral over this time range are shown in Figure 6.19 for the samples heated above T_m. For neither of the parameters, an effect on the DOC is observed. Similarly as for other temperature parameters, the DOC shows a relatively constant behavior. The fact that time spent above T_m does not influence the DOC indicates that the same melt condition is obtained for all samples, and the tested laser inputs do not affect the melting. Two possible scenarios are formulated as a hypothesis for the lack of DOC dependence on the melt phase:

- The rapid laser heating leads to superheating in all samples. In the superheated state the crysallinity prior to melting is maintained. The increase in DOC with respect to the as-received tape can then be explained by either cold-crystallization during heating, or melt-crystallization of the superheated state during cooling, or a combination of the two.
- A perfect melt without residual nuclei is achieved as a result of the rapid laser heating. This would mean that the as-received crystallinity and any DOC gains due to cold-crystallization are lost during the melting phase, and the final DOC is the result of the melt-crystallization during cooling.

The main difference between the hypotheses is the crystallinity of the sample in the molten state, directly affecting the processing viscosity and thus the intimate contact and laminate quality achieved during LAFP. For the superheated state, the crystallinity remains unchanged and at least equal to DOC of the as-received, whereas the DOC of the perfect melt approaches zero.

In the section discussing the effect of maximum temperature on crystallinity, a decrease in DOC was observed as the maximum temperature approaches T_m., caused by the melting onset at 250°C. The decrease in DOC related to the onset of melting contradicts the superheating hypothesis and provides strong support for the second hypothesis, as a further decrease in DOC would be expected with longer melting times.

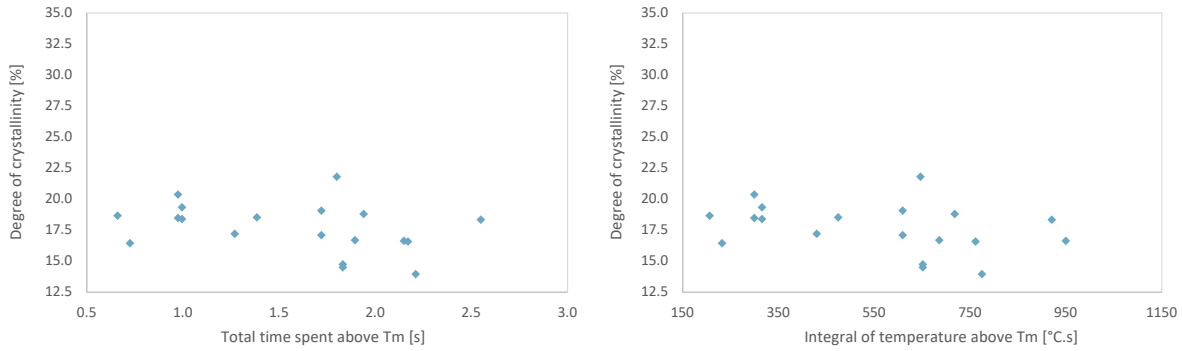

Figure 6.19: The relationship between the DOC and the total time spent above T_m (top plot) and the temperature integral for temperatures above T_m (bottom plot)

6.4.7. Heated area

Finally, the samples heated using 12 emitters and a pyramid laser power distribution, and thus a bigger heated area, are analyzed. Compared to the samples heated with 2 emitters, the surrounding tape temperature for the samples heated with 12 emitters is higher. This temperature affects the boundary conditions of the samples analyzed using DSC. The surrounding tape temperature determines to what extend the boundary conditions of the tested sample act as a heat sink. For higher surrounding temperatures, a smaller heat sink and thus slower cooling is observed. Additionally, the mobility of the polymer chains surrounding the tested sample increases with temperature, and might affect the crystallization within the sample itself.

From the plot in Figure 6.20, showing the relation between cooling time between T_g and T_m, it can be seen that the longer cooling time achieved with the bigger heating area does not affect the DOC. As the range of DOC values obtained when heated with 2 and 12 emitters is similar, in can be concluded that either no difference in chain mobility is achieved for the surrounding tape of the tested samples or that the surrounding chain mobility does not have a strong effect on the DOC.

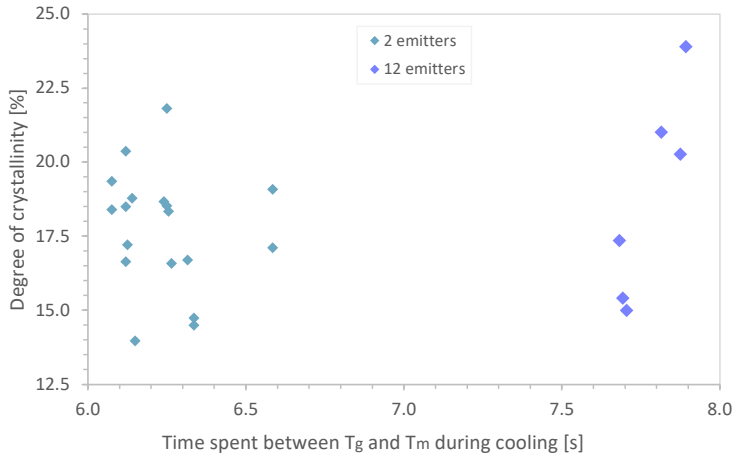

Figure 6.20: The relation between DOC and time spent between T_g and T_m during cooling for sample sets heated with a different number of emitters, resulting in a different heated area

As shown in Figure 6.21, longer times spent at temperatures above T_g result in a decrease in DOC. This is unexpected, as it suggest that as the time available for crystallization to take place increases the DOC decreases. From the separate analysis of the heating time and cooling time, the same unexpected relation is observed for the heating time, while the cooling time shows the expected increase in DOC for longer times. A hypothesis formed based on these results is that the cooling phase is determining for the final DOC, and the effect of heating time on the DOC can be disregarded due to the elimination of crystals formed during cold-crystallization during melting.

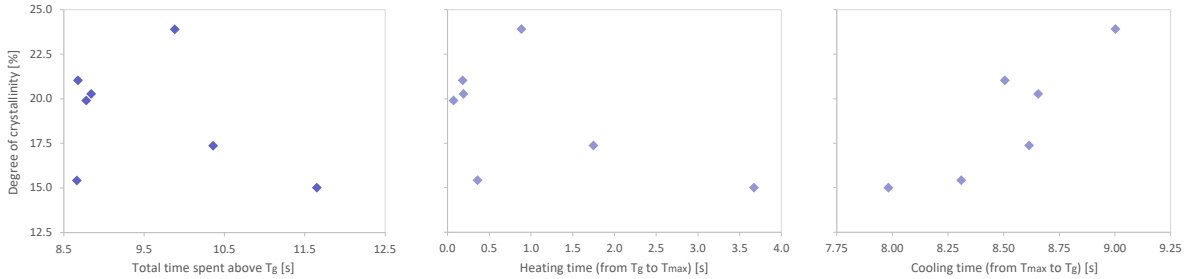

Figure 6.21: The relation between DOC and:
a) total time spent above T_g, **b)** heating time, and **c)** cooling time

No all temperature parameters are discussed in this section, as no relevant data was obtained from them. All additional plots showing the relation between DOC and temperature parameters can be found in Appendix D.

6.5. Conclusion

In this chapter, the outcomes of the TGA, XRD and DSC analysis were presented and the results discussed. In this section, the main findings and conclusions will be summarized.

The TGA analysis showed that the degradation temperature at which a decrease in weight is observed lies at 475°C when heated at a rate of 5°C/min and further increases for higher heating rates. As the heating rates for the laser heated samples are significantly higher, it was assumed no degradation phenomena related to weight loss take place in the tested samples. However, as degradation is a complex process that involves chemical and physical changes in the material, and weight loss may not always be the most sensitive indicator, the occurrence of degradation at lower temperatures can not be ruled out.

The XRD characterization of samples heated both above and below T_m revealed a relatively constant diffraction pattern with variation only in diffraction peak height but not in peak location. This result indicated that despite differences in heating conditions and temperature evolution, the same type of crystal was formed in all samples.

The DSC analysis was performed with the TA Instruments DSC and Perkin Elmer DSC. The comparison of the obtained results showed that the variation between the two types of equipment is negligible, and no differentiation between them was made in the subsequent analysis of the data.

For the samples heated to temperatures below T_g a significant increase in DOC compared to the as-received tape was observed and a big variation in results obtained. The DOC of the samples heated above T_m also increases with respect to the as-received tape, but this increase is lower and the variation in DOC values obtained smaller.

The surface temperature and time spent above T_g show the best correlation to the DOC for samples heated below T_m. An S-shaped trend is observed with an initial strong increase in DOC which flattens off both at higher temperatures and longer heating times. This behavior is attributed to the variation of crystallization rate throughout the laser heating temperature cycle.

For the samples heated to temperatures above T_m, no relation of the DOC to any of the studied temperature parameters is observed. A possible explanation for this is the narrow range of cooling times obtained, resulting in the same time available for melt-crystallization. Finally, the same range of DOC was obtained for samples heated with 2 and 12 emitters, from which it was concluded that the heated area has no significant effect on the crystallization for the samples tested.

7

Conclusions

The aim of this master thesis was to gain more insight into the effects of rapid laser heating on the development of crystallinity in CF/PPS composite tapes.This was done by first studying the effect of laser heating on the temperature evolution in the tape, followed by the analysis of the effect of temperature parameters on the degree of crystallinity of heated samples.

In this chapter, a summary of the research conclusions based on Chapters 5 and 6 is presented. First, the key findings will be related to the research questions in Section 7.1. In Section 7.2 the relevance of the thesis for the research and development of laser-assisted fiber placement (LAFP) will be highlighted. Finally, recommendations for further research based are proposed in Section 7.3.

7.1. Answers to research questions

RQ1. Effect of laser energy input on temperature

For the analysis of heating input settings on the sample temperature, 57 samples were produced and measured in total, of which 24 samples were heated to temperatures below T_m, and 33 samples to temperatures above T_m. Different combinations of laser power (ranging from 25W to 400W), heating time (ranging from 100ms to 4200ms) and heated area (using 2 or 12 emitters) were applied. As a result, significant differences in temperature histories were obtained, including maximum surface temperatures between 172°C and 582°C. Additionally, various parameters quantifying the temperature evolution over time were defined and studied.

The **laser power** is found to be the main factor affecting the speed of the temperature evolution. This effect is seen during the heating phase and initial cooling phase, where more rapid rates are observed as the laser power increases. This became especially clear for the sample set with an increased heated area. On the other hand, the cooling rate at temperatures below the melting temperature (T_m) remains constant regardless of the laser power.

For the variation of **heated area** an effect on the cooling time is observed. As the number of emitters used to heat the sample increased from 2 to 12, an increase in cooling time and time spent between glass-transition temperature (T_g) and melting temperature was observed. However, for samples heated with the same number of emitters, relatively constant cooling times are measured. This is explained by the decrease in heat sink induced on the measured sample by the surrounding tape, as a more constant temperature throughout the tape is observed.

Finally, the **heating time** primarily affects the maximum temperature achieved in the tape. This parameter was therefore used to regulate the maximum temperature achieved in the tape when varying the laser time and heated area inputs.

RQ2. Effect of temperature on degree of crystallinity

To answer this research question, the temperature parameters derived from the thermal camera measurements and the degree of crystallinity (DOC) obtained using differential scanning calorimetry (DSC)

characterization were plotted and visually analyzed, and the observed behavior was discussed.

For the samples heated to temperatures below T_m, a good correlation between the DOC and a number of temperature parameters is obtained. Both the maximum temperature and time spent above T_g show an S-shaped trend, and an increase in DOC values as the temperature and time increase.

For the maximum temperature, a drop in DOC is observed for samples approaching the melting temperature. This was explained by the onset of melting, observed to be around 250°C based on the DSC heat flow curves. The low DOC obtained for samples heated to low temperatures was explained by the slower crystallization rates, due to the low chain mobility at these temperatures.

The study found that the total time above T_g, as well as the heating and cooling times, have a positive effect on the DOC. The results showed that separating the effect of heating and cooling time on DOC was difficult, and the strongest correlation to DOC was seen when considering the total time above T_g. This implies a complex interaction of crystallization kinetics during both heating and cooling. The results also showed an S-shaped, and the trend was found to be similar to the relationship between annealing time and DOC for isothermal crystallization. For the isothermal crystallization, the S-shaped trend was ascribed to the different rates of primary and secondary crystallization. The results indicate that the varying rates of primary and secondary crystallization may also impact non-isothermal crystallization during rapid laser heating.

In contrast, no dependency of the DOC on any of the temperature parameters is observed for the samples heated above T_m using 2 emitters. However, an increase in DOC is observed compared to the as-received tape, meaning that either cold- or melt-crystallization play a role in the final DOC obtained.

Samples heated to temperatures both above and below the equilibrium melting temperature (T_{m_0}) were tested, with a variation of time spent above T_m from 0.66 to 2.55 seconds. The constant DOC obtained independently of the temperature parameters associated with the melting phase suggests that similar melting conditions were achieved for all tested heating inputs, which could range from a complete melt with no residual nuclei to a superheated semi-crystalline state. For samples heated below T_m a dependence of the DOC on temperature was determined, which showed a decrease in DOC as the sample approached the melt. This trend supports the hypothesis of a further decrease in crystallinity during melting, ruling out the possibility of full superheating. However, the results of the experiments and data collected are not comprehensive enough to form definite conclusions regarding the composition of the melt and the evolution of crystallinity at temperatures above T_m.

For the parameters related to the heating and cooling phase, an namely the times spent between T_g and T_m during heating and cooling, no dependency of the DOC was observed. For the cooling time between T_g and T_m, assumed to be related to the melt-crystallization, a small range of times between 6 and 6,6 seconds was tested, which could be the explanation for the constant DOC values obtained. For the heating time between T_g and T_m, a wider range of times was measured between 0.1 and 1.6 seconds, and the lack of relation insinuates the cold-crystallization has a less pronounced effect on the final DOC. From the analysis of the samples heated above T_m using 12 emitters, two additional conclusions are obtained. Firstly, an increase in cooling time between T_g and T_m with respect to the samples heated with 2 emitters is obtained, but no difference in DOC observed. This affirms the conclusion that the DOC is not dependent on the cooling time. On the other hand, a dependency of DOC on cooling time is observed for the sample set tested using 12 emitters.

Due to the lack of correlation between the temperature parameters and DOC and some contradicting trends observed, it remains uncertain what the effect of cold- and melt-crystallization on the final DOC is. The data strongly suggest that melt-crystallization is the main source of crystallinity in the final sample, but further research necessary to establish a solid relationship between these parameters.

The conclusions lead to the following new hypotheses formed for **RQ2**, that should be further researched:

- For the samples heated below T_m the increase in crystallinity is attributed to cold-crystallization during both heating and cooling.
- The rate of cold-crystallization during the temperature cycle of samples heated below T_m is not constant, and varies both as a function of time and temperature.
- Even for very short times spent above T_m, melting takes place and the crystallinity decreases.

- The main factor causing the increase in DOC for samples heated above T_m is the melt-crystallization upon cooling.

7.2. Relevance for LAFP

In the study, two different sets of samples were analyzed, heated to temperatures either completely below or above T_m. During LAFP, a combination of both these types of heating can be observed. The incoming tape and the substrate are heated to temperatures above T_m by direct exposure to the laser. Depending on the laser power applied, different temperature gradients are achieved, as was shown in Chapter 5. With higher laser powers resulting in greater temperature gradients, it is likely that the directly heated tape and substrate will experience strong temperature gradients during LAFP. As a result, the incoming tape may not be fully heated to temperatures above T_m and portions of the tape might remain at temperatures below T_m. Additionally, parts of the laminate in earlier layers that are farther away from the laser source may experience heating to temperatures between T_g and T_m.

For the samples heated to temperatures above Tm, no significant effect of the whole laser heating process on the final crystallinity is observed, with the DOC values measured lying between 14% and 20.4%. The crystallinity in the molten state is expected to be lower, which is beneficial for the consolidation process during LAFP, due to the associated reduction in processing viscosity. The research was however not successful in determining the exact crystallinity evolution throughout the whole laser heating and cooling cycle, which remains to be relevant gap in knowledge for the optimization of the laser heating applied during LAFP. Additionally, it is important to note that the experiments did not include the application of pressure and did not account for the effect of shear thinning that would occur under the compaction roller.

For the samples heated below T_m, the most relevant conclusion of LAFP is the ability for the material to cold-crystallize under the rapid laser heating conditions. This will result in an increase in crystallinity for previously placed layers, as more layers are added to the laminate.

7.3. Recommendations

The presented research provided many useful insights about the crystallization behavior as a result of rapid laser heating, which can be related to the LAFP process. However, a lot of conclusions are still based on hypotheses, new questions are formulated and phenomena are observed that cannot be explained with the currently available knowledge. The following research focus is suggested to improve the performed experiments and to further understand the phenomenons observed in this research:

- **Staged heating:** In the tested samples, many parameters vary simultaneously making it difficult to distinguish between their effect on the crystallinity. A way to improve the suitability of the samples to analyze the effect of certain parameters separately is the use of staged heating. This allows to heat samples to the same temperature and apply a dwell, and this way more objectively study the effect of a single parameter. For example for the effect of time above T_m this would mean samples can be heated at the same heating rate to the same temperature above T_m, and kept at this temperature for varying times. What would vary per sample is the cooling time and rate, as due to longer melting times a bigger part of the material is expected to melt and the heat sink effect becomes less strong. Additionally, it is known that the heat sink and mobility barrier differences could also affect the crystallinity. The effect of this on the measurements could be limited by using a big laser heating area and only studying a central located sample.
- **Fast scanning calorimetry (FSC):** DSC is performed at significantly lower heating and cooling rates compared to laser heating. This means DSC cannot be used to simulate the heating phase of LAFP and only to characterize the outcomes of the process. A newly developed type of DSC able to overcome the temperature rate limitation is FSC. By using micro-machined sensors ultra-high scanning rates of up to 50000°C/s can be achieved. This allows to investigate crystallization kinetics during the separate phases of the LAFP process, namely heating to T_m, melting above T_m and cooling. The downside of FSC is the small sample weight and size. To get results representative for the whole laminate grinded powder samples could be used. As material melting is needed to obtain good contact of the sample with the sensor, the thermal history of the sample is affected prior to measurements. This limitation could be overcome by using DSC to characterize the effect of this thermal history alteration.

- **Multiple heating cycles:** During LAFP, parts of the tape might be heated multiple times. Studying whether previous heating cycles to temperatures above T_m have an impact on the crystallinity obtained during subsequent heating cycles to temperatures below T_m is therefore relevant for LAFP. Additionally, this could provide valuable information regarding the melting and crystallization kinetics, as previous cooling rates have been reported to impact crystallization in the literature.
- **Crystallinity extremes:** With the current research, little information is gained about the effect of melting on the crystallization. It would be interesting to increase the time spent at temperatures above T_m until a minimum in crystallinity is found. Similarly, increasing the time spent in the cold-crystallization region until a maximum in achievable crystallinity is found could provide new insights.
- **Simultaneous top and bottom surface measurement:** For the purpose of this thesis, only one IR camera was available. This was a big limitation, as this means the top and bottom surface temperature could not both be measured for each sample. As the temperature differences between the samples heated with identical laser heating settings, the effect of this limitation is also significant. Additionally, by using two IR cameras and performing simultaneous temperature measurements, more accurate information about the temperature gradient in the sample can be obtained and the effect of this parameter on the DOC analyzed. As the bulk DOC is measured during DSC, this could have an impact on the interpretation of the results.

References

[1] Khaled, Y., & Mehdi, H. (2017). Processing of thermoplastic matrix composites through automated fiber placement and tape laying methods: A review. *Journal of Thermoplastic Composite Materials*, *31*(12), 1676–1725.

[2] Carlsson, L., Adams, D., & Pipes, R. (2014). *Experimental characterization of advanced composite materials* (4th). CRC Press.

[3] Vaidya, U., & Chawla, K. (2008). Processing of fibre reinforced thermoplastic composites. *International Materials Reviews*, *53*(4), 185–218.

[4] Askeland, D. (1996). *Polymers," in the science and engineering of materials*. Springer.

[5] Mu, Q., An, L., Hu, Z., & Kuang, X. (2022). Fast and sustainable recycling of epoxy and composites using mixed solvents. *Polymer Degradation and Stability*, *199*, 109895. https://doi.org/https://doi.org/10.1016/j.polymdegradstab.2022.109895

[6] Wang, Y., Mahapatra, S., Belnoue, J. P.-H., Ivanov, D. S., & Hallett, S. R. (2023). Understanding tack behaviour during prepreg-based composites' processing. *Composites Part A: Applied Science and Manufacturing*, *164*, 107284. https://doi.org/https://doi.org/10.1016/j.compositesa.2022.107284

[7] CompositesWorld. (2019). Thermoplastic composites gain leading edge on the a380. https://www.compositesworld.com/articles/thermoplastic-composites-gain-leading-edge-on-the-a380

[8] Murray, R., Beach, R., Barnes, D., Snowberg, D., Berry, D., Rooney, S., Jenks, M., Gage, B., Boro, T., Wallen, S., & Hughes, S. (2021). Structural validation of a thermoplastic composite wind turbine blade with comparison to a thermoset composite blade. *Renewable Energy*, *164*, 1100–1107.

[9] Çelik, O., Peeters, D., Dransfeld, C., & Teuwen, J. (2020a). Intimate contact development during laser assisted fiber placement: Microstructure and effect of process parameters. *Composites Part A: Applied Science and Manufacturing*, *134*.

[10] Mehdikhani, M., Gorbatikh, L., Verpoest, I., & Lomov, S. (2019). Voids in fiber-reinforced polymer composites: A review on their formation, characteristics, and effects on mechanical performance. *Journal of Composite Materials*, *53*(12), 1579–1669.

[11] Batista, N., Olivierb, P., Bernhartb, G., Rezendec, M., & Botelho, E. (2016). Correlation between degree ofcrystallinity, morphology and mechanical properties of pps/carbon ber laminates. *Materials Research*, *19*(1), 195–201.

[12] Khan, M. A., Mitschang, P., & Schledjewski, R. (2010). Identification of some optimal parameters to achieve higher laminate quality through tape placement process. *Advances in Polymer Technology*, *29*(2), 98–111. https://doi.org/https://doi.org/10.1002/adv.20177

[13] Pantani, R., De Meo, A., Speranza, V., & Titomanlio, G. (2015). Effect of crystallinity on the viscosity of an isotactic polypropylene. *AIP Conference Proceedings*, *1695*(1), 020065. https://doi.org/10.1063/1.4937343

[14] Beyeler, E., Phillips, W., & Güçeri, S. (1988). Experimental investigation of laser-assisted thermoplastic tape consolidation. *Journal of Thermoplastic Composite Materials*, *1*(1), 107–121. https://doi.org/10.1177/089270578800100109

[15] Çelik, O. (2021). *Consolidation during laser assisted fiber placement: Heating, compaction and cooling phases (phd thesis*. Delft University of Technology.

[16] Stokes-Griffin, C., & Compston, P. (2015). The effect of processing temperature and placement rate on the short beam strength of carbon fibre–peek manufactured using a laser tape placement process. *Composites Part A: Applied Science and Manufacturing*, *78*, 274–283.

[17] Comer, A., Ray, D., Obande, W., Jones, D., Lyons, J., Rosca, I., O' Higgins, R., & McCarthy, M. (2015). Mechanical characterisation of carbon fibre–peek manufactured by laser-assisted automated-tape-placement and autoclave. *Composites Part A: Applied Science and Manufacturing*, *69*, 10–20. https://doi.org/https://doi.org/10.1016/j.compositesa.2014.10.003

[18] Francesco, M., Valverde, M., Ward, C., Giddings, P., Dell'Anno, G., & Potter, K. (2016). Influence of layup speed on the quality of thermoplastic preforms manufactured by laser-assisted automated fibre placement. *ECCM17 - 17th European Conference on Composite Materials*.

[19] Kok, T. (2018). *On the consolidation quality in laser assisted fiber placement* ((PhD Thesis),"). University of Twente. Enschede.

[20] Choudhary, A. (2019). *Thermal deconsolidation of thermoplastic prepreg tapes during laser-assisted fiber placement (msc thesis*. Delft University of Technology.

[21] Wudy, K., Drummer, D., Kühnlein, F., & Drexler, M. (2014). Influence of degradation behavior of polyamide 12 powders in laser sintering process on produced parts. *AIP Conference Proceedings*.

[22] Hosseini, S., Baran, I., Drongelen, M., & Akkerman, R. (2021). On the temperature evolution during continuous laser-assisted tape winding of multiple c/peek layers: The effect of roller deformation. *International Journal of Material Forming*, *14*, 203–221.

[23] Grouve, W., Warnet, L., Rietman, B., Visser, H., & Akkerman, R. (2013). Optimization of the tape placement process parameters for carbon–pps composites. *Composites Part A: Applied Science and Manufacturing*, *50*, 44–53. https://doi.org/https://doi.org/10.1016/j.compositesa.2013.03.003

[24] Weiler, T., Striet, P., Janssen, H., & Emonts, M. (2016). Optical modelling of vcsel-assisted thermoplastic tape placement. *ECCM17 - 17th European Conference on Composite Materials*.

[25] Schaefer, P., Gierszewski, D., Kollmannsberger, A., Zaremba, S., & Drechsler, K. (2017). Analysis and improved process response prediction of laser- assisted automated tape placement with pa-6/carbon tapes using design of experiments and numerical simulations. *Composites Part A: Applied Science and Manufacturing*, *96*, 137–146.

[26] Jaeschke, P., Wippo, V., Suttmann, O., & Overmeyer, L. (2015). Advanced laser welding of high-performance thermoplastic composites. *Journal of Laser Applications*, *27*(S2).

[27] Batista, N., Olivier, P., Bernhart, G., Rezende, M., & Botelho, E. (2016). Correlation between degree of crystallinity, morphology and mechanical properties of pps/carbon fiber laminates. *Materials Research*, *19*(1), 195–201.

[28] Nohara, L., Nohara, E., Moura, A., Gonçalves, J., Rezende, M., & Costa, M. (2006). Study of crystallization behavior of poly(phenylene sulfide. *Polímeros: Ciência e Tecnologia*, *16*(2), 104–110.

[29] López, L. C., & Wilkes, G. L. (1988). Crystallization kinetics of poly(p-phenylene sulphide): Effect of molecular weight. *Polymer*, *29*(1), 106–113. https://doi.org/https://doi.org/10.1016/0032-3861(88)90207-8

[30] Grouve, W., Poel, G., Warnet, L., & Akkerman, R. (2013). On crystallisation and fracture toughness of poly(phenylene sulphide) under tape placement conditions. *Plastics, Rubber and Composites*, *42*(7), 282–288.

[31] Biron, M. (2018). Chapter 9 - future prospects for thermoplastics and thermoplastic composites. In *Thermoplastics and thermoplastic composites* (3rd). William Andrew Publishing.

[32] Auer, C., Kalinka, G., Krause, T., & Hinrichsen, G. (1994). Crystallization kinetics of pure and fiber-reinforced poly(phenylene sulfide. *Journal of Applied Polymer Science*, *51*(3), 407–413.

[33] Brasington, A., Sacco, C., Halbritter, J., Wehbe, R., & Harik, R. (2021). Automated fiber placement: A review of history, current technologies, and future paths forward. *Composites Part C: Open Access*, *6*.

[34] Key, J. (2020). *Laser induced thermal degradation of carbon fiber-carbon nanotube hybrid laminates*. AFIT Scholar.

[35] Stokes-Griffin, C., & Compston, P. (2016). Investigation of sub-melt temperature bonding of carbon-fibre/peek in an automated laser tape placement process. *Composites Part A: Applied Science and Manufacturing*, *84*, 17–25.

[36] Zhao, D., Chen, J., Zhang, H., Liu, W., Yue, G., & Pan, L. (2021). Effects of processing parameters on the performance of carbon fiber reinforced polyphenylene sulfide laminates manufactured by laser-assisted automated fiber placement. *Journal of Composite Materials*, *0*(0), 1–13. https://doi.org/https://doi.org/10.1177/00219983211055827

[37] Ye, L., Chen, Z.-R., Lu, M., & Hou, M. (2005). De-consolidation and re-consolidation in cf/pps thermoplastic matrix composites. *Composites Part A: Applied Science and Manufacturing*, *36*(7), 915–922.

[38] Ye, L., Lu, M., & Mai, Y.-W. (2002). Thermal de-consolidation of thermoplastic matrix composites—i. growth of voids author links open overlay panel. *Composites Science and Technology*, *62*(16), 2121–2130.

[39] Brzeski, M., & Mitschang, P. (2015). Deconsolidation and its interdependent mechanisms of fibre reinforced polypropylene. *Polymers and Polymer Composites*, *23*(8), 515–524.

[40] Bussink, T. (2021). *Effect of rapid laser deconsolidation on intimate contact development (msc thesis*. Delft University of Technology.

[41] Saenz-Castillo, D., Martín, M., Calvo, S., Rodriguez-Lence, F., & Güemes, A. (2019). Effect of processing parameters and void content on mechanical properties and ndi of thermoplastic composites. *Composites Part A: Applied Science and Manufacturing*, *121*, 308–320. https://doi.org/https://doi.org/10.1016/j.compositesa.2019.03.035

[42] Dara, P., & Loos, A. (1985). *Thermoplastic matrix composite processing model*. Virginia Polytechnic Institute; State University. https://ntrs.nasa.gov/citations/19860012148

[43] Mantell, S. C., & Springer, G. S. (1992). Manufacturing process models for thermoplastic composites. *Journal of Composite Materials*, *26*(16), 2348–2377. https://doi.org/https://doi.org/10.1177/002199839202601602

[44] Çelik, O., Peeters, D., Dransfeld, C., & Teuwen, J. (2020b). Intimate contact development during laser-assisted fiber placement: Microstructure and effect of process parameters. *Composites Part A: Applied Science and Manufacturing*, *134*, 105888.

[45] Huo, P., & Cebe, P. (1992). Effects of thermal history on the rigid amorphous phase in poly(phenylene sulfide). *Colloid and Polymer Science*, *270*, 840–852.

[46] Yan, P., Yang, F., Xiang, M., Wu, T., & Fu, Q. (2020). New insights into the memory effect on the crystallization behavior of poly(phenylene sulfide. *Polymer*, *195*.

[47] Kumar, N. (1980). Viscosity–molecular weight–temperature–shear rate relationships of polymer melts: A literature review. *Journal of Polymer Science: Macromolecular Reviews*, *15*(1), 255–325. https://doi.org/10.1002/pol.1980.230150106

[48] de Bruin, A. (2020). *Investigating the degree of crystallinity in ultrasonically welded thermoplastic composite joints (msc thesis)*. Delft University of Technology.

[49] Chu, Q., Li, Y., Xiao, J., Huan, D., Zhang, X., & Chen, X. (2018). Processing and characterization of the thermoplastic composites manufactured by ultrasonic vibration–assisted automated fiber placement. *Journal of Thermoplastic Composite Materials*, *31*(3), 339–358. https://doi.org/10.1177/0892705717697781

[50] Torre, L., Maffezzoli, A., & Kenny, J. M. (1995). A macrokinetic approach to crystallization applied to a new thermoplastic polyimide (new tpi) as a model polymer. *Journal of Applied Polymer Science*, *56*(8), 985–993. https://doi.org/https://doi.org/10.1002/app.1995.070560812

[51] Ageorges, C., Ye, L., & Hou, M. (2000). Experimental investigation of the resistance welding of thermoplastic- matrix composites. part ii: Optimum processing window and mechanical performance. *Composite Science and Technology*, *60*(8), 1191–1202.

[52] Furushima, Y., Schick, C., & Toda, A. (2018). Crystallization, recrystallization, and melting of polymer crystals on heating and cooling examined with fast scanning calorimetry. *Polymer Crystallization*, *1*.

[53] Kadi, H. E., & Denault, J. (2001). Effects of processing conditions on the mechanical behavior of carbon-fiber-reinforced peek. *Journal of Thermoplastic Composite Materials*, *14*(1), 34–53. https://doi.org/10.1106/XDX9-U8K4-E0PM-70MX

[54] Ray, D., Comer, A. J., Lyons, J., Obande, W., Jones, D., Higgins, R. M. O., & McCarthy, M. A. (2014). Fracture toughness of carbon fiber/polyether ether ketone composites manufactured by autoclave and laser-assisted automated tape placement. *Journal of Applied Polymer Science*, *132*(11). https://doi.org/10.1002/app.41643

[55] Chen, J., Fu, K., & Li, Y. (2021). Understanding processing parameter effects for carbon fibre reinforced thermoplastic composites manufactured by laser-assisted automated fibre placement (afp). *Composites Part A: Applied Science and Manufacturing*, *140*, 106160. https://doi.org/https://doi.org/10.1016/j.compositesa.2020.106160

[56] Shrivastava, A. (2018a). Introduction to plastics engineering. In *Plastics design library* (pp. 1–16). William Andrew Publishing.

[57] Ronkay, F., Molnár, B., Nagy, D., Szarka, G., Iván, B., Kristály, F., Mertinger, V., & Bocz, K. (2020). Melting temperature versus crystallinity: New way for identification and analysis of mul-

tiple endotherms of poly(ethylene terephthalate). *Journal of Polymer Research*, *27*(372). https://doi.org/10.1007/s10965-020-02327-7

[58] Zhang, R.-C., Lu, A., Xu, Y., Min, M., Xia, J.-Q., Zhou, J.-H., Huang, Y.-G., & Li, Z.-M. (2009). Equilibrium melting temperature and spherulitic growth rate of poly(phenylene sulfide. *European Polymer Journal*, *45*(10), 2867–2872.

[59] Carraher, C., Jr. (2013). *Introduction to polymer chemistry* (3rd). CRC Press.

[60] Shrivastava, A. (2018b). Introduction to plastics engineering. In *Plastics design library*. William Andrew Publishing.

[61] Yamazaki, S., Hikosaka, M., Toda, A., Wataoka, I., & Gu, F. (2002). Role of entanglement in nucleation and 'melt relaxation' of polyethylene. *Polymer*, *43*(24), 6585–6593.

[62] Piorkowska, E., & Rutledge, G. (2013). *Handbook of polymer crystallization*. John Wiley & Sons.

[63] Toda, A., Androsch, R., & Schick, C. (2021). Melting kinetics of superheated polymer crystals examined by isothermal and nonisothermal fast scanning calorimetry. *Macromolecules*, *54*, 8770 8779.

[64] Hellmuth, E., & Wunderlich, B. (1965). Superheating of linear high□polymer polyethylene crystals. *Journal of Applied Physics*, *36*(10), 3039–3044. https://doi.org/10.1063/1.1702924

[65] Gao, H., Wang, J., Schick, C., Toda, A., Zhou, D., & Hu, W. (2014). Combining fast-scan chip-calorimeter with molecular simulations to investigate superheating behaviors of lamellar polymer crystals. *Polymer*, *55*(16), 4307–4312. https://doi.org/https://doi.org/10.1016/j.polymer.2014.06.048

[66] Toda, A., Hikosaka, M., & Yamada, K. (2022). Superheating of the melting kinetics in polymer crystals: A possible nucleation mechanism. *Polymer*, *43*(5), 1667–1679.

[67] D'Ilario, L., Martinelli, A., & Piozzi, A. (2002). Memory effect in isothermal melt-crystallization of poly(p-phenylene sulfide) single crystals grown from dilute solution. *Journal of Macromolecular Science, Part B*, *41*(1), 47–59.

[68] Bruger, M. (2004). Crystal growth and impingement in polymer melts. In *Free boundary problems* (pp. 65–74).

[69] Lovinger, A., Davis, D., & Padden, F. (1985). Kinetic analysis of the crystallization of poly(p-phenylene sulphide. *Polymer*, *26*(11), 1595–1604.

[70] Young, R. J., & Lövell, P. A. (2011). *Introduction to polymers* (3rd ed.). CRC Press.

[71] Kristiansen, P. (2004). Nucleation and clarification of semi-crystalline polymers (dissertation. *Eidgenössische Technische Hochschule Zürich, Zürich*.

[72] Kelly, C. A., & Jenkins, M. J. (2020). Modeling the crystallization kinetics of polymers displaying high levels of secondary crystallization. *Polymer Journal*, *54*, 249–257. https://doi.org/10.1038/s41428-021-00581-0

[73] Lorenzo, A. T., & Müller, A. J. (2008). Estimation of the nucleation and crystal growth contributions to the overall crystallization energy barrier. *Journal of Polymer Science Part B: Polymer Physics*, *46*(14), 1478–1487. https://doi.org/https://doi.org/10.1002/polb.21483

[74] Wei, Z., & Song, P. (2018). Chapter 14 - crystallization behavior of semicrystalline polymers in the presence of nucleation agent. In *Crystallization in multiphase polymer systems* (pp. 433–469). Elsevier.

[75] Chen, E., & Hsiao, B. (1992). The effects of transcrystalline interphase in advanced polymer composites. *Polymer Engineering and Science*, *32*(4), 280–286.

[76] Furushima, Y., Nakada, M., Yoshida, Y., & Okada, K. (2018). Crystallization/melting kinetics and morphological analysis of polyphenylene sulfide. *Macromolecular Chemistry and Physics*, *219*(2), 1700481.

[77] Zhuravlev, E., Schmelzer, J., Wunderlich, B., & Schick, C. (2011). Kinetics of nucleation and crystallization in poly(□-caprolactone) (pcl. *Polymer*, *52*(9), 1983–1997.

[78] Di Lorenzo, M., & Silvestre, C. (1999). Non-isothermal crystallization of polymers. *Polymer Science*, *24*(6), 917–950.

[79] Mönch, H., & Derra, G. (2014). High power vcsel systems: A tool for digital thermal processing. *Laser Technik Journal*, *11*(2), 43–47.

[80] Philips GmbH Photonics Aachen. (2017). Laser system with laser module ppm412-12-980- 24-c and supply unit ppu104-12 reference and installation manual version 1.0.

[81] Spruiell, J. E. (2005). A review of the measurement and development of crystallinity and its relation to properties in neat poly(phenylene sulfide) and its fiber reinforced composites. https://doi.org/10.2172/885940

[82] Brady, D. (1976). The crystallinity of poly(phenylene sulfide) and its effect on polymer properties. *Journal of Applied Polymer Science*, *20*(9), 2541–2551. https://doi.org/10.1002/app.1976.070200921

[83] Ishio, A., Saitoh, K., & Kobayashi, S. (2011). Polyphenylene sulfide resin composition (u.s. patent no. 8076423).

[84] López, L., & Wilkes, G. (1988). Crystallization kinetics of poly(p-phenylene sulphide): Effect of molecular weight. *Polymer*, *29*(1), 106–113.

[85] Zuo, P., Tcharkhtchi, A., Shirinbayan, M., Fitoussi, J., & Bakir, F. (2019). Overall investigation of poly (phenylene sulfide) from synthesis and process to applications—a review. *Macromolecular Materials and Engineering*, *304*(5), 1800686. https://doi.org/https://doi.org/10.1002/mame.201800686

[86] Koutras, N. (2020). *Thermal effects on thermoplastic composites welded joints: A physical and mechanical characterisation* ((PhD Thesis),"). Delft University of Technology. Delft.

[87] Höhne, G. W. H., Hemminger, W., & Flammersheim, H.-J. (1996). *Differential scanning calorimetry: An introduction for practitioners*. Springer.

[88] *Plastics — Differential Scanning Calorimetry (DSC)— Part 3: Determination of temperature and enthalpy of melting and crystallization (ISO 11357-3:2018(E))* (Standard). (2018). International Organization for Standardization. Geneva, CH.

[89] *Standard Test Method for Transition Temperatures of Polymers By Differential Scanning Calorimetry (ASTM D 3418–03)* (Standard). (2003). American Society for Testing and Materials. West Conshohocken, PA, United States.

[90] Mettler-Toledo International Inc. (2022). Evaluation and Interpretation of Peak Temperatures of DSC Curves. Part 1: Basic Principles. https://www.mt.com/de/en/home/supportive_content/matchar_apps/MatChar_UC232.html

[91] Çelik, O., Choudhary, A., Peeters, D., Teuwen, J., & Dransfeld, C. (2021). Deconsolidation of thermoplastic prepreg tapes during rapid laser heating. *Composites Part A: Applied Science and Manufacturing*, *149*.

[92] Ficai, A., & Grumezescu, A. M. (Eds.). (2017). Chapter 23 - mesoporous silica nanoparticles: A promising multifunctional drug delivery system. In *Nanostructures for cancer therapy* (pp. 593–621). Elsevier. https://doi.org/https://doi.org/10.1016/B978-0-323-46144-3.00023-4

[93] Day, M., Cooney, J. D., & Wiles, D. M. (1989). The thermal stability of poly(aryl-ether–ether-ketone) as assessed by thermogravimetry. *Journal of Applied Polymer Science*, *38*(2), 323–337. https://doi.org/https://doi.org/10.1002/app.1989.070380214

[94] Chang, D. Q., Liu, J. X., Mao, N., & Chen, B. Z. (2013). Study on the thermal stability of polyphenylene sulfide filter media by non-isothermal thermogravimetry. *Health, Structure, Material and Environment*, *663*, 988–992. https://doi.org/10.4028/www.scientific.net/AMR.663.988

[95] Callister, W., & Rethwisch, D. (2009). *Materials science and engineering: An introduction, 8th edition*. Wiley. https://books.google.nl/books?id=OaIbAAAAQBAJ

[96] Saldivar-Guerra, E., & Vivaldo-Lima, E. (2013). *Handbook of polymer synthesis, characterization, and processing*. Wiley. https://books.google.nl/books?id=4WHvBFnJ-g4C

[97] Wang, G., & Harrison, I. R. (1994). Polymer melting: Heating rate effects on dsc melting peaks. *Thermochimica Acta*, *231*, 203–213. https://doi.org/https://doi.org/10.1016/0040-6031(94)80023-5

A

Temperature parameters

In this appendix the Tables with all measured and generated temperature parameters are presented.

Heated below T_m (2 emitters)

Top surface values

Table A.1: Maximum top surface temperature parameters for samples heated below T_m

	Top surface measurement								
	Laser power	Laser heating time	Maximum temperature	Heating time	Cooling time	Total time above Tg	Heating rate	Cooling rate	Temperature integral >Tg
	[W]	[ms]	[°C]	[s]	[s]	[s]	[°C / s]	[°C / s]	[°C . S]
Maximum value	20	1000	172	0.68	3.09	3.76	121	27	470
	20	1250	193	0.96	3.75	4.70	109	28	632
	20	1500	222	0.64	4.42	5.05	99	30	741
	20	1500	197	1.08	3.85	4.92	100	28	669
	20	1500	203	1.10	3.74	4.83	104	30	671
	20	1600	235	1.38	4.66	6.03	114	31	890
	20	1750	251	1.45	4.93	6.38	112	33	980
	20	1800	221	1.40	4.44	5.83	94	30	847
	20	1800	225	1.40	4.30	5.69	97	31	838
	30	850	204	0.63	3.91	4.54	182	29	618
	30	950	221	0.74	4.34	5.08	177	30	722
	30	1100	240	0.88	4.80	5.68	171	31	847
	30	1100	229	0.86	4.39	5.24	163	32	768
	30	1100	232	0.86	4.47	5.33	167	32	787
	40	700	211	0.53	4.01	4.54	231	30	628
	40	800	236	0.64	4.73	5.36	231	31	788
	50	500	192	0.37	3.73	4.10	279	27	736
	50	600	213	0.46	3.99	4.45	268	31	620
	50	600	212	0.45	4.12	4.57	273	30	632
	50	600	209	0.45	3.91	4.35	269	30	595
	75	550	260	0.46	5.40	5.86	371	31	1 183
	100	300	217	0.24	3.88	4.11	550	33	565
	100	300	203	0.23	3.80	4.03	497	30	542
	100	450	279	0.38	5.46	5.84	498	34	1 193

Table A.2: Average top surface temperature parameters for samples heated below T_m

	Top surface measurement								
	Laser power	Laser heating time	Maximum temperature	Heating time	Cooling time	Total time above Tg	Heating rate	Cooling rate	Temperature integral >Tg
	[W]	[ms]	[°C]	[s]	[s]	[s]	[°C / s]	[°C / s]	[°C . S]
Average sample value	20	1000	153	0.61	2.39	2.99	105	27	353
	20	1250	166	0.74	2.99	3.72	103	25	461
	20	1500	199	0.63	3.70	4.32	88	29	597
	20	1500	187	1.05	3.24	4.28	93	30	566
	20	1500	190	1.07	3.23	4.30	94	31	573
	20	1600	206	1.21	3.83	5.03	96	30	699
	20	1750	217	1.38	4.02	5.39	93	32	778
	20	1800	208	1.36	3.87	5.22	87	30	737
	20	1800	208	1.37	3.60	4.96	87	33	703
	30	850	178	0.58	3.07	3.65	152	29	462
	30	950	193	0.69	3.53	4.21	152	29	558
	30	1100	211	0.84	3.98	4.81	146	31	671
	30	1100	213	0.83	3.86	4.68	149	32	662
	30	1100	222	0.84	4.05	4.88	158	33	706
	40	700	186	0.49	3.20	3.68	197	30	477
	40	800	207	0.60	3.99	4.37	196	30	618
	50	500	173	0.34	3.05	3.39	246	27	419
	50	600	183	0.42	3.17	3.59	223	29	459
	50	600	201	0.43	3.65	4.08	258	30	549
	50	600	197	0.43	3.43	3.85	252	31	513
	75	550	236	0.44	4.80	5.24	333	30	758
	100	300	195	0.22	3.36	3.57	489	31	468
	100	300	191	0.22	3.25	3.47	469	31	451
	100	450	241	0.37	4.56	4.92	413	33	716

Bottom surface values

Table A.3: Maximum bottom surface temperature parameters for samples heated below T_m

	Bottom surface measurement								
	Laser power	Laser heating time	Maximum temperature	Heating time	Cooling time	Total time above Tg	Heating rate	Cooling rate	Temperature integral >Tg
	[W]	[ms]	[°C]	[s]	[s]	[s]	[°C / s]	[°C / s]	[°C . S]
Maximum value	20	1000	142	0.57	2.45	3.01	93	21	343
	20	1250	162	0.82	3.22	4.03	90	23	492
	20	1500	183	1.07	3.74	4.81	87	25	587
	20	1500	199	1.08	3.07	4.15	102	31	860
	20	1500	206	1.10	4.01	5.10	107	29	716
	20	1600	192	1.20	3.97	5.16	85	26	697
	20	1750	197	1.32	4.16	5.47	82	26	747
	20	1800	220	1.39	4.58	5.96	94	28	876
	20	1800	232	1.42	4.81	6.22	101	30	938
	30	850	172	0.58	3.47	4.05	142	24	490
	30	950	187	0.68	3.76	4.43	145	26	583
	30	1100	200	0.84	4.25	5.08	132	26	696
	30	1100	221	0.84	4.51	5.32	157	29	770
	30	1100	231	0.85	4.66	5.50	167	30	816
	40	700	179	0.50	3.75	4.25	184	24	543
	40	800	200	0.60	3.87	4.47	185	28	615
	50	500	169	0.35	3.55	3.90	227	22	484
	50	600	185	0.48	4.02	4.27	201	24	582
	50	600	206	0.46	4.14	4.59	257	28	633
	50	600	208	0.44	4.17	4.60	272	28	637
	75	550	229	0.50	5.35	5.85	314	26	1 125
	100	300	189	0.27	3.93	4.19	370	25	557
	100	300	205	0.24	4.09	4.32	497	28	592
	100	450	251	0.38	4.65	5.03	281	26	703

Table A.4: Average bottom surface temperature parameters for samples heated below T_m

	Bottom surface measurement								
	Laser power	Laser heating time	Maximum temperature	Heating time	Cooling time	Total time above Tg	Heating rate	Cooling rate	Temperature integral >Tg
	[W]	[ms]	[°C]	[s]	[s]	[s]	[°C / s]	[°C / s]	[°C . S]
Average sample value	20	1000	127	0.47	1.74	2.19	79	21	236
	20	1250	144	0.71	2.38	3.09	77	23	355
	20	1500	175	1.01	2.99	4.00	84	28	511
	20	1500	182	1.04	3.12	4.15	89	30	545
	20	1500	159	0.97	2.90	3.86	72	24	469
	20	1600	169	1.09	3.17	4.25	73	25	535
	20	1750	169	1.18	3.26	4.43	67	24	558
	20	1800	198	1.32	3.65	4.96	82	30	684
	20	1800	212	1.37	4.05	5.41	90	30	776
	30	850	153	0.52	2.68	3.19	122	23	377
	30	950	163	0.61	2.94	3.55	121	25	435
	30	1100	199	0.79	3.64	4.42	138	30	603
	30	1100	204	0.80	3.68	4.48	143	31	619
	30	1100	175	0.76	3.40	4.15	113	25	529
	40	700	158	0.44	2.90	3.34	157	23	411
	40	800	173	0.54	3.15	3.69	154	26	465
	50	500	157	0.33	2.92	3.24	209	23	387
	50	600	188	0.43	3.42	3.84	228	29	505
	50	600	187	0.42	3.30	3.71	235	29	486
	50	600	163	0.41	3.10	3.50	182	24	427
	75	550	211	0.38	4.65	5.03	281	26	703
	100	300	168	0.22	2.97	3.18	358	26	396
	100	300	189	0.23	3.41	3.64	442	29	479
	100	450	226	0.37	4.61	4.98	368	29	715

Heated above T_m (2 emitters)

Top surface values

Table A.5: Maximum top surface temperature parameters for samples heated above T_m

	Top surface measurement												
	Laser power	Laser heating time	Maximum temperature	Heating time	Cooling time	Total time above Tg	Total time above Tm	Time from Tg to Tm (heating)	Time from Tg to Tm (cooling)	Heating rate	Cooling rate	Temperature integral >Tg	Temperature integral >Tm
	[W]	[ms]	[°C]	[s]	[s]	[s]	[s]	[s]	[s]	[°C / s]	[°C / s]	[°C . S]	[°C . S]
Maximum value	25	2500	324	2.19	6.66	8.84	1.01	1.62	6.22	107	35	1 625	311
	25	2500	321	2.19	6.44	8.62	0.95	1.65	6.03	106	36	1 584	289
	50	1300	352	1.14	6.71	7.84	1.05	0.76	6.04	230	39	1 450	333
	50	1300	344	1.14	6.71	7.84	0.95	0.78	6.11	224	38	1 432	298
	50	1750	421	1.61	7.48	9.08	2.21	0.72	6.15	206	44	1 902	775
	50	2000	447	1.85	7.71	9.55	2.55	0.75	6.26	193	46	2 045	921
	100	600	348	0.53	6.77	7.29	0.70	0.38	6.21	496	38	1 286	220
	100	600	340	0.52	6.77	7.29	0.62	0.40	6.27	484	37	1 274	193
	100	850	444	0.77	7.60	8.37	1.80	0.37	6.25	479	46	1 721	647
	100	900	472	0.82	7.80	8.62	2.15	0.35	6.12	468	47	1 866	950
	150	500	419	0.52	7.20	7.72	1.27	0.32	6.13	756	46	1 462	430
	150	600	482	0.54	7.92	8.46	1.90	0.25	6.32	732	50	1 752	686
	150	650	491	0.59	7.90	8.48	2.17	0.25	6.27	691	51	1 772	762
	200	300	389	0.28	6.64	6.90	0.83	0.17	5.90	1098	45	1 247	271
	200	300	366	0.28	6.64	6.90	0.62	0.19	6.10	1021	42	1 206	194
	200	450	492	0.43	8.06	8.48	1.88	0.20	6.41	960	50	1 745	678
	200	450	454	0.45	0.74	8.19	1.79	0.14	6.26	711	52	2 039	625
	250	350	491	0.34	7.98	8.31	1.73	0.16	6.42	1203	50	1 685	620
	300	300	519	0.29	8.19	8.48	1.78	0.14	6.56	1502	52	1 723	636
	300	300	504	0.32	8.12	8.44	1.66	0.17	6.61	1483	51	2 083	583
	400	200	462	0.19	7.55	7.74	1.39	0.10	6.25	1972	49	1 505	475
	400	250	582	0.25	7.94	8.18	1.94	0.10	6.14	1984	62	1 738	718

Table A.6: Average top surface temperature parameters for samples heated above T_m

	Top surface measurement												
	Laser power	Laser heating time	Maximum temperature	Heating time	Cooling time	Total time above Tg	Total time above Tm	Time from Tg to Tm (heating)	Time from Tg to Tm (cooling)	Heating rate	Cooling rate	Temperature integral >Tg	Temperature integral >Tm
	[W]	[ms]	[°C]	[s]	[s]	[s]	[s]	[s]	[s]	[°C/s]	[°C/s]	[°C . S]	[°C . S]
Average sample value	25	2500	305	2.15	6.08	8.22	0.52	1.82	5.88	100	35	1 566	156
	25	2500	301	2.17	5.71	7.87	0.45	1.87	5.55	98	37	1 512	133
	50	1300	328	1.12	6.06	7.18	0.68	0.85	5.65	213	39	1 387	210
	50	1300	326	1.12	6.06	7.17	0.64	0.86	5.68	211	39	1 369	196
	50	1750	389	1.59	6.71	8.29	1.71	0.82	5.76	189	45	1 654	575
	50	2000	405	1.83	6.79	8.61	2.04	0.83	5.74	172	46	1 781	702
	100	600	324	0.52	6.16	6.67	0.41	0.42	5.85	457	38	1 227	124
	100	600	321	0.51	6.16	6.66	0.35	0.42	5.90	454	38	1 216	106
	100	850	415	0.76	6.88	7.64	1.41	0.41	5.77	448	47	1 497	554
	100	900	433	0.81	7.01	7.82	1.80	0.40	5.62	431	49	1 469	778
	150	500	375	0.45	6.29	6.74	0.75	0.30	5.69	638	45	1 197	242
	150	600	444	0.53	6.81	7.33	1.42	0.27	5.65	670	52	1 454	494
	150	650	454	0.58	7.09	7.66	1.53	0.27	5.86	639	51	1 547	540
	200	300	352	0.27	6.07	6.33	0.51	0.20	5.63	990	43	1 193	160
	200	300	341	0.27	6.06	6.33	0.42	0.22	5.70	947	41	1 151	129
	200	450	459	0.42	7.18	7.59	1.42	0.21	5.96	895	51	1 488	494
	200	450	454	0.45	6.95	7.40	1.32	0.18	5.91	660	52	1 432	448
	250	350	448	0.33	7.08	7.41	1.23	0.18	6.00	1095	51	1 413	422
	300	300	462	0.29	7.25	7.53	1.28	0.15	6.11	1327	51	1 445	439
	300	300	459	0..32	7.52	6.44	1.22	0.19	6.44	1354	49	1 471	414
	400	200	420	0.19	6.67	6.86	0.94	0.12	5.81	1793	50	1 265	308
	400	250	507	0.25	6.99	7.23	1.45	0.12	5.66	1706	60	1 452	513

Bottom surface values

Table A.7: Maximum bottom surface temperature parameters for samples heated above T_m

Maximum value	Bottom surface measurement												
	Laser power	Laser heating time	Maximum temperature	Heating time	Cooling time	Total time above Tg	Total time above Tm	Time from Tg to Tm (heating)	Time from Tg to Tm (cooling)	Heating rate	Cooling rate	Temperature integral >Tg	Temperature integral >Tm
	[W]	[ms]	[°C]	[s]	[s]	[s]	[s]	[s]	[s]	[°C / s]	[°C / s]	[°C . S]	[°C . S]
	25	2500	317	2.18	6.25	8.43	0.95	1.64	5.84	104	35	1 994	289
	25	2500	320	2.17	6.25	8.42	0.97	1.63	5.82	106	36	2 016	299
	50	1300	349	1.15	6.69	7.83	1.14	0.76	5.93	227	39	1 466	364
	50	1300	355	1.14	6.70	7.84	1.15	0.75	5.94	233	40	1 464	370
	50	1750	349	1.81	7.03	8.69	1.17	1.17	6.36	178	37	1 661	377
	50	2000	378	1.84	7.07	8.90	1.83	0.98	6.10	157	41	1 777	610
	100	600	339	0.55	6.78	7.32	0.79	0.39	6.14	457	37	1 312	249
	100	600	333	0.55	6.70	7.24	0.73	0.40	6.12	450	36	1 285	227
	100	850	372	0.79	7.13	7.91	1.34	0.47	6.11	362	40	1 512	437
	100	900	384	0.86	7.26	8.11	1.48	0.48	6.15	345	41	1 579	496
	150	500	355	0.49	7.26	0.75	1.01	0.31	6.43	540	36	1 770	330
	150	600	379	0.58	7.38	7.95	1.33	0.32	6.30	507	39	1 517	444
	150	650	402	0.59	7.77	8.35	1.61	0.31	6.44	530	40	1 649	551
	200	300	360	0.30	6.85	7.14	0.92	0.18	6.04	915	39	1 304	299
	200	300	340	0.30	6.84	7.14	0.75	0.20	6.20	835	37	1 260	236
	200	450	389	0.48	7.45	7.93	1.45	0.24	6.25	624	40	1 545	489
	200	450	397	0.56	7.87	8.43	1.51	0.33	6.58	662	39	1 618	516
	250	350	402	0.43	7.16	7.59	1.36	0.23	6.00	886	44	1 456	471
	300	300	398	0.36	7.34	7.69	1.39	0.16	6.14	876	42	1 482	474
	300	300	410	0.51	8.16	8.66	1.50	0.34	6.82	751	39	1 646	517
	400	200	366	0.26	7.14	7.39	1.02	0.13	6.25	1116	39	1 362	333
	400	250	401	0.35	7.74	8.09	1.56	0.14	6.39	907	40	1 595	538

Table A.8: Average bottom surface temperature parameters for samples heated above T_m

	Bottom surface measurement												
	Laser power	Laser heating time	Maximum temperature	Heating time	Cooling time	Total time above Tg	Total time above Tm	Time from Tg to Tm (heating)	Time from Tg to Tm (cooling)	Heating rate	Cooling rate	Temperature integral >Tg	Temperature integral >Tm
	[W]	[ms]	[°C]	[s]	[s]	[s]	[s]	[s]	[s]	[°C/s]	[°C/s]	[°C . S]	[°C . S]
Average sample value	25	2500	281	2.14	5.38	7.51	0	2.14	5.37	90	36	1 467	0
	25	2500	279	2.13	5.37	7.49	0	2.13	5.37	89	35	1 484	0
	50	1300	327	1.13	5.92	7.04	0.74	0.85	5.46	210	40	1 390	228
	50	1300	318	1.12	5.79	6.90	0.60	0.88	5.43	205	40	1 374	183
	50	1750	319	1.57	6.05	7.61	0.79	1.11	5.71	147	39	1 421	244
	50	2000	332	1.78	6.21	7.93	1.07	1.24	5.63	137	39	1 474	332
	100	600	298	0.53	5.72	6.24	0.23	0.46	5.56	397	36	1 207	69
	100	600	305	0.53	5.92	6.45	0.34	0.45	5.67	406	36	1 209	103
	100	850	326	0.76	6.19	6.94	0.66	0.57	5.71	314	38	1 224	203
	100	900	337	0.83	6.35	7.17	0.81	0.59	5.77	298	39	1 291	255
	150	500	316	0.47	6.30	6.77	0.47	0.37	6.77	483	36	1 153	143
	150	600	334	0.54	6.34	6.88	0.70	0.38	5.80	457	38	1 218	220
	150	650	355	0.59	6.77	7.33	1.00	0.38	5.95	451	39	1 352	338
	200	300	334	0.30	6.08	6.37	0.64	0.20	5.54	831	40	1 231	202
	200	300	313	0.30	6.08	6.37	0.39	0.22	5.76	763	37	1 186	120
	200	450	342	0.45	6.57	7.02	0.81	0.29	5.92	564	38	1 260	258
	200	450	315	0.34	7.11	7.45	0.89	0.20	6.36	775	37	1 336	287
	250	350	350	0.42	6.38	6.80	0.83	0.23	5.74	781	41	1 217	299
	300	300	342	0.34	6.45	6.78	0.79	0.20	5.79	757	39	1 218	253
	300	300	316	0.47	6.30	6.77	0.47	0.37	5.94	483	36	1 153	143
	400	200	311	0.24	6.10	6.33	0.41	0.16	5.77	950	36	1 077	124
	400	250	351	0.31	6.90	7.21	0.91	0.17	6.13	869	38	1 307	293

Heated above T_m (12 emitters)

Top surface values

Table A.9: Maximum and average top surface temperature parameters for samples heated above T_m

	Top surface measurement											
	Laser power	Laser heating time	Maximum temperature	Heating time	Cooling time	Total time above Tg	Total time above Tm	Time from Tg to Tm (heating)	Time from Tg to Tm (cooling)	Heating rate	Cooling rate	Temperature integral >Tg	Temperature integral >Tm
	[W]	[ms]	[°C]	[s]	[s]	[s]	[s]	[s]	[s]	[°C / s]	[°C / s]	[°C . S]	[°C . S]
Maximum value	4-6-4	4200	305	3.67	8.10	11.76	0.93	2.99	7.85	59	27	2 152	275
	4-6-4	4200	305	3.68	7.87	11.55	0.99	3.00	7.57	59	27	2 125	293
	9-12-9	2000	357	1.76	8.55	10.30	1.73	1.11	7.47	153	31	1 947	554
	9-12-9	2000	338	1.74	8.68	10.42	1.30	1.22	7.90	143	29	1 924	404
	18-24-18	1000	377	0.89	9.01	9.89	1.63	0.55	7.71	325	32	1 905	533
	18-24-18	1000	361	0.88	9.00	9.88	1.22	0.58	8.08	309	30	1 805	388
	38-50-38	400	357	0.36	8.32	8.67	0.93	0.25	7.49	748	32	1 557	294
	38-50-38	400	329	0.36	8.31	8.66	0.47	0.29	7.90	683	29	1 485	144
	75-100-75	200	366	0.19	8.66	8.84	0.84	0.13	7.88	1490	32	1 565	263
	75-100-75	200	344	0.18	8.51	8.68	0.72	0.14	7.82	1426	30	1 527	222
	150-200-150	100	421	0.07	8.72	8.78	1.24	0.04	7.51	4813	38	1 642	401
Sample surface average value	4-6-4	4200	273	3.54	6.73	10.26	0.00	3.54	6.73	52	27	1 773	0
	4-6-4	4200	246	3.50	5.87	9.36	0.00	3.50	5.86	45	27	1 508	0
	9-12-9	2000	293	1.68	6.55	8.33	0.17	1.68	6.48	121	31	1 406	52
	9-12-9	2000	283	1.67	6.84	8.50	0.00	1.67	6.83	116	28	1 405	0
	18-24-18	1000	312	0.85	6.96	7.94	0.37	0.85	6.73	263	32	1 331	113
	18-24-18	1000	318	0.85	7.55	8.55	0.47	0.85	7.23	269	30	1 435	146
	38-50-38	400	304	0.34	6.36	6.73	0.10	0.34	6.29	641	34	1 089	32
	38-50-38	400	285	0.34	6.73	7.07	0.00	0.34	6.73	582	29	1 112	4
	75-100-75	200	319	0.19	6.81	7.02	0.13	0.19	6.70	1279	34	1 137	41
	75-100-75	200	319	0.18	7.43	7.62	0.26	0.18	7.19	1327	31	1 252	80
	150-200-150	100	390	0.06	7.08	7.13	0.51	0.04	6.59	5468	42	1 219	161

Bottom surface values

Table A.10: Maximum and average bottom surface temperature parameters for samples heated above T_m

		Bottom surface measurement										
	Laser power	Laser heating time	Maximum temperature	Heating time	Cooling time	Total time above Tg	Total time above Tm	Time from Tg to Tm (heating)	Time from Tg to Tm (cooling)	Heating rate	Cooling rate	Temperature integral >Tg	Temperature integral >Tm
	[W]	[ms]	[°C]	[s]	[s]	[s]	[s]	[s]	[s]	[°C / s]	[°C / s]	[°C . S]	[°C . S]
Maximum value	4-6-4	4200	302	3.64	8.22	11.85	0.93	3.05	7.88	58	26	2 187	276
	9-12-9	2000	350	1.75	8.57	10.32	1.66	1.14	7.52	149	30	1 974	529
	18-24-18	1000	362	0.89	9.07	9.95	1.55	0.59	7.82	306	30	1 892	502
	38-50-38	400	318	0.39	8.44	8.83	0.68	0.29	7.86	593	27	1 542	209
	75-100-75	200	325	0.21	8.37	8.58	0.70	0.15	7.74	1132	28	1 496	215
	150-200-150	100	337	0.13	8.60	8.73	0.87	0.08	7.79	1961	29	1 556	271
Sample surface average value	4-6-4	4200	253	3.44	6.48	9.91	0	3.44	6.47	47	25	1 625	0
	9-12-9	2000	291	1.67	6.88	8.63	0	1.67	6.78	121	29	1 451	60
	18-24-18	1000	311	0.85	7.17	8.16	0.51	0.85	6.80	261	31	1 384	157
	38-50-38	400	281	0.36	6.69	7.05	0.00	0.36	6.69	540	29	1 128	0
	75-100-75	200	284	0.20	6.76	6.95	0.00	0.20	6.75	976	29	1 115	0
	150-200-150	100	304	0.14	7.12	7.31	0.29	0.14	6.88	1586	30	1 203	86

B

DSC data analysis

In this appendix, the results of the heat flow peak integration obtained using DSC characterization are presented for all tested samples. A sigmoidal baseline was utilized to integrate both the cold-crystallization and melting peaks. The linear region of the heat flow was considered to determine the endpoints for the integration. The manual selection of tangential arms for the sigmoidal baseline was required during data analysis using the Perkin Elmer software, whereas the TRIOS software, used for the analysis of TA Instrumentation results, is capable of performing this step automatically.

Perkin Elmer

As-received

Figure B.1: PE 1

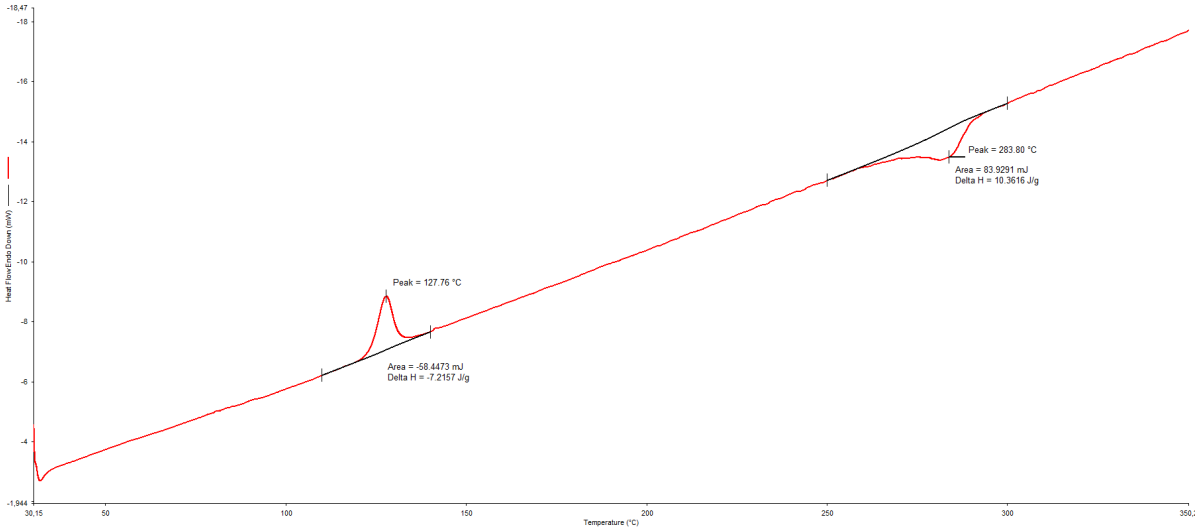

Figure B.2: PE 2

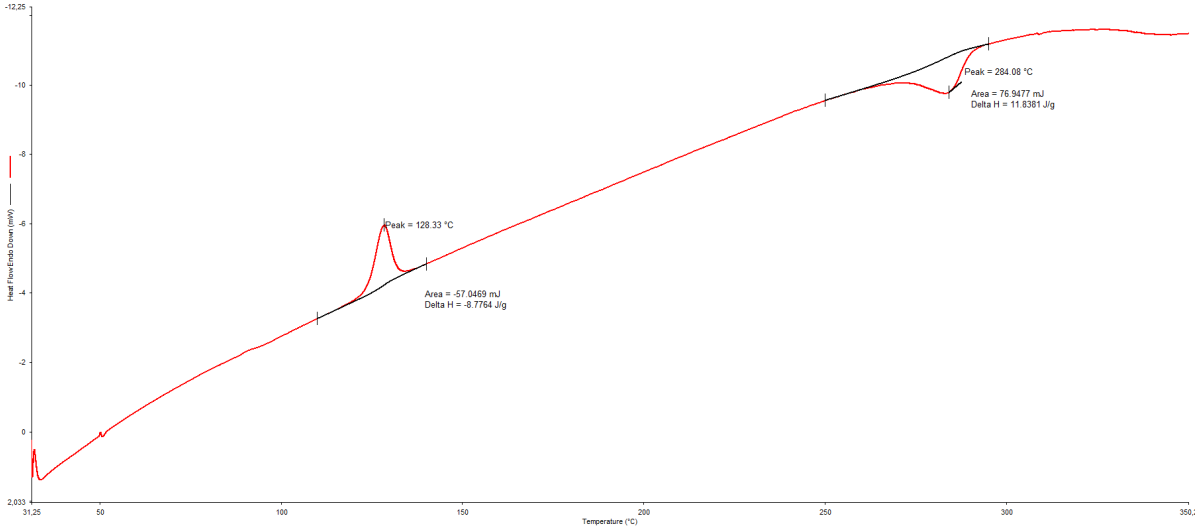

Figure B.3: PE 3

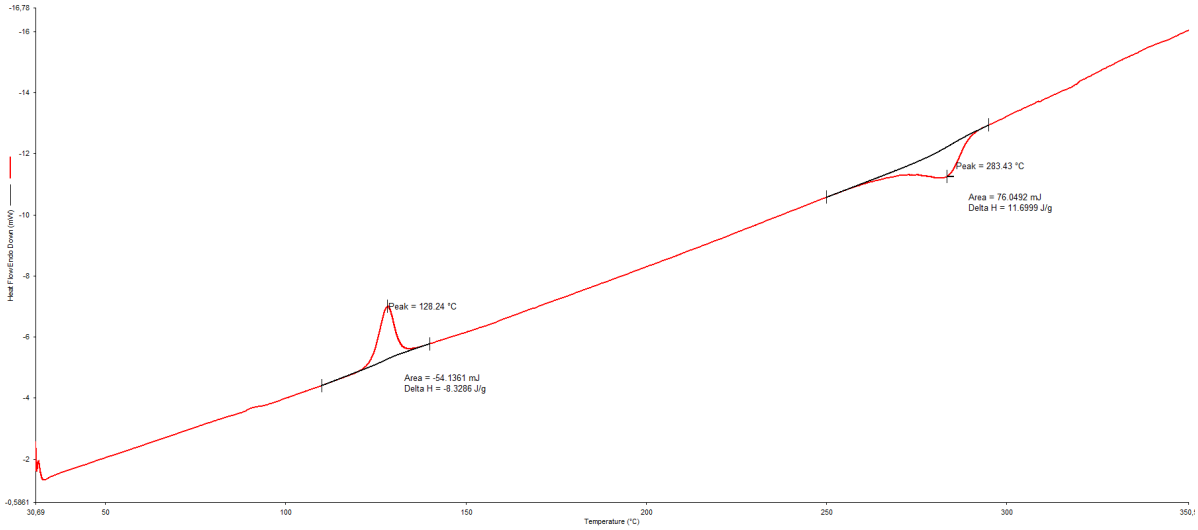

Figure B.4: PE 4

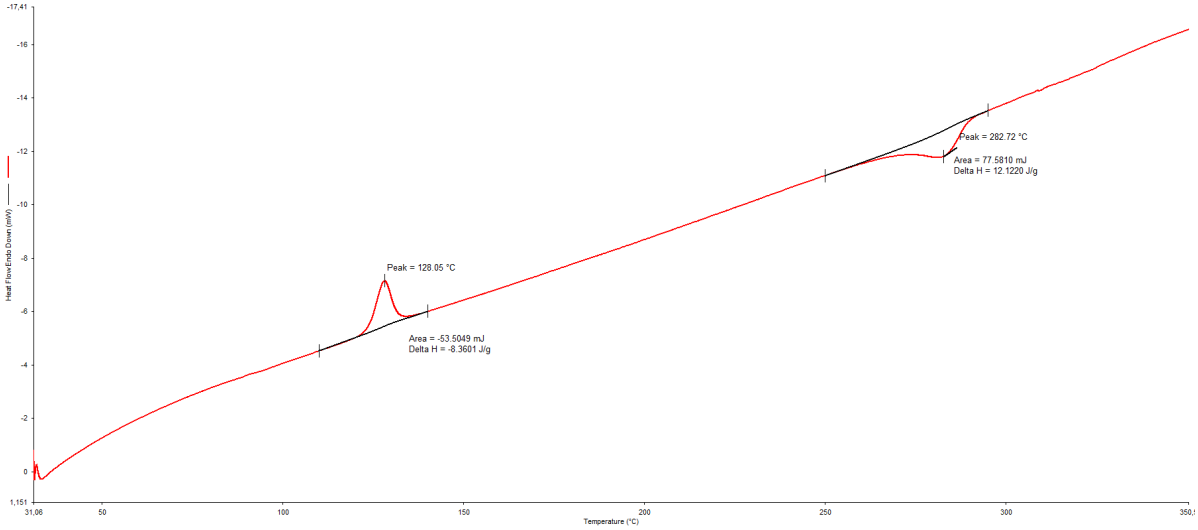

Figure B.5: PE 5

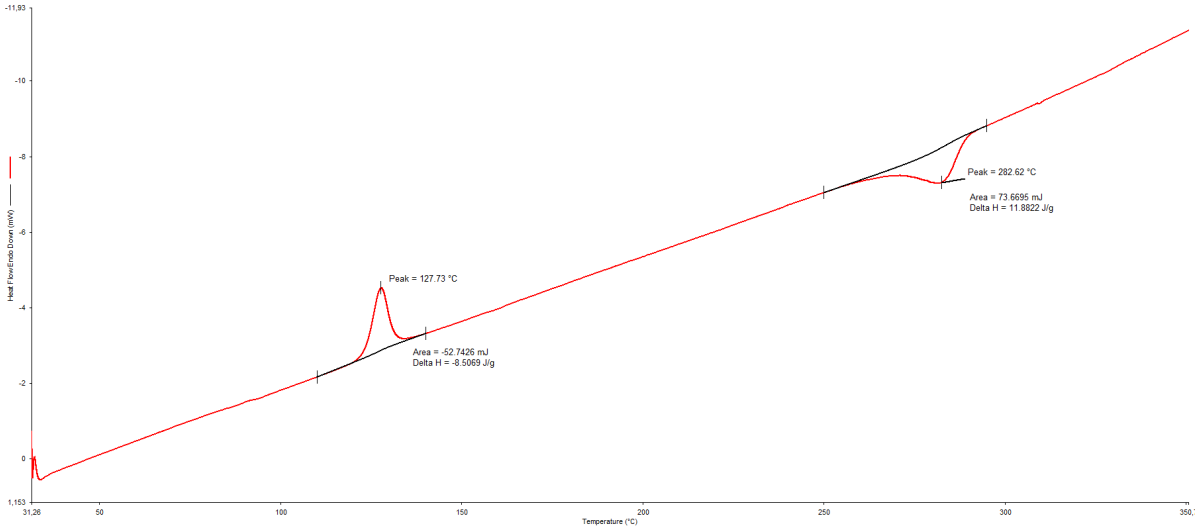

Figure B.6: PE 6

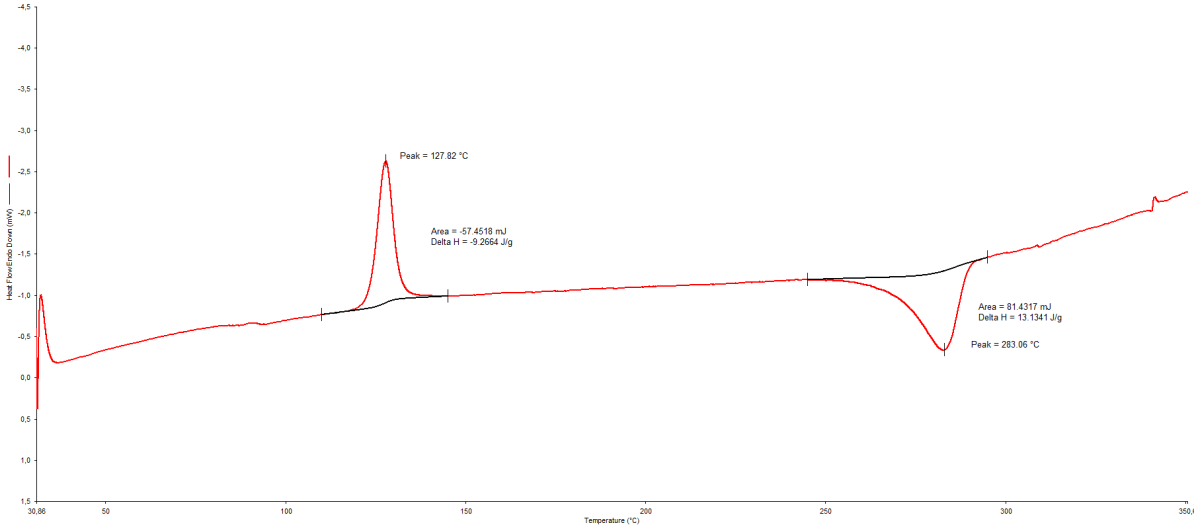

Figure B.7: PE 7

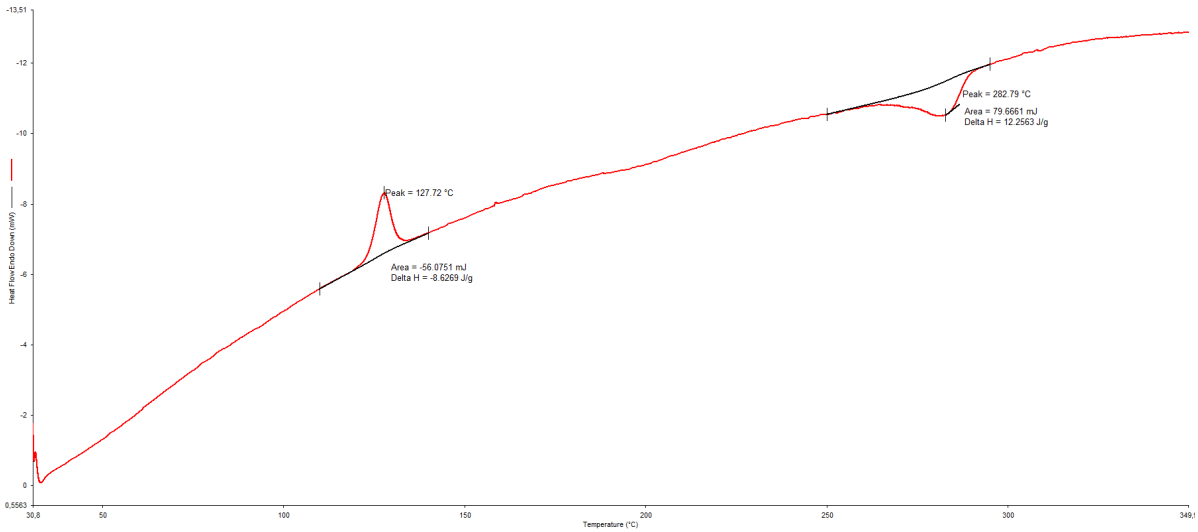

Figure B.8: PE 8

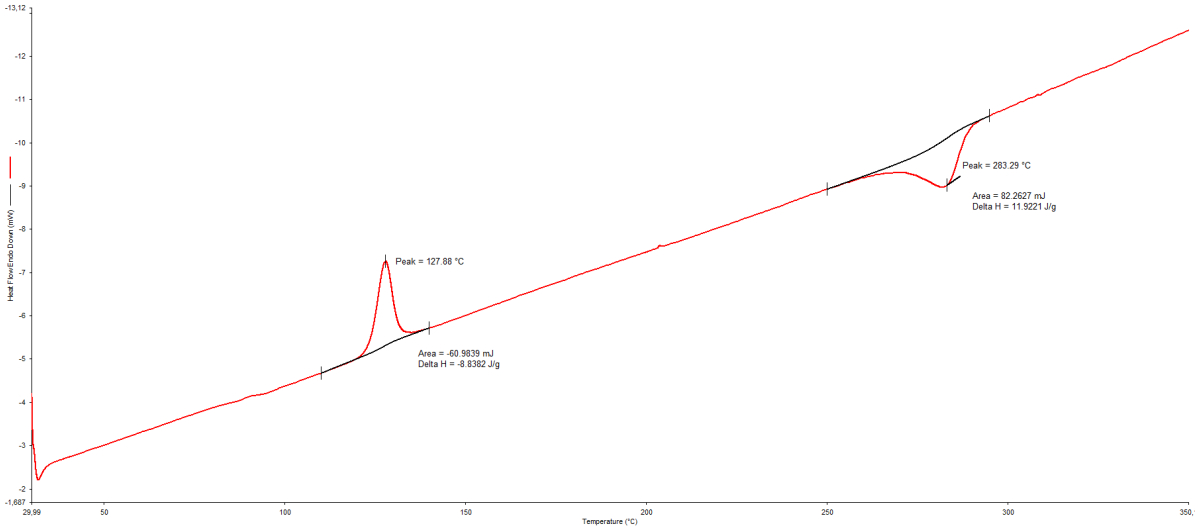

Heated below T_m

Figure B.9: PE: 20W 1500ms

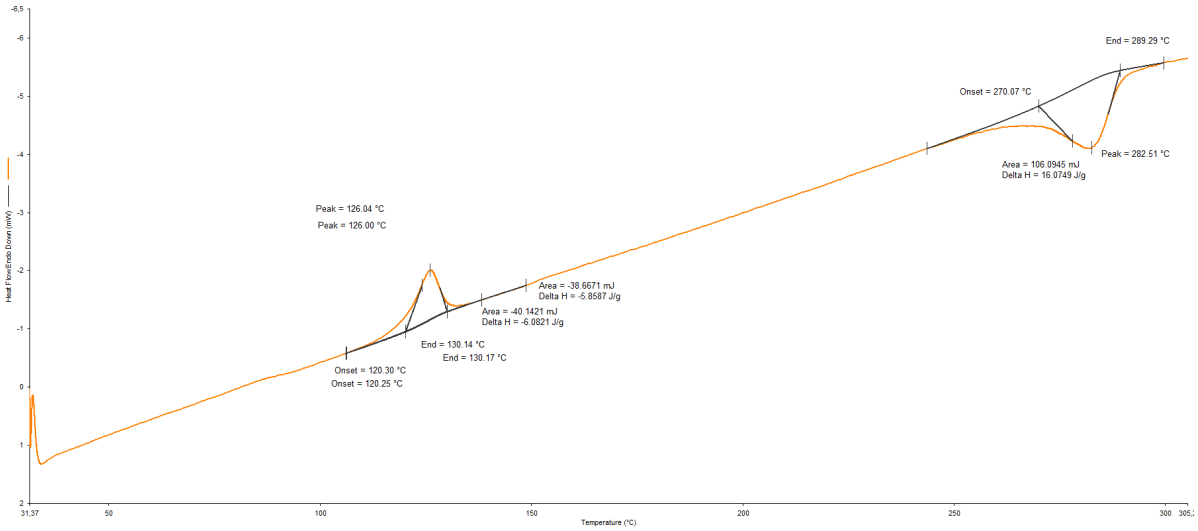

Figure B.10: PE: 20W 1500ms

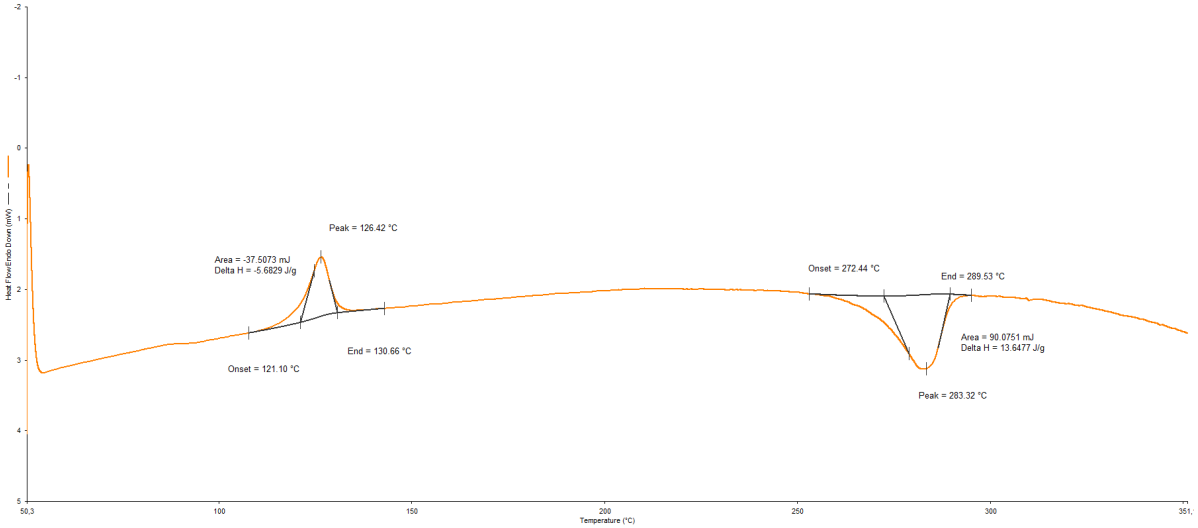

Figure B.11: PE: 20W 1800ms

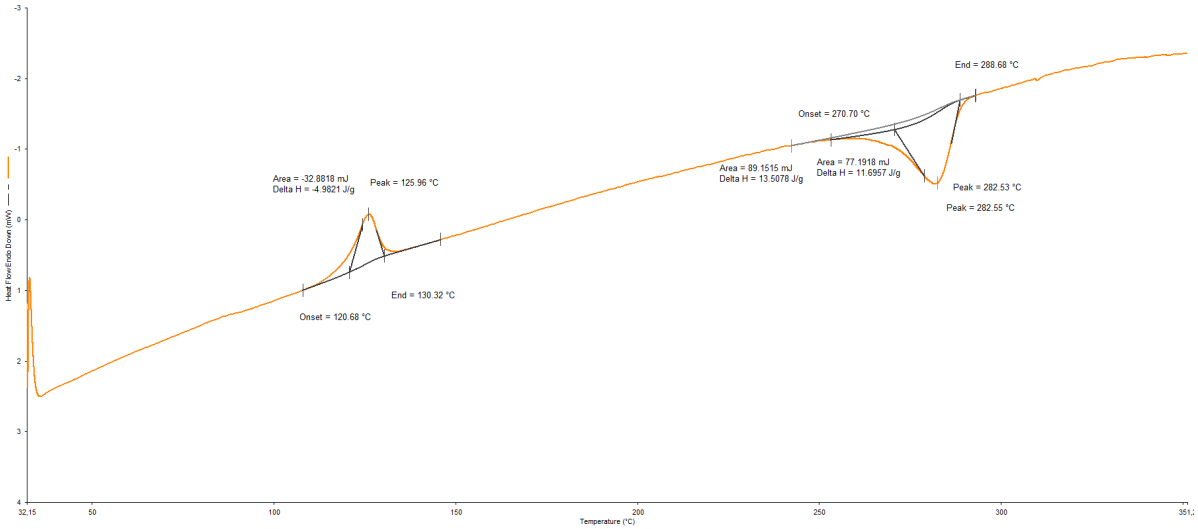

Figure B.12: PE: 30W 1100ms

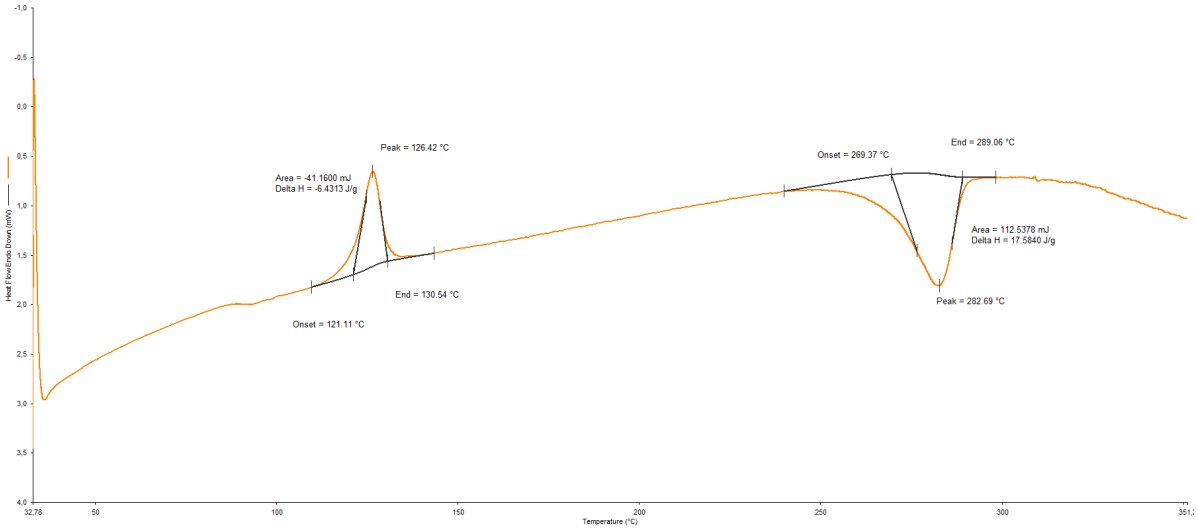

Figure B.13: PE: 30W 1100ms

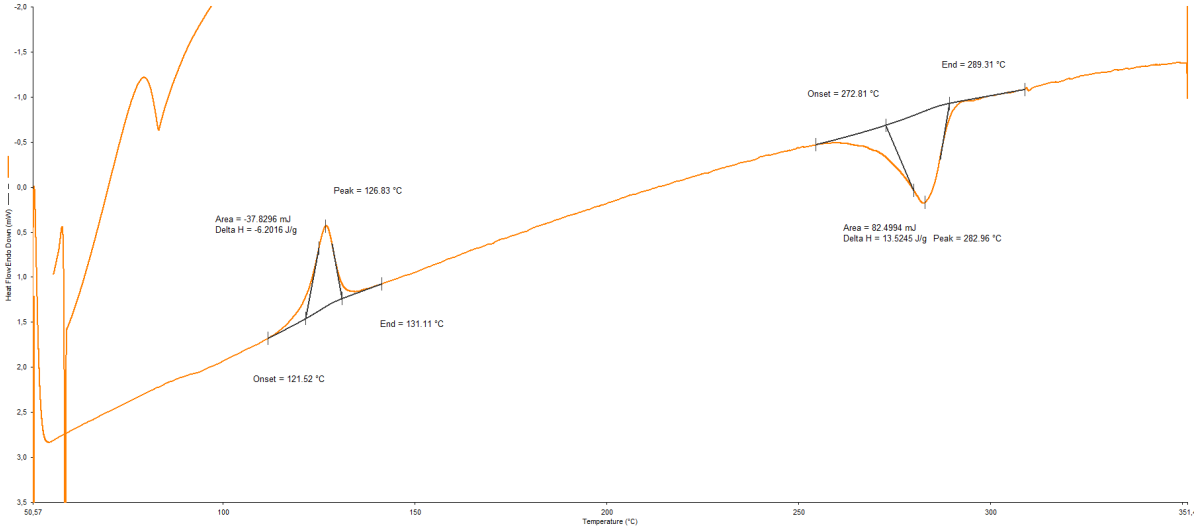

Figure B.14: PE: 50W 600ms

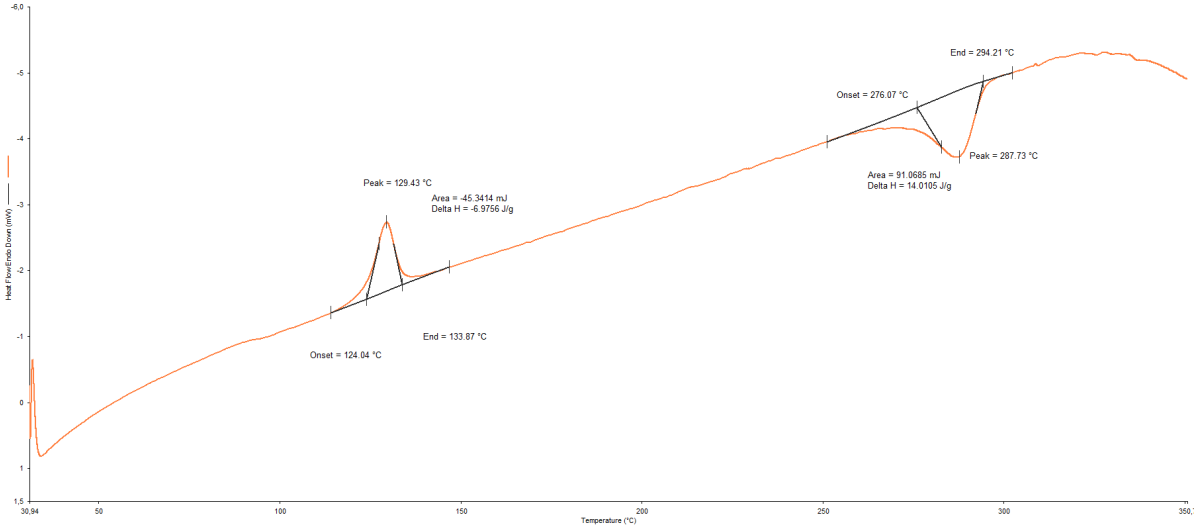

Figure B.15: PE: 50W 600ms

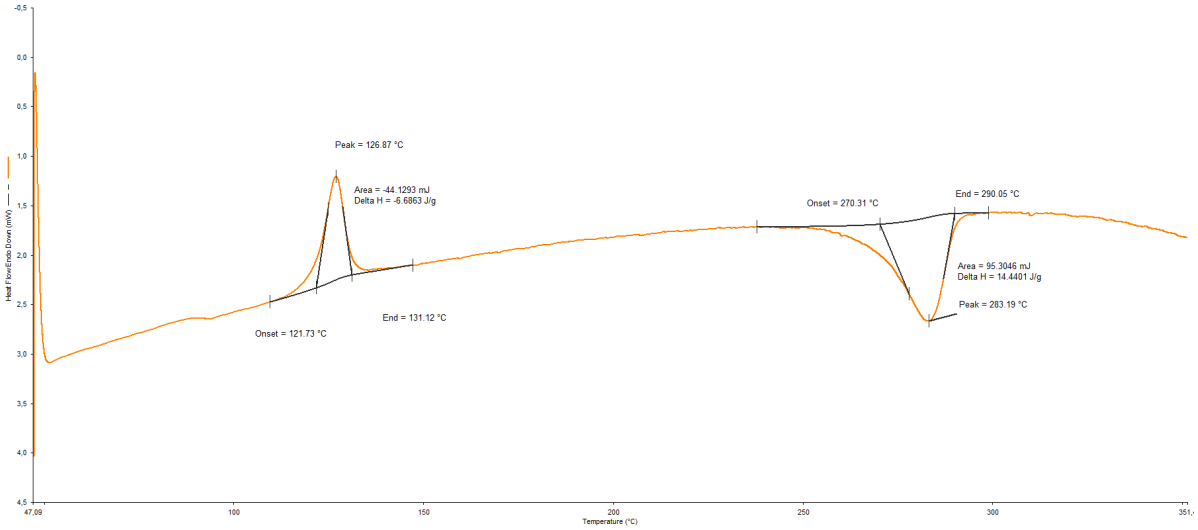

Figure B.16: PE: 100W 300ms

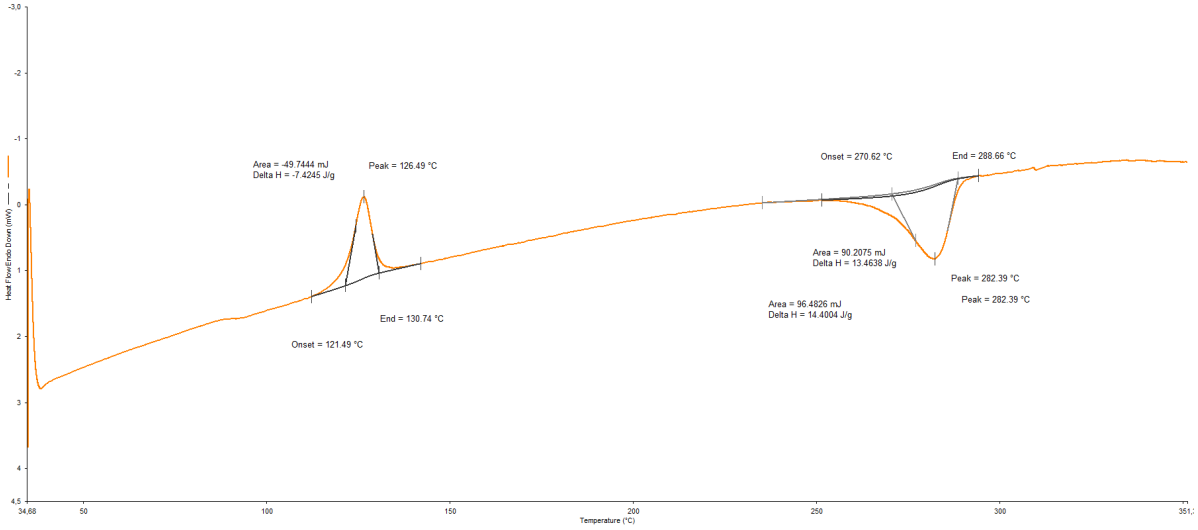

Heated above T_m

Figure B.17: PE: 25W 2500ms

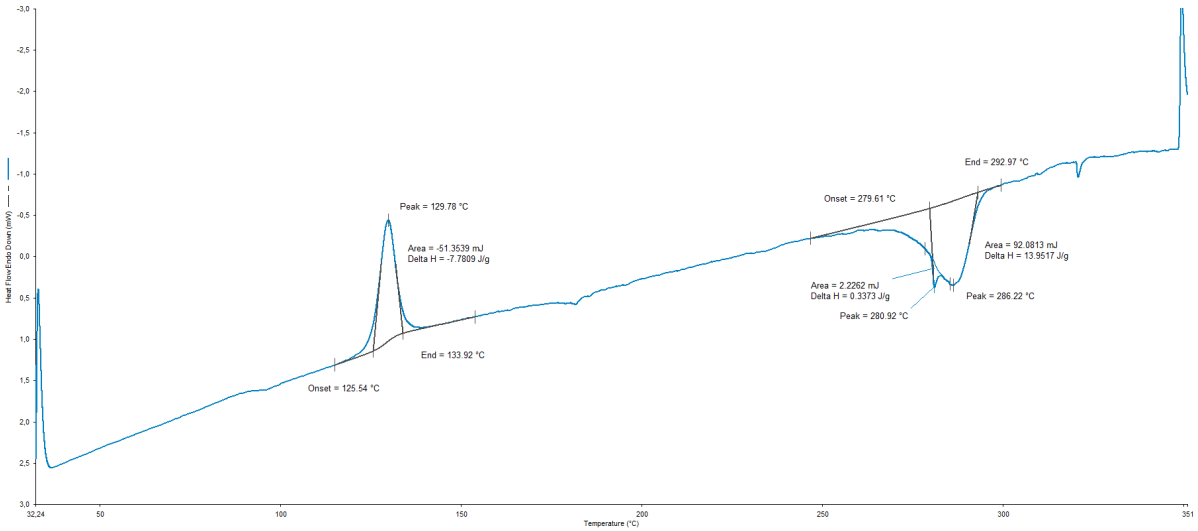

Figure B.18: PE: 25W 2500ms

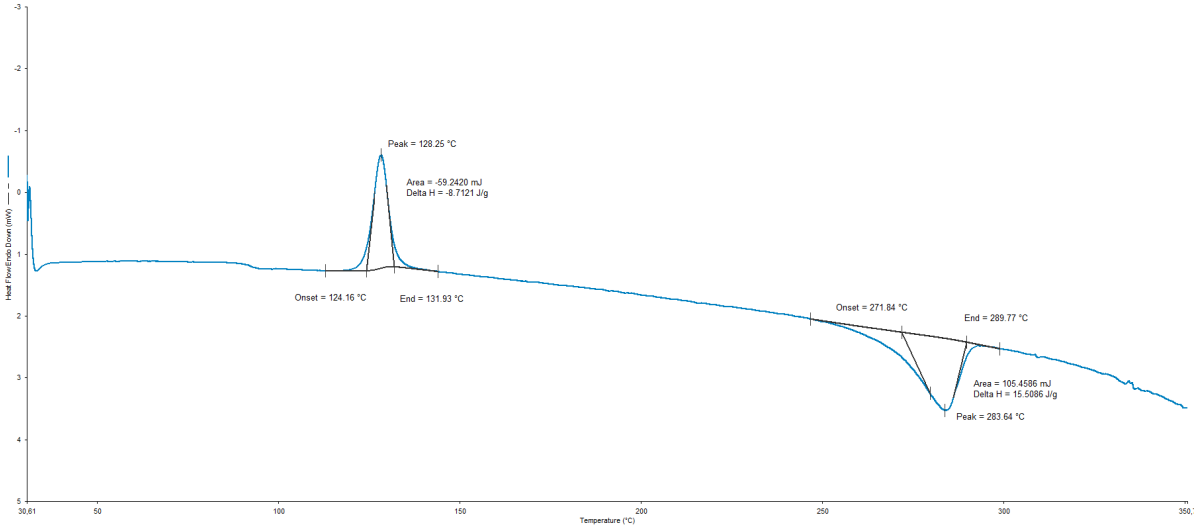

Figure B.19: PE: 50W 1300ms

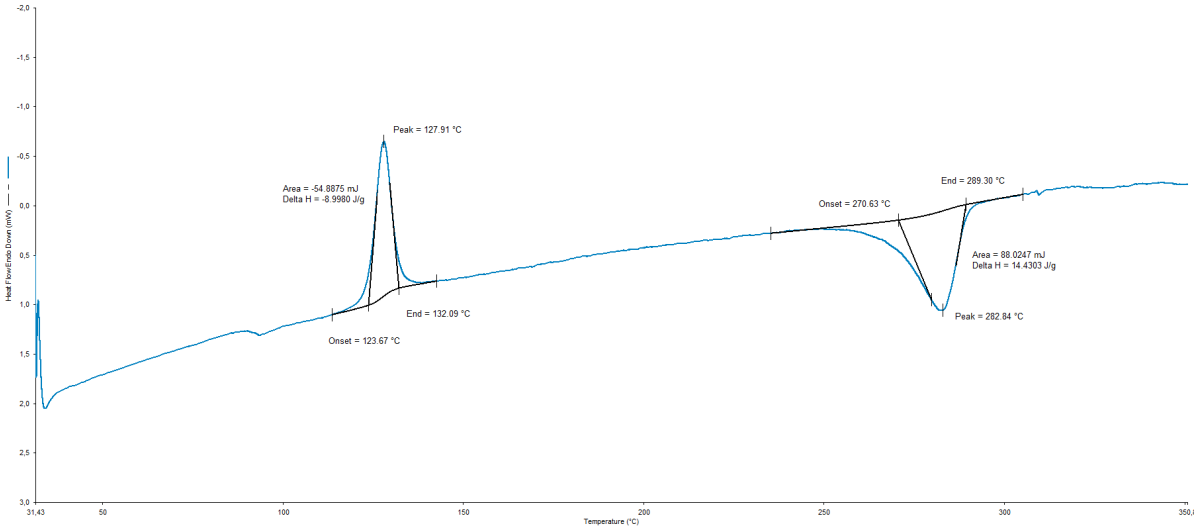

Figure B.20: PE: 50W 1300ms

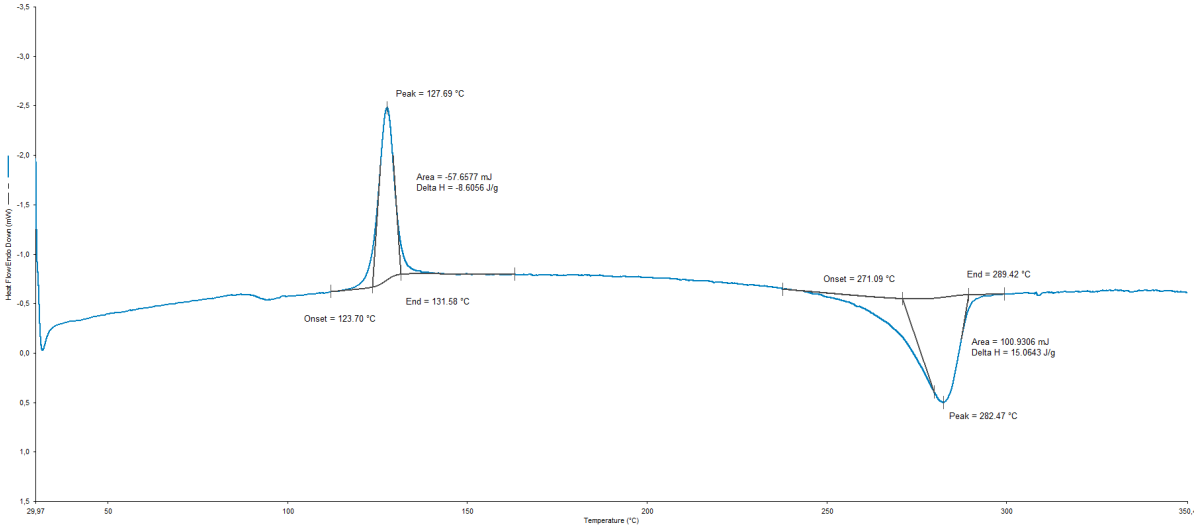

Figure B.21: PE: 100W 600ms

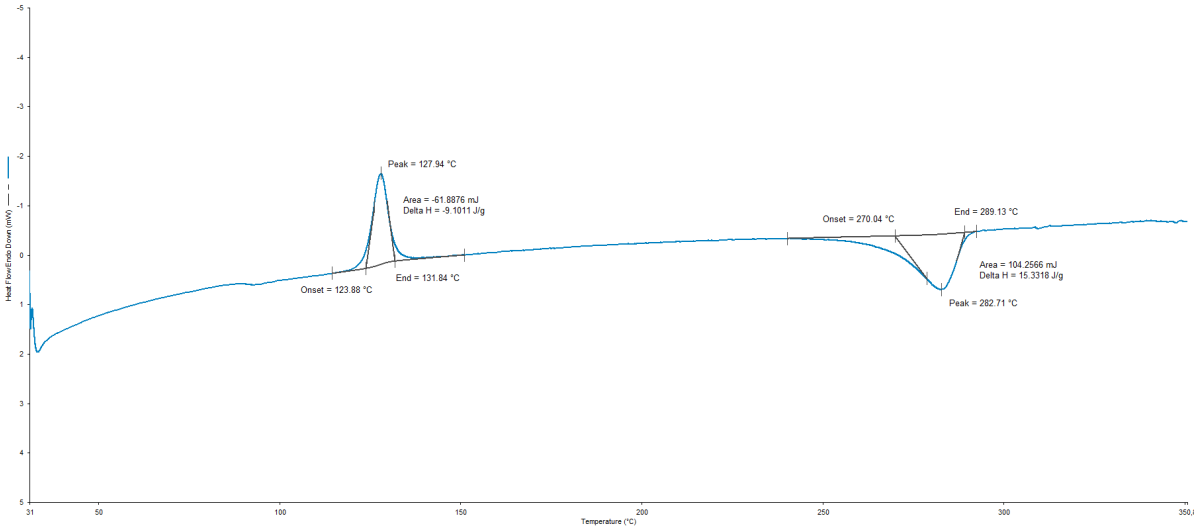

Figure B.22: PE: 200W 300ms

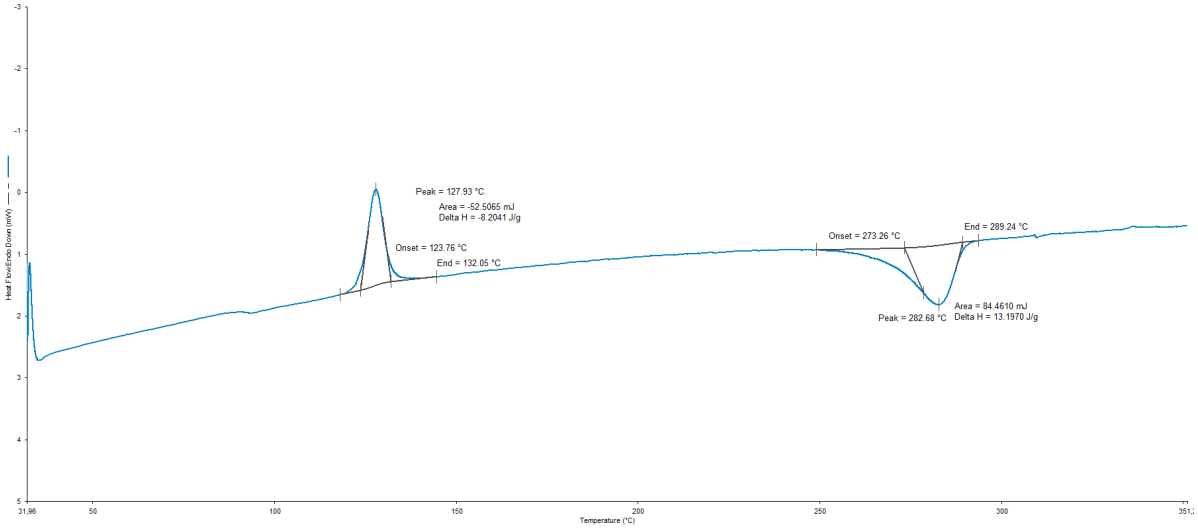

Heated above T_m using a pyramid laser power distribution

Figure B.23: PE: 4-6-4W 4200ms

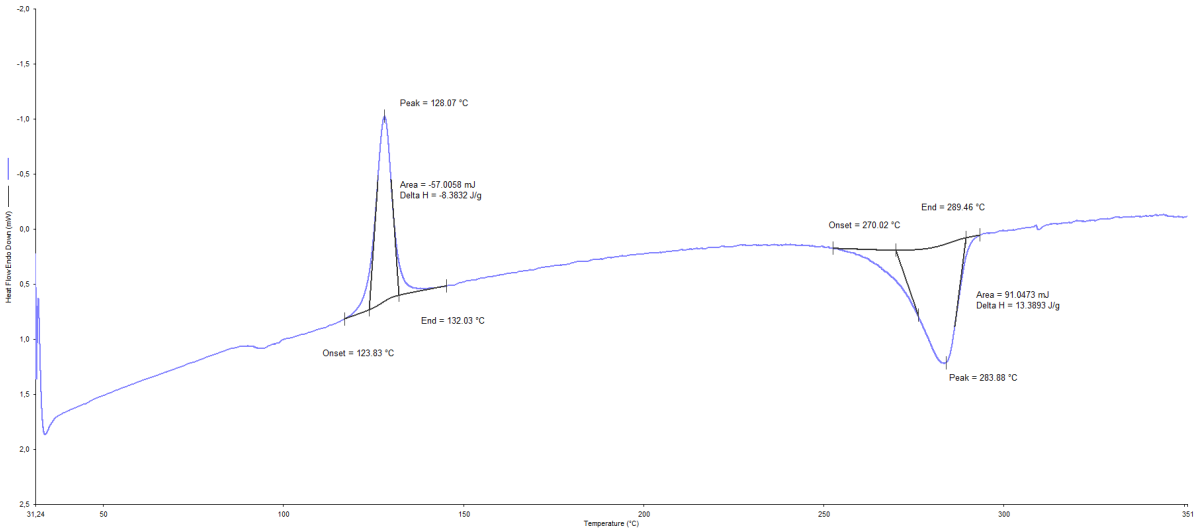

Figure B.24: PE: 9-12-9W 2000ms

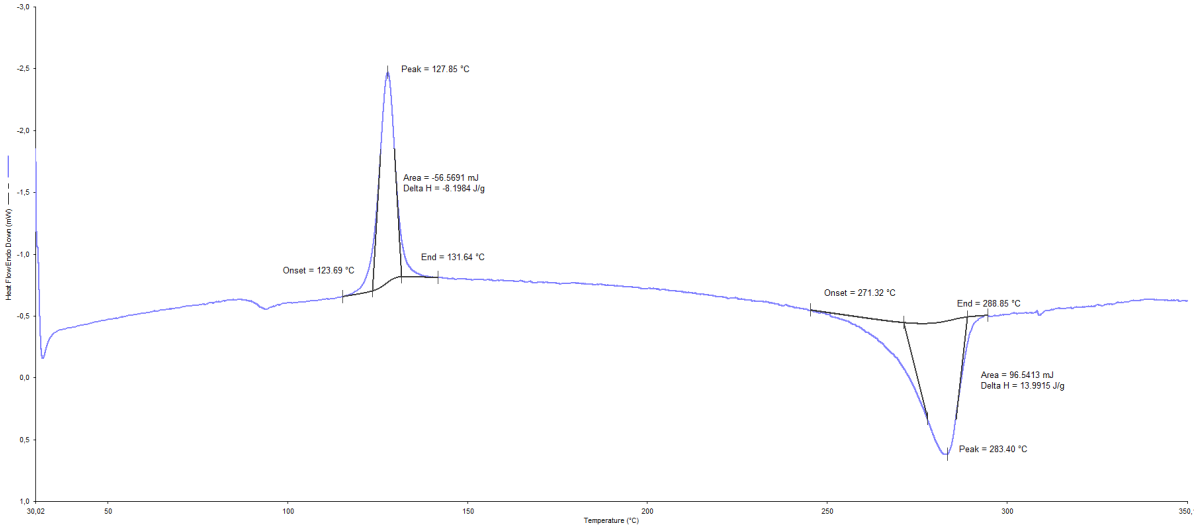

Figure B.25: PE: 18-24-18W 1000ms

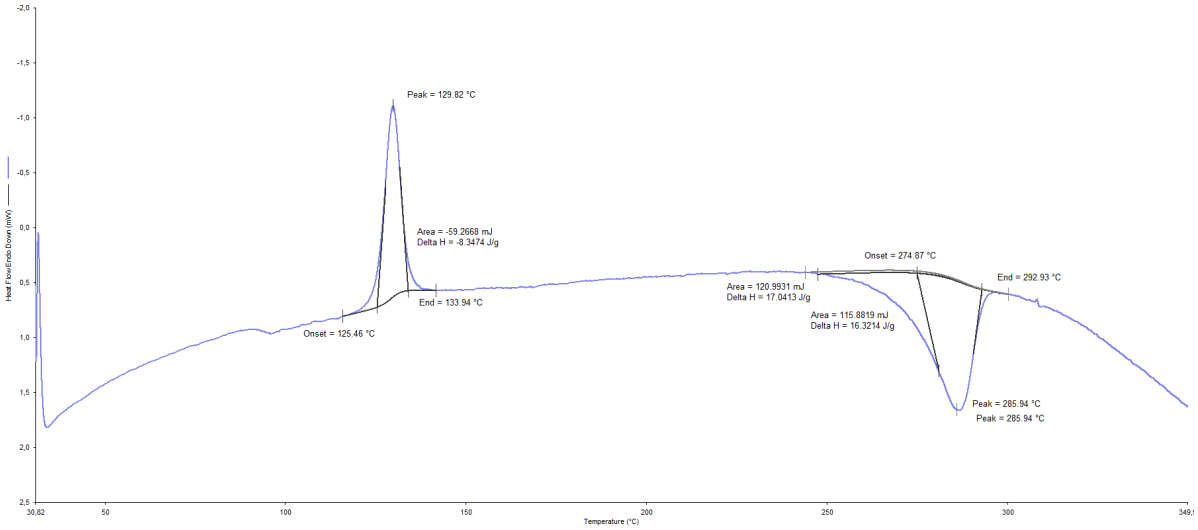

Figure B.26: PE: 38-50-38W 400ms

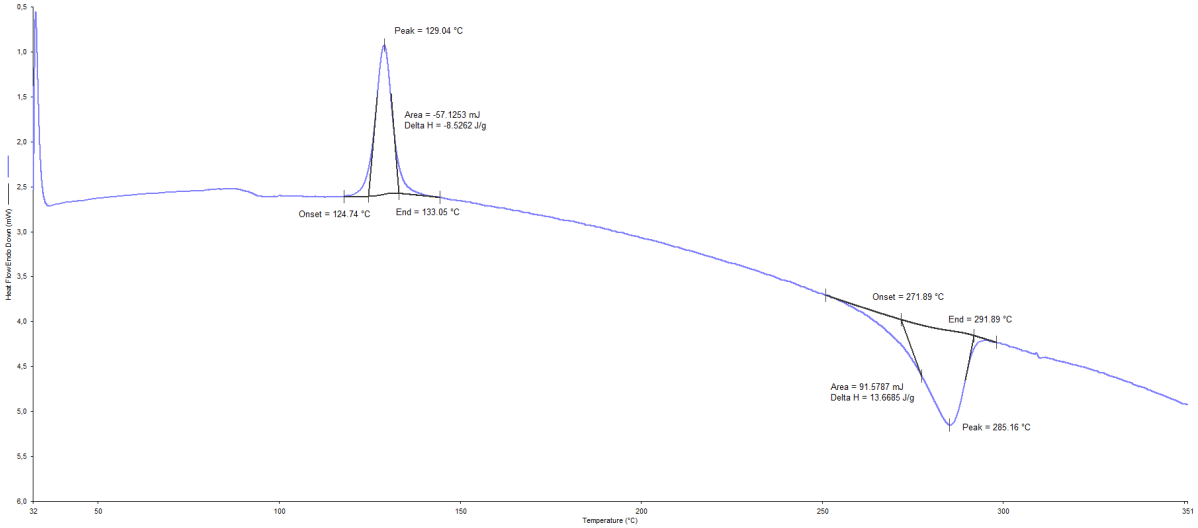

Figure B.27: PE: 75-100-75W 200ms

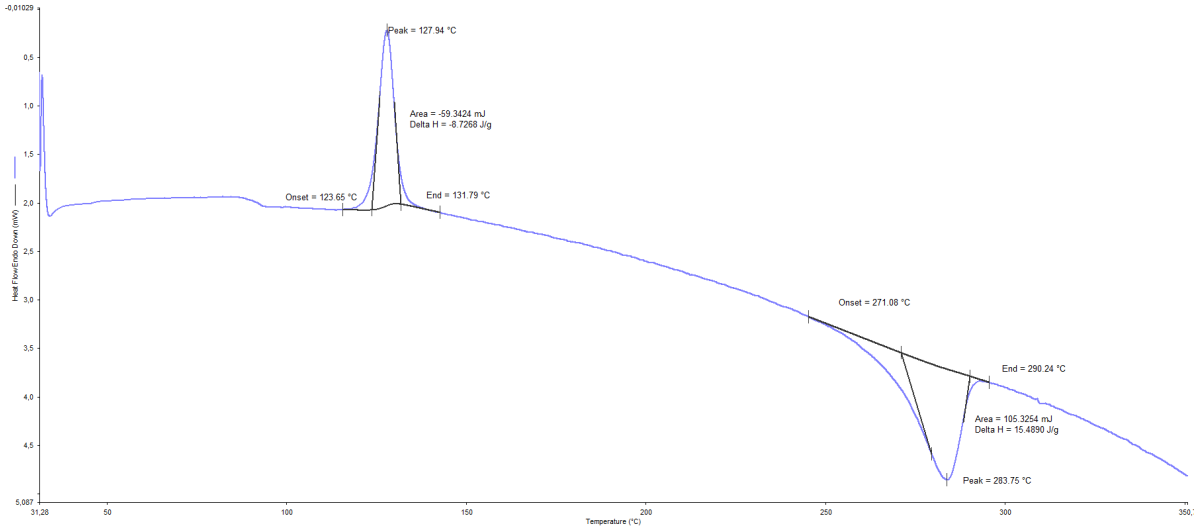

Figure B.28: PE: 75-100-75W 200ms

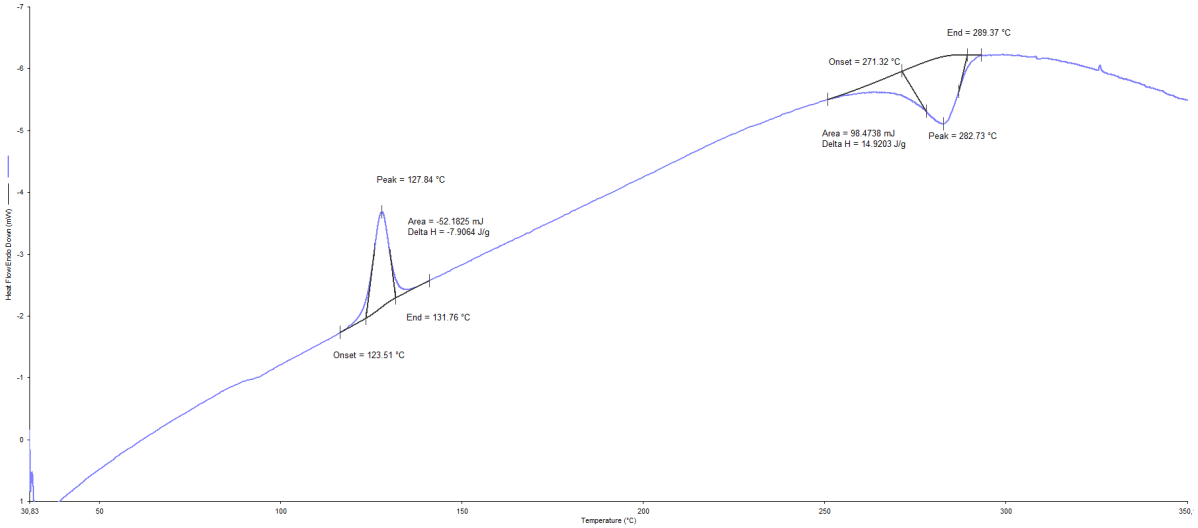

Figure B.29: PE: 150-200-150W 100ms

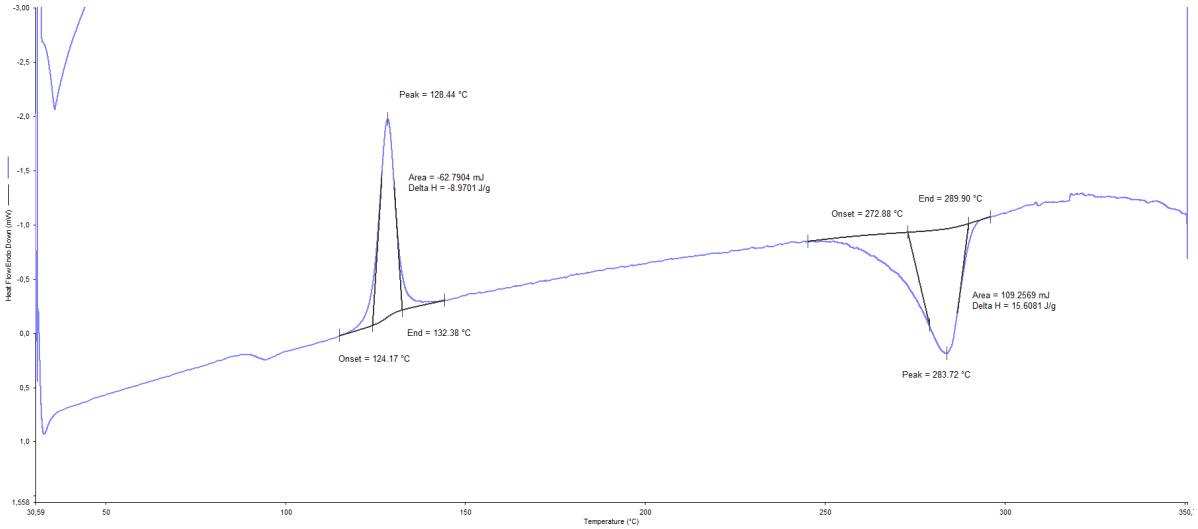

Heated below T_m

Figure B.30: TA: 20W 1000ms

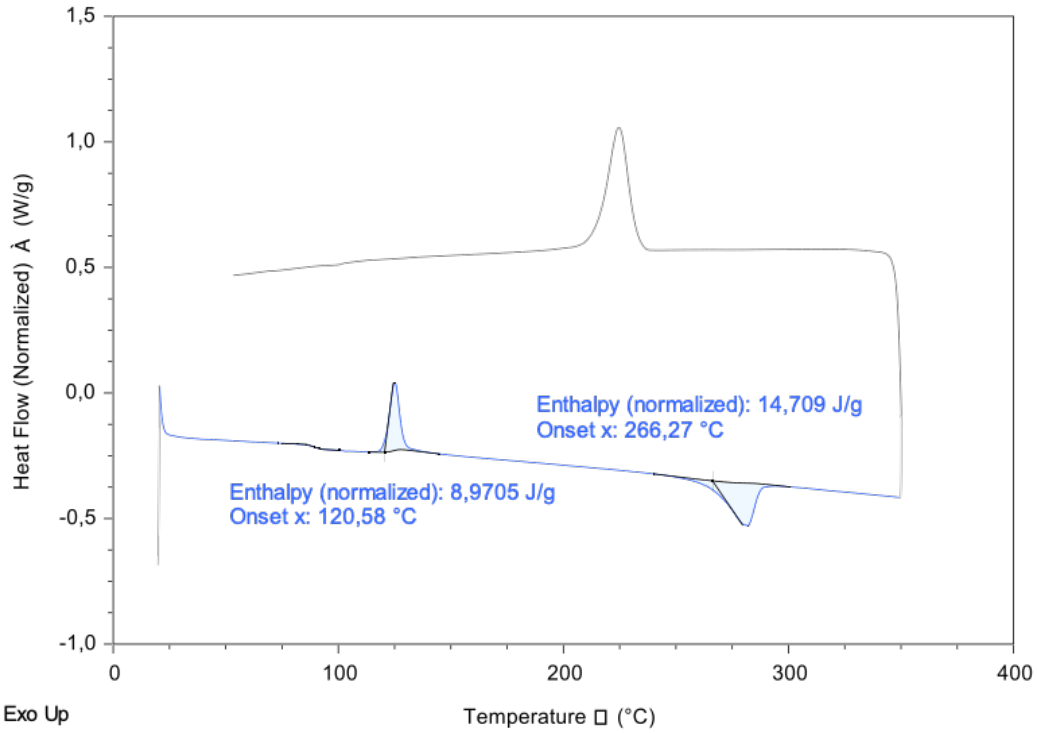

Figure B.31: TA: 20W 1250ms

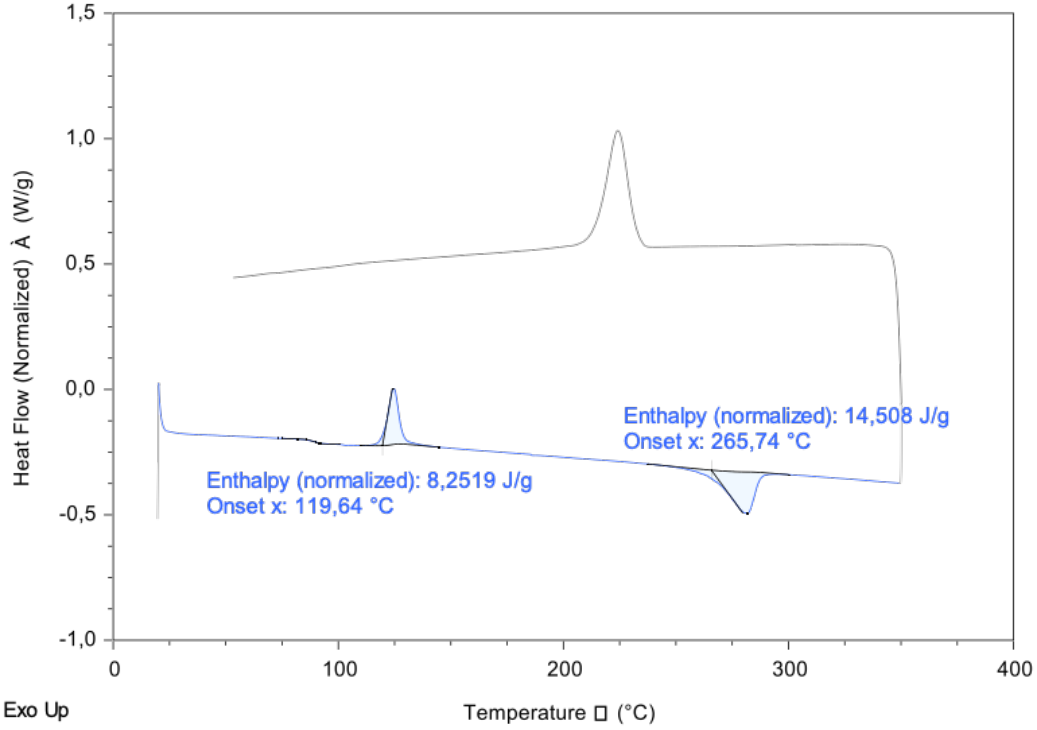

Figure B.32: TA: 20W 1500ms

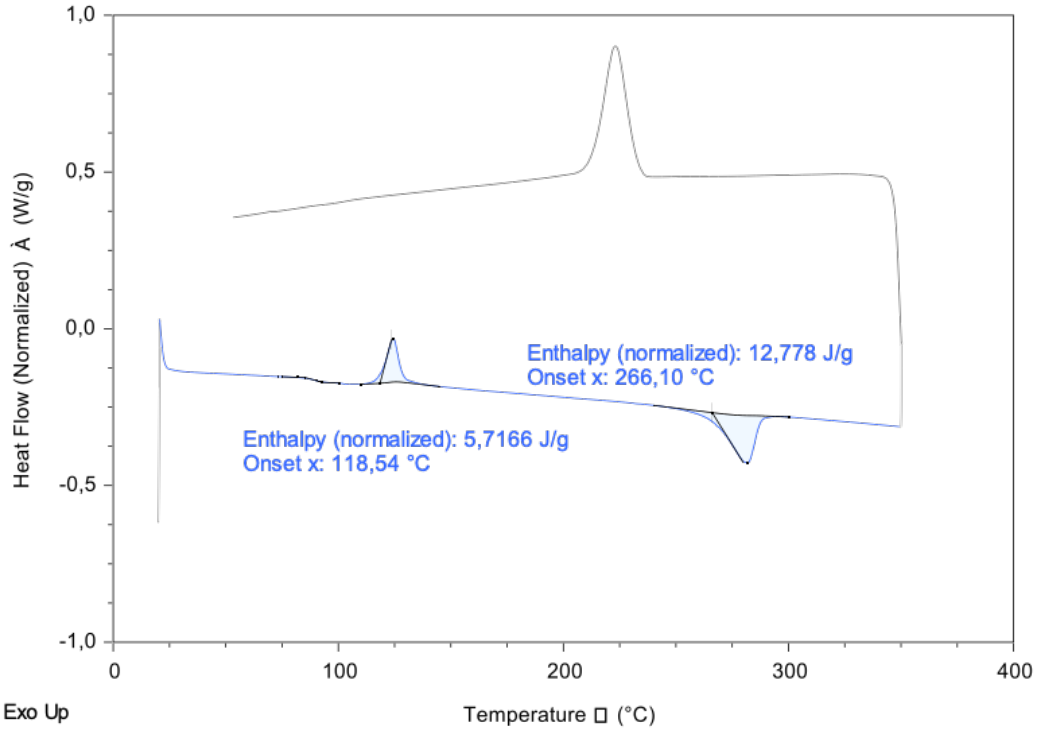

Figure B.33: TA: 20W 1600ms

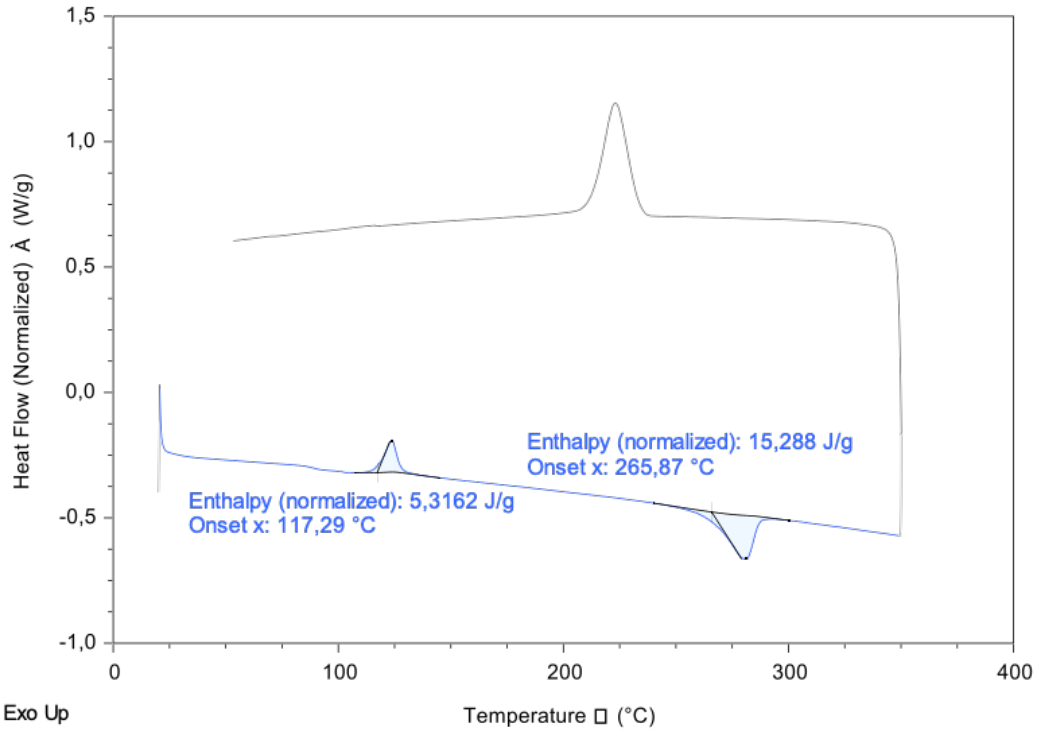

Figure B.34: TA: 20W 1750ms

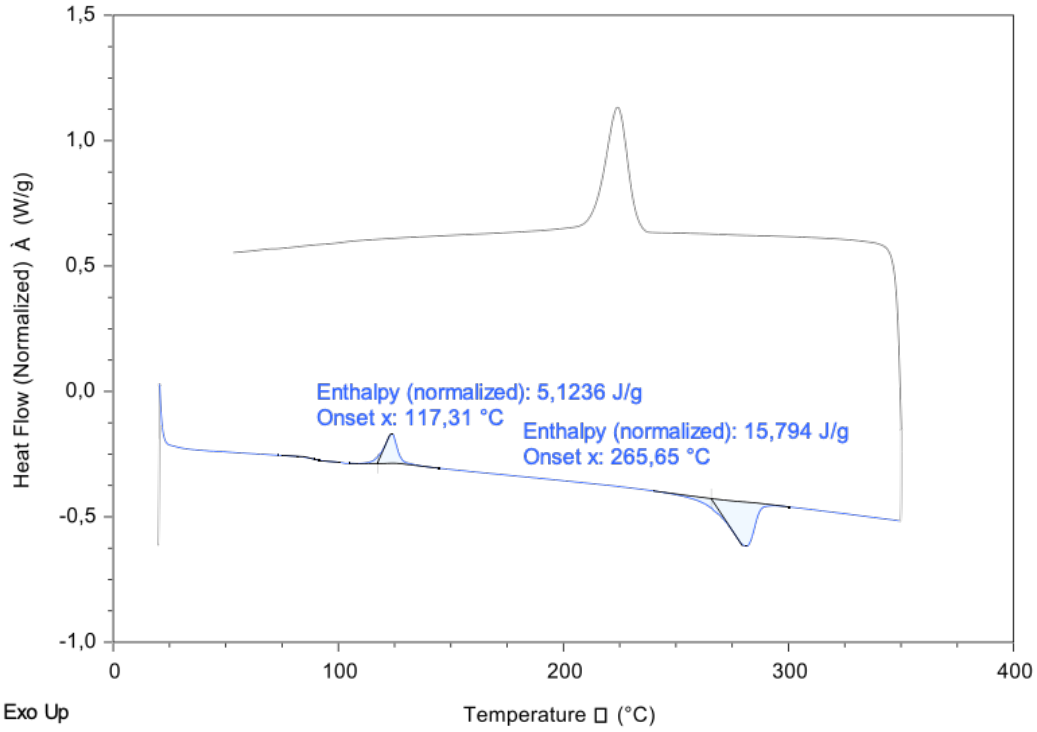

Figure B.35: TA: 30W 950ms

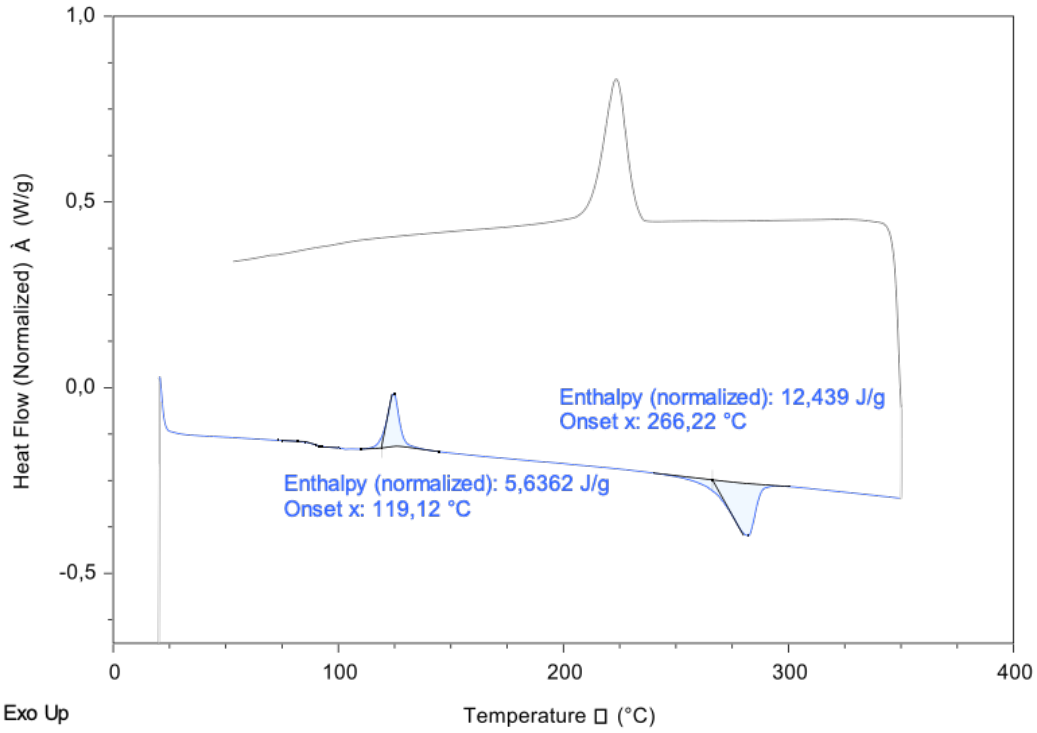

Figure B.36: TA: 30W 1100ms

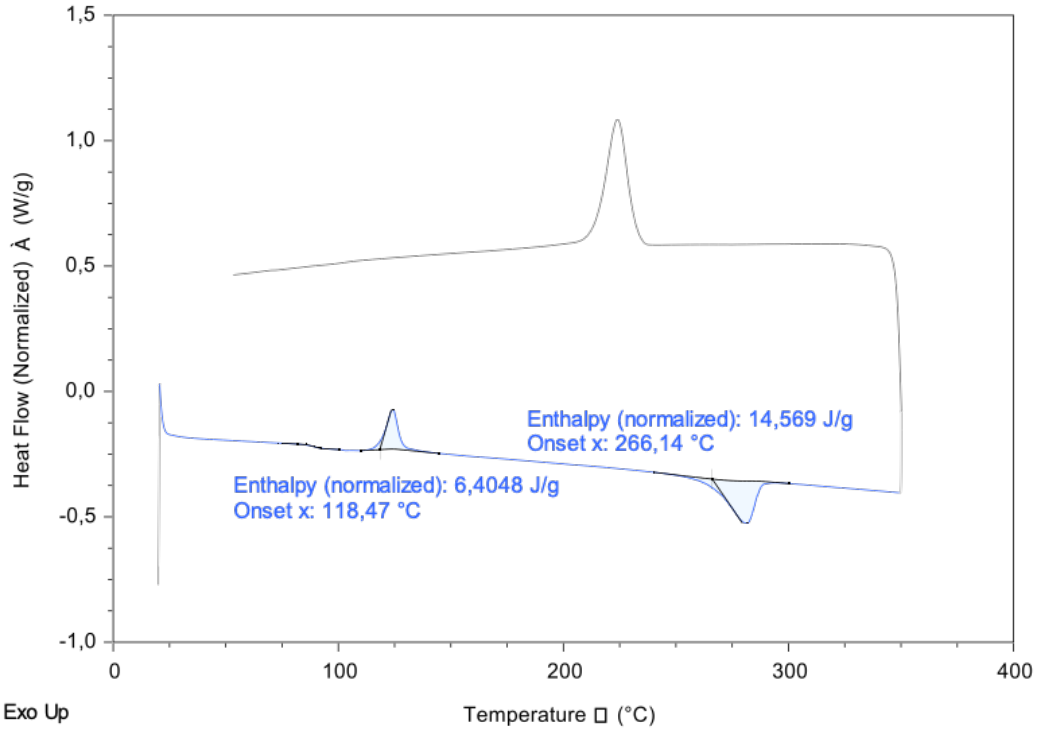

Figure B.37: TA: 40W 700ms

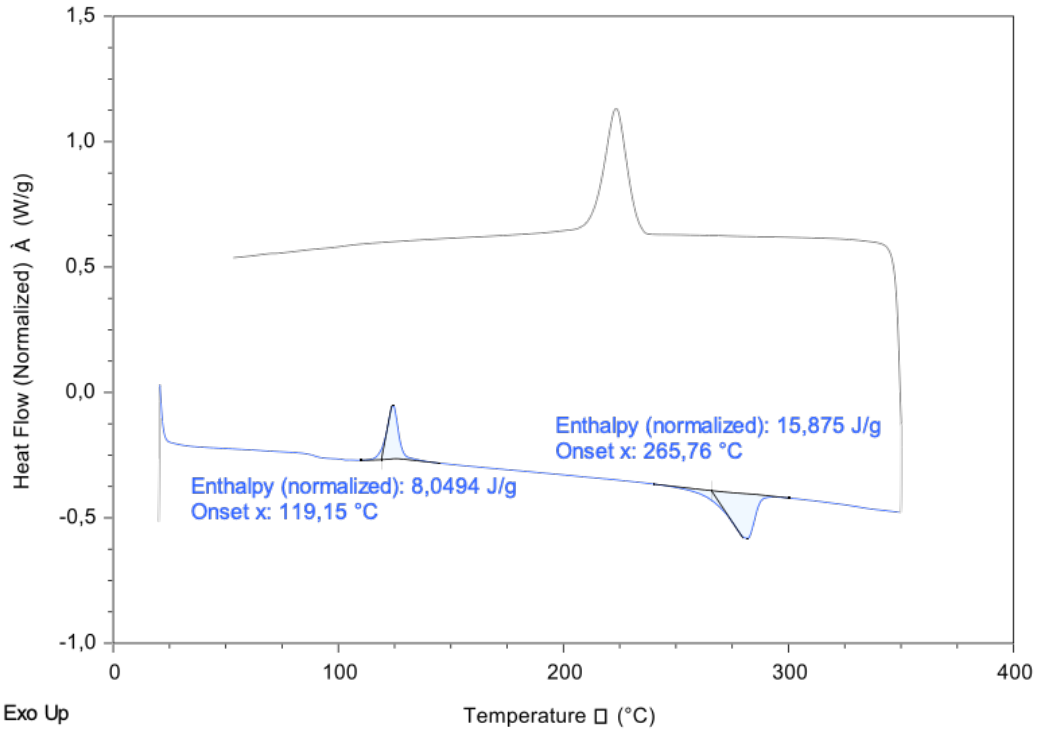

Figure B.38: TA: 40W 800ms

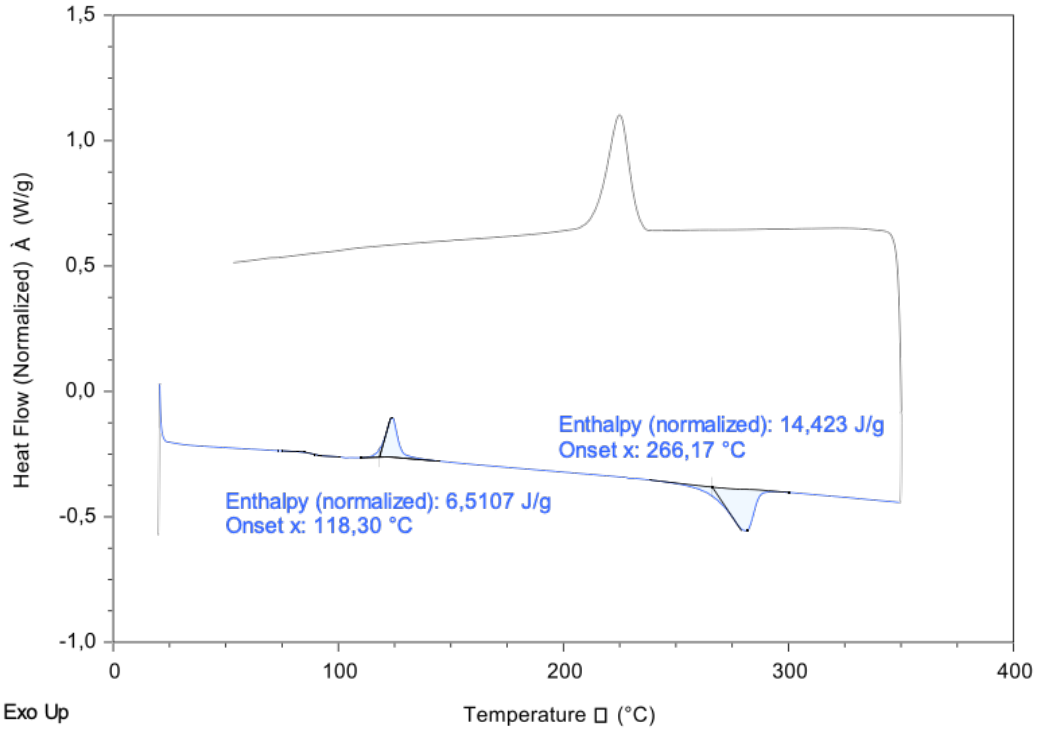

Figure B.39: TA: 50W 500ms

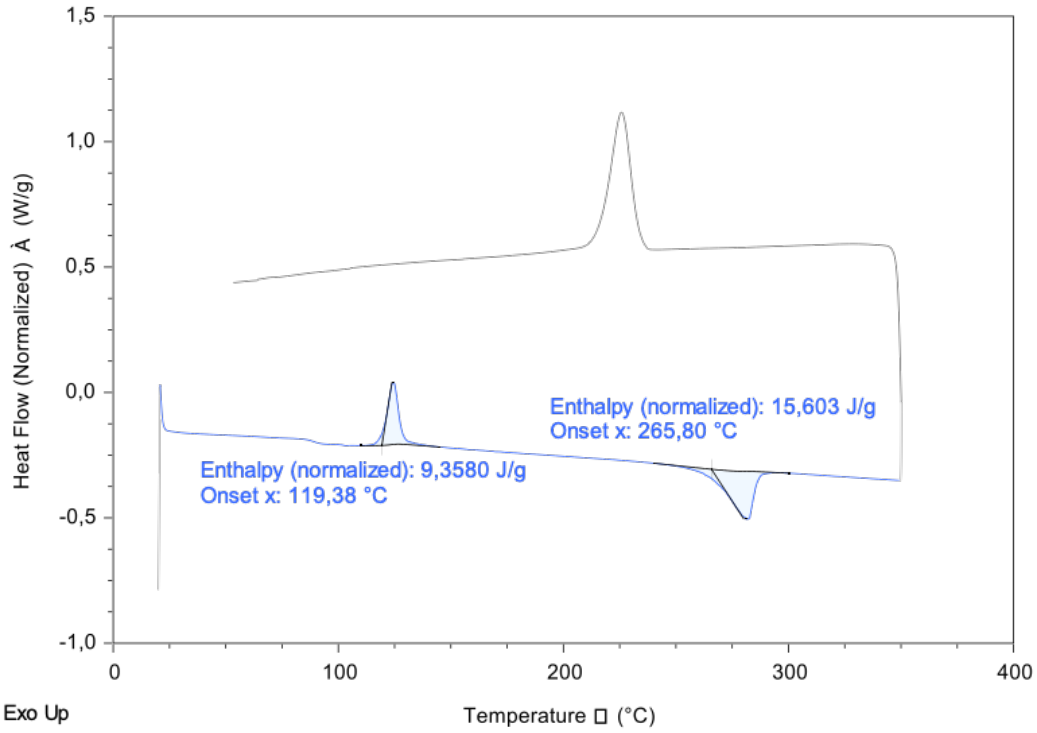

Figure B.40: TA: 50W 600ms

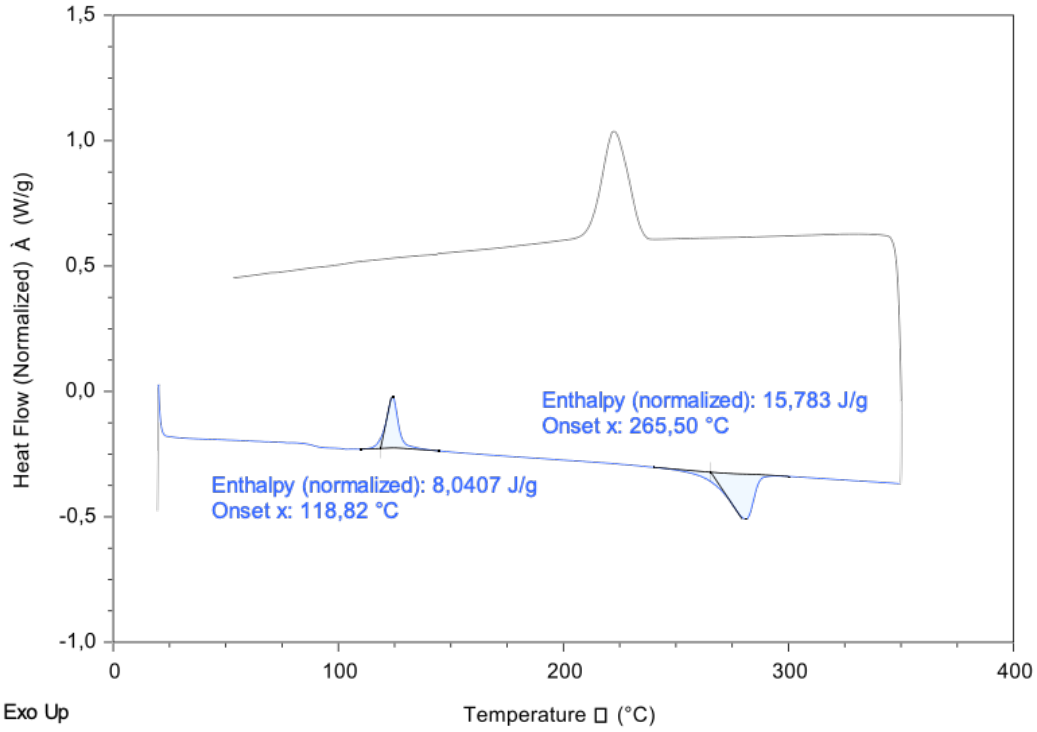

Figure B.41: TA: 75W 550ms

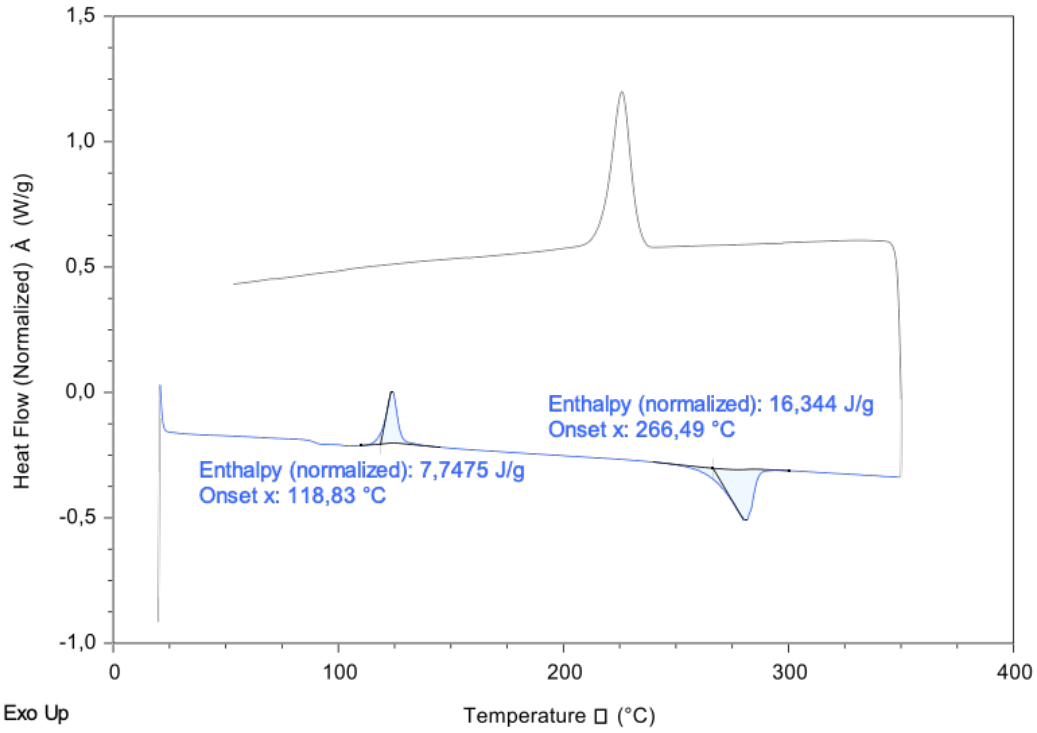

Figure B.42: TA: 100W 450ms

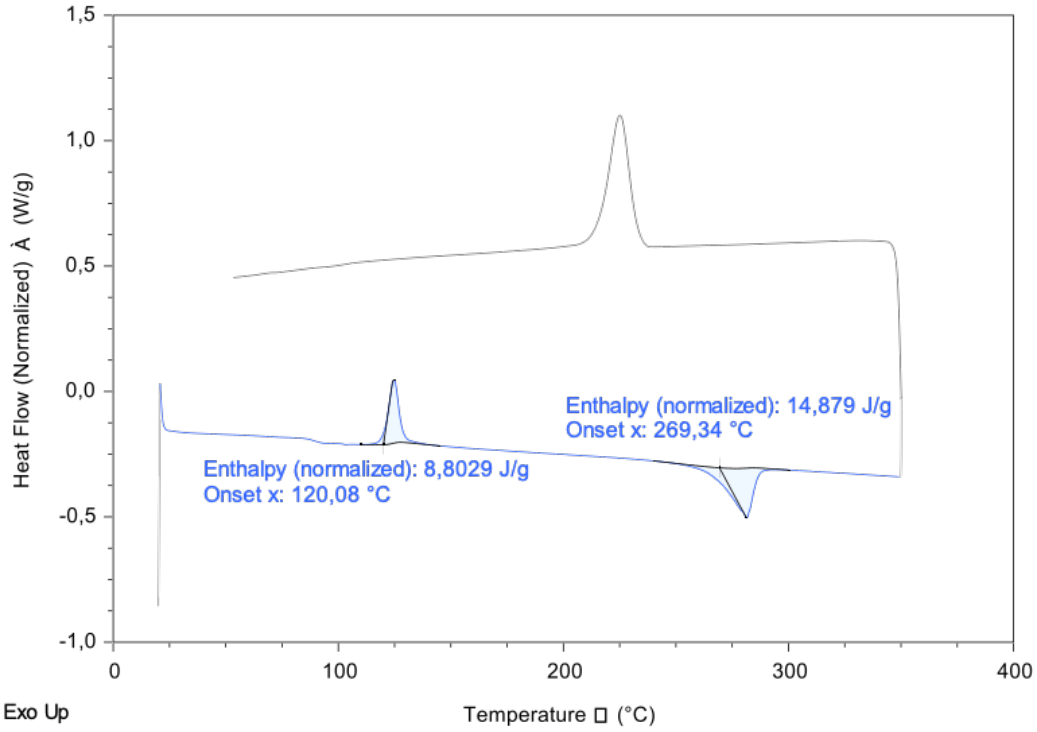

Heated above T_m

Figure B.43: TA: 50W 1750ms

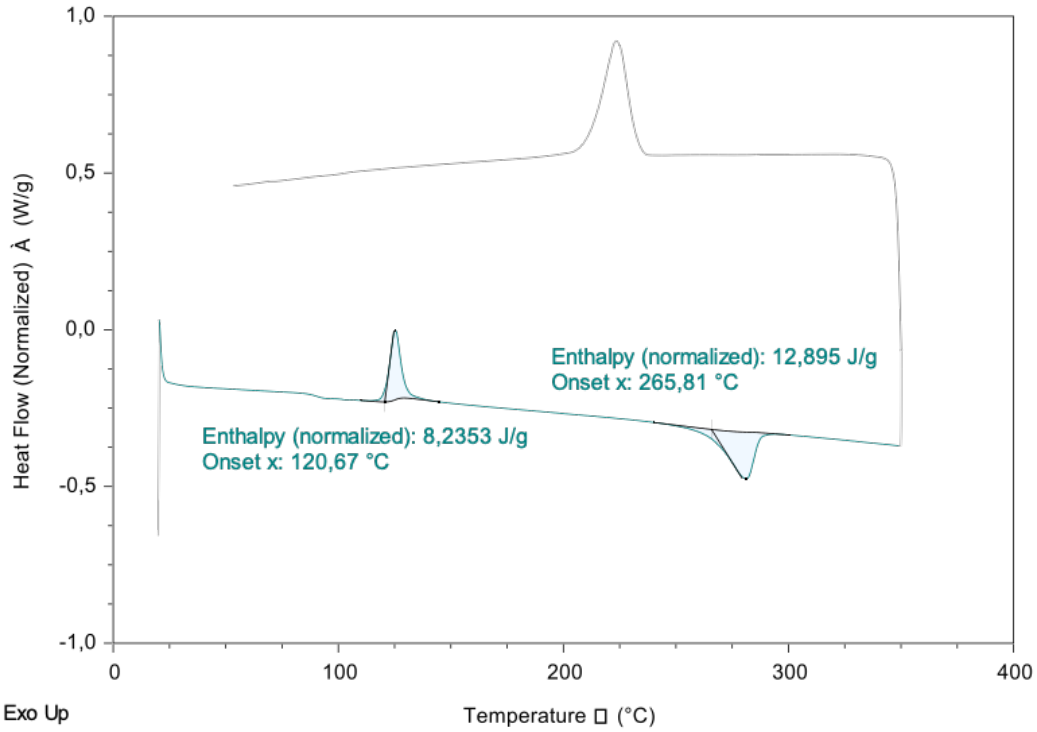

Figure B.44: TA: 50W 2000ms

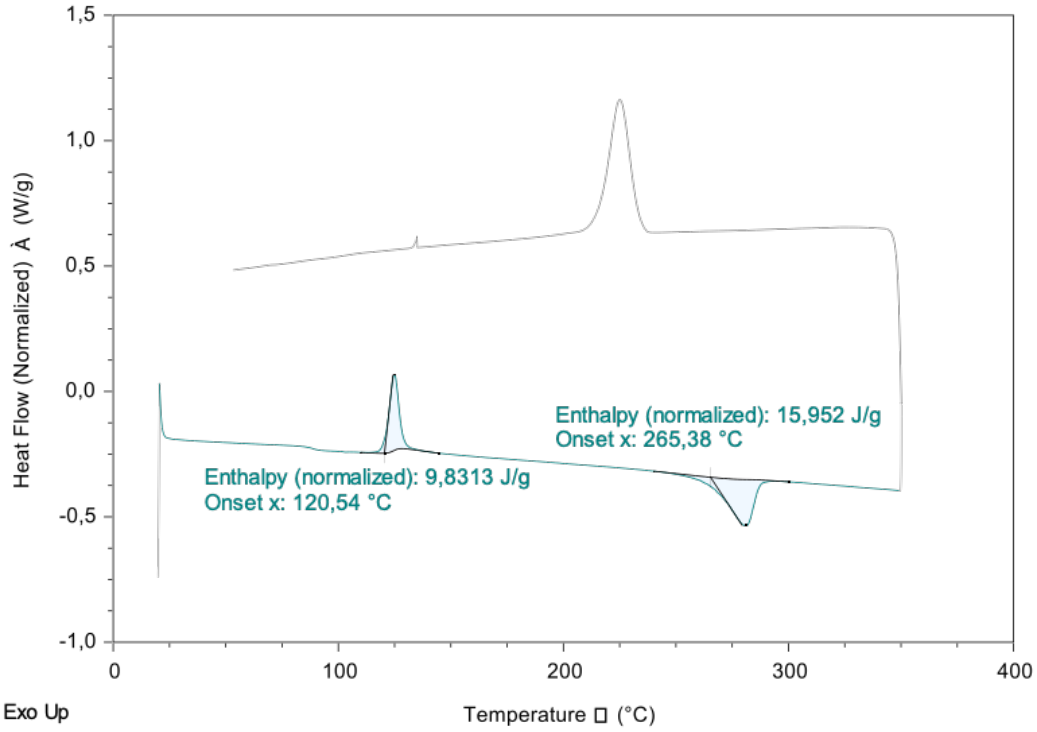

Figure B.45: TA: 100W 850ms

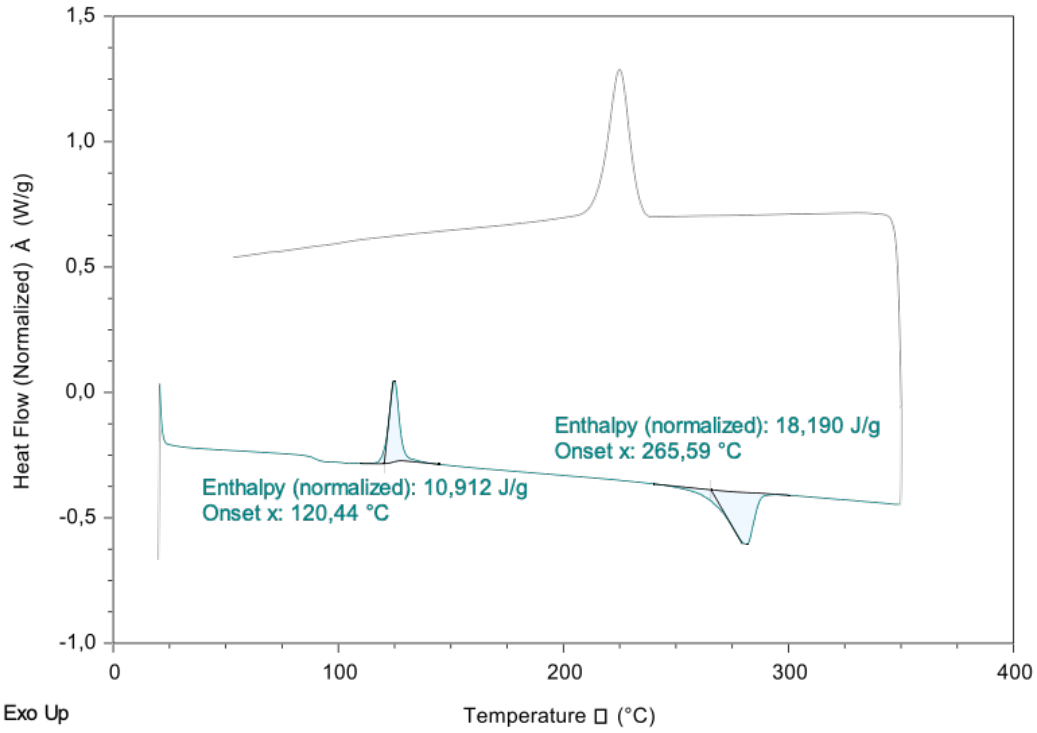

Figure B.46: TA: 100W 900ms

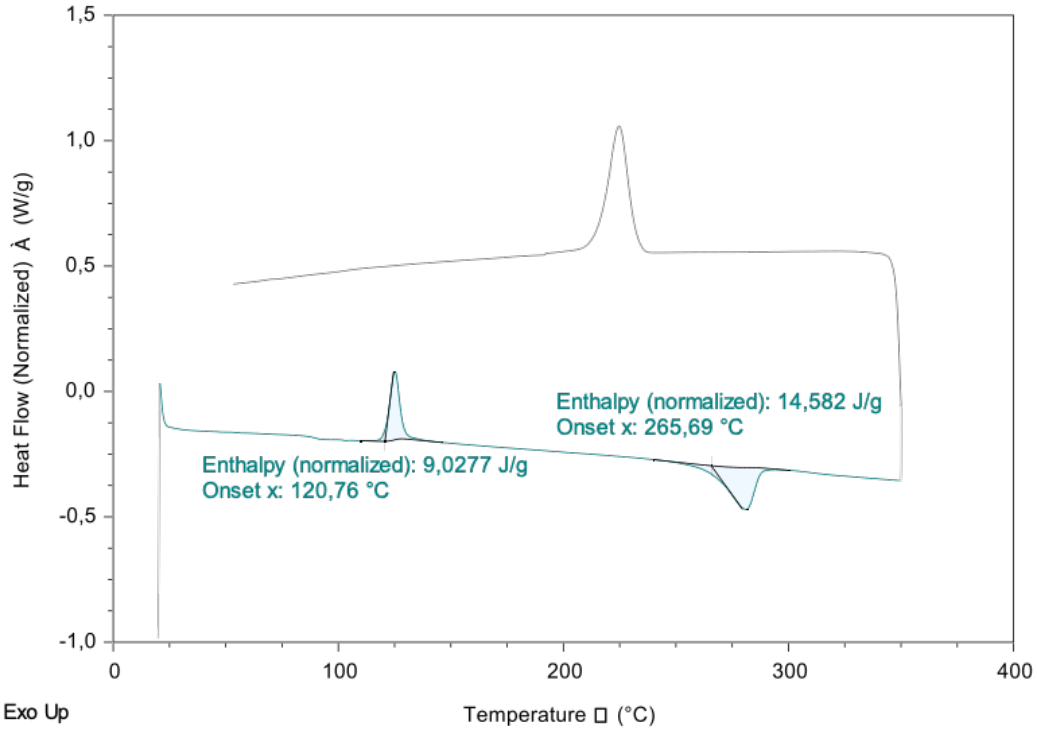

Figure B.47: TA: 150W 500ms

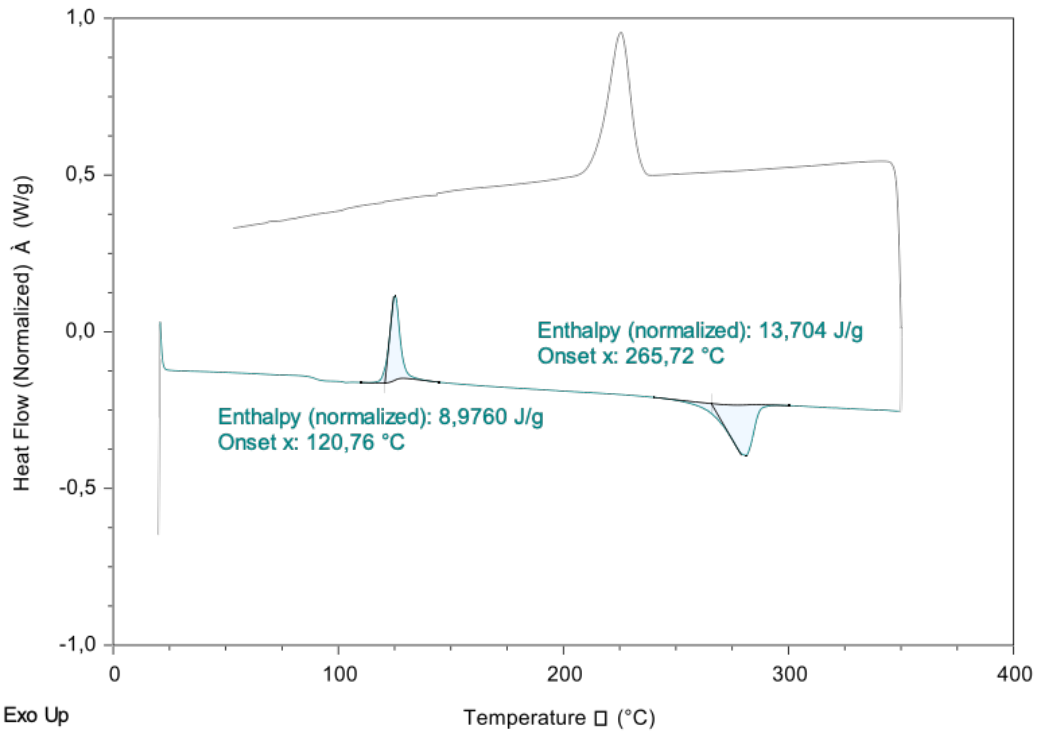

Figure B.48: TA: 150W 600ms

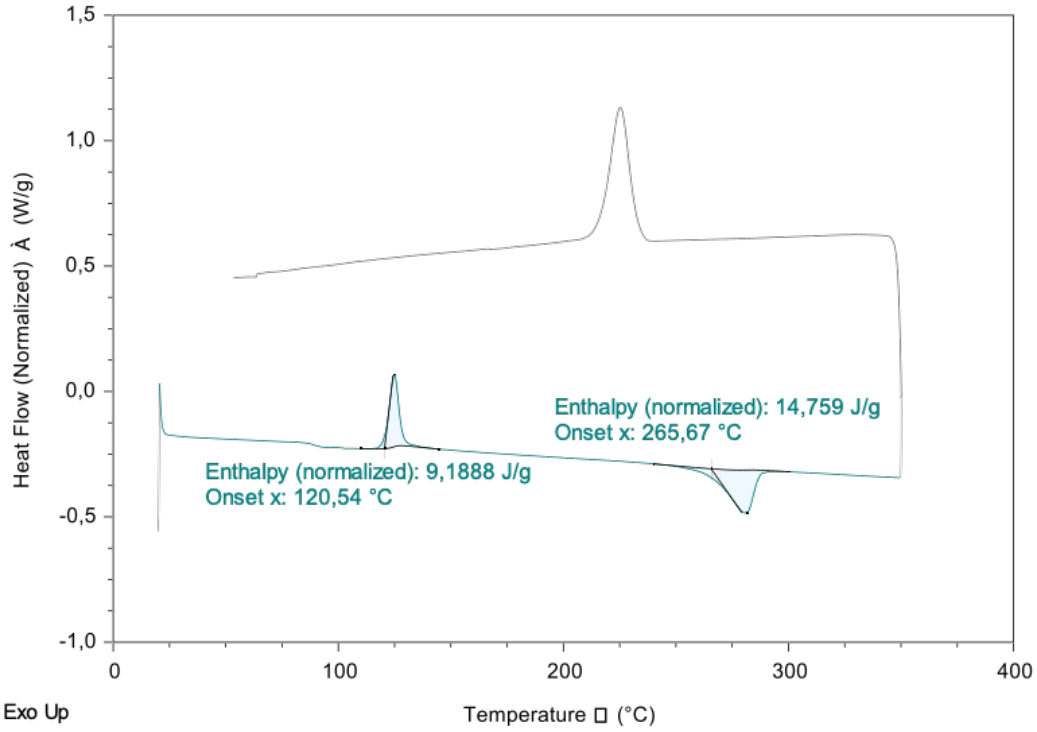

Figure B.49: TA: 150W 650ms

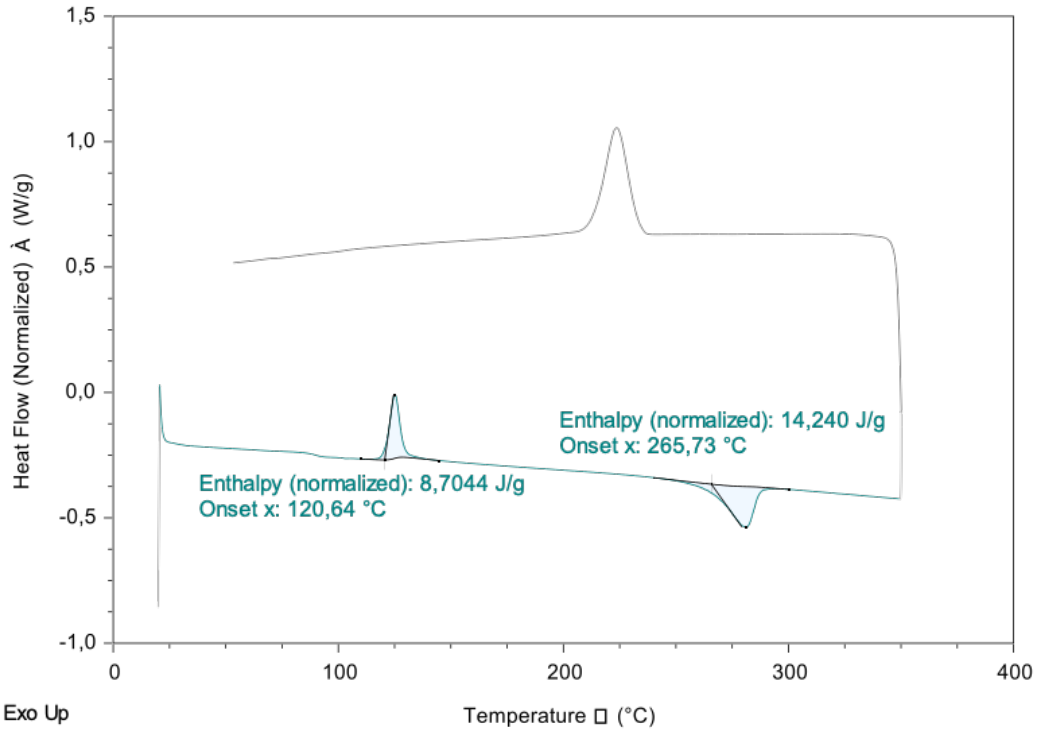

Figure B.50: TA: 200W 450ms

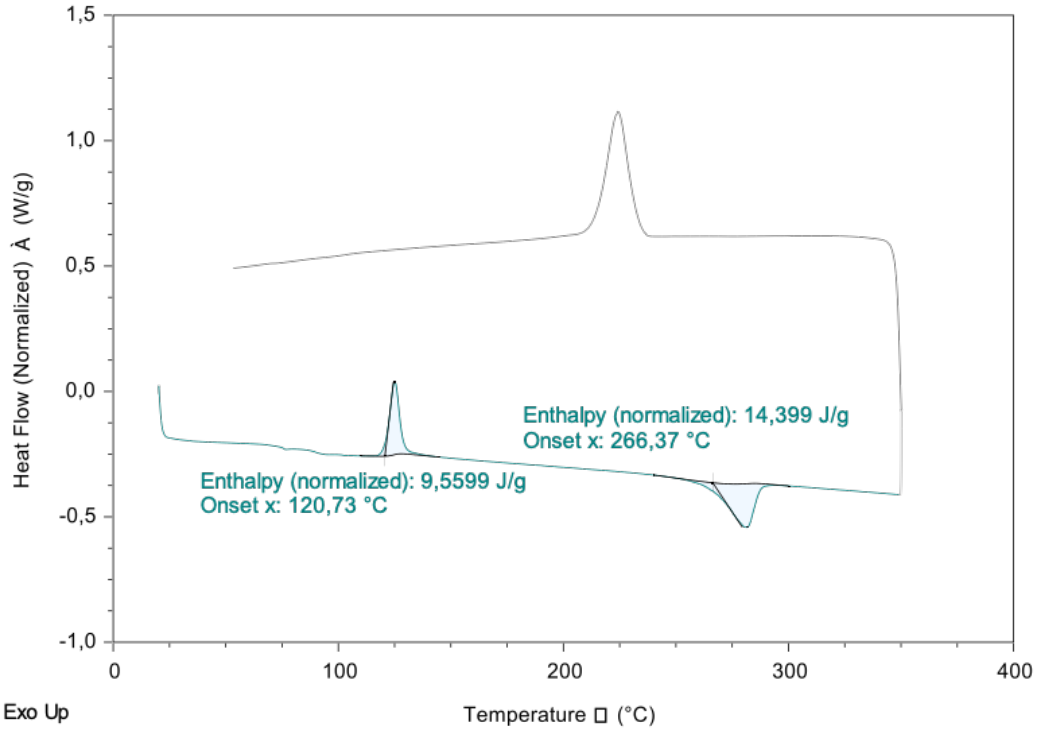

Figure B.51: TA: 200W 450ms

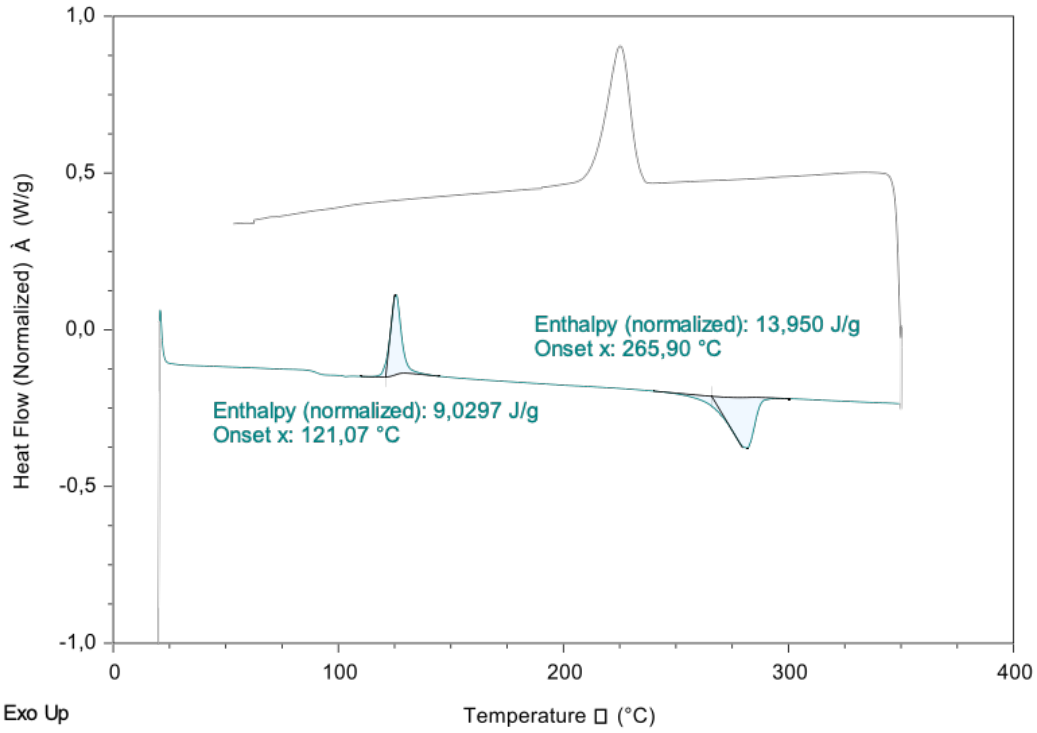

Figure B.52: TA: 300W 300ms

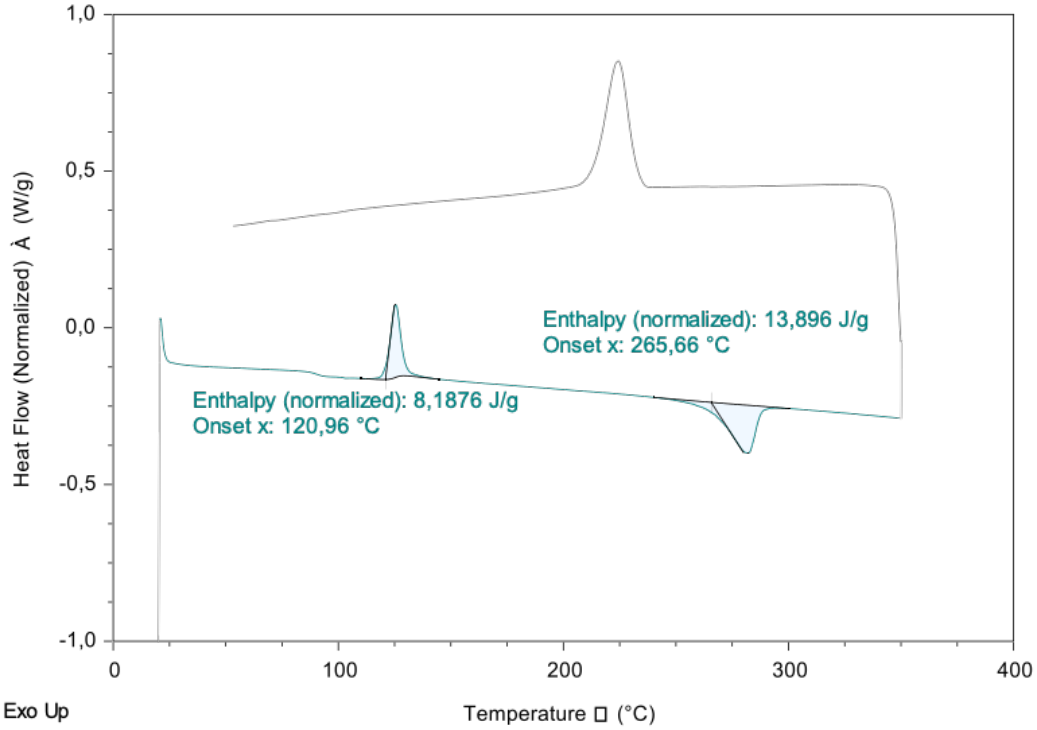

Figure B.53: TA: 300W 300ms

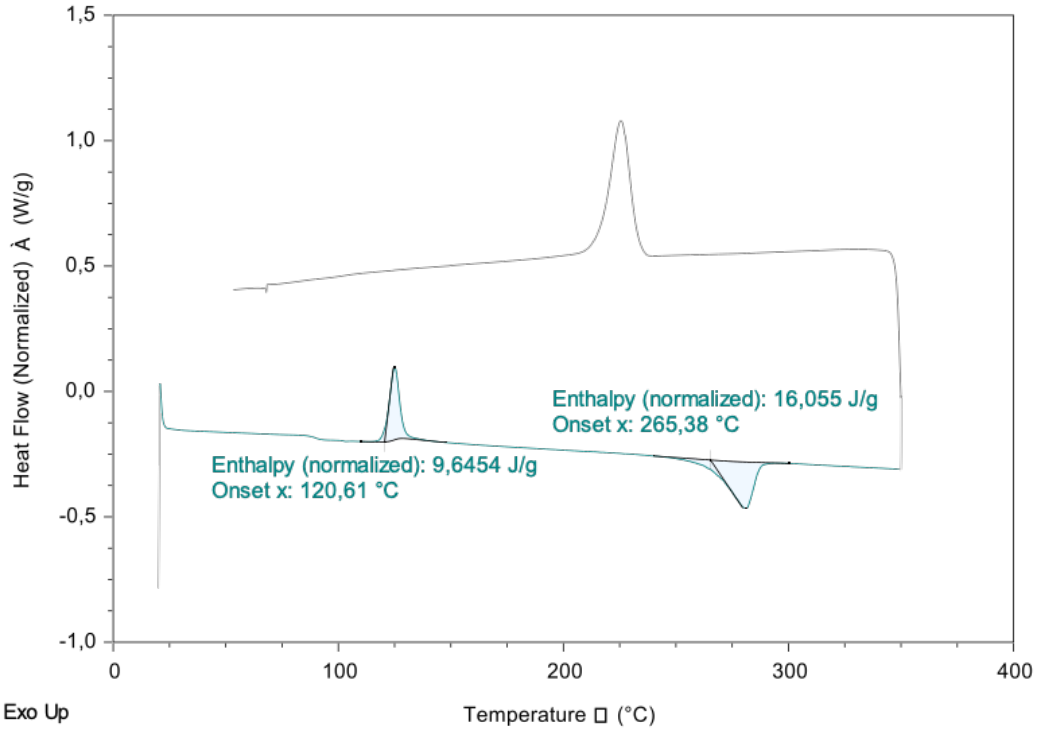

Figure B.54: TA: 400W 200ms

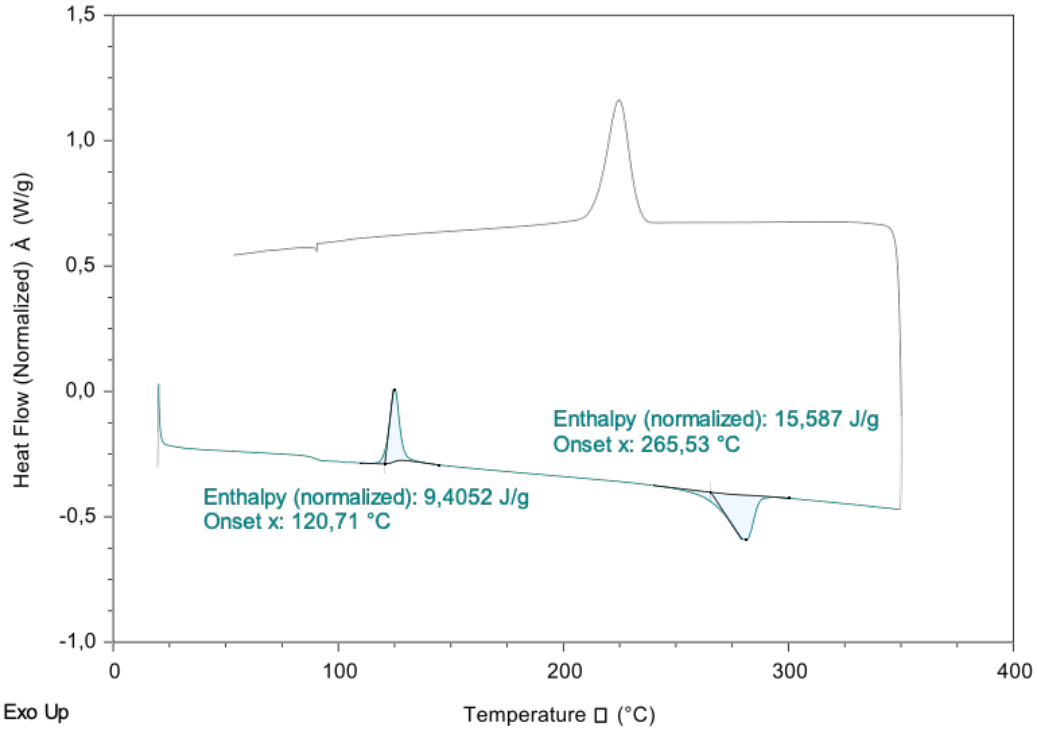

Figure B.55: TA: 400W 250ms

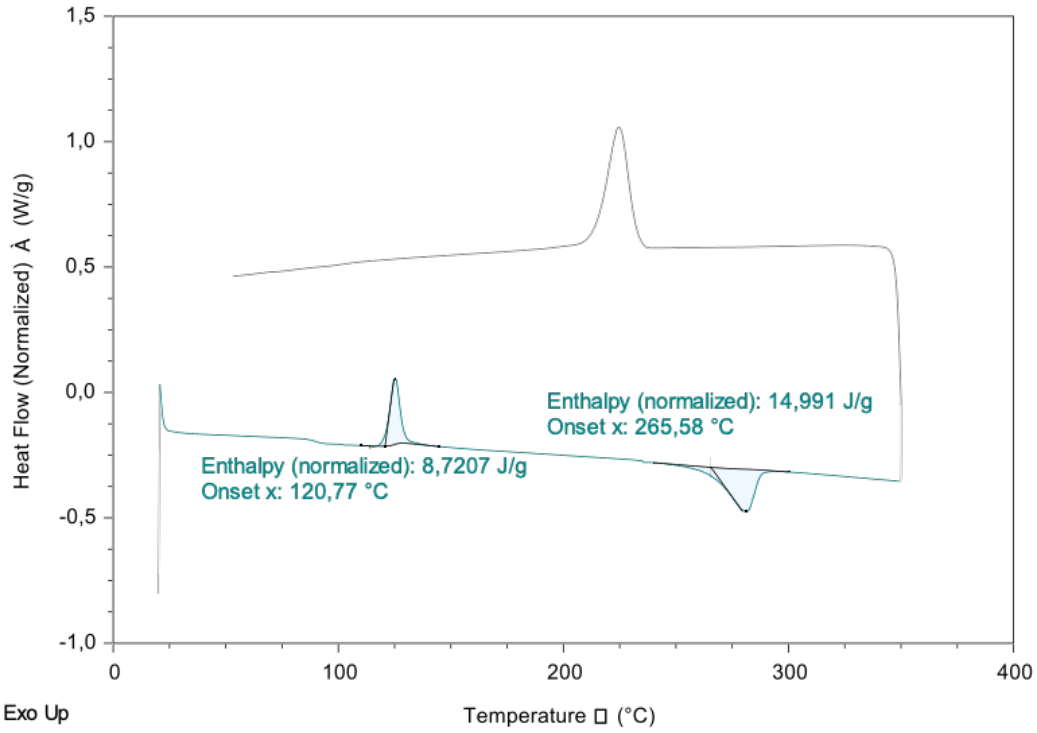

C

Temperature rate evolution

In the plots in this section, the sample temperature evolution over time is plotted together with the corresponding temperature rate. To minimize the noise in the derived temperature rate, the average per 25 time steps was taken, resulting in an average offset of 0.0625 seconds between the temperature and temperature rate curves.

The green box in the plots indicates the time range in which the temperature lies within the range between T_g and T_m, and the cooling rate is between 25 and 0°C/s. For samples heated above T_m, this corresponds to the time frame in which melt-crystallization is theoretically possible. Due to the irregular time step size in the temperature measurements and noise obtained in the temperature, it was difficult to determine the exact time at which the cooling rate slows down below the critical 25°C/s. Additionally, the crystallization temperature range is know to end a few degrees above T_g, but the exact range for the used material is unknown. Similarly, the exact critical cooling rate for the used material is also unknown and suspected to be higher that 25°C/s. Therefore, the melt-crystallization window should be used purely as an approximate indication, and no exact times are listed.

In Figure C.1 the plots for samples heated above T_m are shown. In Figure C.2 the plots for samples heated below T_m are shown.

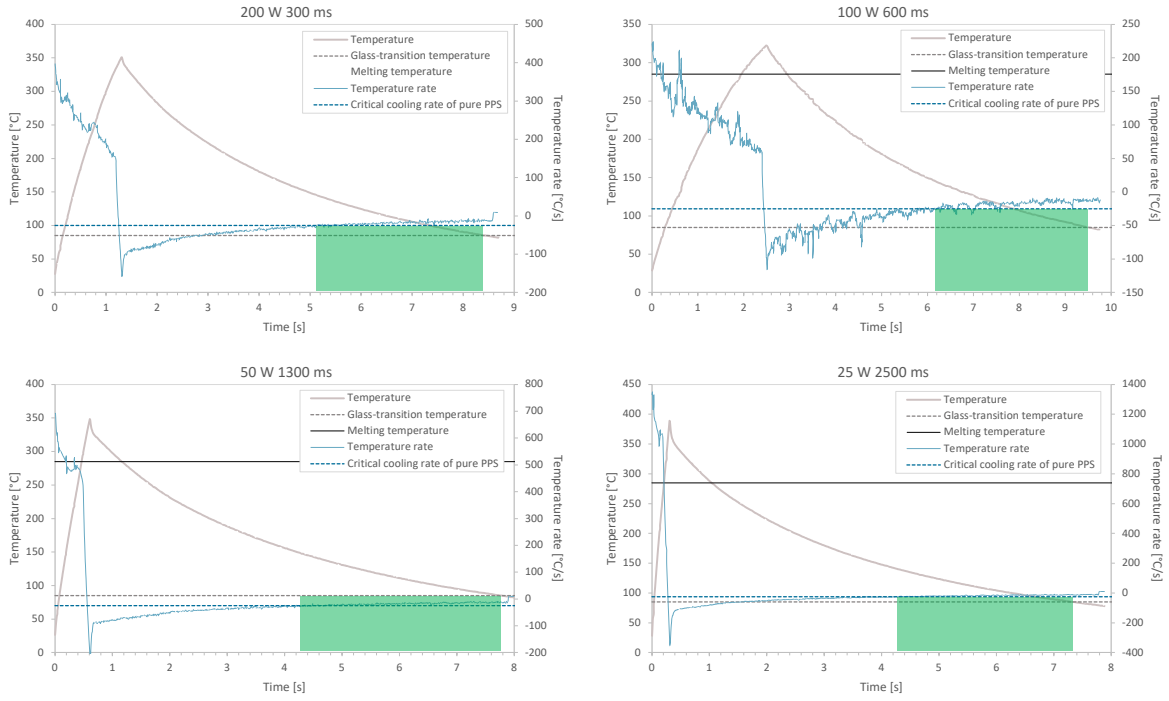

Figure C.1: Temperature rate evolution for samples heated above T_m

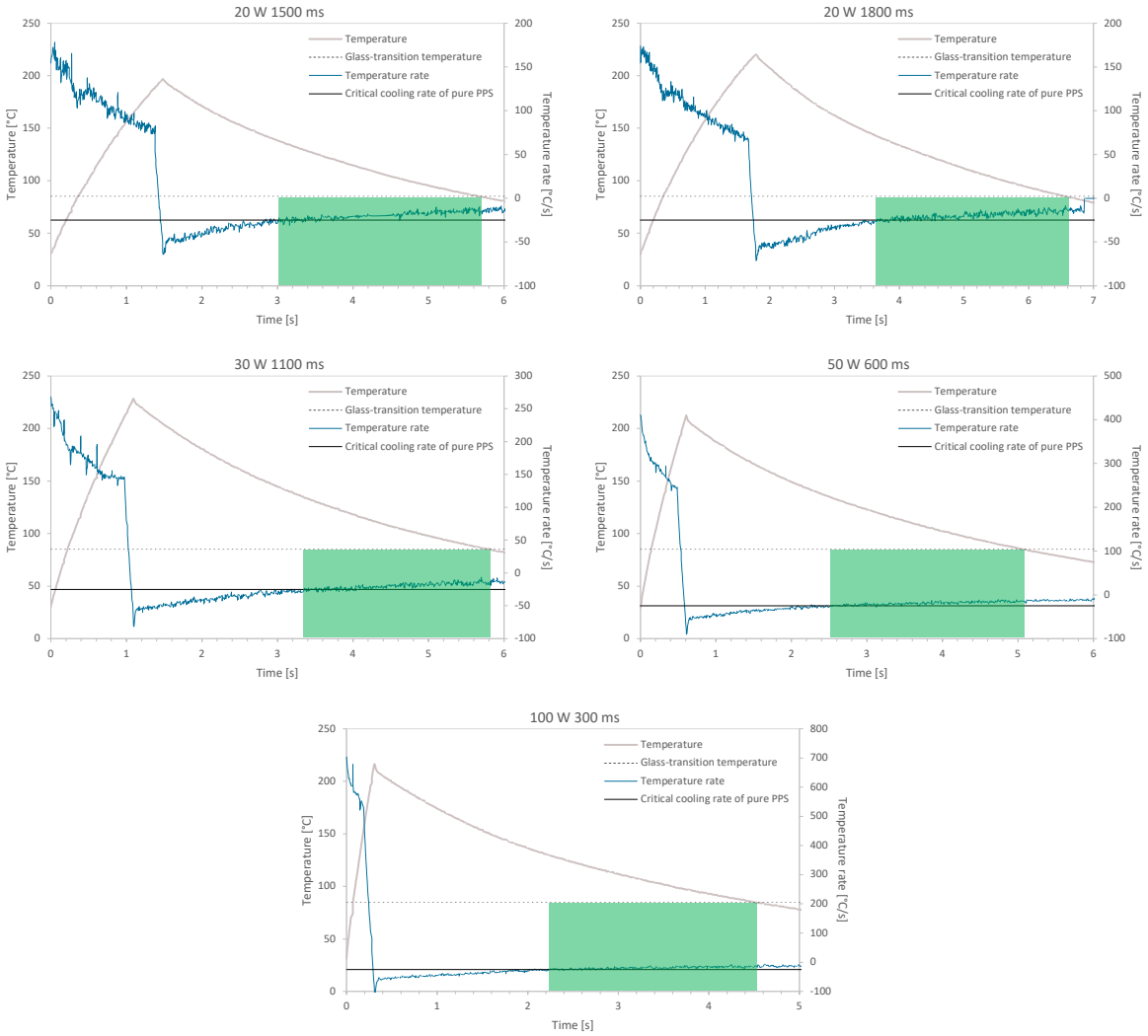

Figure C.2: Temperature rate evolution for samples heated below T_m

D

Additional crystallinity - temperature plots

Figure D.1: Additional plots for the sample set heated with 12 emitters to temperatures above T_m, showing the relation between DOC and: Maximum top and bottom surface temperature, heating and cooling rate, heating and cooling time

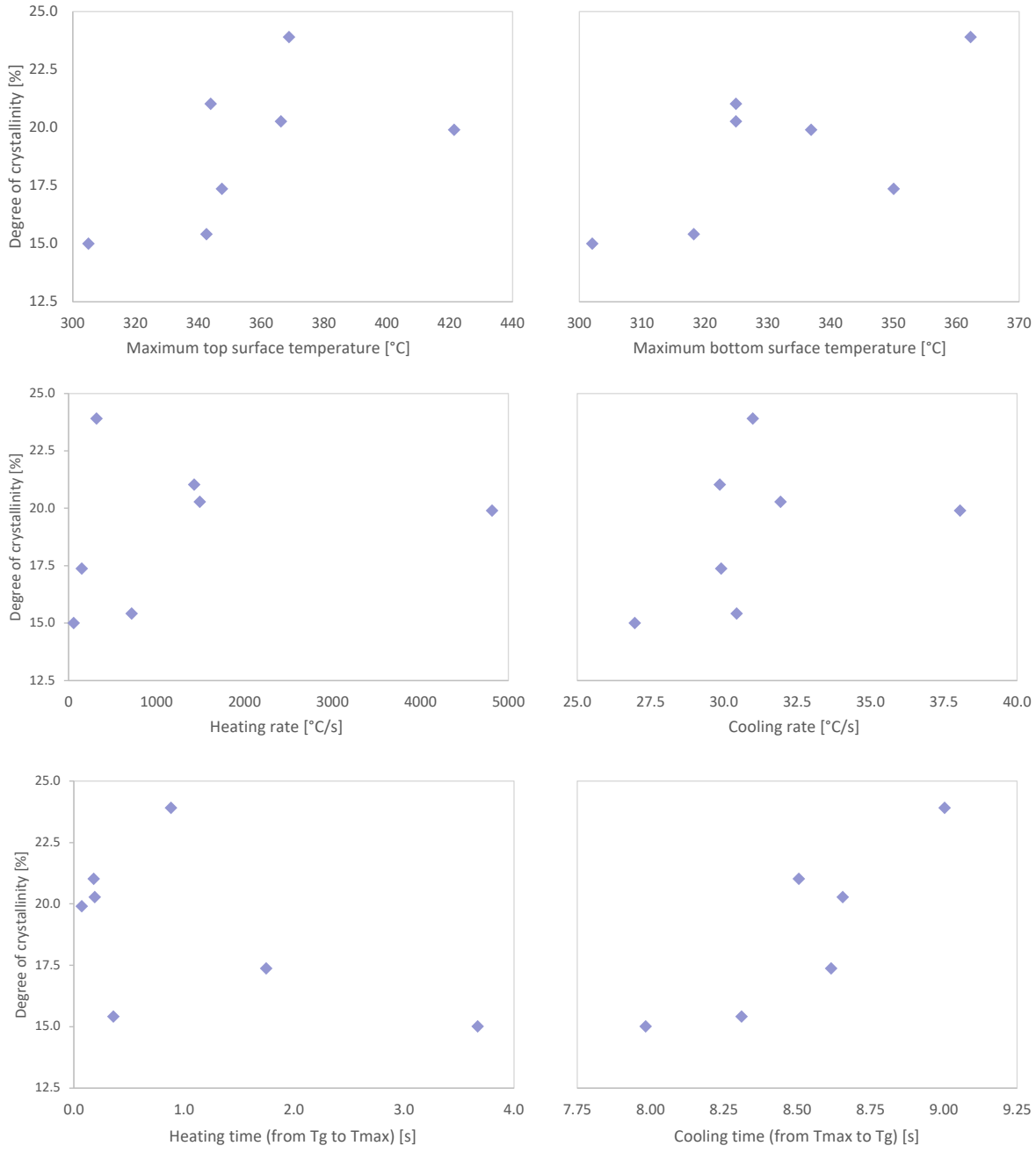

Figure D.2: Additional plots for the sample set heated with 12 emitters to temperatures above T_m, showing the relation between DOC and: Time spent above T_g and T_m, time spent between T_g and T_m during heating and cooling, Temperature integral for temperatures above T_g and T_m